OBSERVATIONAL STUDY OF THE ROLE OF MAGNETIC FIELDS IN STAR FORMATION

BY

NICHOLAS SZANDOR HAKOBIAN

DISSERTATION

Submitted in partial fulfillment of the requirements
for the degree of Doctor of Philosophy in Astronomy
in the Graduate College of the
University of Illinois at Urbana-Champaign, 2013

Urbana, Illinois

Doctoral Committee:

Professor Emeritus Richard Crutcher, Chair
Professor Charles Gammie
Associate Professor Leslie Looney
Professor Thomas Troland, University of Kentucky

Abstract

This project is a multi-faceted approach to establish a link between proposed theories of star formation and direct observation. Some key factors explored include: if magnetic fields cause significant support against gravitational collapse, which physical parameters are sampled by different tracer molecules, and what these results tell us about the structure and development of the regions observed. Until recently, only ambipolar diffusion theory had numerical models that simulated possible physical results that could be compared to observational data. These theories interpret the models in terms of a physical parameter: the ratio of the mass to the magnetic flux (M/Φ). Performing measurements of the magnetic field, to determine the magnetic flux (Φ), is complicated. It is only possible to obtain direct measurements of the strength of the line-of-sight component of the magnetic field through the normal Zeeman effect. Only a few molecules have Zeeman splitting factors large enough to be successfully used to measure magnetic fields. Of these few, OH traces lower density molecular species, while CN is believed to trace higher density regions. Using the Green Bank Telescope (GBT) we mapped the magnetic fields of cores and envelopes of dark cloud cores using OH as a tracer molecule. From this, the ratio of M/Φ between the cores and envelopes were computed, and were consistently determined to be < 1. This is inconsistent with published ambipolar diffusion theory which expects this ratio to be > 1. This study can be extended to other types of objects by using different tracer molecules. CN can be used to probe hot dense regions; however, it requires high resolution mapping currently only obtainable with an interferometer. Using CARMA, we obtained maps of 6 high mass star formation regions with a spatial resolution of approximately $2''$ by combining data from the C, D, and E arrays. CARMA's correlator was used to sample several spectral lines simultaneously in order to compare the structure of the CN emission with emission of other tracer molecules. We determined that CN is a good high density tracer which correlates well with other tracers such as HCO^+ and HCN. From this, we concluded that these regions can be observed at high resolution and long integration times with an instrument capable of performing CN Zeeman measurements, when such an interferometer array becomes available. A study was additionally performed to apply the Li & Houde method of estimating magnetic field strengths from linewidth differences of ion and neutral molecular species. We were unable to replicate the previously published results; however, there were several differences in the datasets that may contribute to the non-detection of this effect. Several possible reasons for this discrepancy were determined, and further investigation may be able to determine whether this analysis technique holds significant merit.

Acknowledgments

I would like to thank my advisor, Richard Crutcher, for the excellent guidance and advice he has provided over the last eight years. Without him, this project would not have been possible. I would also like to thank the other members of my committee, Charles Gammie, Leslie Looney, and Tom Troland, for taking time out of their schedules to read and comment on this thesis.

I would like to thank my parents, Alex and Carol Hakobian, and my brother, Christopher Hakobian, for their ongoing and everlasting support and advice through my undergraduate and graduate years. Even though I have been two thousand miles away for most of the last decade, they somehow still were able to tell if I was busy, or frustrated, or just needed a short break from what I was working on. I would also like to thank my grandmother, Ruth Hakobian, who passed away two weeks before this written thesis was completed. She was a strong supporter of anyone who wanted to pursue education and without her tireless effort to complete her own education and support her family, my family and I would not be where we are today.

There have been many people whose friendship have been crucial in helping me complete my graduate career. In particular, I would like to thank the other students of the incoming 2005 class: Brett Hayes, Amy Lien, Nicholas Indriolo, Hsin-Fang Chiang, and Jonathan Seale. Many long nights spent working on coursework and studying brought us together as friends; while we have all now completed our graduate careers and dispersed across the country, this friendship has remained. I would also like to thank Scott Bain, Jana Bilikova, Nachiketa Chakraborty, Jessica Evans, Gary Foreman, Doug Friedel, Katherine Lee, Britt Lundgren, Kuo-Chuan Pan, David Rebolledo, Ashley Ross, Dominique Segura-Cox, and Ian Stephens. Their friendship made my graduate career more enjoyable and I would also like to thank them for letting me bounce ideas off of them, even if the ideas made absolutely no sense at the time. I would also like to thank Jeri Cochran, who works very hard ensuring that the graduate students are on the right track and is always willing to lend an ear. The department and all of the graduate students are very lucky to have her help.

I would like to thank everyone else who I have not listed by name who have helped or given advice to me over my graduate years. Listing all of your names and how you have helped would require a book all of its own. Your friendship has not been forgotten.

Table of Contents

List of Tables

List of Figures

Chapter 1

Introduction

This project is a multi-faceted approach to establish a link between proposed theories of star formation and direct observation. Several models have been proposed over the last 35 years; however, predictions derived from these models could not be observationally tested. When the role of magnetic fields in these models became apparent, tests were designed to sample these fields. Many of these theories require the presence of strong magnetic fields when compared to the mean galactic field of $\sim 6\mu$G. Through sampling the Zeeman effect, it was determined that strong magnetic fields do exist around developing high density molecular cores. The variance of these measured magnetic field strengths is large: on the order of μG for dark cores, to mG in dense hot cores, to significantly stronger fields in exotic and super dense regions (such as in some types of masers). These early studies determined that magnetic fields do exist and are strong enough to influence the development of stars.

Following these determinations, development of tests that link the strength and morphology of magnetic fields to other measurable parameters and with theory are required. Ideally, these tests will result in whether one of the proposed theories has direct measurable proof. Even if concrete proof is not able to be determined, it should provide direction to development of future theories. Additionally, recent work has direct ramifications and has provided natural progression to this project. Troland & Crutcher (2008) surveyed a large number of dark cloud cores for evidence of the presence of strong magnetic fields and measured mass to magnetic flux (M/Φ) ratios using Zeeman measurements of OH. Their work provides the basis of selection of a number of the sampled objects in this project. Falgarone et al. (2008) completed a similar study using CN in denser cores and provided the basis for the selection of objects used for mapping molecular cloud regions.

One goal of this project is to assist in determining if star formation theory has support from observations. Some key factors that will be explored include: if magnetic fields cause significant support against gravitational collapse, which physical parameters are sampled by different tracer molecules, and what these results tell us about the structure and development of the regions observed. Technical complexities of performing these observations have previously prevented them from being performed at the high angular resolution obtained here.

1.1 Background

Two competing, yet opposite, theories currently exist for star formation: ambipolar diffusion and turbulence. Ambipolar diffusion requires a strong magnetic field to "freeze out" ions and allow neutral molecules to drift through the field and ions. If the density of neutral and ion species are large, gravitational contraction will occur with the magnetic field regulating the rate of collapse. This occurs through the magnetic field coupled with charged particles that prevents a clump from gravitationally contracting until its mass is significantly large enough such that its gravitational field overpowers the resistance created by the magnetic field (Mouschovias & Ciolek, 1999). Turbulence, on the other hand, favors the idea that molecular clouds are short lived structures formed by colliding turbulent flows in the interstellar medium. Molecular cores (and the resulting stars) are formed when the turbulent molecular gas becomes self-gravitating. Magnetic fields are not a dominant driving force in this theory. Both theories were developed in part to assist in solving the problem of angular momentum transport during star formation. An unexpected disparity in the observed angular momentum between molecular clouds and stars cannot otherwise be explained.

Until recently, only the ambipolar diffusion theory had numerical models that simulated possible physical results that could be compared to observational data. These theories interpret the models in terms of a set of physical parameters: the ratio of the mass to the magnetic flux (M/Φ). A method of measuring the M/Φ ratio is required to proceed. While the mass measurements are straightforward, the measurement of the magnetic flux is more complex. From the intensity of a particular transition, the column density of gas can be established. If the physical conditions that a particular molecule traces is known, the column densities can be converted to measured mass values. This analysis depends on accurately determining which density regions a specific species traces. If these parameters are not well understood, then large uncertainties in the M/Φ ratio will be present. Some species, such as OH, have parameters that are better understood than others.

Performing measurements of the magnetic field, on the other hand, are significantly more complicated. Since magnetic fields are a vector quantity, a measurement of the total field requires sampling the two components of the magnetic field in the plane of the sky in addition to the line-of-sight component. Unfortunately, it is only possible to obtain direct measurements of the strength of the line-of-sight component of the magnetic field through the normal Zeeman effect that occurs when an atom or molecule is in the presence of a magnetic field. It causes splitting of otherwise degenerate energy levels, the amount of which is directly proportional to the strength of the magnetic field present, to the Lande g-factor of the corresponding molecule, and to the Zeeman splitting factor of the particular transition. Choosing the correct transitions to measure is key to extracting meaningful results, as most transitions have small Zeeman splitting factors, such that the frequency splitting cannot be measured with current instruments. A few cases exist in extreme environments where magnetic field measurements can be performed in some difficult species. These regions typically have very extreme gas densities and magnetic field strengths that are not present in the environments in this study. Only a few molecules have Zeeman splitting factors large enough to be successfully used to measure magnetic fields. Of these few, OH traces lower density molecular species, while CN is believed to trace higher density regions. The conditions that CN traces have yet to be well established, and improving knowledge of these conditions is one of the goals of this project.

To add to the already complex nature of the detections, the transitions that correspond with Zeeman split levels are circularly polarized (either clockwise or counter-clockwise depending on the individual transition). As a result, these signatures of the presence of magnetic fields can only be performed through polarimetry. While making the measurements harder, it is something that is possible to accomplish with modern equipment.

We present a multi-faceted approach of sampling the M/Φ ratios between the core and envelopes of cloud cores. Previous measurements of the M/Φ ratio have only been able to provide upper limits, with statistical analysis of large numbers of clouds providing estimates for the mean M/Φ over the ensemble of clouds. The measured Φ is dependent on the angle between the magnetic field and our line of sight: $\mathbf{B} = \mathrm{B}_{los} \cos\theta$. Since it is not possible to measure the angle θ, it is necessary to develop a method of comparing sources which is independent of θ. If the same strong magnetic field threads both the envelope and the core, then θ would also be identical in both regions. If we examine the *ratio* of the M/Φ ratios between the envelope and the core, the dependence on the $\cos\theta$ term is removed.

This multi-faceted approach will be comprised of several sections: the first is a study of OH in low density cores; the second is a mapping project to improve the understanding of the morphology of CN cores and the density regime of gas that CN samples; and the third is the application of the Li & Houde (2008) technique of estimating plane-of-sky magnetic field intensities through comparing the linewidths of ion and neutral molecular species.

1.2 The GBT Experiment

Troland & Crutcher (2008) performed an extensive survey of 34 dark cloud cores in order to detect the OH

Zeeman effect, and were awarded approximately 500 hours of time on the Arecibo telescope for this purpose. Out of the 34 objects sampled, only 9 satisfied the rigid criteria necessary to qualify as a detection. In addition to the magnetic field measurements done at Arecibo, coarse mapping was performed to inspect the large scale spatial distribution of OH in the region. A non-detection does not preclude the possibility of a source having a magnetic field, whether it be strong or weak. These sources may have a magnetic field that is oriented away from out line of sight. From the 9 objects with Zeeman detections, the objects with the largest core magnetic field strengths were chosen to perform envelope measurements, as those have the greatest likelihood of yielding further magnetic field detections.

Few observatories have the capability of performing long-integration magnetic field measurements due to the requirement that it has the capability of performing radio polarimetry at the frequency of the two OH transitions (1665 MHz and 1667 MHz) observed. An ideal instrument for this project is the Green Bank Telescope (GBT) located in Green Bank, West Virginia. It has the capability of sampling both lines simultaneously in addition to having an ideal beamsize for sampling these cloud envelopes. The GBT has a beam size of $\sim 8'$ in diameter at this frequency, compared with the $3'$ beam of Arecibo. While the Arecibo beam is only slightly larger than the size of the cloud core, the GBT beam is large enough to encompass the envelope around the core. The observations towards the core positions performed at Arecibo do not need to be repeated since the cores fill the Arecibo beam. A similar measurement at the GBT would sample both the core and the envelope simultaneously, due to the larger beamsize. Instead, four positions around the core were sampled at equal spacings, forming a "ring" around the core. To achieve the necessary signal to noise, approximately 10 hours of observation time per position was needed. The data can be analyzed and reduced so that it produces one average core / envelope M/Φ ratio per source. This ratio can be compared to theory.

1.3 CARMA Mapping

CN can be used as a tracer molecule for Zeeman measurements. The CN N=1–0 transition has seven strong hyperfine components with a large distribution of Zeeman splitting factors. The two strongest hyperfine components, with relative strengths of 27 and 10, respectively, additionally have the largest splitting factors. Previous CN Zeeman work has been carried out with the IRAM 30-meter telescope (Falgarone et al., 2008) with an effective resolution of $23''$. The source with the strongest magnetic field measurements from this study is W3(OH), an ultra-compact HII region (UCHII) in the W3 molecular cloud complex. This source is ~ 2 kpc away, and with a $23''$ beam, the region sampled is approximately 50,000 AU across. With little prior information as to the spatial structure of CN, it is very likely that it contains complex structure.

Using CARMA, it is possible to obtain maps with a spatial resolution of approximately $2''$ by combining data from the C, D, and E arrays. By using three different array configurations, it is possible to probe small scale structure while retaining the ability to image large scale features that would otherwise be resolved out in the C and D arrays. At the time this observational project was carried out, CARMA did not have dual polarization receivers and therefore could not perform magnetic field measurements. However, by mapping these regions at high resolution we can gain crucial information about the structure of the regions sampled by the IRAM observations. The advanced features of CARMA's correlator can be used to sample several spectral lines simultaneously in order to compare the structure of the CN emission with emission of other tracer molecules. This will also supply information about regions to be observed at high resolution and long integration times with an instrument capable of making dual-polarization measurements, when such an interferometer array becomes available.

Chapter 2

Testing Magnetic Star Formation Theory*

2.1 Introduction

Understanding star formation is a fundamental astrophysical problem. McKee & Ostriker (2007) have comprehensively reviewed the field. For thirty years what has sometimes been called the “standard model” has been that magnetic fields control the formation and evolution of the molecular clouds from which stars form, including the formation of cores and their gravitational collapse to form protostars. However, in recent years doubts about the validity of this model have been raised by those who argue that turbulence controls the formation of clouds and cores, with cores either dissipating back into the general interstellar medium or collapsing and forming stars if they are self-gravitating when formed. In spite of decades of intense research, there is still not consensus on the role that magnetic fields play in the star formation process.

Detailed theoretical work on the strong magnetic field “standard model” has been carried out by a number of groups: Shu et al. (1999) and Mouschovias & Ciolek (1999) have reviewed and summarized the state of this theory. The fundamental principle is that clouds are formed with subcritical masses ($M < M_\Phi = \Phi/2\pi\sqrt{G}$). Here Φ is the magnetic flux and G is the gravitational constant, and the expression for M_Φ is from Nakano (1978); other expressions for M_Φ differ slightly from this depending on cloud structure (e.g., Mouschovias & Spitzer 1976). The magnetic field is frozen only into the ionized gas and dust; neutral gas and dust contract gravitationally through the field and the ions, increasing mass (but not to first order flux) in the cloud cores. This process is known as ambipolar diffusion. When the core mass reaches and exceeds M_Φ, the core becomes supercritical ($M > M_\Phi$), collapses, and forms stars. The magnetic flux remains behind in the envelope. Because the ambipolar diffusion time scale for the formation of supercritical cores is fairly long ($\geq 10^7$ yr), molecular clouds would have long lifetimes. The star formation efficiency (the ratio of mass in stars in a molecular cloud complex to the interstellar mass) is low (as observed) due to the slow rate of star formation and to the fact that much of the mass of the molecular cloud is left behind in the subcritical envelope as the core collapses.

---

*This chapter was previously published as **“Testing Magnetic Star Formation Theory”**, in The Astrophysical Journal (Crutcher, Hakobian, & Troland, 2009).

The idea that star formation is primarily regulated by ambipolar diffusion was standard for many years. However, doubts about the validity of this assumption were raised by the development of a weak-field, super-Alfvénic model of dark clouds (Padoan & Nordlund, 1999). The new weak-field theory had molecular clouds being intermittent phenomena, with short ($\sim 10^6$ yr) lifetimes. In this theory clouds form at the intersection of turbulent supersonic flows in the interstellar medium. Generally, clouds do not become gravitationally bound and dissipate; those that are self-gravitating form stars in essentially a free-fall time (Elmegreen, 2000). Star formation occurs only in the small fraction of the molecular gas that is sufficiently dense to be self-gravitating. The star formation efficiency is low due to a small fraction of the mass of clouds becoming gravitationally bound. Magnetic fields are present in this theory, but they are too weak to be energetically dominant. The role of turbulence in the energetics of the interstellar medium has been a very active area. Padoan et al. (2004) presented evidence in favor of the weak field, super Alfvénic model. Elmegreen & Scalo (2004) have written an excellent review of interstellar turbulence, and Mac Low & Klessen (2004) have extensively reviewed arguments that supersonic turbulence controls star formation.

Early work focused on extreme-case models, either strong magnetic field models that did not (at least directly) include the effects of turbulence, or strong turbulence models that neglected the effects of ambipolar diffusion. More recent theoretical work has introduced supersonic turbulence into numerical star formation models (e.g., Nakamura & Li, 2005; Kudoh & Basu, 2008; Nakamura & Li, 2008). These more recent models apply to magnetically subcritical regions, and they include the effects of ambipolar diffusion. The role of turbulence proves to be important in these models, significantly shortening, for example, the ambipolar diffusion timescale. In this paper we focus on a direct comparison of observational results with the strong field, ambipolar diffusion model without turbulence. Such models have a smooth morphology of the magnetic field which deforms into an hourglass shape with axis along the mean field direction, and make an analytic prediction that can be tested directly. The more complicated models that come from simulations that include both magnetic fields and turbulence can also be tested against the results of this paper, and we discuss how such tests might be carried out.

Our approach to testing star formation theory has been to measure magnetic field strengths in molecular clouds in order to see whether they are weak or strong. The crucial parameter is the ratio of the mass to the magnetic flux, M/Φ, which is of course closely related to M_Φ. If M/Φ is observed to be significantly supercritical, particularly at lower densities, the magnetic support theory is not viable. If it is observed to be subcritical at lower densities, magnetic fields would be too strong for the intermittent, turbulent theory to hold. The M/Φ parameter provides in principle a straightforward, direct test to discriminate between the two extreme theories of star formation.

The Zeeman effect provides the only known method to directly measure magnetic field strengths in dense gas. In this paper we first briefly review Zeeman results and argue that they have not yet provided an unambiguous discrimination between the two star formation theories. We then describe a new experiment to attempt to overcome the limitations of existing Zeeman results and to test directly a prediction of the "standard model". Finally, we describe the observations made for this experiment and the results, and discuss the implications of those results.

2.2 The Zeeman Effect

2.2.1 The Technique

If a spectral line forming region is permeated by a magnetic field **B**, the line is split by the normal Zeeman effect into three separate frequencies, $\nu_0 - \nu_z$, ν_0, and $\nu_0 + \nu_z$, where $\nu_z = B \times Z$, B is the magnitude of **B**, and Z is the Zeeman coefficient in Hz/μG (note that Z is often defined as two times our Z). Unfortunately, most molecules do not have large values of Z. In general, only those molecules with an unpaired outer electron will have a Z of order the Bohr magneton, $M_B = eh/4\pi mc = 1.40$ Hz/μG. For the 1420 MHz H I line, $Z = 1.4$ Hz/μG, so if $B = 1$ μG, the total splitting of the two circularly polarized components would be 2.8 Hz, or 6×10^{-4} km s^{-1}. This very small magnitude of the Zeeman splitting makes Zeeman observations difficult and consuming of large amounts of telescope time. For most molecules, Z will be of order the nuclear magneton, which is 1840 times smaller than M_B. Except for the very strong H_2O masers, all Zeeman work has involved the few species with large Zs: H I, OH, CN, CH, CCS, and SO, with Zeeman detections to date in only the first three species.

The observed data are Stokes parameter I and V spectra for each position. From these data we infer the column density N and the line-of-sight component B_{LOS} of the magnetic vector **B**. The I and V spectra have channel-to-channel noise that has a Gaussian probability density function (PDF) − noise dominated by the stochastic receiver noise. Hence, the random error in N is Gaussian, or very nearly so. For the usual case of Zeeman splitting much smaller than the line width ($\nu_z << \delta\nu$), only B_{LOS} can be determined (e.g., Crutcher et al. 1993). The Stokes V spectrum actually consists of a possible scaled-down Stokes I signal (due to a possible gain difference between the two receivers) and a Zeeman signal that is proportional to the first derivative of the Stokes I spectrum. To infer B_{LOS} we do a linear least-squares fit of $a \times I + b \times dI/dv$ to the observed Stokes V spectrum, where the Stokes I and V spectra are functions of radial velocity v, and dI/dv is obtained by numerically differentiating the Stokes I spectrum. Both of the parameters a and b may be positive or negative. Hence, the position and shape of the Zeeman signal are set entirely by the Stokes I spectrum; only the amplitude (positive or negative) of the Zeeman signal is a free parameter. The sign of b indicates whether the line-of-sight component of the magnetic vector $\mathbf{B}$ points toward or away from the observer, and the magnitude of b is proportional to the magnitude of B_{LOS}. The parameters a and b and the mean errors in each parameter come in the standard way from this straightforward linear least-squares fitting procedure. Hence, the error in B_{LOS} that comes from the linear least-squares fit is expected to be Gaussian normal, or very nearly so. During the beginning years of Crutcher's observations of the Zeeman effect in OH lines, he confirmed by Monte Carlo tests that the linear least-squares fitting procedure gives correct results with very nearly Gaussian PDFs.

Since the magnitude of only one of the three components of the vector $\mathbf{B}$ can be measured, in general it is necessary to apply statistical techniques in order to determine astrophysically meaningful parameters. If one observes a large sample of clouds distributed over the sky, the direction of the magnetic fields should be random with respect to the lines of sight from the observer. The usual approach is to assume that the total field strength B is the same in an observed sample of clouds in order to infer B from measurements of B_{LOS}. As discussed by Heiles & Crutcher (2005), for this case both the median and mean values of $B_{LOS} = B/2$, so the mean and median of B may be obtained for the observed sample of clouds. As Heiles & Crutcher (2005) noted, for PDFs for B other than a delta function, the mean and median of $B_{LOS} \approx B/2$, so useful information about magnetic field strengths from Zeeman observations can be obtained even if the PDF of B is unknown (as is of course the case).

Since the magnetic flux is just the magnetic field strength times the spatial area over which it is measured, $\Phi = B \times Area$. The mass within this area can be inferred from the hydrogen column density, $N_H = N(HI) + 2N(H_2)$; allowing for 10% He, $M_{obs} = 1.4 m_H N_H \times Area$. Thus, $M/\Phi \propto N_H/B$.

2.2.2 Previous Zeeman Work

Most of the earlier Zeeman detections in molecular clouds (e.g., Crutcher 1999) have been toward clouds associated with H II regions. Dark clouds offer the possibility of measuring the role of magnetic fields at an earlier stage of the star formation process, especially for the low-mass star formation case where the "standard model" may best apply. However, until recently there were only two dark cloud molecular Zeeman detections (Goodman et al., 1989; Crutcher et al., 1993).

In order to improve our knowledge of magnetic field strengths in dark cloud cores, Troland & Crutcher (2008) used the Arecibo telescope to carry out an extensive program to observe the Zeeman effect in the 1665 and 1667 MHz lines of OH. Thirty-three dark cloud core positions were observed. They achieved nine detections of B_{LOS} and sensitive upper limits for the other positions. Also needed to compute M/Φ is an estimate for the column density of H_2. They obtained this estimate from the OH lines themselves. The Arecibo OH spectra yield N(OH). With OH/H $= 4 \times 10^{-8}$ (Crutcher, 1979), one can infer N(H_2). The Troland & Crutcher (2008) Arecibo maps of OH emission around the core positions showed that OH does peak up on the CO and/or NH_3 cores, and that OH samples densities up to around n(H_2) $\sim 2 \times 10^4$ cm^{-3}.

Although the Troland & Crutcher (2008) analysis of their data gave the mean value of B for their dark-cloud sample, it provided no information about the possible variation of B from core to core. They inferred $\overline{\lambda}$, the ratio of the observed mean M/Φ to the critical value. The data were consistent with the prediction of the strong magnetic field theory – a slightly supercritical M/Φ if the core morphology is that of a disk, as predicted by the strong-field theory.

The Arecibo Zeeman observations had the potential to eliminate one of the two extreme-case theories for the star formation process. If M/Φ had been found to be unambiguously highly supercritical, the ambipolar diffusion driven theory would have been eliminated. If M/Φ had been found to be unambiguously subcritical, the turbulence driven theory would have been eliminated. The statistical result was that the mean M/Φ in molecular clouds was observed to be approximately critical, i.e., $\overline{\lambda} \approx 2$. Because of the many non-detections, and since the OH/H_2 ratio is uncertain by a factor ~ 2, a mean M/Φ ranging from critical to supercritical by ~ 4 was consistent with the data. Of course, there could be a real variation with an unknown range in M/Φ from cloud to cloud. Hence, although the observations have shown that magnetic fields are sufficiently strong that they cannot be ignored, the very hard-won observational results cannot rule out either extreme-case theory of star formation.

2.3 This Experiment

The goal of the experiment described in this paper is to perform a definitive test of the extreme-case (no turbulence) ambipolar diffusion theory of star formation that circumvents the ambiguities inherent in previous Zeeman observational tests. In addition, the experiment will supply valuable observational data against which more complicated models (involving both ambipolar diffusion and turbulence) may be tested. This definitive test is measurement of the change in M/Φ between the envelope and the core of a cloud. The magnetic support/ambipolar diffusion theory makes a specific prediction that can be tested. It requires that M/Φ of the original cloud be subcritical, with ambipolar diffusion accumulating mass but not flux in the cloud center, building up a higher density core. Eventually, the core becomes supercritical and starts a collapse which is slower than free fall due to the magnetic pressure. During this supercritical collapse phase, magnetic flux is dragged inward, so the rate of increase of M/Φ is slowed. The result is a prediction that the ratio of the core to the original cloud $M/\Phi > 1$, by approximately the inverse of the amount by which the original cloud was subcritical.

Is the prediction of the ambipolar diffusion theory sufficiently different from the expectations of the turbulence-driven theory? The answer is clearly yes, for the turbulence theory generally predicts the opposite behavior of the mass-to-flux ratio between envelope and core. Simulations of the formation of cores by turbulence (Vázquez-Semadeni et al., 2005) made the usual assumptions for this theory of initially uniform density and magnetic field, driven turbulence, and ideal MHD (strict flux freezing, i.e., no ambipolar diffusion). They found that M/Φ usually decreased with increasing density, the opposite of the ambipolar diffusion result. A change in M/Φ with ideal MHD seems impossible, but it occurs due to the way M/Φ is measured. No change in M/Φ occurs when an entire flux tube is considered. But converging flows perpendicular to $\mathbf{B}$ increase B and M within a fixed volume, while flows parallel to $\mathbf{B}$ can increase or decrease M within that fixed volume. Hence, when measuring M/Φ within the volume chosen to define a cloud or core, M/Φ can be either larger or smaller than the original value. Vázquez-Semadeni et al. (2005) noted that for mass and magnetic flux conservation, a clump or core within a cloud has a larger density than the mean, but a mass smaller than its parent cloud, so a core would generally have a smaller M/Φ than the parent cloud (since the magnetic flux would be unchanged by core formation but the core mass would be only a fraction of the mass within the flux tube). Hence, this turbulent simulation result may be general, although of course it would require more studies to verify that conclusion.

Strong magnetic field cases can obtain a similar result. If the mass within a flux tube fragments into several cores on a shorter time scale than the ambipolar diffusion one, each core will have only a fraction of the mass in the flux tube, and the M/Φ of these cores would have decreased with respect to that of the original material (Mouschovias, 1991). Although the physics driving this fragmentation is different from that considered by the turbulence theory, the fundamental reason for the decrease in M/Φ is the same, and it is not related to ambipolar diffusion. Here we address only testing the ambipolar diffusion driven formation of dense cores, for which M/Φ must increase.

A quantitative test of a theoretical prediction requires the design of an experiment to test specific numerical models. We designed our experiment to test the “idealized” models that have been published by the ambipolar diffusion theorists. We call these models idealized because they do not follow the evolution in a consistent way through the formation of clouds from a diffuse interstellar medium to the formation of cores in those clouds driven by ambipolar diffusion. Instead, the models generally start with an isolated, uniform, spherical cloud that is allowed to relax to an equilibrium state, which then evolves due to ambipolar diffusion. The non-thermal motions and irregular structures of observed clouds, which themselves are embedded in a complex interstellar medium, are not directly considered in these idealized models. So the models are two-dimensional (with azimuthal symmetry about the magnetic field direction) with regular (non-twisted) magnetic fields. To design the experiment, we looked at three such idealized ambipolar diffusion models: (1) a dimensionless parameter model (Ciolek & Mouschovias, 1994) for which they listed specific physical parameters for comparison with actual molecular clouds; this model with their listed physical parameters had an unevolved cloud radius of 4.3 pc; (2) one specifically computed for L1544 (Ciolek & Basu, 2000) with an unevolved cloud radius of about 2.5 pc; and (3) a specific model for B1 (Crutcher et al., 1994) with an unevolved cloud radius of 2.9 pc. These radii would become the radii of the "envelopes" surrounding the cores formed by ambipolar diffusion, since the region of the cloud outside the cores would be "held in place" (an ambipolar diffusion theorist phrase) by their subcritical magnetic fields. Moreover, the radii of the cores in these models were all ~ 0.1 pc. So we need to sample the core with a filled beam of radius ~ 0.1 pc and the envelope with a beam radius less than ~ 2 pc that excluded the core. A second aspect of the idealized ambipolar diffusion models was that the magnetic fields were smooth and regular within their unevolved cloud radii, although with an "hourglass" morphology strongest in the core. Although this regularity of the field was by construction in the models, the requirement that M/Φ in the clouds be subcritical meant that the magnetic fields must be strong, so that even if turbulence had been included in the models, magnetic energy would likely dominate turbulent energy and field lines would in fact be quite regular. Hence, these two inputs from the actual ambipolar diffusion models guided our design of the experiment – we needed to sample cores and envelopes on the relevant spatial scales and we could (to first order) assume that the magnetic fields in the clouds were not significantly twisted but mainly ordered.

We chose four clouds for our experiment – two in the Taurus molecular cloud complex (distance ~ 150 pc) and two in the Perseus molecular cloud complex (distance ~ 300 pc). A 0.1 pc core radius would be $\sim 1'(2')$ and a 2 pc cloud (or envelope) radius would be $\sim 20'(40')$ at the 300 (150) pc distance. At the OH line frequency, the primary-beam radius of the Arecibo telescope is $\sim 1.5'$, so this is well matched for measurement of core properties at the densities sampled by OH. The Green Bank telescope (GBT) beam radius is $\sim 3.9'$; by pointing the GBT at positions $6'$ from the Arecibo pointing position, the GBT beams would exclude the molecular core and sample (at half-power response) the radius range $2.1'$ to $9.9'$, or $\sim 0.2(0.1)$ pc to $\sim 0.9(0.45)$ pc at the 300 (150) pc distance. Figure 2.1 displays these beam sizes and positions. This choice of beams was set by the specifications of the ambipolar diffusion models cited above. The sampling of the envelope had to be sufficiently far from the core to obtain a significantly different result from the core result, but *well* within the outer boundary of the unevolved clouds; the GBT beamsize was ideally suited to these objectives. We could then "synthesize" a toroidal or ring beam to sample the envelopes by appropriately combining the observations from the four GBT beams in order to produce exactly the envelope sampling called for by the ambipolar diffusion models.

The Arecibo OH survey of dark clouds produced detections of B_{LOS} in 9 of 33 cores observed; earlier, Goodman et al. (1989) obtained a detection with Arecibo toward the B1 core. The Arecibo observations have therefore selected 10 cores for which there are measurements (not just limits) for N_{OH}/B_{LOS} ($\propto M/\Phi$) with a $3'$ beam, well matched to the core diameters of $\sim 2'$. Additional observations that are needed are measurements of N_{OH}/B_{LOS} in the envelopes of these cores to test the prediction that ambipolar diffusion increases the mass but not (at least very much initially) the field in cloud cores. Zeeman observations in molecular envelopes have generally not been attempted before, since line strengths are weaker and Zeeman detections are difficult to obtain.

In order to measure M/Φ in the envelopes surrounding the Arecibo cores, for this experiment we made a four-point Zeeman map with the GBT at positions $6'$ from each of four cores with detected B_{LOS} (see Figure 2.1), dividing the observing time about equally between the four positions. Combining the four envelope results for each cloud can then give results that would be obtained with the required toroidal or ring telescope beam; of course, sensitivity around the ring is not uniform due to four telescope beams that make up the ring. This sampling of the envelope regions is exactly what we require to measure M/Φ in the envelopes, excluding the cores. Therefore, we have B_{LOS} and N_{OH} separately for the core and envelope material. The ratios $[N_{OH}/B_{LOS}]_{core}$ and $[N_{OH}/B_{LOS}]_{envelope}$ will then be available for the clouds. The strong field/ambipolar diffusion theory for core formation requires $[M/\Phi]_{core}/[M/\Phi]_{envelope} = [N_{OH}/B_{LOS}]_{core}/[N_{OH}/B_{LOS}]_{envelope} > 1$ (that is, that M/Φ increases from envelope to core). So these observations could result in the ambipolar diffusion theory being proved wrong if the observations find this core/envelope M/Φ ratio to be less than one. It could also result in the driven turbulence, ideal MHD simulations being proved wrong, if this experiment finds this core/envelope M/Φ ratio to be greater than 1. It is of course impossible to prove that a theory is correct, but this experiment has the potential to rule out one of the two competing extreme-case theories of star formation. Such a result would have a profound effect on further theoretical work on star formation, and would be a major advance in understanding the star formation process.

We define

$$\mathcal{R} \equiv \frac{M_{core}/\Phi_{core}}{M_{envelope}/\Phi_{envelope}}. \tag{2.1}$$

The mass (the OH lines are optically thin) is given by

$$M \propto I \; \Delta V \; A \tag{2.2}$$

and the magnetic flux by

$$\Phi \propto (B_{LOS}/cos\theta)\ A. \tag{2.3}$$

Here I is the peak intensity of the spectral line, ΔV is the FWHM line width, A is the area of sky sampled, $A = \pi r_c^2$ for the core and $A = 4\pi r_e^2$ for the envelope, with r_c and r_e being the radii of the telescope beams used respectively for the core and envelope observations, B_{LOS} is the magnitude of the line-of-sight component of the magnetic field, and θ is the angle between the line of sight and $\mathbf{B}$. Since A is the same for measuring M and Φ for the core, it divides out of the numerator of $\mathcal{R}$; similarly in the denominator for the envelope. The factor $cos\theta$ also divides out.

Theoretical calculations for ambipolar diffusion generally do not predict $\mathcal{R}$ as we have defined it, but rather M/Φ in the central flux tube as a function of the central density, which increases with time (e.g., Ciolek & Mouschovias 1994, Figure 2.2e). For a disk morphology with the field along the line of sight, the central flux tube would include contributions from the foreground and background parts of the envelope, but these would be small and the central result would be dominated by the core M/Φ. In any case, our measurement of $(M/\Phi)_{core}$ corresponds to what the models give. Hence, for a quantitative comparison with those predictions, we would need M/Φ through the center of the initial cloud before ambipolar diffusion had created the core. Before ambipolar diffusion has acted, the initial central M/Φ is equal to the M/Φ of the initial cloud as a whole. We can infer that original central M/Φ from our observations. The total mass and flux of the cloud do not change as the cloud evolves due to ambipolar diffusion, so the present $(M/\Phi)_{core+envelope}$, obtained by adding together the Arecibo result for the core and the four results for the envelope, gives the initial central mass-to-flux ratio $(M/\Phi)_{c0}$ used as the starting point of the ambipolar diffusion calculations. We therefore define

$$\mathcal{R}' \equiv \frac{M_{core}/\Phi_{core}}{M_{core+envelope}/\Phi_{core+envelope}}. \tag{2.4}$$

$\mathcal{R}' \approx (M/\Phi)_c/(M/\Phi)_{c0}$, the quantity predicted by ambipolar diffusion models (e.g., Ciolek & Mouschovias 1994). The expressions in equations 2.2 and 2.3 for M and Φ are used in equation 2.4, but now the areas A do not divide out in the denominator and explicit values must be used. The factor $cos\theta$ still divides out, however.

Measuring relative values of M/Φ ($\mathcal{R}$ or $\mathcal{R}'$) will eliminate or at least greatly reduce the uncertainties inherent in absolute measurements of M/Φ. We seek only a change in M/Φ from envelope to core, not the absolute values themselves. This avoids all of the geometrical correction problems in going from B_{LOS} to the total B and from N_{obs} to N_B (the column density along $\mathbf{B}$, which is what is required to properly compute

M/Φ). We do not need to know the angle $cos\theta$ between the line of sight and $\mathbf{B}$, because we will be making a relative measurement, so $cos\theta$ in equation 2.3 will divide out. Similarly, no geometrical correction for the measured column densities will be necessary. Also, by observing B_{LOS} in the core and envelope using the same tracer, in this case OH, the ratio OH/H that would be needed to convert measured OH column density to total (H_2) column density in order to find the absolute value of M/Φ is not needed. $\mathcal{R}$ and $\mathcal{R}'$ are inferred from the directly measured quantities I, ΔV, B_{LOS}, and the radii of the telescope beams used for the core and envelope observations.

2.4 Observations

2.4.1 Arecibo Observations

The Arecibo[1] observations of cores used here are not new observations, but have been reported already: B1 (Goodman et al., 1989), L1544 (Crutcher & Troland, 2000), B217-2 and L1448CO (Troland & Crutcher, 2008). Details of these observations are described in these papers. These core positions were selected from catalogs of molecular peaks observed in CO, NH_3, and other tracers. The exact positions for which OH Zeeman observations were carried out were refined by small Arecibo OH maps to determine the peak OH line strength positions. The B1 observations were carried out with the old Arecibo line feed, while the others used the new Gregorian feed. The spectral resolution of the B1 observations was lower due to the older spectrometer in use at that time, but the line is well resolved so this does not affect the line strength and the Zeeman measurement. The Gregorian feed data were originally not calibrated exactly correctly. This did not affect the determination of B_{LOS}, which depends on the ratio of the Stokes I and V spectra that would have been affected precisely the same way. But for this study, we re-calibrated the spectra using the best known value of the L-band feed noise diode. This resulted in about a 7% reduction in the line strengths from those published previously.

The characteristics of the Arecibo telescope beam have been carefully studied by Heiles et al. (2001a). This study was of the Gregorian feed, but the essential characteristics of the line feed for the purposes of this paper are not significantly different. One important parameter is the main beam diameter at the half-power point, $2.9'$. This is the size of the core region sampled by the Arecibo observations. Second, there is the main beam efficiency, which is only 0.48. This means that slightly more than half the area of sky to which the Arecibo observations were sensitive lies outside the $2.9'$ diameter of the main beam, mostly in sidelobes. Heiles et al. (2001a) measured the telescope response out to the first sidelobe, which lies $\sim 5'$ from the beam

---

[1] The Arecibo Observatory is part of the National Astronomy and Ionosphere Center, which is operated by Cornell University under a cooperative agreement with the National Science Foundation.

center, close to the positions where the GBT envelope observations were centered. This first sidelobe has 0.14 of the spatial response of the telescope, so in addition to the response of the Arecibo telescope to the cores, there is a response to the envelope emission equal to $0.14/0.48 = 29\%$ of the core response. This first sidelobe is a "ring" beam similar to the pseudo-ring beam formed by the four telescope beams used for the envelope observations (see Figure 2.1). Hence, for two reasons, the Arecibo results for $(M/\Phi)_{core}$ are "contaminated" by input from the envelope region. First is the fact that the Arecibo beam must pass through the near and far regions of the envelope along the line of sight. This is okay, however, for the theoretical models predict M/Φ for the central flux tube that would include the near and far envelope. The second is the "ring" beam produced by the first sidelobe. The effect of this would be to make $(M/\Phi)_{core}$ look more like $(M/\Phi)_{envelope}$ than its "real" value, i.e., to make $\mathcal{R}$ and $\mathcal{R}'$ closer to 1 than either would be if the core only could be sampled. Without much more detailed information, it is impossible to deconvolve the envelope contribution out of the measured $(M/\Phi)_{core}$. This means that a difference between a measured $\mathcal{R}$ or $\mathcal{R}'$ and 1 is more statistically significant than the significance determined solely from the measurement uncertainties.

2.4.2 Green Bank Telescope Observations

The observations of the envelope positions were carried out with the L-band receiver of the NRAO[2] 100-m Robert C. Byrd Green Bank Telescope (GBT) between Oct 2007 and Apr 2008. The main beam diameter of the GBT at 1666 MHz is $7.8'$ and the main beam efficiency is 0.81; these quantities come from our own "spider" scan polarization calibration observations (see below). A negligibly small fraction of the GBT response comes from the core region of each cloud, due to the small sidelobe intensity, the fact that the cores lie near the first null of the beam response, and the fact that the core fills only a small fraction of the 360° surrounding the GBT beam center. Observing time at each of the 16 positions ($6'$ north, south, east, and west of each of four Arecibo cores, see Figure 2.1) was approximately equal, averaging about 9.5 hours of actual on-source Zeeman integrations per position. The NRAO Spectral Processor was used as the backend correlation spectrometer and polarimeter. Simultaneous observations were made in both horizontal and vertical linear polarization of the 1665 and 1667 MHz OH lines. The total spectrometer bandwidth for each line in each polarization was 156.25 kHz or about 28 km s^{-1}, which yielded a spectral channel width of about 0.055 km s^{-1}. Bandpass calibration was carried out by frequency switching between -15/64 and +15/64 of the total bandwidth; after appropriately combining the two halves of the band, this resulted in a final velocity coverage for each spectrum of about 13 km s^{-1}. The initial data processing made use of IDL

---

[2] The National Radio Astronomy Observatory is a facility of the National Science Foundation operated under cooperative agreement by Associated Universities, Inc.

software written by C. Heiles and T. Robishaw, which provided calibrated Stokes I, V, Q, and U spectra. Linear baselines were removed from the Stokes I and V spectra. The polarization calibrations used “spider” scans of the continuum source 3C286 over several hours surrounding its transit. Heiles et al. (2001b) provide details of the polarization calibration procedure. In addition to the molecular cloud envelope observations, we briefly observed the polarized OH maser sources W49 and W3(OH) in order to verify the observing setup and data processing procedures. In addition, we observed the previously well-studied OH Zeeman absorption line source NGC2024 (Orion B, W12) in order to verify that the procedures produced the same B_{LOS}, including the sign or direction of the magnetic field, as had been obtained previously (Crutcher & Kazes, 1983; Heiles & Stevens, 1986; Crutcher et al., 1999a; Bourke et al., 2001). (Note that the field direction reported in the Crutcher & Kazes (1983) paper was wrong; the correct direction is given in the latter three papers.) The GBT Zeeman results for NGC2024 agree with the previous results.

Although the Heiles-Robishaw software produces a Zeeman fit to the spectra, it does so over the full bandwidth. The Stokes I spectra at the molecular core positions are dominated by a single strong component, but at the envelope positions this component is weaker and additional components are present that are sometimes comparable in strength with the core component. We therefore used our software, the same code used previously to fit the Arecibo survey data (Troland & Crutcher, 2008), to fit for B_{LOS} only over those spectral channels in which the strong core line component dominates; these are the results reported here. Details of the procedure are given by Troland & Crutcher (2008) and briefly described in §2.2.1 above.

There are several possible methods to combine the results for the four envelope positions surrounding each core in order to produce a measurement of B_{LOS} for each envelope. These include (1) taking the mean of the four envelope results for B_{LOS}, or (2) first averaging the Stokes I and V spectra for the four envelope positions before fitting for B_{LOS}. The second method has the disadvantage that the radial velocities and line widths are not the same at each envelope position, so the averaged spectra would be broader than any of the individual spectra, which would slightly reduce the sensitivity to B_{LOS}. We feel that instead of either of these two, the best analysis technique is to fit all eight spectra (the 1667 and 1665 MHz spectra for the four envelope positions for each cloud) *simultaneously* in order to obtain the best-fit single value for B_{LOS} and its uncertainty from the entire envelope data set. This preserves the information content of each of the eight spectral lines, so no broadening takes place that would reduce the sensitivity. It also imposes the constraint that a single value of B_{LOS} describes all of the data, which is the desired result for a synthesized toroidal beam measurement of B_{LOS} in each envelope.

Table 2.1. Observational Results

Cloud	$I_{OH}(K)$	$\Delta V(km/s)$	$B_{LOS}(\mu G)$
L1448CO(env)	0.63	1.16	-0 ± 5
L1448CO(core)	1.30	0.93	-26 ± 4
B217-2(env)	0.59	0.79	$+2 \pm 4$
B217-2(core)	1.28	0.47	$+14 \pm 4$
L1544(env)	0.96	0.67	$+2 \pm 3$
L1544(core)	2.43	0.48	$+11 \pm 2$
B1(env)	1.21	1.32	-8 ± 3
B1(core)	1.93	1.14	-27 ± 4

2.5 Results

Results for the core and envelope observations are shown in Table 2.1 and in Figures 2.2-2.5. Table 2.1 gives the numerical values for $I_{OH} = T_A(1665) + T_A(1667)$, ΔV, and B_{LOS}. The values listed for the envelopes are the results from the simultaneous fit for a single B_{LOS} and its mean error over both OH lines and all four envelope positions. Plotted in each panel of Figures 2.2-2.5 is the observed antenna temperature T_A of the 1667 MHz line at each of the observed positions, in order to show the relative line strengths and widths at the core and the envelope positions. The 1665 MHz line strengths are typically about 60% of the 1667 MHz line strengths and show the same relative strengths from position to position. In the upper left of each panel is B_{LOS} and its 1σ uncertainty for that position. Although the line strength does not decrease uniformly in all directions from the cores, and in most cases there is OH emission at velocities slightly away from the velocity of the main core component, the line strength in the envelope is typically about 50% that of the core. Moreover, in all cases, the line width at the core position is only about 75% that at the envelope positions. A decrease in line width from envelope to core is a standard feature of molecular clouds, seen even more strongly in molecular tracers that sample higher densities than does OH. So both the increase in line strength and the decrease in line width from the GBT to the Arecibo spectra argue that the Arecibo OH observations do sample molecular cores, and that the GBT observations are dominated by non-core emission.

B_{LOS} at L1544west is twice B_{LOS} at L1544core in spite of the OH column density ratio being 0.6; this is the only case of a stronger field at an envelope position than in the core. Toward B1 there appears to be a north-south ridge of B_{LOS} with much weaker B_{LOS} to the east and west of the core. At all of the remaining 13 envelope positions the signal/noise ratio is low, although at all 16 positions the sensitivity to

Table 2.2. Relative Mass/Flux

Cloud	$\mathcal{R}$	$\mathcal{R}'$	Probability $\mathcal{R}$ or $\mathcal{R}' > 1$
L1448CO	0.02 ± 0.36	0.07 ± 0.34	0.005
B217-2	0.15 ± 0.43	0.19 ± 0.41	0.05
L1544	0.42 ± 0.46	0.46 ± 0.43	0.11
B1	0.41 ± 0.20	0.44 ± 0.19	0.010

B_{LOS} is sufficient to provide significant results for $\mathcal{R}$ and $\mathcal{R}'$. A hypothetical measured envelope $B_{LOS} = 0$ is a perfectly acceptable experimental result for computing $\mathcal{R}$ and $\mathcal{R}'$; the only requirement is that the sensitivity to B_{LOS} be sufficient to yield statistically meaningful results for $\mathcal{R}$ and $\mathcal{R}'$.

Table 2.2 shows $\mathcal{R}$ and $\mathcal{R}'$ and the 1σ uncertainties for each cloud. The uncertainties in $\mathcal{R}$ and $\mathcal{R}'$ depend on the uncertainties for the B_{LOS} given in Table 2.1 and the uncertainties in I_{OH} and ΔV. The uncertainty in the ΔV is about 0.02 km s^{-1} in each case. The nominal uncertainty in I_{OH} from the channel-to-channel noise in the spectra is only about 0.01 K. The uncertainties in both I_{OH} and ΔV are too small to contribute to the uncertainties in $\mathcal{R}$ and $\mathcal{R}'$. However, the absolute calibration of the line strengths is uncertain by about 10%. Although this systematic uncertainty would divide out in $\mathcal{R}$ and $\mathcal{R}'$ if the same telescope had been used for all observations, it may be that there is a calibration difference between the Arecibo telescope and the GBT. We have therefore used an uncertainty of 10% in each of the core and envelope values for I_{OH}. Even so, this uncertainty is insignificant in the error budgets for $\mathcal{R}$ and $\mathcal{R}'$. Those error budgets are dominated by the uncertainty in the B_{LOS} of each envelope, since the signal/noise ratio for those quantities is by far the lowest of any of the four measured quantities that go into $\mathcal{R}$ and $\mathcal{R}'$. We assume that the PDFs of these four measured quantities are Gaussian normal distributed (see §2.2.1).

We obtained the results for $\mathcal{R}$ and $\mathcal{R}'$ and their 1σ uncertainties with two different methods. First, we compute the uncertainties in $\mathcal{R}$ and $\mathcal{R}'$ by normal error propagation. This procedure is justified by the fact that the uncertainties in B_{LOS} are Gaussian normal (or very nearly so), and the possible systematic uncertainty in the N contribute insignificantly in comparison with the uncertainties in the B_{LOS}. However, due to the low signal-to-noise ratio in the B_{LOS} (especially in the envelope field strengths), the assumption of Gaussian normal errors in $\mathcal{R}$ and $\mathcal{R}'$ may not be strictly correct. We have therefore computed the PDF for $\mathcal{R}$ and $\mathcal{R}'$ for each of the four clouds by Monte Carlo simulations; for each Monte Carlo simulation, 10^6 trials were used. The results for $\mathcal{R}$ are shown in Figure 2.6; results for $\mathcal{R}'$ are extremely similar. Note that $\mathcal{R}$ and $\mathcal{R}'$ may be positive or negative. Over plotted on the Monte Carlo PDFs are the Gaussian normal error curves with the parameters given by the error propagation method. In all cases, the means and standard deviations from the two methods are essentially identical. However, the Monte Carlo PDF generally has a stronger tail at the high values of $\mathcal{R}$ and $\mathcal{R}'$, which slightly increases the probability that $\mathcal{R}$ (and $\mathcal{R}'$) are greater than one. These probabilities are essentially identical for $\mathcal{R}$ and $\mathcal{R}'$, so we list only one probability for each cloud in Table 2.2. Each of the four clouds is unlikely to have $\mathcal{R}$ and $\mathcal{R}' > 1$, with probabilities of being greater than one varying from less than 1% to about 10% (table 2). The probability that all four of our clouds have $\mathcal{R}' > 1$ is just the product of the probabilities in Table 2.2, or 3×10^{-7}, a highly significant result. Our experiment is therefore in contradiction with the hypothesis that these four cores were formed by ambipolar diffusion.

There are several possible biases that could affect $\mathcal{R}$ and $\mathcal{R}'$. First, as discussed above, the Arecibo telescope beam pattern biases the observed $\mathcal{R}$ and $\mathcal{R}'$ to be closer to 1 than the "real" values. Since the observed $\mathcal{R}$ and $\mathcal{R}' < 1$, these observed values are biased to be higher than the actual values. In addition, there is a factor that may systematically raise or lower $\mathcal{R}$ and $\mathcal{R}'$ – the possible curvature of the magnetic field lines. Field lines will be drawn into an "hourglass" morphology as a core forms. Because the four cores out of 34 that we have observed in this experiment are among the few with strong B_{LOS}, it is likely that $\mathbf{B}$ points approximately along the line of sight for these four cores. The field line through the cloud center would then point along the line of sight, so B_{LOS} would equal the total B. However, other field lines passing through a core would be curved away from the line of sight in the near and far side of the core, so B_{LOS} would be less than the total B. In the envelope a similar effect would hold, but the curving of magnetic field lines in the "hourglass" would be less extreme in this lower density outer region. See Galli & Shu (1993) Figure 2.5b for an example of the morphology of magnetic field lines; for a typical distance of 150 pc, the radius of the Arecibo beam would be 2×10^{17} cm. Hence, one might generally expect B_{LOS} to underestimate B by a smaller factor in the envelope than in the core of a cloud, which would bias $\mathcal{R}$ and $\mathcal{R}'$ to be too high – the same sense as the Arecibo sidelobe bias. However, exactly which direction the field curvature bias would go and by how much would depend on the detailed structure of the magnetic field morphology. But in any case, the bias must be insignificant. Even if the mean field directions over the GBT and Arecibo beams differed by 30° due to an hourglass morphology, a very unrealistically large value, the change in the measured B_{LOS} would be by the factor $cos 30^\circ = 0.87$, and $\mathcal{R}$ and $\mathcal{R}'$ would be biased high by the factor 1/0.87. The resulting $\mathcal{R}$ and $\mathcal{R}'$ would be changed by only about 1σ by such an unrealistically large net angle difference. (Of course, if the magnetic fields are not regular, this angle could be much larger, but for our comparison with the "idealized" ambipolar diffusion model this is not relevant.) Finally, since we assume that $N(OH) \propto$ the mass M, if [OH/H] varies between the envelope and core, $\mathcal{R}$ and $\mathcal{R}'$ would be affected. It seems unlikely that there is a significant systematic variation in [OH/H] between the envelopes and cores that we have observed. There is only a 50% difference in the column density of OH between core and envelope, so the physical regions being sampled are not that different. Moreover, Crutcher (1979) found no evidence for a variation in [OH/H] up to $n(H_2) \sim 2 \times 10^4$ cm^{-3}, which includes the range our observations sample. So our measured $\mathcal{R}$ and $\mathcal{R}'$ can be slightly biased, probably overall in the direction of being closer to 1 than the "real" values, but not by sufficiently large amounts to change the significant result of this experiment.

2.6 Discussion

We have found that M/Φ decreases significantly from envelope to core, or from the initial central value to the present evolved central value, for the clouds we have studied. How does this observational result compare with the prediction of the strong field, ambipolar diffusion driven theory and the weak field, turbulence driven theory?

We first consider the ambipolar diffusion theory. We compare our results with what we called above idealized models, which include only gravity, regular magnetic fields, and thermal pressure. The non-thermal motions and irregular structures of observed clouds, which themselves are embedded in a complex interstellar medium, are not directly considered in these idealized models. Perhaps for this reason, the ambipolar diffusion models are not compatible with the structure we observe in both column density and magnetic field strength. Figures 2.2-2.5 show clearly that the column densities vary considerably around the core positions of our clouds, rather than the uniform result that would be expected from a idealized model with **B** oriented closely along the line of sight. Also, the observed B_{LOS} in two envelopes clearly show structure, with B_{LOS} at the west envelope position of L1544 being about twice as strong as toward the core, and much stronger than toward the other three envelope positions. B1 shows a north-south "ridge" of B_{LOS}, with weaker B_{LOS} toward the east and west envelope positions. These observations cannot be reproduced by an ambipolar diffusion idealized model.

The strong magnetic field/ambipolar diffusion theory *requires* that M/Φ increase in the core as evolution proceeds; after all, this increase *is* ambipolar diffusion, the heart of this theory. Hence, this theory predicts $\mathcal{R}' > 1$. The amount by which $\mathcal{R}'$ exceeds 1 would be dependent on the specific parameters for a model cloud – mainly the assumed initial M/Φ. For example, Ciolek & Mouschovias (1994) discussed a model cloud broadly consistent with the parameters of the clouds we observe. Although their model is in terms of dimensionless parameters, they state that the original unevolved cloud is consistent with a temperature of 10 K, a central density of 2.6×10^3 cm^{-3}, a central magnetic field of 35 μG, a radius of 4.3 pc, and a total mass of 98 $M_{\odot}$. At the time when the core becomes magnetically critical, the central density has increased by a factor ~ 37 while the central B has increased by less than 1.7. The initial M/Φ is subcritical with the central $M/\Phi = 0.256$ of critical; for this model, the predicted $\mathcal{R}' \approx 4$. However, our results for all four observed clouds is $\mathcal{R}' << 4$ with high degrees of significance.

There have been ambipolar diffusion models calculated specifically for two of the clouds in our sample, for comparison with observational data available at that time. Crutcher et al. (1994) discussed a model specifically for B1; it had a core mass of 13 $M_{\odot}$, an envelope mass of 600 $M_{\odot}$, an envelope radius of 2.9 pc, an initial central $B = 43$ μG, and an initial central $M/\Phi = 0.42$ of critical. The model assumed that the cloud was a disk whose minor axis was at an angle $\theta = 70^{\circ}$ to the line of sight; all observed properties of B1 available at that time were given accurately by the model. The prediction of this model would be $\mathcal{R}' = 1/0.42 = 2.4$, a factor of 5 larger than our result (Table 2.2) for B1. Moreover, now that the Troland & Crutcher (2008) survey of dark cloud cores has shown that B1 has the greatest B_{LOS} of any core with a detected B_{LOS}, it seems more likely that **B** is nearly along the line of sight, and that the true central total B is close to the observed $B_{LOS} = 27$ μG and not the model result $B = 85$ μG, which implied $B_{LOS} = 85 cos 70^{\circ} = 29$ μG. When B1 was among a very small number of dark clouds with sensitive OH Zeeman observations, it was not unreasonable to hypothesize that its field lay nearly in the plane of the sky. However, other clouds similar to B1 with similar total field strengths should have **B** nearly along the line of sight, yielding $B_{LOS} \sim 85$ μG; these are not found in the Troland & Crutcher (2008) survey results.

Ciolek & Basu (2000) computed a model for L1544. The model had 30 $M_{\odot}$ within a radius of 0.45 pc, with additional mass that does not participate in the evolution in the envelope at larger radius (not clearly specified, but apparently about 2.5 pc based on their Figure 2.1c). They assumed $\theta \approx 74^{\circ}$, again a very large angle between **B** and the line of sight, which was necessary in order to have the required large central B agree with the small observed value of B_{LOS}. The initial M/Φ was 0.8 of critical, or closer to critical than other ambipolar diffusion models discussed above. This would imply $\mathcal{R}' \approx 1.25$, which differs from our measurement $\mathcal{R}' = 0.46 \pm 0.43$, although not by a highly significant amount. However, as for B1, the large value for θ they had to assume in order to make the field strength of the model agree with the observation of B_{LOS} seems unreasonably large. Not all **B** can lie near the plane of the sky!

The ambipolar diffusion model results are all $\mathcal{R}' > 1$, with the actual value depending on the initial assumed M/Φ. But even if all clouds start only very slightly subcritical, which would in itself minimize the importance of ambipolar diffusion in cloud evolution, our results are not consistent with the ambipolar diffusion requirement.

A possible way out of this conclusion might be to hypothesize that the magnetic fields in our envelope regions are not the regular ones of the idealized models, but rather that these magnetic fields twist and indeed reverse direction. By fitting for a single value of B_{LOS} for each envelope, we obtain a smaller value for B_{LOS} (and hence a smaller $\mathcal{R}'$) in the entire envelope surrounding the core than we would have gotten if we had (for example) just taken the largest value of B_{LOS} at any of the four positions. If the field at the GBT positions twisted significantly, then perhaps the largest absolute value of B_{LOS} would be the appropriate one to use in calculating the magnetic flux in the envelope region. At the other three positions surrounding a core, B_{LOS} could be smaller due to $\mathbf{B}$ being twisted into the plane of the sky or even to pointing in the opposite direction from the field in the core. However, our fit for a single envelope value of B_{LOS} is the proper one for testing at least the idealized models of this theory. This single value gives (approximately) the result that would be obtained with a ring telescope beam as it would sample the envelope regions. But more importantly, the GBT beams are centered only $6'$ from the center of each core, or at a radius of 0.26 pc for a typical cloud distance of 150 pc. This radius is about an order of magnitude smaller than the cloud radii in the three idealized ambipolar diffusion models discussed above, where the models require a smooth and not tangled magnetic field. The GBT positions are not far enough away from the cores that they could be sampling unrelated flux tubes that may have nothing to do with the envelopes of the cores. Moreover, such a twisted (indeed reversed) field explanation would have to hold for all four of our cores, which seems statistically unlikely. Finally, the good agreement in radial velocities of the core and envelope OH spectral lines (Figures 2.2-2.5) suggests that the GBT observations do sample the envelope regions of the cores.

What about predictions of initially weak magnetic field, turbulent theories? Such simulations are of course also idealized, with artificial boundary conditions, simple turbulence algorithms without a physical mechanism for generating the turbulence, and neglect of some physics. Nonetheless, our comparison is with state-of-the-art simulations. Recently, Lunttila et al. (2008) have computed synthetic Zeeman profiles for their super-Alfvénic (weak magnetic field) simulations of molecular clouds and cores formed by turbulence in an initially uniform interstellar medium. The mean field strength in their simulations is quite low; $\overline{B}_{LOS} \approx 2.1\ \mu$G along the direction of the original uniform $\mathbf{B}$. They performed numerically the same experiment for which we report here the observational results. That is, they "observed" the synthetic Stokes I and V spectra at each of their core positions with a $3'$ beam and at four envelope positions around each core with $8'$ beams pointed $6'$ north, south, east, and west of the core positions. They computed $N(OH)$ from their Stokes I profiles and B_{LOS} by fitting their synthetic Stokes $dI/d\nu$ to their V profiles (the same technique used observationally). They analyzed 36 (out of 139 total) cores with $B_{LOS} > 10\ \mu$G, corresponding roughly to field strengths in the four cores we have observed. For these 36 cores, the mean $N(H_2) = 6.6 \times 10^{21}$ cm^{-2}, which agrees reasonably well with the mean $N(H_2) = 4.3 \times 10^{21}$ cm^{-2} for our four cores. The mean line width of the 36 cores was $\Delta V \approx 1$ km s^{-1}, which also agrees with our four observed cores. For these cores they found that $\mathcal{R}$ had a large scatter, $0.08 \leq \mathcal{R} \leq 1.6$, with the PDF favoring values less than 1. Hence, the weak field, turbulent calculation of the formation of molecular clouds and cores seems to agree in physical properties with the four cores we have observed. Given that our experiment included only four clouds, the range in $\mathcal{R}$ corresponds well with the observed range.

We suggest that other simulations, such as those with stronger magnetic fields that include both ambipolar diffusion and turbulence, should be compared with our experimental results in the same manner as did Lunttila et al. (2008).

2.7 Conclusion

Previous Zeeman studies of magnetic fields in molecular clouds have not been definitive in testing the two extreme-case models of star formation. The mean mass-to-flux ratios M/Φ found from these statistical studies were slightly supercritical – consistent with either theory. Detailed ambipolar diffusion models for two clouds found excellent agreement with the observations, although both required the field to be nearly in the plane of the sky in order not to produce line-of-sight fields much stronger than observed. Uncertainties in the angle between $\mathbf{B}$ and the line of sight and in the total hydrogen column density are inherent in measuring with Zeeman observations. In order to mitigate these uncertainties, we have measured the ratio of M/Φ between the envelopes and cores of four molecular clouds in order to test ambipolar diffusion (strong magnetic fields) versus turbulence (weak magnetic fields) driven star formation theory. The theory of star formation that hypothesizes clouds initially supported by strong magnetic fields, with evolution and core formation being driven by ambipolar diffusion, predicts that the central M/Φ must increase as ambipolar diffusion acts. Idealized models predict that the increase in M/Φ up to the point when the core becomes supercritical and gravitational collapse proceeds is approximately equal to the inverse of the amount by which the original cloud was subcritical; that is, $\mathcal{R}' > 1$. The probability that all four of our clouds have $\mathcal{R}' > 1$ is 3×10^{-7}, a highly significant result. On the other hand, simulations which form clouds and cores by turbulence acting in a weak magnetic field environment preferentially yield a M/Φ ratio between core and envelope $\mathcal{R} < 1$, in agreement with our results.

Telescope availability limitations allowed only four clouds to be observed; unfortunately the extremely large amount of telescope time required precludes expanding this experiment beyond four clouds for the foreseeable future. The theoretical predictions of $\mathcal{R}$ and $\mathcal{R}'$ are based on idealized ambipolar diffusion models and idealized turbulence simulations. Nonetheless, the clear conclusion from our experiment is that at least for these four clouds, the prediction of the idealized ambipolar diffusion models does not agree with our observational results, while the prediction of initially supercritical turbulence-driven simulations does. Still untested is whether simulations that include both significant magnetic fields and turbulence better match the data than either of the extreme cases. We suggest that all theorists who simulate the formation and evolution of molecular clouds and cores test their simulations against the results of this experiment in the manner of Lunttila et al. (2008); that is, by calculating Stokes I and V spectra of OH from the simulations and "observing" B_{LOS} with our beam patterns (Figure 2.1).

We thank the National Radio Astronomy Observatory for the allocation of about 300 hours of observing time on the GBT in response to proposal GBT07A-029, and the observatory staff for help in making the observations successful. We thank Phil Perillat of the Arecibo Observatory for help in re-calibrating the Arecibo spectra, and we especially thank Carl Heiles and Tim Robishaw for allowing us to use their GBT software and for helping us understand how to make it work. Finally, we thank two conscientious referees who provided valuable suggestions to refine the scientific and statistical arguments in this paper. This research was partially supported by NSF grants AST 0307642 and 0606822, and by NRAO grant GSSP07-0007.

2.8 Figures

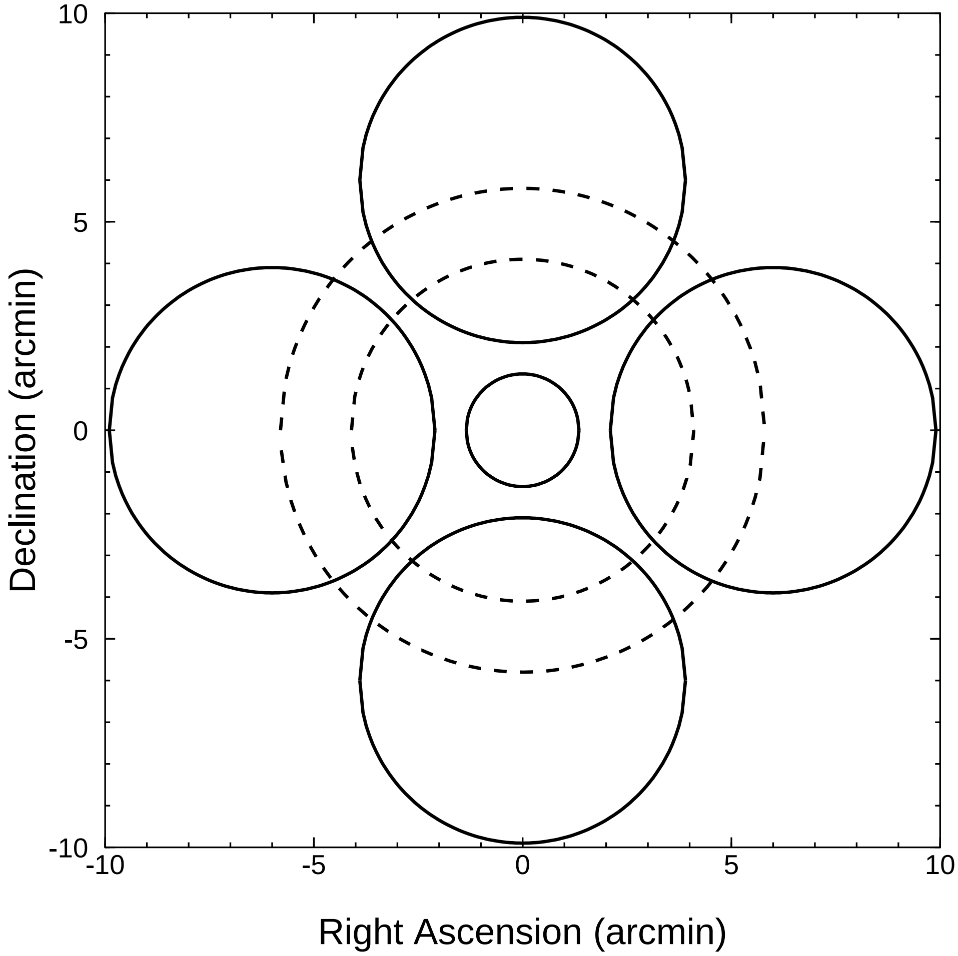

Figure 2.1 The Arecibo telescope primary beam (small circle centered at 0,0) and the four GBT telescope primary beams (large circles centered 6′ north, south, east, and west of 0,0). The dotted circles show the first sidelobe of the Arecibo telescope beam. All circles are at the half-power points.

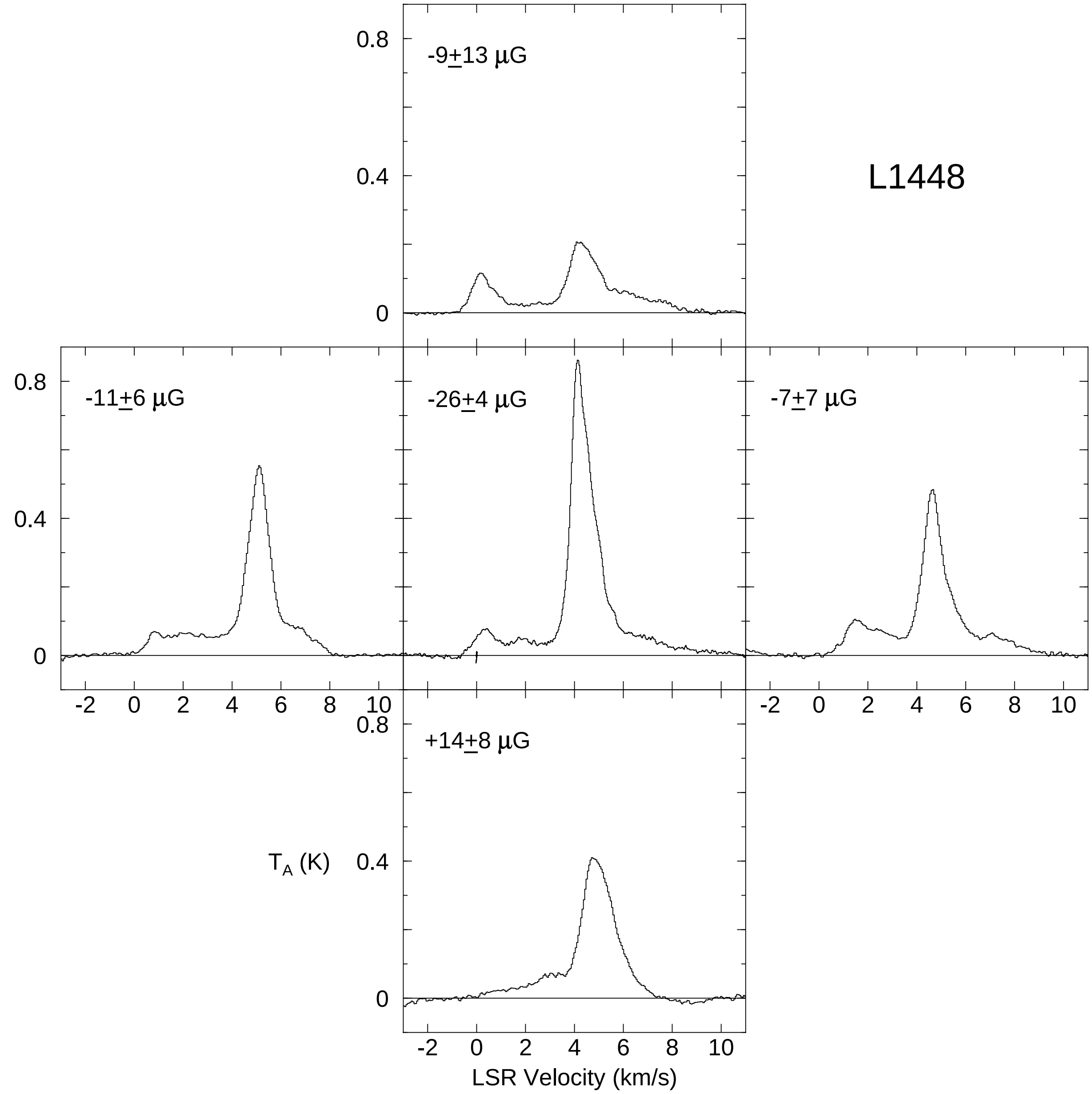

Figure 2.2 OH 1667 MHz spectra toward the core of L1448CO obtained with the Arecibo telescope (center panel) and toward each of the envelope positions 6′ north, south, east, and west of the core, obtained with the GBT. In the upper left of each panel is the inferred B_{LOS} and its 1σ uncertainty at that position. A negative B_{LOS} means the magnetic field points toward the observer, and vice versa for a positive B_{LOS}.

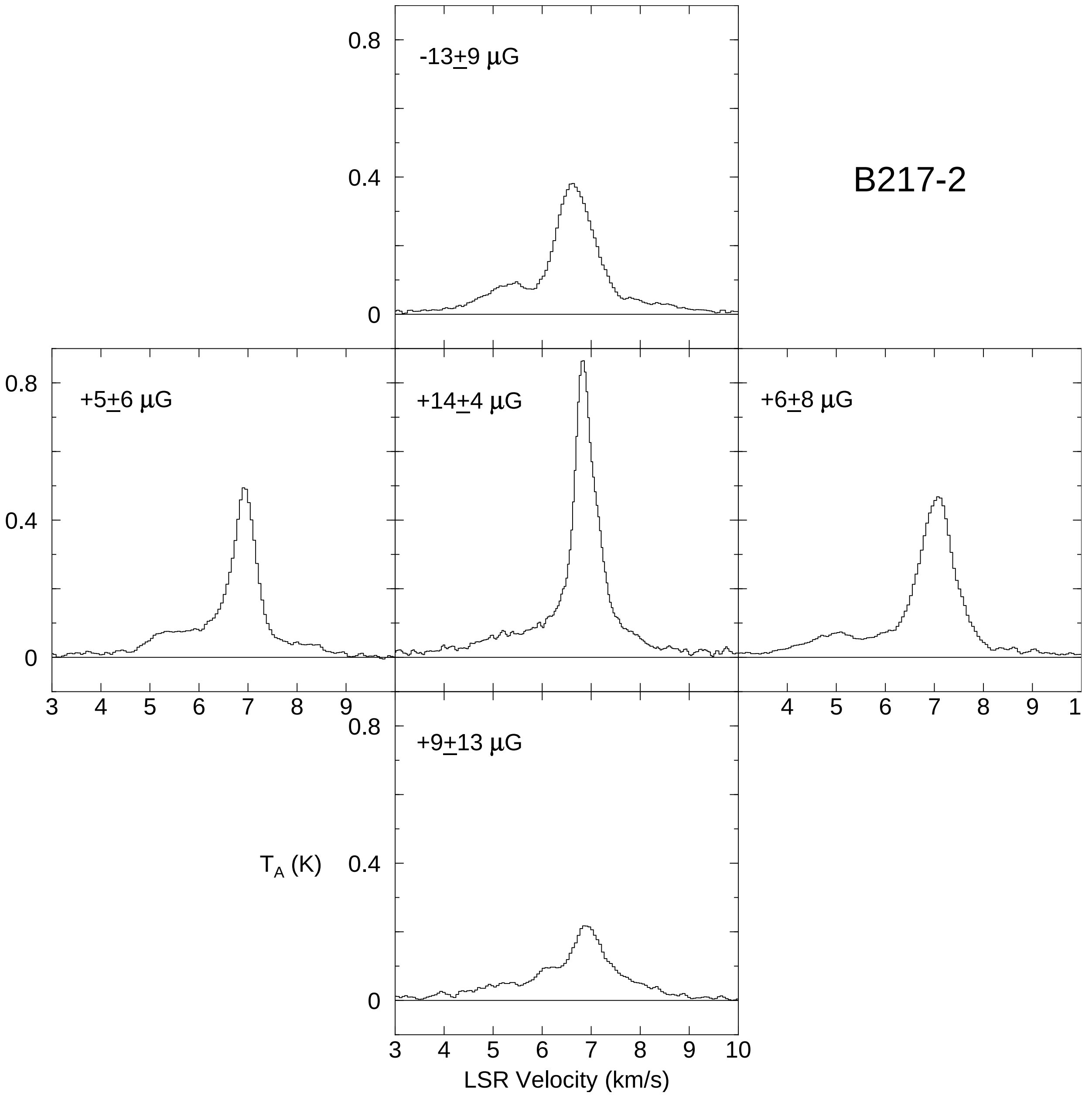

Figure 2.3 As in Figure 2.2, but for B217-2.

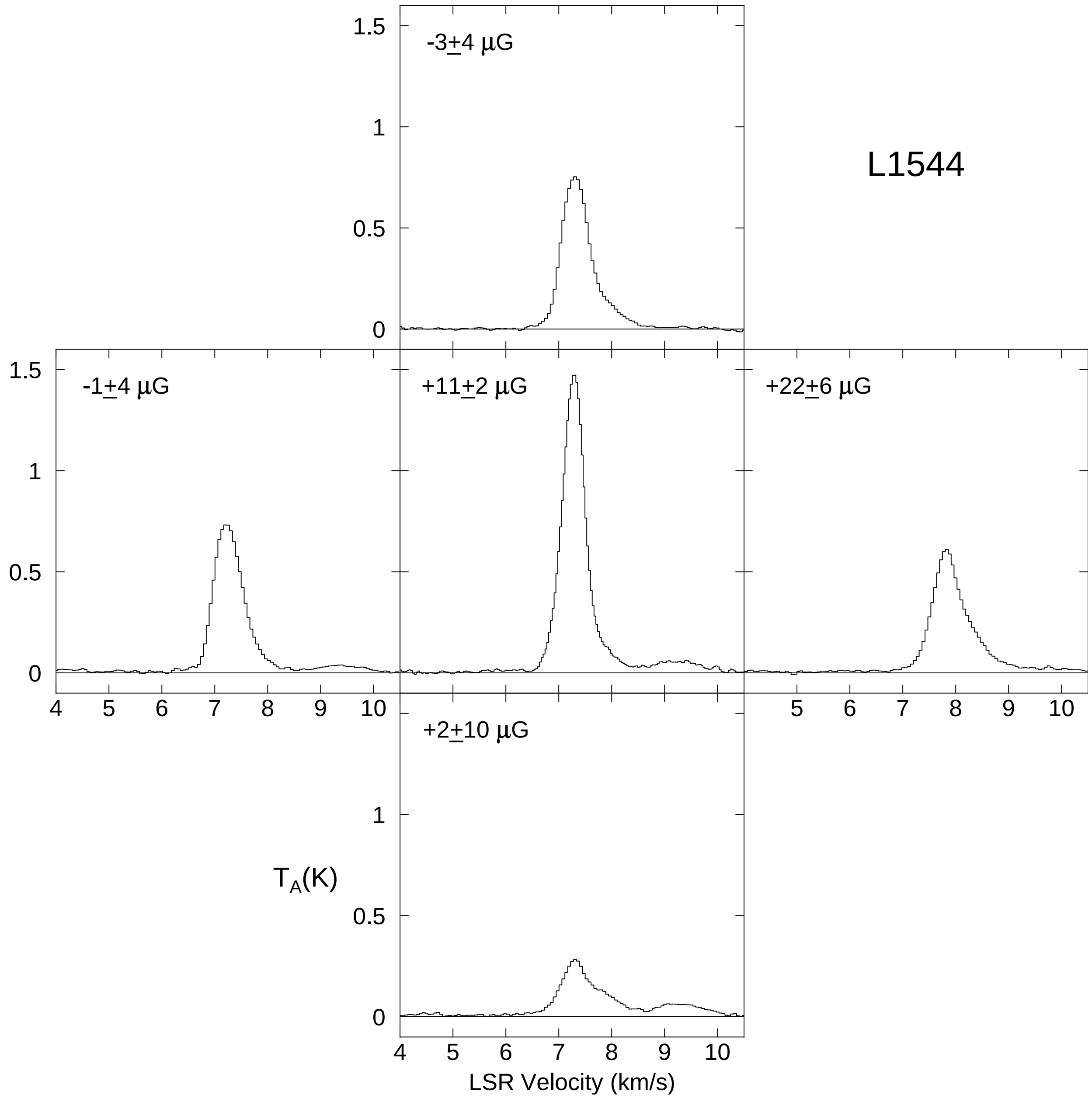

Figure 2.4 As in Figure 2.2, but for L1544.

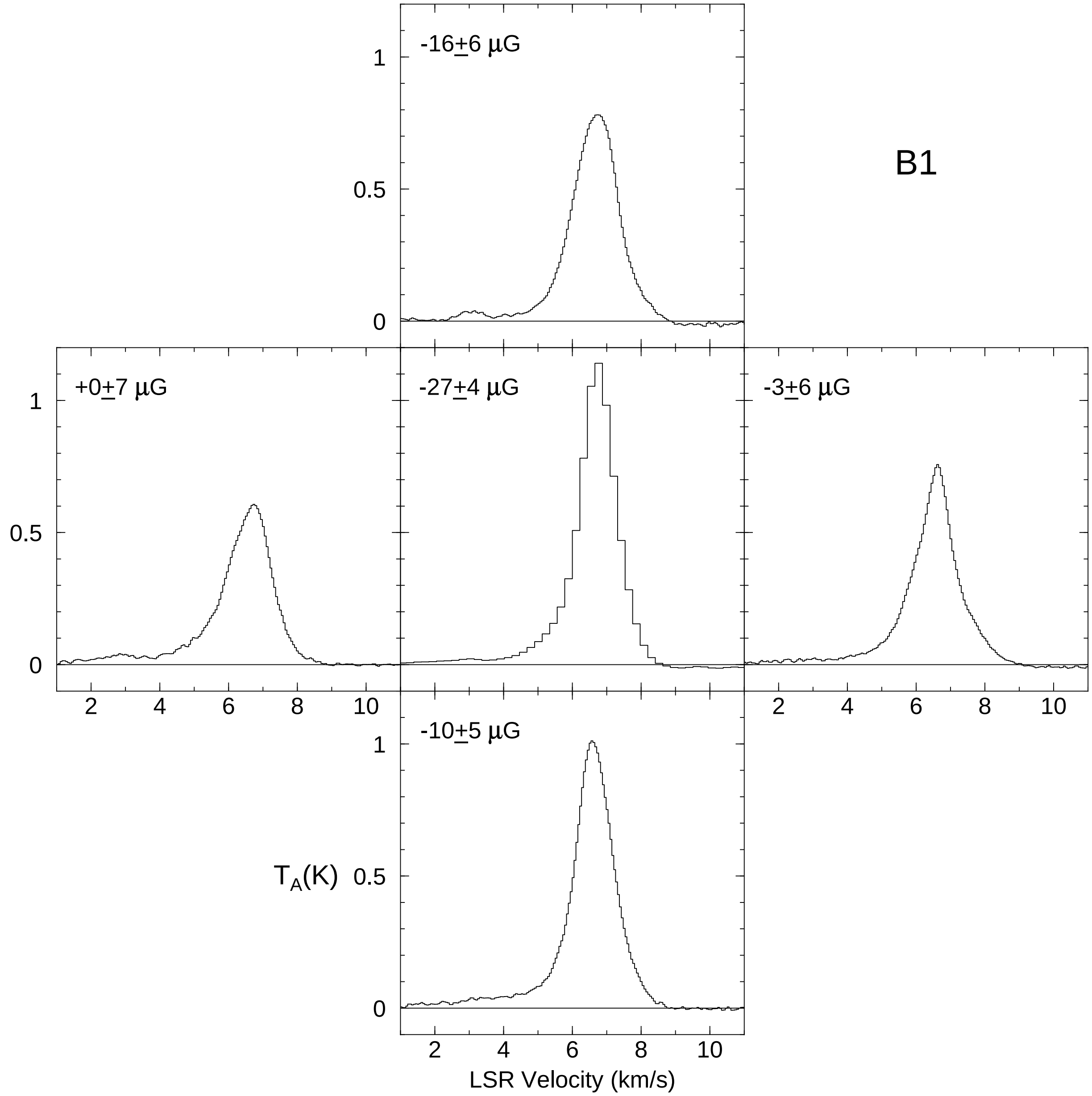

Figure 2.5 As in Figure 2.2, but for B1.

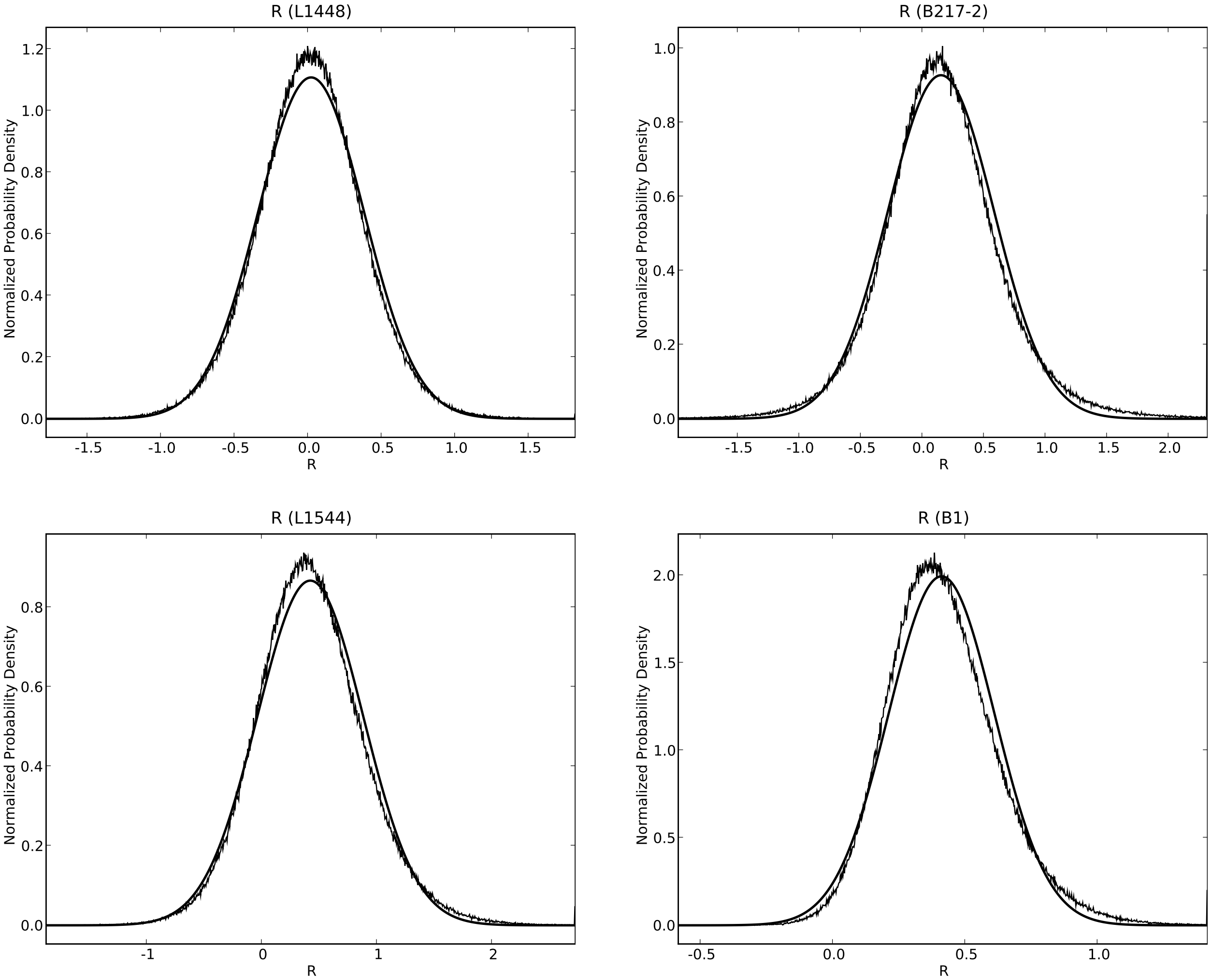

Figure 2.6 Monte Carlo estimate of $\mathcal{R}$ for each cloud. The Gaussian normal error curve for the error propagation results given in Table 2.2 are also shown.

Chapter 3

Self-Consistent Analysis of OH Zeeman Observations[*]

3.1 Introduction

The relative importance of magnetic fields and turbulence in driving the formation of molecular cores is a central question in current star formation theory. Measuring magnetic field strengths in order to infer ratios of mass to magnetic flux (M/Φ) has been a focus of observational efforts to answer this question. However, the only technique for directly measuring interstellar magnetic field strengths, the Zeeman effect, has only yielded results for the line-of-sight component B_{LOS} of the magnetic vector $\mathbf{B}$. A statistical analysis carried out with several assumptions has been the standard analysis technique for Zeeman results, but this only determines the mean or median value of $|\mathbf{B}|$ for the observed set of clouds, which significantly limits tests of the theory.

To overcome this limitation, Crutcher et al. (2009) (hereinafter CHT) carried out OH Zeeman observations toward the envelope regions surrounding four molecular dark cloud cores, selected from a survey of 34 cores for having strong B_{LOS}, and evaluated the *ratio* $\mathcal{R}$ of M/Φ in a cloud core to that in the envelope. The goal was to test published strong magnetic field models that have uniform initial fields. The value of this technique is that published models of core formation driven by ambipolar diffusion have strong, regular magnetic field morphology such that the unknown angle θ between $\mathbf{B}$ and the line of sight is approximately the same in core and envelope regions, allowing θ to be eliminated from the expression for $\mathcal{R}$. The CHT analysis depended on the assumptions that the magnetic field direction was essentially uniform in each cloud and that the ratio of strengths of the quasi-thermal OH lines between envelope and core gave an accurate indicator of the ratio of column densities between envelopes and cores. The idealized ambipolar diffusion theory of core formation requires $\mathcal{R}$ to be approximately equal to the inverse of the original subcritical M/Φ, or $\mathcal{R} > 1$. CHT were able therefore to directly test this prediction. They found that the probability that all four of the clouds have $\mathcal{R} > 1$ is 3×10^{-7}; the results are therefore significantly in contradiction with the

---

[*] This chapter was previously published as **"Self-Consistent Analysis of OH Zeeman Observations"**, in The Monthly Notices of the Royal Astronomical Society (Crutcher, Hakobian, & Troland, 2010) in response to comments raised in Mouschovias & Tassis (2009).

Table 3.1. Observational Results

Position	B_{LOS} (μG)	$\frac{(n-s)}{\sigma}$	$\frac{(n-e)}{\sigma}$	$\frac{(n-w)}{\sigma}$	$\frac{(s-e)}{\sigma}$	$\frac{(s-w)}{\sigma}$	$\frac{(e-w)}{\sigma}$
L1448n	-9 ± 13	1.5	0.1	0.3	2.4	0.8	0.4
L1448s	$+14 \pm 8$						
L1448e	-11 ± 6						
L1448w	-7 ± 7						
B217n	-13 ± 9	1.4	1.7	1.7	0.3	0.2	0.1
B217s	$+9 \pm 13$						
B217e	$+5 \pm 6$						
B217w	$+6 \pm 8$						
L1544n	-3 ± 4	0.5	0.4	3.6	0.3	1.7	3.2
L1544s	$+2 \pm 10$						
L1544e	-1 ± 4						
L1544w	$+22 \pm 6$						
B1n	-16 ± 6	0.7	1.6	1.4	1.2	0.9	0.4
B1s	-10 ± 5						
B1e	$+0 \pm 7$						
B1w	-3 ± 6						

hypothesis that all four of these cores were formed by ambipolar diffusion.

Mouschovias & Tassis (2009) (hereinafter MT) have strongly criticized the CHT result, arguing both that the CHT analysis is internally inconsistent and that a different analysis technique that they apply to the CHT data shows that $\mathcal{R} > 1$ is consistent with the data. In this letter we show that the CHT analysis is internally consistent, and that the MT analysis is itself internally inconsistent.

3.2 Consistency of the CHT Analysis

CHT measured B_{LOS} at the four cardinal envelope positions (labeled n, s, e, w) surrounding each core, but they inferred the mean B_{LOS} in each envelope by fitting simultaneously over all the Stokes I and V spectra from the envelope. This enabled them to synthesize a toroidal telescope beam that sampled the envelope while excluding the core. B_{LOS} for the core was measured separately by fitting spectra from a single beam that covered the core area. They then calculated $\mathcal{R}$ from

$$\mathcal{R} \equiv \frac{M_{core}/\Phi_{core}}{M_{envelope}/\Phi_{envelope}}. \tag{3.1}$$

The mass (the OH lines are optically thin) and magnetic flux are given by

$$M \propto I\,\Delta V \quad \text{and} \quad \Phi \propto (B_{LOS}/cos\ \theta), \tag{3.2}$$

where I is the line intensity, ΔV the line width, and θ the angle between $\mathbf{B}$ and the line of sight.

With the assumption, based on published strong **B** models (see CHT for references), that $\theta_{core} \approx \theta_{envelope}$, the $cos\ \theta$ terms in the numerator and denominator of $\mathcal{R}$ cancel, and one is left with directly observable quantities only. Thus $\mathcal{R}$ and its uncertainty could be evaluated. CHT evaluated the uncertainty with a Monte Carlo analysis that utilized the known uncertainties in I, ΔV, and B_{LOS}. This analysis hinged on one crucial assumption – that the mean magnetic field direction in the envelope immediately surrounding a core putatively formed by ambipolar diffusion had the same (or nearly the same) direction as in the envelope. MT argued that the data are demonstrably inconsistent with this assumption and that therefore the CHT analysis is invalid.

Table 3.1 and Figure 3.1 show the relevant data. MT claim that the B_{LOS} shown in Table 3.1 show clear variation in field strength and perhaps even reversals in field direction among the four envelope positions for each cloud. They then argue that this variation violates the CHT assumption that the field direction is essentially uniform in direction for each cloud.

We also give in Table 3.1, after the north envelope B_{LOS} entry for each cloud, each of the six possible differences between envelope values of B_{LOS}, divided by the 1σ uncertainty in each difference from the individual measurement uncertainties. If MT are correct, these data should show a scatter significantly greater than that imposed by the measurement uncertainties. However, the mean of the 24 differences is 1.12 ± 0.25, where the uncertainty takes into account that there are 16 and not 24 independent measurements. The mean for the normal error function is 0.80. Hence, the scatter in the B_{LOS}, including the nominal reversals in direction, is only marginally larger than the scatter that would result from measurement uncertainty. Most of the larger scatter is produced by the single position L1544w; excluding this position, the mean of the remaining 21 differences is 0.87 ± 0.18, in agreement with measurement error being entirely responsible for the scatter in the 15 measured B_{LOS} excluding the L1544w position. The differences are also shown graphically in Figure 3.1, along with the normal error function for comparison. If the scatter in the B_{LOS} were due entirely to measurement uncertainty, these two plots would agree. These plots confirm the conclusion drawn from the mean of the differences. Even with the L1544w position included, the measured differences agree fairly well with the normal error function, while if L1544w is excluded, the agreement is excellent. Hence, while the L1544w position may be anomalous – as discussed originally by CHT – there is no statistically significant evidence for the MT claim that the CHT assumption of a fairly uniform field direction for each cloud is invalid. The scatter in the differences is entirely attributable to the measurement uncertainties and not to any intrinsic scatter in the B_{LOS}. Even if the L1544 cloud were excluded from the CHT analysis, the CHT conclusion that these cores were not formed by ambipolar diffusion remains valid.

MT give an example of possible measurements of 10 μG and 14 μG, each with uncertainty 0.1 μG, and note that the mean differs from each value by 2 μG, not the 0.07 μG given by propagation of errors. However, these 100σ and 140σ examples are not germane to the CHT case of roughly $1 - 2\sigma$ measurements. Moreover, CHT did not average the four envelope results for each cloud and obtain the uncertainty by error propagation; they synthesized a toroidal beam to sample the envelopes and obtained the uncertainties directly from the single envelope B_{LOS} measurement for each cloud.

3.3 Consistency of the MT Analysis

MT argue that an arbitrarily twisted field morphology (see the cartoon shown in MT Figure 1) must be included in the analysis for $\mathcal{R}$. Although we have argued above that the data do not require that such a morphology is present, let us follow MT and assume that it is. The MT analysis of the CHT data should then be consistent with this proposed model of the field morphology – that is, that the angle θ between the core and envelope fields are arbitrarily large. But then the MT analysis *itself* is internally inconsistent with this model. CHT defined $\mathcal{R}$ in order to eliminate the unknown angle θ between the field direction and the line of sight; CHT assumed that between the core and the envelope of a cloud those directions are the same (except for minor differences in the θ that do not significantly affect the analysis, see discussion in CHT). That assumption allowed the unknown angle θ between the field and the line of sight, which enters as $cos\ \theta$, to drop out of the ratio $\mathcal{R}$ (see Equations 1 and 2). If the θs for the four envelope positions and the core of each cloud vary greatly, as suggested in MT Figure 1, then θs do not drop out of $\mathcal{R}$. For a self-consistent MT analysis, each of the five different θs (core and four envelope) would have to be explicitly included in the expression for $\mathcal{R}$. However, MT do not do so; such an expression would have the five unknown θs and could not be evaluated. Instead, MT use our expression for $\mathcal{R}$ with the $cos\ \theta$s missing. MT stated that they were only allowing for different *magnitudes* in $\mathbf{B}$ over the four envelope positions, not for different directions θ. But this assumption is completely inconsistent with the astrophysical motivation of strongly twisted field lines (MT Figure 1 and discussion) that they give for rejecting the CHT analysis and substituting their own. MT offer no astrophysical explanation for fields at the envelope positions varying significantly in strength and perhaps even being antiparallel while the angle θ remains invariant. The MT analysis is therefore not self-consistent, and cannot be used to analyze the CHT data.

Even within the framework of the MT analysis, it appears that the uncertainty in the $\mathcal{R}s$ is overestimated. MT considered the variation of the measured B_{LOS} as one component of the uncertainty, and then added as a second component the measurement uncertainties. However, as we showed above, the variation in the measured B_{LOS} is consistent with being due to the measurement uncertainties and not to a real variation. MT appear to be doubly counting the uncertainties.

3.4 Conclusion

CHT concluded that their measurements of the ratios of M/Φ between envelopes and cores did not agree with the prediction of the ambipolar diffusion model. Here we have shown that the CHT analysis is internally self consistent; their conclusions are valid within the framework of the assumptions they made. The validity of the MT paper rests on two pillars: (1) that the CHT data analysis procedure is unambiguously inconsistent with the data itself, and (2) that MT have a superior analysis technique. We have demonstrated that neither of these pillars of their paper is correct. The conclusions of Crutcher et al. (2009) therefore stand – the observed variations of M/Φ from envelope to core are not consistent with the prediction of the ambipolar diffusion driven theory of star formation. This conclusion does not, of course, rule out the possibility that there are structures in magnetic field morphology near dark cloud cores; higher resolution and higher sensitivity observations would be necessary to investigate this possibility.

The approach of CHT to test the ambipolar diffusion driven model of star formation by measuring the change in M/Φ between envelope and core is a powerful one that should be further exploited, since it reduces uncertainties in actual values of magnetic field direction and mass estimates by taking ratios. Unfortunately, such experiments will require very large amounts of telescope time. However, use of the eVLA for OH Zeeman mapping and ALMA for CN Zeeman mapping may make it possible to extend this technique to smaller scales without requiring such large assignments of telescope time.

Although the data do not require this, if we do assume that the magnetic fields in the four cores we observed are twisted such that there are field reversals, the presence of such field reversals would imply that a region has a weak magnetic field. This is fundamentally incompatible with ambipolar diffusion theory, not because there are field reversals, but due to the implication that the magnetic field is inherently weak. MT's comments suggest that the technique of averaging the four envelope B-field measurements together is incorrect due to the presence of field reversals; however, this suggestion is inherently inconsistent with their stance that these data do not rule out the possibility that the magnetic fields are sufficiently strong that they dominate cloud support against gravity, the central tenant of ambipolar diffusion star formation theory.

This work is partially supported by the NSF under grants AST 0307642, 0606822 and 0908841.

3.5 Figures

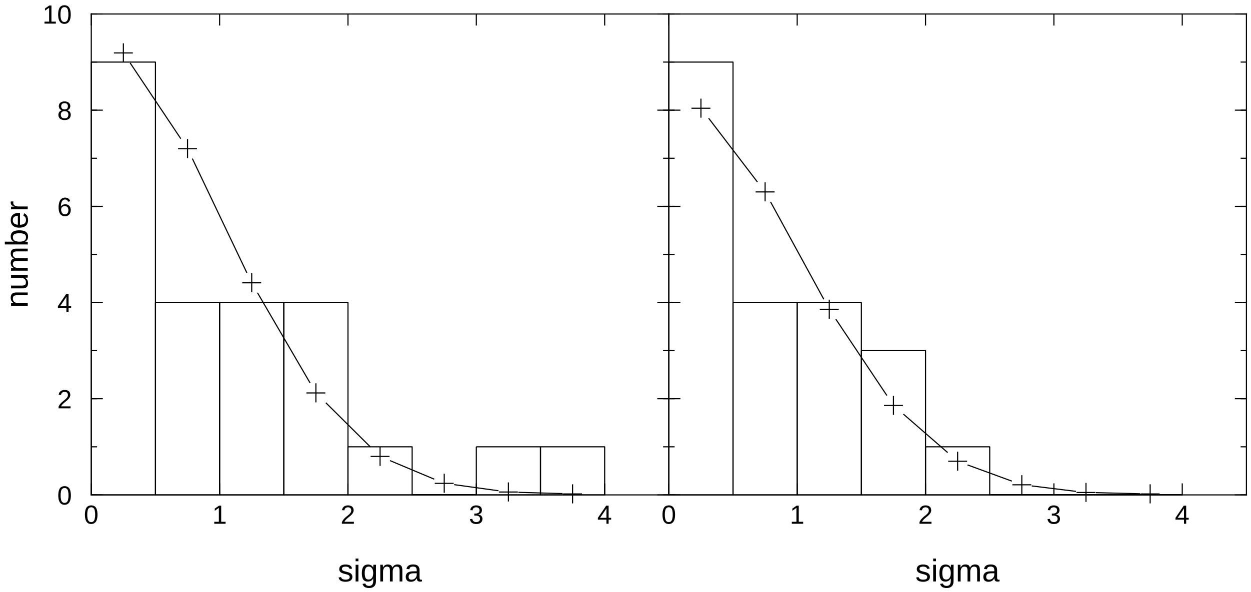

Figure 3.1 Left: Histogram plot shows the difference data from Table 3.1, (position 1 - position 2)/σ, in 0.5σ bins; plus signs show the normal error function for 24 data points. Right: Same as left, except the three differences produced by the L1544w position have been removed, and the normal error function is for 21 data points.

Chapter 4

Structure and Composition of Molecular Clouds with CN Zeeman Detections I: Data*

4.1 Introduction

The measurement of magnetic fields harbors several difficulties due to the fact that they are a vector quantity. In order to measure the absolute magnitude and direction of the magnetic field, it is necessary to sample the two components in the plane of the sky and the line-of-sight component. While dust polarization can measure the direction of a magnetic field in the plane of the sky, the line-of-sight component intensity can be directly measured. This is accomplished through the detection of the normal Zeeman effect that occurs when an atom or molecule is in the presence of a magnetic field. Most transitions have a Zeeman splitting factor that is too small to measure unless in dense, spatially-compact environments with exceedingly large magnetic field strengths. However, HI, OH, and CN have splitting factors that are large enough to measure the weaker magnetic fields that are expected around sites of active star formation in molecular clouds. The CN N = 1-0 transition has seven strong hyperfine components (Table 4.1) that have a large distribution of Zeeman splitting factors. The two strongest hyperfine components, with relative strengths of 27 and 10 respectively, also have large splitting factors.

Falgarone et al. (2008) continued the pioneering work of Crutcher et al. (1999b). Including the earlier results, they surveyed 14 molecular cloud cores and measured the line-of-sight magnetic field strength using the CN Zeeman effect. The strongest magnetic field detected was 1.10 ± 0.33 mG towards the Ultra-Compact HII (UCHII) region of W3(OH) (Hoare, 2005), a high mass star formation site in the W3 molecular cloud complex. For these measurements, Falgarone et al. (2008) used the IRAM 30-meter telescope. Due to the relatively large beam size of the IRAM-30 meter telescope ($23''$ or 46,000 AU in diameter at the 2 kpc distance (Hachisuka et al., 2006) of W3(OH)), only very limited mapping to find the emission peak was performed. From these data, it is not possible to determine the structure of the magnetic field or which material the field is associated with.

---

*This chapter contains portions of the previously published paper, **"Structure and Composition of Molecular Clouds with CN Zeeman Detections I: W3OH"**, in The Astrophysical Journal (Hakobian & Crutcher, 2011) as well as portions from a paper that is currently in preparation for publication.

Table 4.1. CN Hyperfine Components

Molecule	Transition	ν (MHz)	Z (Hz/μG)[a]	RI[b]
CN	N=1 – 0 J=$\frac{1}{2}-\frac{1}{2}$ F=$\frac{1}{2}-\frac{1}{2}$	113123.337	–[c]	1
CN	N=1 – 0 J=$\frac{1}{2}-\frac{1}{2}$ F=$\frac{1}{2}-\frac{3}{2}$	113144.192	2.18	8
CN	N=1 – 0 J=$\frac{1}{2}-\frac{1}{2}$ F=$\frac{3}{2}-\frac{1}{2}$	113170.528	-0.31	8
CN	N=1 – 0 J=$\frac{1}{2}-\frac{1}{2}$ F=$\frac{3}{2}-\frac{3}{2}$	113191.317	0.62	10
CN	N=1 – 0 J=$\frac{3}{2}-\frac{1}{2}$ F=$\frac{3}{2}-\frac{1}{2}$	113488.140	2.18	10
CN	N=1 – 0 J=$\frac{3}{2}-\frac{1}{2}$ F=$\frac{5}{2}-\frac{3}{2}$	113490.982	0.56	27
CN	N=1 – 0 J=$\frac{3}{2}-\frac{1}{2}$ F=$\frac{1}{2}-\frac{1}{2}$	113499.639	0.62	8
CN	N=1 – 0 J=$\frac{3}{2}-\frac{1}{2}$ F=$\frac{3}{2}-\frac{3}{2}$	113508.944	1.62	8
CN	N=1 – 0 J=$\frac{3}{2}-\frac{1}{2}$ F=$\frac{1}{2}-\frac{3}{2}$	113520.414	–[c]	1

[a] Z is the Zeeman Splitting Factor for each hyperfine component of CN.

[b] RI is the relative intensity of each component.

[c] The Z's for these hyperfine components were not calculated due to their low RI.

References. — Falgarone et al. (2008)

W3(OH) contains a high-mass O star and has been extensively studied over the years since the discovery of several OH maser sites within it (Raimond & Eliasson, 1969). A star forming region $6''$ east of W3(OH) was later discovered by Turner & Welch (1984) in HCN. This smaller region was also studied for maser activity and found to contain several H_2O masers (Wynn-Williams et al., 1972). While this second source was initially not observed in the continuum, with the development of more sensitive instruments, it was eventually detected in dust continuum studies (Wilner et al., 1995; Wyrowski et al., 1997). Within the last few years, further high resolution studies with instruments such as BIMA have led to the detection of multiple dense cores believed to be sites of active star formation within the Turner-Welch Object (Chen et al., 2006).

In order to determine the spatial distribution of the magnetic field, an understanding of the CN gas is needed. There is some question, however, as to the exact physical conditions that CN traces. Hily-Blant et al. (2008) used the IRAM 30-m telescope to conclude that CN in prestellar cores stays in the gas phase at densities close to 10^6 cm^{-3} and can serve as a kinematic tracer of high density gas. They compared their CN maps with N_2H^+, another high density tracer, and found the results to be in good agreement. Therefore, it is expected that the measured magnetic field strength derived from CN measurements would be in gas that is associated with high density regions of active star formation. However, before detailed conclusions can be drawn from these magnetic field measurements, a high angular resolution study of the CN gas distribution is required. An ideal instrument for this is an interferometer such as CARMA, as its high spatial resolution and ability to sample baselines as short as 6m allow us to sample material both spatially compact and widespread.

4.2 CARMA Observational Technique

With CARMA (Bock et al., 2006) it is possible to achieve a resolution of approximately 2.5″ by combining maps generated with the C, D, and E arrays. By using three different array configurations, we have the ability to probe small scale structure while retaining the ability to image large scale features that would otherwise be resolved out in the C and D arrays. At the time of the observations carried out for this PhD thesis, CARMA did not have polarization capability and therefore could not perform magnetic field measurements; however, by mapping these regions at high resolution we can gain crucial information as to the structure of the regions that are being sampled by the IRAM observations. To assist with this, we use the advanced features of CARMA's correlator to sample several spectral lines simultaneously, so we can compare the structure of the CN emission with emission of other well studied tracer molecules. We will also gain information on which regions are possible to map in the Zeeman effect at high resolution and for long integration times with an instrument capable of making dual-polarization measurements, when such an interferometer array becomes available.

The CARMA observations began in Spring 2007 and were completed in Fall of 2009. About 66 hours of observing time was used to map a 1 arcmin^2 region around W3(OH). This time was used to observe the following molecular tracers: CN, C^{18}O, N$_2$H$^+$, HCN, and HCO$^+$ (Table 4.2). Due to the design of the CARMA correlator and the relatively large frequency range within the 3-mm band that these tracers span, the measurements had to be performed in two separate tracks: one for CN and C^{18}O, and a second for N$_2$H$^+$, HCN, and HCO$^+$. Approximately 50 hours (Table 4.3) was spent for the CN band and 16.2 hours was spent for the N$_2$H$^+$ band (not counting additional time spent in B array, discussed below). In order for us to reach our signal to noise goal, the tracks containing N$_2$H$^+$ required much less observing time. Table 4.3 shows the observing array details. Our pointing center is located on the continuum source, an ultra-compact HII region, located at: 02:27:03.7 RA, +61:52:25 DEC (J2000). This is slightly offset from the IRAM pointing position.

We produced maps for 3-mm lines of CN, C^{18}O, N$_2$H$^+$, HCN, and HCO$^+$ at a resolution of approximately 2.5″. The composite CARMA primary beam at half power at this frequency is slightly more than 60″ in diameter, reflected in our maps, which are 64″ on a side. Since baselines as short as 6m are included, the

Table 4.2. Observed Transitions

Molecule	Transition	ν (MHz)
HCN	N=1 – 0 F=1 – 1	88630.415
HCN[a]	N=1 – 0 F=2 – 1	88631.847
HCN	N=1 – 0 F=0 – 1	88633.936
HCO^+	N=1 – 0	89188.526
N_2H^+	N=1 – 0 F_1=1 – 1 F=0 – 1	93171.621
N_2H^+	N=1 – 0 F_1=1 – 1 F=2 – 2	93171.917
N_2H^+	N=1 – 0 F_1=1 – 1 F=1 – 0	93172.053
N_2H^+[b]	N=1 – 0 F_1=2 – 1 F=2 – 1	93173.480
N_2H^+[a,c]	N=1 – 0 F_1=2 – 1 F=3 – 2	93173.777
N_2H^+	N=1 – 0 F_1=2 – 1 F=1 – 1	93173.967
N_2H^+	N=1 – 0 F_1=0 – 1 F=1 – 2	93176.265
$C^{18}O$	N=1 – 0	109782.176
CN	N=1 – 0 J=$\frac{3}{2}-\frac{1}{2}$ F=$\frac{3}{2}-\frac{1}{2}$	113488.140
CN[a]	N=1 – 0 J=$\frac{3}{2}-\frac{1}{2}$ F=$\frac{5}{2}-\frac{3}{2}$	113490.982

[a] Velocity scale in channel maps are calibrated with respect to this hyperfine component.

[b] Hakobian & Crutcher (2011) calibrated the N_2H^+ velocity scale with respect to this component; Daniel et al. (2006) shows the 122-011 and 123-012 transitions as having similar intensities in molecular clouds with densities $> 10^5$ cm^{-3}.

[c] Strongest hyperfine component as reported by Daniel et al. (2006)

Table 4.3. Observation Times

Source	CN, $C^{18}O$				HCN, HCO^+, N_2H^+				Total
	B	C	D	E	B	C	D	E	
W3(OH)	30.0h	28.0h	8.1h	11.0h	12.0h	7.4h	4.3h	4.5h	105.3h
DR21(OH)	–	10.4h	7.7h	6.5h	4.0h	4.2h	4.3h	3.7h	40.8h
OMC1	–	11.2h	7.4h	5.8h	–	5.9h	5.6h	4.6h	40.5h
S140	–	12.4h	9.4h	4.3h	–	5.3h	3.1h	4.4h	38.9h
S255	–	–	4.1h	14.9h	–	–	8.9h	4.0h	31.9h
G10.6	–	5.3h	5.2h	6.5h	–	5.5h	5.0h	4.7h	32.2h

maps are sensitive to structure smaller than about 90″, so that the spatial dynamic range is almost 40:1. At the distance of W3(OH) (2 kpc), this means the maps are about 0.62 pc across, and the resolution is about 0.024 pc or 5,000 AU. For all of the spectral line observations, we used the 8 MHz spectral line mode, which for CN (N_2H^+) provides a velocity coverage of ∼21 km s^{-1} (∼25.8 km s^{-1}) and a resolution of 0.335 km s^{-1} (0.415 km s^{-1}). The other transitions have similar coverages and resolutions which vary depending on their rest frequency. The large velocity coverage is necessary to simultaneously image several hyperfine components while still maintaining a high spectral resolution. Our data also contains two 500 MHz continuum bands in each track giving us four separate continuum windows between 88 GHz and 113 GHz. These continuum maps, while having a lower spatial resolution than some previously published maps of W3(OH) (Chen et al., 2006), have a significantly higher signal-to-noise ratio.

MIRIAD was used for data reduction, specifically with the modifications for use with CARMA. Due to the nature of CARMA, with 3 distinct primary beams, the data were reduced as a mosaic data set with a common pointing center. Passband calibration was performed on all tracks by utilizing the CARMA system noise source. Even though suitable passband calibrators were observed for every track, it was decided that better passband solutions could be obtained from the noise source. Flux calibration was performed on each individual track with a 15 minute observation of MWC349, Mars, or Uranus, whichever was best suitable at observation time as the intrinsic flux of these sources is very well modeled. Since our data were obtained over such a long period of time, the flux of our primary phase calibrator varied significantly. We determine the flux of the phase calibrator through a bootstrapping process by which our flux calibrator measurements are used to calibrate the flux scale for the point source phase calibrator. It is estimated that there is an inherent 20% error with this flux calibration technique. Phase calibration was performed primarily on 0359+509 with a secondary calibrator 0102+584, used if the primary was not visible for a significant portion of the track. The primary phase calibrator had an averaged bootstrapped flux of 6.16 Jy over 10 tracks obtained over a period of 20 months. The flux steadily increased from 3.9 Jy to 10.7 Jy over this time. In order to corroborate the flux measurements we compared our data with that obtained by the CARMA flux calibration commissioning task. This independent flux measurement of 0359+509 is 9.83 Jy (from Fall 2009), consistent with our measurement of 10.7 Jy from the same time period, assuming the 20% uncertainty mentioned above. Gain and phase calibration was performed with the *gfiddle* routine which fits an n-th order polynomial to the phase measurements on the phase calibrator. This method was chosen in contrast to the more widely used *selfcal* technique (on the calibrator) due to the weak signal strength of some of our spectral lines. However the benefits of this technique over the selfcal technique have not been shown; overall this technique may not have any net advantage. It may be possible to gain an increased signal to noise by performing self-calibration on W3OH itself, as the continuum source in the center of the map remains unresolved in all of the array configurations and is bright enough to perform phase calibration in the spectral channels. However, the absolute position of the phase center of the map is not retained and flux calibration is not guaranteed to succeed. These details are described in detail below in the description of our B-array data.

Since CARMA is composed of two types of telescopes of differing sizes, we have to handle the fact that we have multiple primary beam types associated with our data. CARMA has both 10-meter and 6-meter dishes which form 3 effective primary beams with the same phase center: one for the pairing of 10-meter to 10-meter dish, one for 6-meter to 6-meter, and a third of 10-meter to 6-meter. At the CN line frequency the 6-meter primary beam half power beam width (HPBW) is $\sim 111''$, the 10-meter HPBW is $\sim 66''$(at the N_2H^+ frequency of 93 GHz, these HPBWs are $135''$ and $81''$, respectively), while the 6m-10m primary beam size is in between that of the other two. We conservatively constrained our maps to ~ 1 arcmin^2 in order to easily compare the other maps with the CN data. The restoring beam size is calculated by fitting the dirty beam with a Gaussian beam. This is the effective resolution of a map, and is the value quoted in all of our figures.

Image conversion from the UV-dataset into the spatial domain was performed by the MIRIAD routine *invert*. System temperature weighting was used to properly downweight data taken at low elevation or in the unlikely event that data were improperly flagged. The CARMA control system has an intricate flagging mechanism that operates if one of many error conditions are met including: telescope tracking errors, pointing errors, receiver problems (dewar temperature, LO frequency, etc), system temperature, and other computer or correlator errors that could hinder data integrity. All data were additionally inspected for extreme system temperatures, unphysical antenna gains, time regions without converging phase solutions, and poor weather conditions that could influence the quality of the data. In a few cases (usually in older tracks before some automated flagging conditions were introduced) data that contained systematic errors were manually flagged. This additional flagging increased the signal-to-noise of these few tracks by a factor of 2-3. In the *invert* step, we weighted our UV data using a Briggs visibility weighting robustness parameter of 1 (Briggs et al., 1999), which provides a slightly increased signal-to-noise ratio over uniform weighting at the expense of a larger synthesized beam size. The relatively weak CN emission prompted the weighting of data in this manner. Since we are detecting low-level emission we did not want large sidelobes to obscure the detections. If we changed the weighting more towards Natural weighting, we could have reduced the noise level further; however, the beam size would be significantly larger and we would be affected by significant sidelobes. Cleaning was performed with the MIRIAD task *mossdi*, the mosaic version of the standard Steer clean routine. We used a multi-step cleaning technique in order to prevent under-cleaning the source. A small number of clean iterations was performed in order to remove large scale beam patterns while leaving much of the low intensity source features uncleaned. From this initial clean, we ran the MIRIAD task *restor* which used the clean data to produce a map without beam effects. We used the average off-line noise level in this map to limit how much flux was cleaned from a second iteration of *mossdi* and to prevent overcleaning. This second stage *mossdi* iteration was followed by another invert step to produce a final, deep cleaned map. In theory, this process can be repeated ad infinitum, however, if the noise level calculated in the first step is accurate, and the maximum number of cleaning iterations is large enough such that we are guaranteed to clean down to the noise level, this two step process is adequate.

4.2.1 Expansion to Additional Sources and Observational Technique Improvements

This project was expanded beyond W3(OH) to five additional cores with IRAM CN Zeeman detections. Observations were carried out at the CARMA Observatory (Bock et al., 2006) between May 2007 and December 2011. This dataset comprises 184.3 hours of data obtained on 5 objects (Table 4.4) over 43 tracks (Table 4.3). A detailed description of the observational techniques used can be found in Hakobian & Crutcher (2011). A total of 14 transitions (Table 4.2) of five molecules was observed in addition to four 500 MHz continuum bands. Simultaneously observing all five species would require 24 GHz of IF bandwidth, substantially greater than the 8 GHz available (an additional 8 GHz is available in the LSB) with CARMA. Instead, they were observed in two frequency blocks, one comprising CN and $C^{18}O$, near 113 GHz, and a second for HCN, HCO^+, and N_2H^+, near 90 GHz. Each set was observed in the C, D, and E array configurations to produce a map sensitive to structures as small as $1.5''$ and as large as $85''$. For most of these data, the correlator configuration remained unchanged from that previously reported; however, some of these data were taken with the 2nd generation CARMA correlator, which increases available IF bandwidth and spectral resolution. These tracks are noted in Table 4.3. All of the correlator configurations pair spectral line observations with two 500 MHz continuum bands which are used for calibration and generation of continuum maps (presented in Section 3). Lines observed with the 1st generation CARMA correlator were observed in the 8 MHz spectral line mode (63 channels) with spectral resolutions ranging from 0.32 km s^{-1} and 0.41 km s^{-1} (varies with line frequency). Lines observed with the 2nd generation correlator were observed in the 31 MHz mode (384 channels) with spectral resolutions ranging from 0.215 km s^{-1} to 0.274 km s^{-1}. Maps comprised of data from multiple spectral resolutions had spectral data smoothed to the coarser of the spectral resolutions during the image generation process.

These data have been calibrated and imaged using the MIRIAD software package (Sault et al., 1995)

Table 4.4. Source Coordinates

Source	α (J2000)	δ (J2000)	$V_{\rm LSR}$ (km s^{-1})	Distance
W3(OH)	$02^{h}27^{m}03.7^{s}$	$+61°52'26''$	-45.0	2.0 kps[a]
DR21(OH)	$20^{h}39^{m}00.7^{s}$	$+42°22'47''$	+ 2.0	1.7 kpc[b]
OMC1	$05^{h}35^{m}14.5^{s}$	$-05°22'30''$	+12.0	414 pc[c]
S140	$22^{h}19^{m}17.2^{s}$	$+63°18'35''$	− 7.0	910 pc[d]
S255	$06^{h}12^{m}53.7^{s}$	$+17°59'22''$	0.0	1.6 kpc[e]
G10.6	$18^{h}10^{m}28.7^{s}$	$-19°55'49''$	− 2.0	$\sim$ 6 kpc[f]

[a] Hachisuka et al. (2006)

[b] Schneider et al. (2010)

[c] Menten et al. (2007)

[d] Crampton & Fisher (1974)

[e] Rygl et al. (2010)

[f] Wilson (1974); Caswell et al. (1975)

and a modified technique from that used in Hakobian & Crutcher (2011), resulting in several improvements. Gain calibration is performed through the process of self-calibrating on the phase calibrator and applying the resulting phase and amplitude corrections to the target source. The phase calibrator was observed for 3 minutes per 15 minutes of source observation. This procedure removes the arbitrariness and possibility of human error that can occur when manually fitting polynomial curves to phase calibrator data. The imaged region was expanded to $2'$ to account for increased complexity of these regions and presence of substantial flux outside the $1'$ clean region used for W3(OH) (Hakobian & Crutcher, 2011). However, edges of these maps extend beyond the primary beam of CARMA's 10-m dishes ($\sim$84$''$ at 90 GHz, $\sim$67$''$ at 112 GHz), resulting in decreased sensitivity and increased noise towards the map edges. The UV-data are weighted using Briggs' robustness weighting (Briggs et al., 1999), with a robustness parameter of 1. This provides a middle-ground between uniform and natural weighting by down weighting sparsely sampled UV cells; some of the increased resolution of uniform weighting is gained at a small expense to the signal to noise ($\sim$ 1.8%) without the production of the stronger negative sidelobes found with uniform weighting. The noise cutoff value for map cleaning is calculated as 1.5 times the minimum theoretical sensitivity in the map instead of using an arbitrary corner of an off-line channel to calculate the RMS noise value. This is to allow for maps that have varying sensitivity over the imaged region, in particular due to images extending beyond the 10m primary beam.

For the three molecules with multiple hyperfine components, the velocity scale is calibrated to the rest frequency of the strongest hyperfine component. In the case of CN and HCN, this was an obvious choice; however, this selection is more complicated with species with heavily blended hyperfine components such as N_2H^+. In Hakobian & Crutcher (2011) the velocity scale was calibrated to the rest frequency of the N=1–0 F_1=2–1 F=2–1 hyperfine transition (93173.480 MHz) which in molecular clouds with densities $> 10^5$ cm^{-3} have visible intensities similar to that of the more appropriate N=1–0 F_1=2–1 F=3–2 transition (Daniel et al., 2006). For the data presented in this paper, the N_2H^+ rest frequency has been changed to that of the latter transition.

4.3 Data

4.3.1 W3(OH)

CN

Figure 4.1 shows integrated line maps of the five species, while Figure 4.2 shows channel maps. The continuum source was removed from the spectral line maps by averaging several off-line channels together and subtracting that from each individual channel. Towards the continuum source, we see three of the species strongly in absorption. Besides the Turner-Welch object and the continuum source, there are two other regions that are notable in CN. The western side of the map contains very diffuse CN emission, while the eastern side of the map shows a compact and complex CN emission source. In order to compare the CARMA CN data with the IRAM CN data (Falgarone et al., 2008), we also generated a map where the CARMA channel data were convolved with a 23″ Gaussian beam, effectively smoothing the CARMA data to match the IRAM resolution (see §5.1.2). By comparing these maps, there is evidence that both spectra are dominated by diffuse emission.

Compared to the other molecules, the CN emission appears to be diffuse but "clumpy." Under closer scrutiny, it is much more complex. Our 8 MHz spectral window is centered at 113.490982 GHz, the frequency of CN's strongest hyperfine component. This frequency and window size was chosen to allow us to simultaneously image a second hyperfine component of the CN N=1-0 transition at 113.488 GHz in the same spectral window. These two hyperfine components are separated by 7.9 km s^{-1}. Since this window covers approximately 21 km s^{-1} of velocity space, we expect to fully resolve and image both lines. Multiple velocity components in the image make it difficult to determine which hyperfine component some emission belongs to. However, we have been able to identify at least three distinct velocity components, representing separate regions around W3(OH) (Figure 4.3).

The north-west and south-west components appear to be very diffuse. They are centered at approximately -47.25 km s^{-1} and -44.5 km s^{-1}, respectively. It is difficult to completely isolate these two velocity components due to blending and overlap of the hyperfine lines. The maps in Figure 4.3 reflect some of this "blending." It occurs because the second hyperfine component of one velocity partially overlaps the primary hyperfine component of the other velocity. For example, the second and third maps in Figure 4.3 are cross-contaminated. This is easily visible when the positions of the emission in the two maps are compared; they have a significant spatial overlap region.

The north-eastern component is more complex. In addition to containing diffuse emission, multiple denser clumps are visible. The significance of some of these clumps are not clear from the integrated line map. Between the larger southernmost clump and the smaller, northern clump are a string of small, presumably unresolved clumps only seen in a single channel each. When viewing an averaged line map, many of these features are spatially smoothed and are not prominent (as in Figure 4.3). The densest portions of this region are concentrated in two lobes, not unlike the typical signature of an outflow. Figure 4.4 shows channel maps of the 15 channels around the strongest hyperfine component. There does not appear to be any blending as was seen in the south west component, so we are confident that this channel map is not contaminated. An averaged contour plot (Figure 4.5) shows the physical comparison between the two "lobes" of the emission. The top (red shifted) lobe is averaged from the six channels from -47.6 km s^{-1} to -49.2 km s^{-1}, while the bottom (blue shifted) lobe is averaged from the six channels from -49.2 km s^{-1} to -50.8 km s^{-1}. While this does have the signature of a typical outflow, it is not accompanied by any coincident emission from any of the other species, nor is there any accompanying IR emission source visible in publicly available IR catalogs. Due to the extent of the low level emission around the whole region, and lack of evidence of an outflow generating source, it is more likely that this is not an outflow, but rather bulk rotation of a clump of gas.

HCN, HCO^+, $C^{18}O$

The maps for HCN, HCO^+, $C^{18}O$ all appear to be tracing the same material, which does not coincide with either the CN or N_2H^+ emission (see Figures 4.6-4.8 for channel maps). However, the peak position of these spectral lines coincides with the HCN detection of the Turner-Welch object first reported in Turner & Welch (1984). At $2.5''$ resolution we do not appear to be resolving the object; previous high resolution (sub-arcsecond) studies have been conducted in order to resolve this object in the continuum (Chen et al., 2006), which resulted in the detection of multiple cores. Previous HCO^+ studies (Wink et al., 1994) had similar spatial resolution to our data, however, our data has significantly better signal-to-noise and samples material that was resolved out in the previous study. In the HCO^+ spectrum of the Turner-Welch object, a weak, secondary velocity component at -44 km s^{-1} is visible (Fig. 4.9). This velocity component is not reported in any previous studies. The HCN spectra towards the Turner-Welch object shows an unexpected peak at an apparent velocity of -39 km s^{-1} (Fig. 4.9); comparing relative positions of these two peaks, the anomalous HCN peak would be the F=0-1 transition of a secondary velocity component at -44 km s^{-1}. The other hyperfine lines from this velocity component are being masked by the hyperfine lines from the primary velocity component. This can only happen if the separation between the hyperfine lines is approximately the separation between the two velocity components. The $C^{18}O$ line may also show this secondary component, however, it cannot be confirmed due to the relatively low SNR of the $C^{18}O$ emission.

The $C^{18}O$ map does not show any absorption towards the continuum source, unlike HCN, HCO^+, and CN. This is consistent with observations done by Wink et al. (1994), in which they surmised that the line excitation temperature of HCO^+ is significantly lower than the kinetic temperature of 90 K; but the $C^{18}O$ excitation temperature is not low enough to produce absorption. However, our observed absorption in other lines is significant and can yield information about the regions around the continuum source. The HCO^+ spectra, seen in absorption (Figure 4.9), looks similar to an inverse P-Cygni profile which could indicate an expanding shell-like structure or a strong stellar wind. The multiple hyperfine components of HCN make it difficult to tell which gas is causing the absorption; however, it has the same central velocity and line width as the HCO^+ absorption indicating that both features are being generated from the same region. The CN absorption also appears to have similar spectral features as HCN; however the red-shifted CN emission feature is at a level of less than 1σ of the noise level, and cannot be considered as a positive detection.

Another notable feature of the continuum absorption lines is their shape. There is a double trough shape seen in HCO^+, the strongest hyperfine component of HCN, and in CN (these spectra are centered on the strongest hyperfine component). There is also some evidence of this feature in the other hyperfine components; however they are weaker and, as a result, noisier. According to the results of Wink et al. (1994), within the UCHII region of W3(OH) there is an embedded O7 star. It is very likely that W3(OH) is a region surrounding a bright massive star embedded in a dense cloud with a strong solar wind clearing out the region around the star. In looking at a velocity moment map in HCO^+ (HCO^+ was chosen due to its lack of hyperfine components and contamination), there appears to be an East-West velocity gradient on the order of 3 km s^{-1}. Since W3(OH) is unresolved in these maps, higher resolution data of W3(OH) are required to quantify and describe this effect (see below).

N_2H^+

Figure 4.10 shows N_2H^+ channel maps. If N_2H^+ were tracing the same dense material as CN, we would expect to see very similar emission (and absorption) spectra. Most notable is the lack of an absorption feature towards the continuum source, or alternatively, of any emission in N_2H^+ at the continuum position. Also, the rotation feature in CN noted above is not seen in N_2H^+. The N_2H^+ emission appears to be concentrated in the south western region of the map, roughly coincident with one of the velocity components of CN; however, this is where the similarity ends. In the N_2H^+ spectra (Figure 4.9), only 3 peaks appear when there are 7 hyperfine lines within our window. The central peak, at about -47.5 km s^{-1}, contains 3 hyperfine components which, having only 0.487 MHz (1.56 km s^{-1}) between them, are blended together. The peak centered at -42.5 km s^{-1} contains another three hyperfine components whose transition frequencies all lie within 0.432 MHz (1.39 km s^{-1}) and would also appear blended. The last hyperfine component is seen at -56 km s^{-1} and is the only one that is not blended. Our N_2H^+ map contains some similarities to the ammonia (NH_3) map presented by Wilson et al. (1993) and Tieftrunk et al. (1998). The major difference between the two is the lack of N_2H^+ emission around the Turner-Welch object. The major similarity comes from an east-west elongated clump present in the northeast corner of both the N_2H^+ emission and the NH_3 emission. This stands out since none of the other molecules show any sign of emission from this region. The closest emission is the north lobe of the possible CN outflow. It is unclear if these regions are related.

It is possible that the regions of CN emission much more closely matches the regions of N_2H^+ than is readily apparent, even though the spatial peaks do not coincide. Since CN is significantly weaker than N_2H^+, it is possible that emission, particularly in the lower west side of the map that is detectable in N_2H^+, is significantly below the noise threshold in CN. To emphasize this fact, which may not be noticeable in the individual channel maps, we constructed a channel map with 20% contours from all five detected species (Fig. 4.11). Most noticeable in the -48 km s^{-1} and -47 km s^{-1} panels, CN (with several other of the species) does seem to trace much of the N_2H^+ emission. In the -51 km s^{-1} and -50 km s^{-1} panels, it appears that the N_2H^+ emission borders on the regions with emission in the other species. If we assume that the two molecules do trace the same density gas, it is quite possible that some of these regions are undergoing a chemical reaction that selectively annihilates N_2H^+.

B-array Observations

From the observations described above, several significant features warranted even higher resolution observations. The continuum source is seen in absorption in some species; however, it remains unresolved. CARMA's B-array should be able to probe the region at significantly higher resolution than in our previous data. This will additionally allow us to study the velocity structure of gas near the continuum source. A velocity map of HCO^+ shows an East-West velocity gradient of ~ 3 km s^{-1}. HCO^+ was chosen specifically since it does not have multiple hyperfine components which, due to blending, could pollute the velocity map, and shows absorption towards the continuum source. In addition, with these data we can see if we can resolve the individual cores of the Turner-Welch object. Previous high resolution continuum maps have shown evidence of multiple cores within the Turner-Welch object which we would expect to also see in corresponding high resolution spectral line maps. We previously choose to map the region with the C, D, and E arrays to study large scale features; with B-array alone we are able to map features that require higher spatial resolution. If we combined the B-array data with the rest, we will produce a map with a synthesized beam that is larger than the beam of the B-array data alone, and larger than some of the smallest features, obscuring them. In addition, the necessity to self-calibrate the data and issues with gain calibration (discussed in detail below) make a separate analysis more informative.

Self calibration results in several issues that need to be overcome. W3(OH)'s physical size is 0.01 pc in diameter (Kawamura & Masson, 1998) which corresponds to an angular size of $\sim 1''$. This means that many of the longer baselines in B-array will be resolving the W3(OH) continuum source. Data from these baselines will make it difficult to self calibrate the data as it assumes a point source model for the source (or requires an accurate model of the source features which we do not have). Running self-cal on the full dataset (including resolved baselines) generates a solution that is appropriate for the data up until a UV-radius of 130kλ, at which the solution fails. This UV-radius corresponds to a physical size of:

$$\begin{aligned} \Theta &\sim \frac{\lambda}{D} \\ &\sim \frac{\lambda}{2 * \mathrm{UVr}} \\ &\sim 0.79'' \end{aligned}$$

Therefore running self-cal on the full dataset assuming a point source will result in large errors in the selfcal solution due to long, resolved baselines. If we "cut" the dataset so we only use the data with UV-radius < 130kλ for use in calculating the phase solution, we will not have this issue.

The selfcal technique fits the phase center of the data to the brightest point source in the map. Our C, D, and E array data is slightly offset in position from the pointing center, so this will result in a slight position offset between the two maps. The can be corrected for by manually fitting and entering the center position of the continuum source from our C, D, E maps, however this is not necessary since we will not be directly combining our B-array data with the rest, since the resulting maps at full angular resolution would have a very low signal-to-noise ratio.

This self-calibration technique also poses several problems with regards to flux and amplitude calibration. Several dishes primarily have long baselines, with only a few baselines that fall under our UV-radius limit of 130kλ. While this worked well for phase calibration, the results of amplitude selfcal was very poor. Many of the amplitude gains, which should be flat and close to unity, were noisy and had many datapoints corresponding to unphysical gains that directly translates to poor image quality. The few remaining baselines also tend to have low signal to noise which further increases the problem.

In the attempt to apply correct gain calibration, several other techniques were tested to amplitude calibrate the data. We attempted to amplitude calibrate our data using the dedicated phase calibrator measurements and transferring the resulting solution to our source. This also failed, and while it produced better results than the amplitude selfcal technique described above, the high resolution, low intensity features were washed out in the final maps. This is most likely due to the gain calibrator being 10^o from our source, far enough that the telescopes are viewing different enough atmosphere to negatively affect the calculated gains. This problem does not affect our C, D, E array data because the maximum baseline length is significantly smaller in these arrays and are not as sensitive to atmospheric fluctuations as the longer B-array baselines. Since these several technique turned out poor results, it was decided not to use amplitude (flux) calibration on the B-array data, which is not an uncommon result when using selfcal. This is another reason why we do not combine this data with our C, D, E data as we would need an accurate gain solution to provide proper weights to combine the datasets.

Continuum

Figure 4.12 represents the combined C, D, E array and B-array only continuum maps. Each map was produced using multi-frequency synthesis (MFS) on two 500 MHz windows, one in the N_2H^+ band (average frequency of 91.2 GHz, not shown), and one in the CN band (average frequency of 112 GHz, shown). In Figure 4.12a, neither the Turner-Welch object nor W3OH are resolved. The peak flux of W3OH decreases by a factor of 2 from 91.2 GHz to 112 GHz, while the center of the Turner-Welch object increases in flux by a factor of two over the same range. In the B-array only data (Figure 4.12b), we resolve two individual clumps within the Turner-Welch object and slightly resolve structure within W3OH (note the off-center position of the highest level contour in Fig. 4.12b). This structure supports the findings of Chen et al. (2006). We additionally see the same change in relative fluxes in the B-array maps as we saw in the C, D, E array maps, over the same frequency range.

4.3.2 DR21(OH)

DR21(OH) is a dense cloud region along a ridge of gas between W75N (Zuckerman et al., 1969; Shepherd et al., 2004) and DR21 (Downes & Rinehart, 1966). Well known for its strong H_2O (Genzel & Downes, 1977), OH (Norris et al., 1982), and methanol masers (Batrla & Menten, 1988), DR21(OH) is one of the densest and massive clouds in the Cygnus X region (Dickel et al., 1978). Figure 4.13 shows integrated line maps for each of the observed species in DR21(OH). Contours were chosen to show the spatial extent of all emission as well as the dynamic range in intensity between a weak transition, such as CN, and a strong transition, such as N_2H^+. In addition, a single negative contour is plotted to show that CARMA is resolving out a non-negligible fraction of large scale emission. While negative emission is present in the weaker species (CN, $C^{18}O$), they occur at a significantly smaller intensity and are not plotted.

Figure 4.14 shows a 500 MHz continuum band centered at 112 MHz. A second continuum band, at 90 GHz, was additionally observed, but it is not shown here. The two cores of DR21(OH) appear to be resolved in this map at a resolution of $3.4'' \times 2.8''$ while they remain unresolved in the second continuum map at 92 GHz ($6.1'' \times 3.9''$). The peak intensity of the continuum emission remains approximately constant between the two bands. Much of the molecular emission appears to be constrained to the regions traced by the continuum emission.

Inspection of the molecular data reveals the presence of two velocity components which each trace separate spatial features. These velocity components have a linewidth of 2.3 km s^{-1} and center velocities of -4.6 km s^{-1} and -0.93 km s^{-1} (Crutcher et al., 1999b). Figure 4.15 shows CARMA maps of these two velocity components. The -4.6 km s^{-1} component is centered around the continuum source MM1 and extends westward, and southward with low level emission associated with DR21(OH)-S, and is present in clumps in the northwest (-N1 and -N2). The -0.93 km s^{-1} component (Fig. 4.16) is strongest towards DR21(OH)-W with additional emission towards MM2. The line parameters are derived from single-dish IRAM-30m data (Crutcher et al., 1999b) with a $23''$ beam. While their beam covers a significant fraction of the two bright continuum objects, it has negligible response towards DR21(OH)-W and DR21(OH)-S. The authors hypothesized that the two velocity components are each associated with a single continuum peak; however, as those data had an angular resolution of $23''$ they did not have the necessary spatial resolution to prove this assertion. The current observations lend support to this hypothesis.

The $C^{18}O$ observations are another example of a weak spectral line (Fig. 4.16). The linewidth is ~ 5 km s^{-1}, significantly larger than the observed CN linewidth of 2.3 km s^{-1}. There are several visible velocity components: -4.7 km s^{-1}, associated with MM1 and the eastern CN peak, -2.0 km s^{-1}, coincident with MM2, and -1 km s^{-1}, which peaks just southeast of MM2. The two latter components appear to be contained within the MM2 clump. The most significant velocity component is centered at $\sim$ -3 km s^{-1}. The $C^{18}O$ emission at -3 km s^{-1} is not seen in other species at that velocity, probably due to this gas being too low in density to excite the transitions in the other species. This emission is constrained to the strongest continuum source, not unexpected for a low density, optically thin tracer molecule. The "ridge" structure in the western region hinted in the continuum observations is visible as is -W; however -S is not. It is possible that emission towards -S is below the detection threshold of the CARMA observations. In the continuum this region has $\sim \frac{2}{3}$ the peak flux of -W (which itself is only weakly detected in $C^{18}O$), making this very likely.

HCN is a difficult high density tracer to analyze due to the presence of three hyperfine lines within our observing window in addition to multiple velocity components. The $\sim$ 4 km s^{-1} separation between the velocity components is similar to the 4.8 km s^{-1} equivalent separation between two of the hyperfine transitions, causing blending between the two (Fig. 4.16). There are two identifiable velocity components, one at -5.8 km s^{-1} and another at -1 km s^{-1}. In addition there is excess emission at -1 km s^{-1} and at +3.8 km s^{-1} that is derived from the 2nd hyperfine line. Therefore, the emission visible at -1 km s^{-1} is blended from the following sources: in the central region from both velocity components, in -S as a 2nd hyperfine component of the -5 km s^{-1} line, and in -W as the -1 km s^{-1} velocity component (visible un-blended in its 2nd hyperfine component at 3.8 km s^{-1}). The third velocity component is offset from the strongest transition by -7.1 km s^{-1}, and for this source we would expect emission at -12.9 km s^{-1} and -8.1 km s^{-1}, outside the narrow band used for these observations. Due to the large velocity offset between the two velocity components, this third hyperfine line was unable to be observed for this source.

HCO^+ is an optically thick tracer molecule which has been observed to be partially self absorbed in previous single-dish measurements (Schneider et al., 2010), which shows the complications in analysis of distorted spectral line features. Since the CARMA data has a significantly increased resolution over the single-dish measurements, the velocity structure of this source is most clearly seen in HCO^+. Towards the map center there are two velocity components (-5.4 km s^{-1} and -0.4 km s^{-1}), consistent with observations of the other high excitation molecular lines in this study. This emission was interpreted by (Schneider et al., 2010) to be a single emission line with a strong self-absorption feature, however these data do not support that conclusion. Their spectra most likely appeared to be self-absorbed due to spatial averaging from a large beam (28″) and the presence of a 1.2 km s^{-1} velocity gradient across the source. While there is a hint of absorption in the E-array maps (10″ beam), the shortest baselines sample large enough size scales to include the -MM2 continuum source (Hakobian & Crutcher, 2012). Additionally, their assumption of self-absorption is derived from comparisons with ^{12}CO 2–1 observations which has a significantly lower critical density than HCO^+ ($\sim 10^3$ cm^{-3} vs $\sim 10^5 - 10^6$ cm^{-3} respectively) and therefore traces different regions within the molecular cloud. Additionally there is a very compact source at +0.78 km s^{-1} to the west of DR21(OH) which is anomalously bright (10.5 Jy beam^{-1}, twice the brightness of any other feature in the map). This source has been identified as an HCO^+ maser (Hakobian & Crutcher, 2012).

N_2H^+ appears to trace both the structure of the cores and the filaments; however, a complicated hyperfine structure makes it difficult to analyze. There are seven hyperfine lines; however two sets of three are located so close in frequency they appear blended together in the spectra. Two of the N_2H^+ peaks appear at -5 km s^{-1} and -1 km s^{-1}, as in the other high density tracer molecules, and are associated with the two millimeter continuum cores (MM1 and MM2). The third peak, at -3 km s^{-1}, appears to trace the DR21 filament which extends almost a full degree in declination from DR21 (in the south) to W75N (in the north), and includes DR21(OH).

Figures 4.17–4.21 show individual channel maps for all five species rebinned in 1 km s^{-1} incrememts.

4.3.3 OMC1

Figure 4.22 shows continuum maps of the Orion Molecular Cloud (OMC1). The combined C, D, and E-array maps trace much of the large scale structure present in this complex source. The primary sources visible are the Orion-KL nebula (Kleinmann & Low, 1967), and the large scale source CS1 (Friedel & Widicus Weaver, 2011). In addition to the combined map, Fig. 4.22 also includes a C-array only continuum map to show the compact sources that remain unresolved in the combined map. This map resolves the sources Orion-BN (Becklin & Neugebauer, 1967), the millimeter sources MM5 and MM6 (Eisner & Carpenter, 2006), and two infrared nebulae, IRc5 and IRc6 (Rieke et al., 1973).

Analysis of the spectral emission is more straightforward for this source since it has only a single velocity component; however, there are other elements which make this source specifically unique. The CN emission is primarily centered near the CS1 continuum source and a source in the south that does not have a corresponding continuum source. The limited bandwidth of the first-generation CARMA correlator prevented full coverage of both strong hyperfine components of CN towards CS1 (Fig. 4.24). Towards Orion-KL, there is no appreciable emission. The two dashed circles in Fig. 4.23 represent the position and size of the beams in the Crutcher et al. (1999b) CN Zeeman measurements. The position in the south appears to be offset from any other site of molecular emission in the map. The $C^{18}O$ emission appears to trace the same material as the continuum with very little deviation. The N_2H^+ emission is extremely weak in this source with the exception of towards CS1, and some continuum contamination towards Orion-KL (also visible in the spectral lines in Fig. 4.24). This significantly contrasts with the other sources observed which tend to be rich in N_2H^+ and is significantly correlated with CN emission which is what is expected for high density tracers (Hily-Blant et al., 2008).

The HCN emission in OMC1 is significantly more complex. Towards Orion-KL HCN appears not only unusually bright at $\sim$ 20 Jy beam^{-1}, but the spectra are almost completely flat. These spectra are the result of bright emission with extremely broad spectral lines (~ 20 km s^{-1}) which causes significant blending of the three hyperfine components. This emission has been seen in previous studies of OMC1 (Vogel et al., 1985; Schilke et al., 1992), in which larger bandwidths were used to observe and measure the wide linewidths. These wide spectral lines are observed not only towards the hot core but over the whole region, even towards CS1, but at a lower intensity.

All of the spectral lines towards Orion-KL show some amount of continuum contamination at a level of about ~ 0.75 Jy beam^{-1}, with the exception of C^{18}O at which it is seen at ~ 2 Jy beam^{-1}. It is unlikely to be weak emission with a large linewidth, such as HCN, since a 20 km s^{-1} wide line would easily fit within the 8 MHz bandwidth of these spectral windows. In three of the spectral lines (CN, HCO^{+}, and N$_2$H^{+}), a faint absorption line is visible at ~ 7.5 km s^{-1}. Further evidence of this is that the absorption is also faintly visible in the second hyperfine component of CN in our window at ~ 15 km s^{-1}. It is possible that this absorption also affects HCN, as it has a dip at the same velocity, but the large linewidths make it difficult to determine if it is actually present. There have been several multiline spectral studies of this region in the past, such as the multiline BIMA survey presented in Wright et al. (1996).

Figures 4.25–4.29 show individual channel maps for all five species rebinned in 1 km s^{-1} incrememts.

4.3.4 S140

Figure 4.30 shows a 112 GHz continuum map of Sharpless 140 (S140). Emission from six individual continuum sources can be seen: three IR sources, and three submillimeter sources. The three IR sources, IRS1-3, were first presented in Beichman et al. (1979) who described this region as being precursors to Trapesium-like OB stars. Falgarone & Gilmore (1981) identified the three IR sources as being a cluster of forming B stars embedded within the structure identified in 21-cm continuum maps. While IRS1 is seen as a very strong continuum source in our 3-mm maps, the other two IR sources are visible as weak continuum objects. Minchin et al. (1995) reported on three submillimeter sources SMM1-3, which only had significant emission at 450 μm. The positions of SMM1 and SMM2 appear to be offset in the CARMA data from the measured coordinates in the Minchin et al. (1995) study, most likely due to their significantly coarser spatial resolution. With large scale emission resolved out in the CARMA maps, the positions of the smaller scale structures are visible and are slightly offset in position. Other previous work in the infrared at 10-20 μm (Hackwell et al., 1982) does not detect these sources. Two additional 1cm continuum sources, VLA4 and NW, were presented in Evans et al. (1989); however these sources are undetected in the CARMA dataset. It is possible, but unlikely, that these sources are weak enough to be below the detection threshold of the CARMA maps.

Figures 4.31 and 4.32 show integrated spectral line maps and spectra towards continuum objects, respectively. The integrated spectral line maps appear to trace three separate features in the 2 arcmin^2 field. HCN and HCO$^+$ trace a cloud which encompasses all six continuum features and peaks near the SMM1 continuum source. HCO$^+$ and HCN (to a smaller degree) additionally have significant negative contours; the maps are not continuum subtracted due to the low peak continuum intensity of 0.07 Jy beam^{-1}. This negative emission is indicative of resolved out large scale emission by CARMA. The CN and N$_2$H$^+$ emission appears to trace a "shell" like structure around the central cloud; again, both molecular tracers appear strongest towards the SMM1 source. Of significant note is the lack of emission towards the strongest continuum source, IRS1, which is believed to contain multiple sites of high mass star formation and a molecular outflow. These two lines also appear to be partially resolved out. The C^{18}O emission differs significantly from the others. The only continuum source that C^{18}O traces is SMM3, and its surrounding regions. The low intensity of this line makes it difficult to determine the true extent of the emission; signal may be buried within the noise.

The spectral emission (Figure 4.32) presents additional information about these continuum sources. Of note is the general lack of emission towards IRS1, with the exception of HCO$^+$. HCO$^+$ has significant high velocity wings, which can be an indication of the presence of an outflow. This is consistent with previous studies of this source. There is only one significant velocity component at -8 km s^{-1}, visible in all spectral lines, even in the negative emission (most noticeable in CN and N$_2$H$^+$. However, HCO$^+$ emission towards SMM2 and IRS2 appears to be slightly shifted, possibly due to self-absorption or being partially resolved out. If the negative emission was due to continuum subtraction, these spectra would be very similar to a P-Cygni profile. Their similarities are most likely due to their relative spatial co-location. The 2nd hyperfine component of CN is visible at the edge of the band, but the limited bandwidth of that spectral line band prevented complete imaging. Towards SMM3, a double peaked feature is visible in HCN and HCO$^+$; the redshifted peak is closest to the -8 km s^{-1} velocity component of the other spectral features. This additionally may be present in C^{18}O, however low signal-to-noise makes this difficult to determine with any certainty.

Figures 4.33–4.37 show individual channel maps for all five species rebinned in 1 km s^{-1} increments.

4.3.5 S255

Figure 4.38 shows the 112 GHz continuum of the S255 region. This object contains multiple IR and millimeter sources within two compact HII regions S255-1 and S255-2 (Snell & Bally, 1986). S255-2 was further associated with IR sources (IRS1-2) (Beichman et al., 1979), one of which has had a high velocity outflow detected towards it (Morgan et al., 1985). These IR sources have been resolved into several high mass YSOs in the near IR with Hubble (Simpson et al., 2009). A detailed description of all the detected sources is presented in Wang et al. (2011), who collected them into two descriptive regions: S255IR (S255-2) that contains the IR objects and the outflows and S255N (S255-1) that mainly emits in the millimeter. They further showed that S255IR contains a highly collimated bipolar outflow, and that both S255N and S255IR show evidence of rotation. The CARMA maps (Fig. 4.38 and 4.39) were initially centered on S255IR, but the edge of the map fell near the center of S255N. The maps were subsequently increased in size by $\sim 30''$ to the north, extending them significantly beyond the primary beam of CARMA's 10-m antennas. As a result, the noise level of the emission in the north is significantly greater (4.5x) than that at the original map center, visible in the spectral line plots (Figure 4.40).

The molecular emission towards S255 is significantly less complicated than in the other sources. With the exception of N_2H^+, which is depleted towards S255IR, the molecular emission appears to trace the same gas in all of the species (Figure 4.39). In the spectral lines towards these sources (Figure 4.40), there is a primary velocity component at ~ 9.5 km s^{-1}, and in a subset of species, a weaker secondary component at 6-7 km s^{-1}. The apparent wide linewidths in HCN are a result of spectral line confusion between the two velocity components and the hyperfine transitions. HCO$^+$ shows evidence of an outflow towards S255IR with both red and blueshifted high velocity wings that span a range of ~ 30 km s^{-1}. This is consistent with previous outflow studies in CO (Bally & Lada, 1983), which observed 30 km s^{-1} wide ^{12}CO lines, and in OH (Ruiz et al., 1992). Heyer et al. (1989) confirmed the presence of a CO outflow and performed a large size scale ($> 1'$ resolution) study of HCN showing its high relative intensity and that it spans an area of several square arcminutes.

The CARMA S255 observations are unique since it is the only source where we have obtained a complete dataset of ^{12}CO, ^{13}CO, and CS observations. This is due to these data being obtained after Fall 2009, when the 2nd generation CARMA correlator was installed that allows for observations of 8 simultaneous bands, an improvement over the 3 bands previously available. The ^{13}CO and CS emission is consistent with the HCO$^+$ emission, with two velocity components, while the ^{12}CO is more complex. The peak is at 10.5 km s^{-1} and has significant structure and evidence of some absorption at 4 km s^{-1}. The extended blue and red wings cover a span of > 30 km s^{-1} which is consistent with HCO$^+$ and previous observations. Towards S255N, ^{12}CO is seen partially in absorption with a peak velocity offset of ~ 3 km s^{-1}.

Figures 4.41–4.45 show individual channel maps for all five species rebinned in 1 km s^{-1} increments.

4.3.6 G10.6

Figure 4.46 shows continuum maps of G10.6, an ultra compact HII region (UCHII). Two continuum sources are visible, identified as G10.6-0.4 and G10.6-0.4 H. Ho & Haschick (1981) identified a set of sources decomposed from continuum maps at 6cm and 2cm into 8 individual objects (A-H), the two strongest being A and H. Sources A-G are in a close configuration, with H offset several arcseconds to the east (corresponding to the 2nd compact region in the CARMA dataset). The elongation of the continuum is consistent with the positions of the 8 sources. They additionally hypothesized that these were associated with O and B stars. OH masers were detected in the core and regions associated with small knots in the continuum emission (Ho et al., 1983; Garay et al., 1985). Furthermore, Ho & Haschick (1986) identified the structure and mechanism of spinup and infall of material in G10.6. Ho et al. (1994) continued this work with 3mm continuum and $C^{18}O$ maps of the region and determined that a flattened structure has developed caused by the spin up of gas due to contraction. As a result, a high velocity gradient was detected.

CARMA G10.6 molecular data are continuum subtracted due to the intensity of the central continuum source ($\sim$ 3.6 Jy beam^{-1}) (Figures 4.47, 4.48). All of the molecular line maps are similar, with the exception of N_2H^+, which contains emission that extends to the north. Of all the sources in the CARMA dataset, G10.6 is located the farthest away at a distance of 6 kpc (Wilson, 1974; Caswell et al., 1975). As a result, the CARMA maps cover a field-of-view 2-3 times greater than the other maps, and image the region at a larger physical scale. It is expected that the images trace different physical structures since the interior remains unresolved.

The negative emission that is observed in the spectra (Figure 4.48) is a direct result of continuum subtraction, not resolving out large scale emission as in S140. One of the HCN hyperfine lines appears in absorption and distorted towards G10.6, possibly a result of blending of the other hyperfine components due to their large linewidths. In addition, some slight CN absorption is present towards the continuum source. The peak velocity of these spectral lines is -4 km s^{-1} in all species except for HCN, which peaks at -3 km s^{-1}; however, a second velocity component is visible in HCO^+ at +3.5 km s^{-1}. The $C^{18}O$ line appears unusually wide at $\sim$ 7 km s^{-1}, which could indicate a second velocity component that is blended with the first. The secondary continuum source, G10.6-0.4 H, has similar spectra to that of the first object but at a lower intensity, with the exception of the N_2H+ emission that appears enhanced towards this object.

Figures 4.49–4.53 show individual channel maps for all five species rebinned in 1 km s^{-1} increments.

4.4 Figures

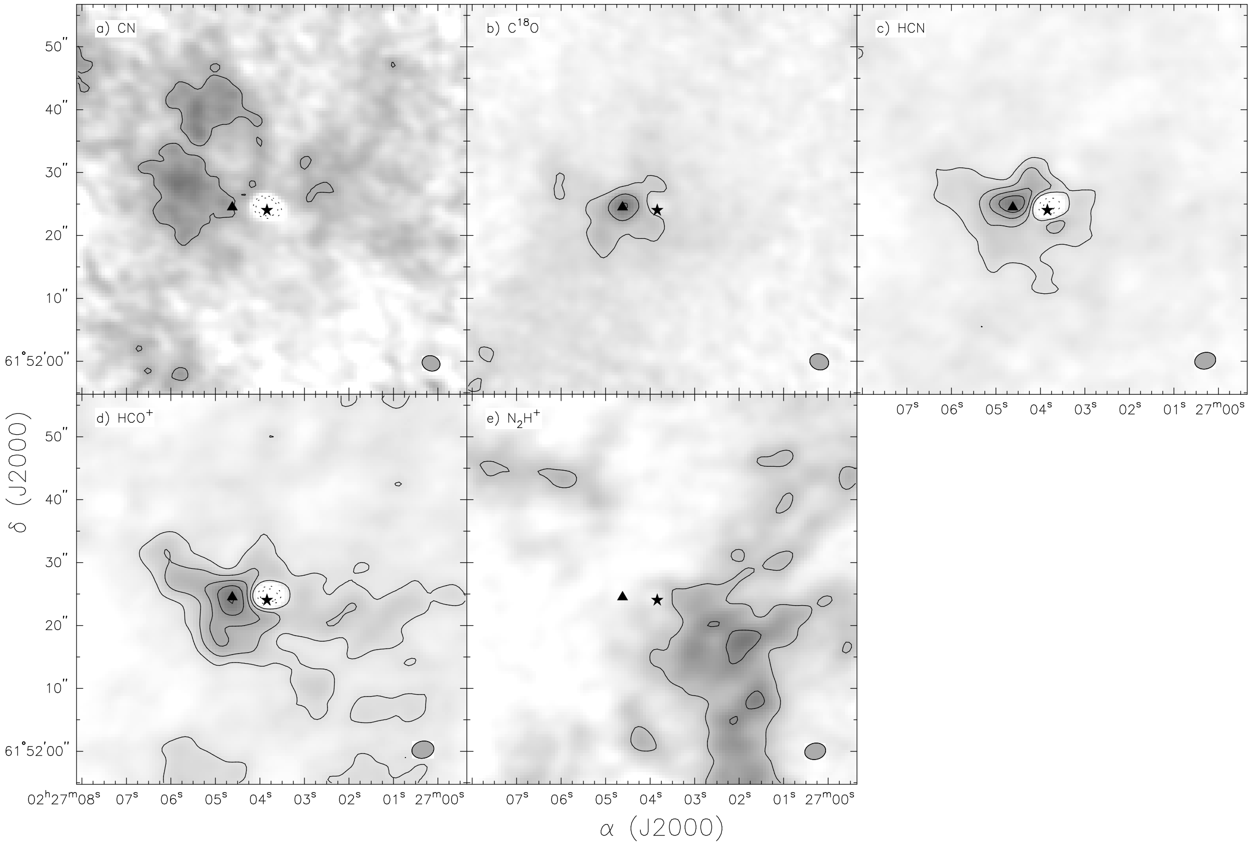

Figure 4.1 CARMA integrated line maps. *(a)* CN, 2.9″ x 2.4″, offline RMS = 0.03 Jy beam^{-1}, Peak intensity = 0.29 Jy beam^{-1}, Peak SNR = 9.6. *(b)* C^{18}O, 3.1″ x 2.5″, offline RMS = 0.015 Jy beam^{-1}, Peak intensity = 0.52 Jy beam^{-1}, Peak SNR = 34.6. *(c)* HCN, 3.4″ x 2.6″, offline RMS = 0.021 Jy beam^{-1}, Peak intensity = 0.84 Jy beam^{-1}, Peak SNR = 40. *(d)* HCO$^+$, 3.5″ x 2.7″, offline RMS = 0.037 Jy beam^{-1}, Peak intensity = 0.86 Jy beam^{-1}, Peak SNR = 23.2. *(e)* N$_2$H$^+$, 3.4″ x 2.6″, offline RMS = 0.023 Jy beam^{-1}, Peak intensity = 0.41 Jy beam^{-1}, Peak SNR = 17.8. The contour levels are 3, 6.5, 10, 13.5, 17 times 0.05 Jy beam^{-1}. The ★ and ▲ represent the peak continuum positions of W3(OH) and the Turner-Welch object, respectively.

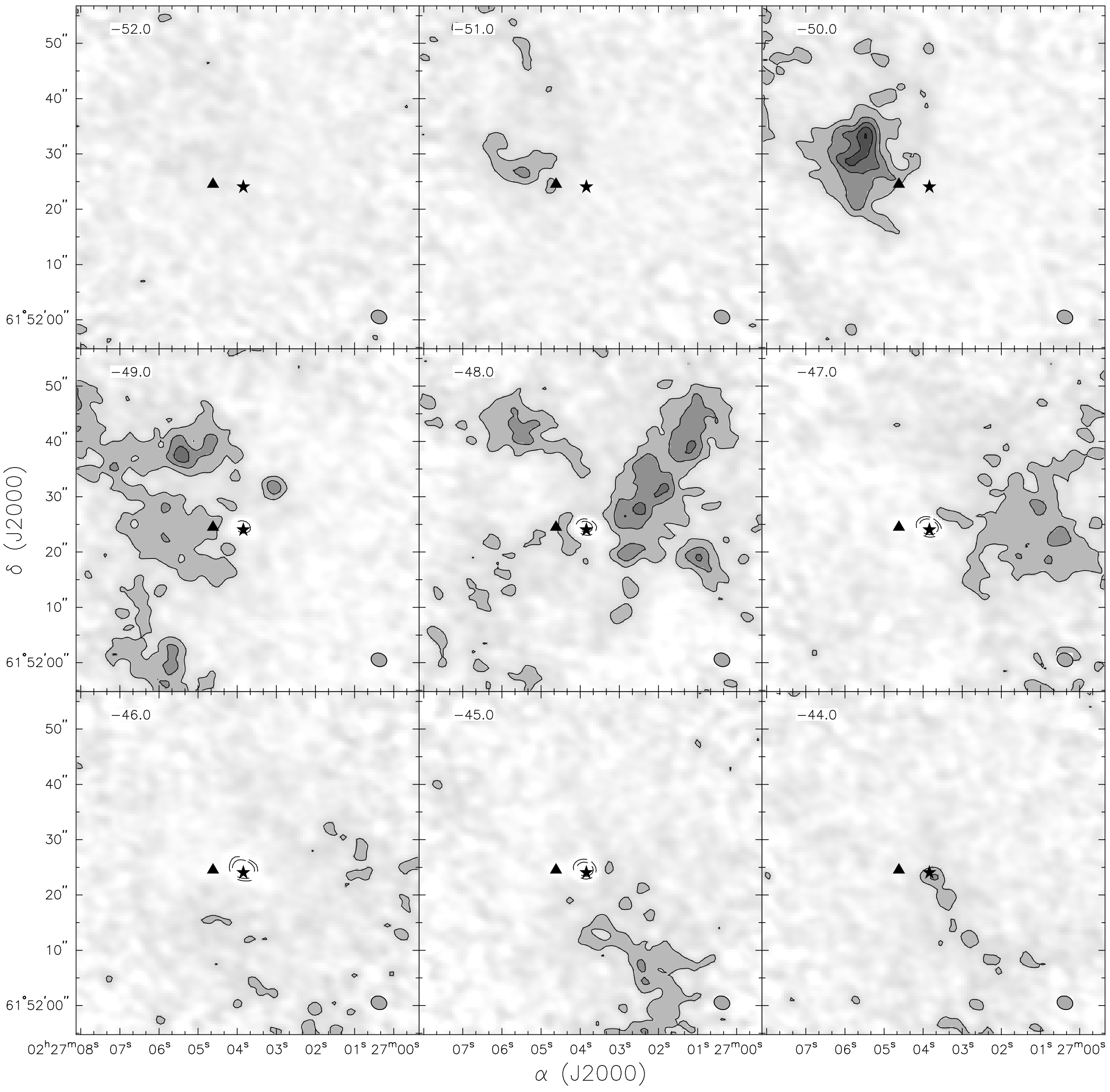

Figure 4.2 W3(OH) – CN Channel Maps, rebinned to 1 km s^{-1} velocity increments. The velocity scale is centered on the strongest CN hyperfine component at 113.490 GHz. The spacial resolution of this map is 2.9 x 2.4 arcsec. The contour levels are -80, -40, 20, 40, 60, 80, 100 times 0.00989 Jy beam^{-1}. The ★ and ▲ represent the peak continuum positions of W3(OH) and the Turner-Welch object, respectively.

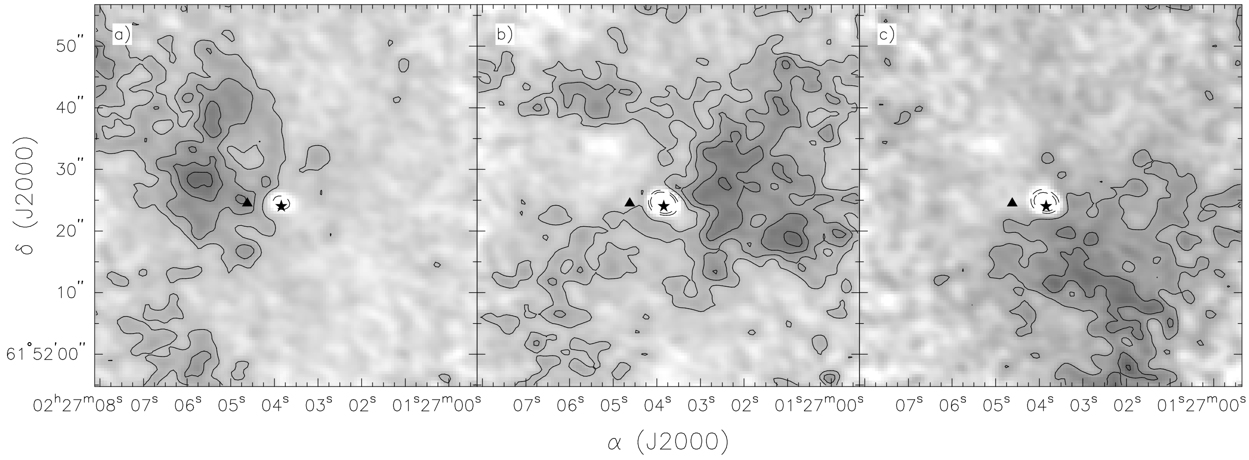

Figure 4.3 Integrated line maps of CN velocity components in W3(OH). These are the three distinct velocity components present in the CN window. Each map is averaged over the two hyperfine components present. The figure *(a)* is averaged from -52.7 to -48.5 km s^{-1}, figure *(b)* from -48.2 to -46.3 km s^{-1}, and figure *(c)* from -46.3 to -43.1 km s^{-1}. Notable features include the dense clumps in the north-east corner of *(a)*, and the continuum source which can be seen in absorption. The contours are 2, 4, 6, and 8 times the noise level of about 0.03 Jy $beam^{-1}$. The ★ and ▲ represent the peak continuum positions of W3(OH) and the Turner-Welch object, respectively.

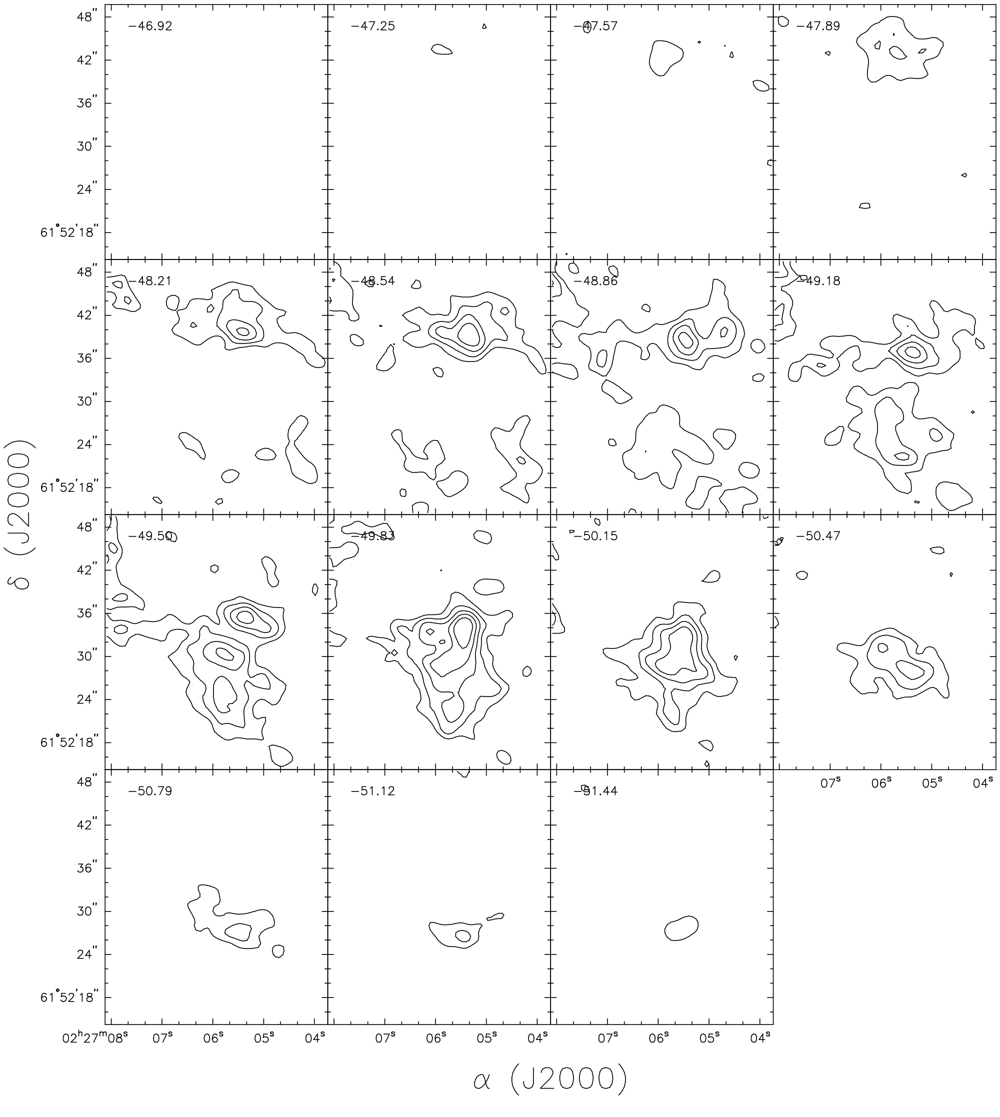

Figure 4.4 Channel maps of the CN clump in the north-eastern corner of the CN map. Displayed are 15 channels from -46.92 km s^{-1} to -51.44 km s^{-1}. There are two visible “lobes”, the northern one which peaks at -48.64 km s^{-1}, and the southern one which peaks at -49.83 km s^{-1}. The contour levels are 5, 8, 11, 14, 17 times 0.05 Jy beam^{-1}.

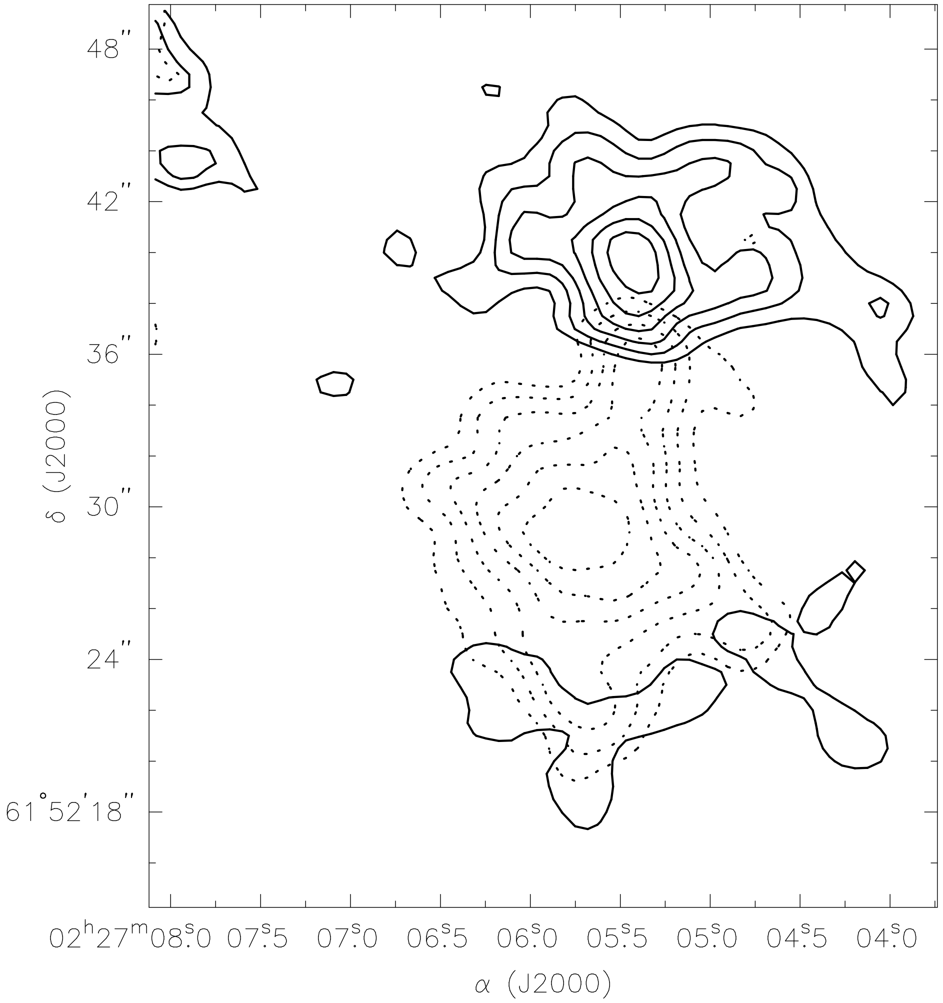

Figure 4.5 Averaged map of the two "lobes" of the outflow-like feature. The emission represented by solid contours is averaged from 6 channels between -47.6 km s^{-1} and -49.2 km s^{-1}. The emission represented by dotted contours is averaged from 6 channels between -49.2 km s^{-1} and -50.8 km s^{-1}. While this does look similar to an outflow, it could also be bulk rotation of a clump of gas. The contour levels of both objects are 4, 5, 6, 7, 8, 9 times 0.06 Jy $beam^{-1}$.

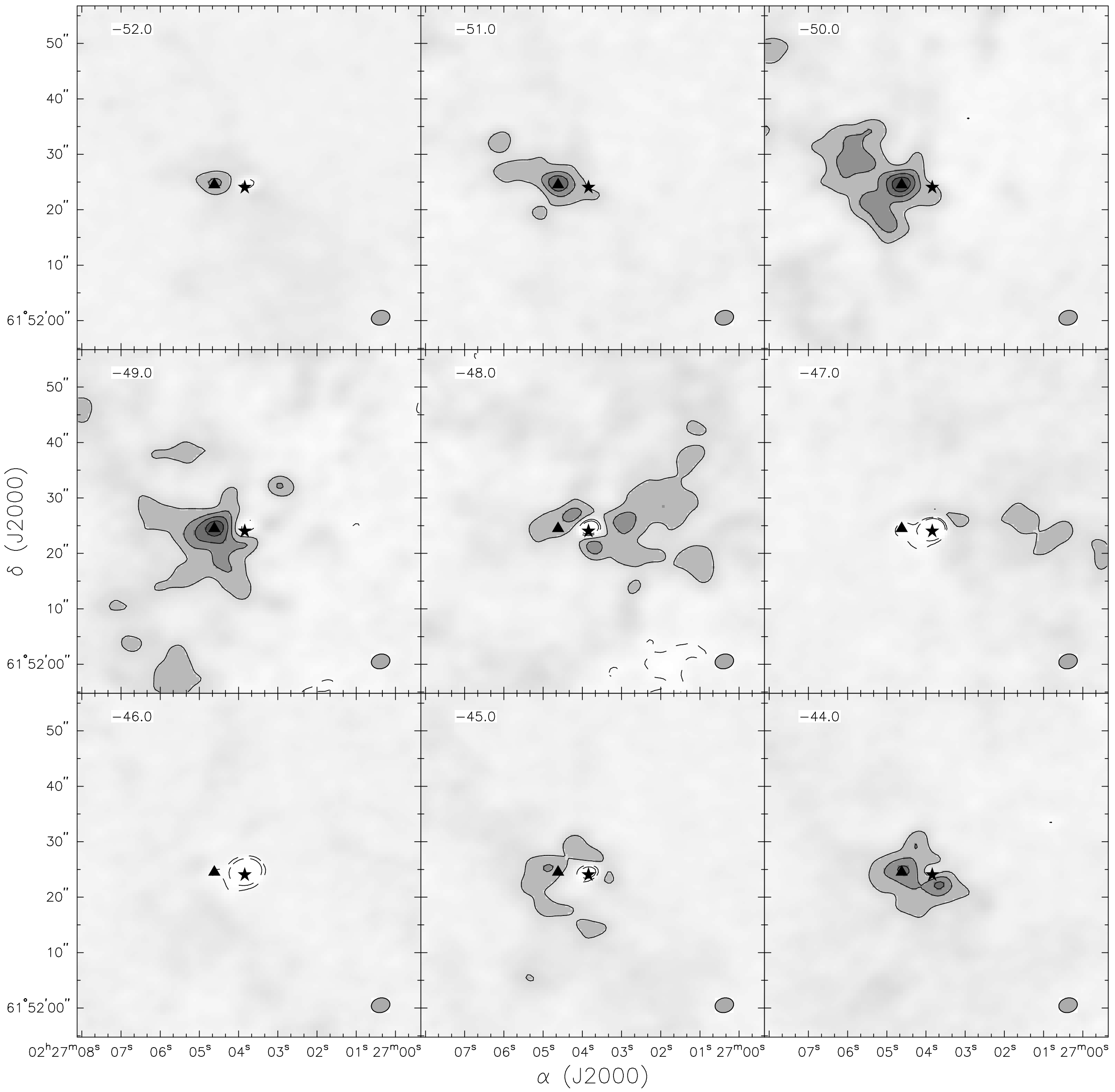

Figure 4.6 W3(OH) – HCN Channel Maps, rebinned to 1 km s^{-1} velocity increments. The velocity scale is centered on the strongest HCN hyperfine component at 88.631 GHz. The spacial resolution of this map is 3.4 x 2.6 arcsec. The contour levels are -80, -40, 20, 40, 60, 80, 100 times 0.0287 Jy beam^{-1}. The ★ and ▲ represent the peak continuum positions of W3(OH) and the Turner-Welch object, respectively.

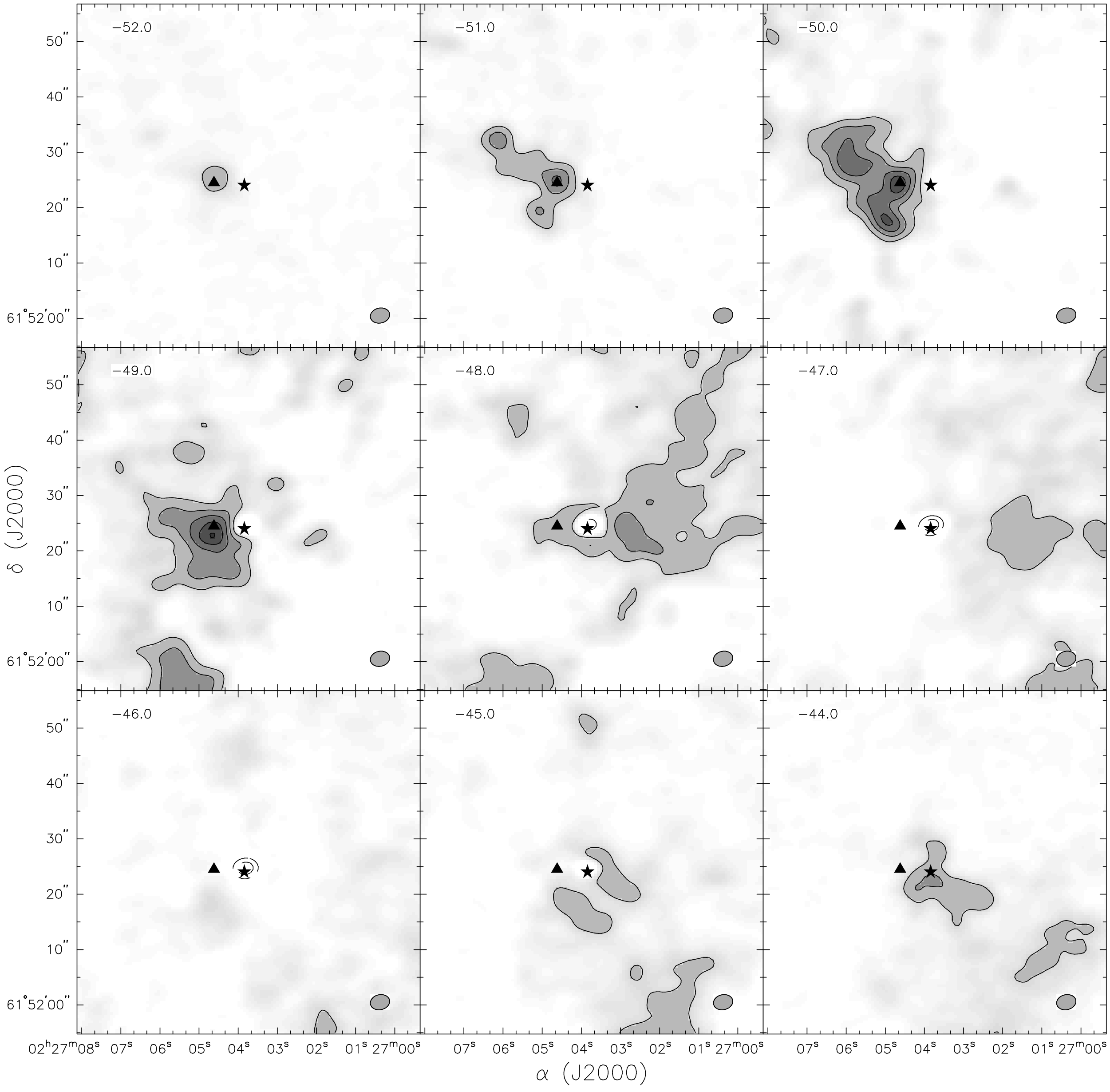

Figure 4.7 HCO$^+$ Channel maps, rebinned to 1 km s^{-1} velocity increments. The spacial resolution of this map is 3.5 x 2.7 arcsec. The contour levels are -80, -40, 20, 40, 60, 80, 100 times 0.0296 Jy beam^{-1}. The ★ and ▲ represent the peak continuum positions of W3(OH) and the Turner-Welch object, respectively.

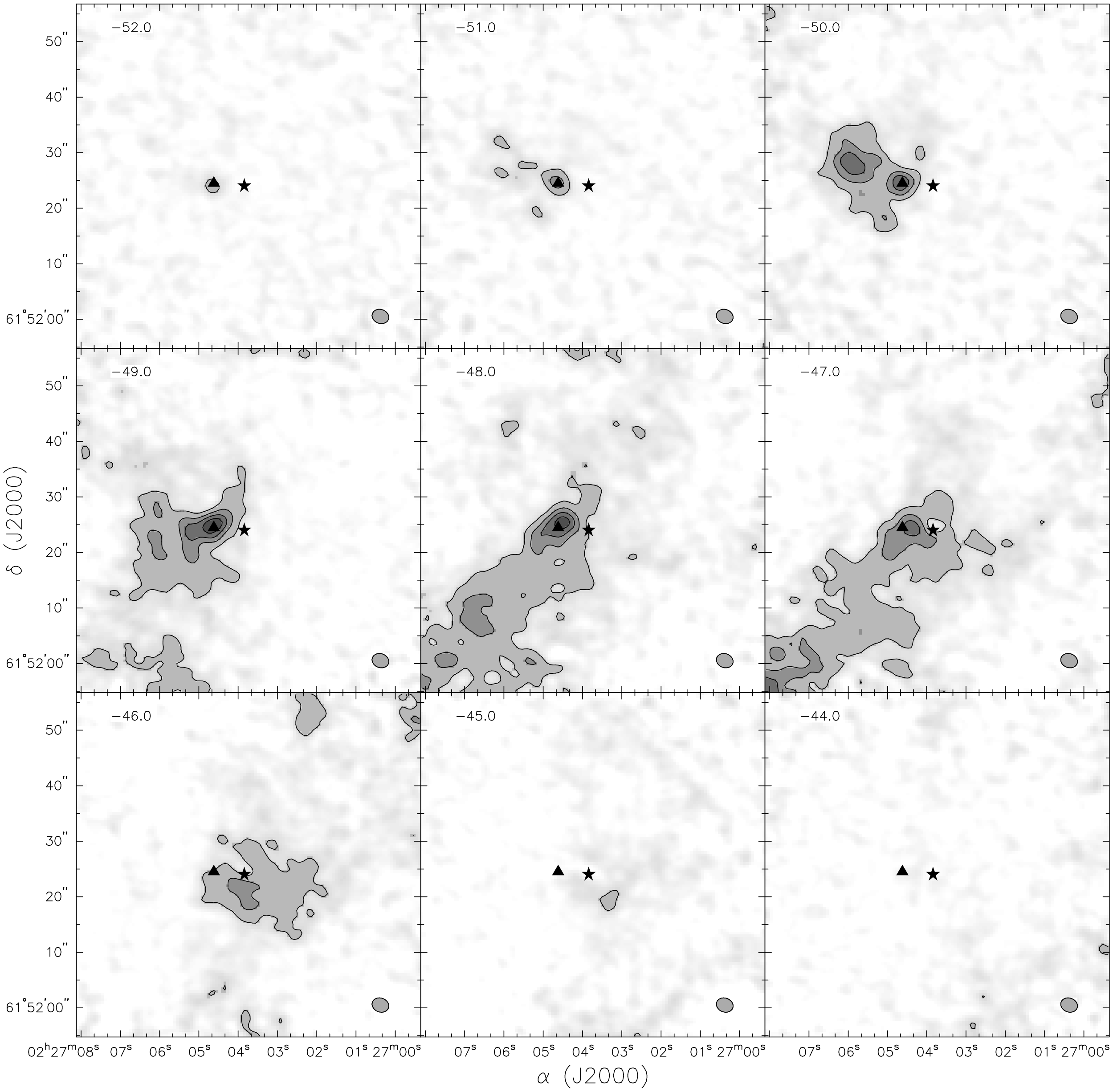

Figure 4.8 W3(OH) – $C^{18}O$ Channel maps, rebinned to 1 km s^{-1} velocity increments. The spacial resolution of this map is 3.1 x 2.5 arcsec. The contour levels are 20, 40, 60, 80, 100 times 0.00988 Jy $beam^{-1}$. The ★ and ▲ represent the peak continuum positions of W3(OH) and the Turner-Welch object, respectively.

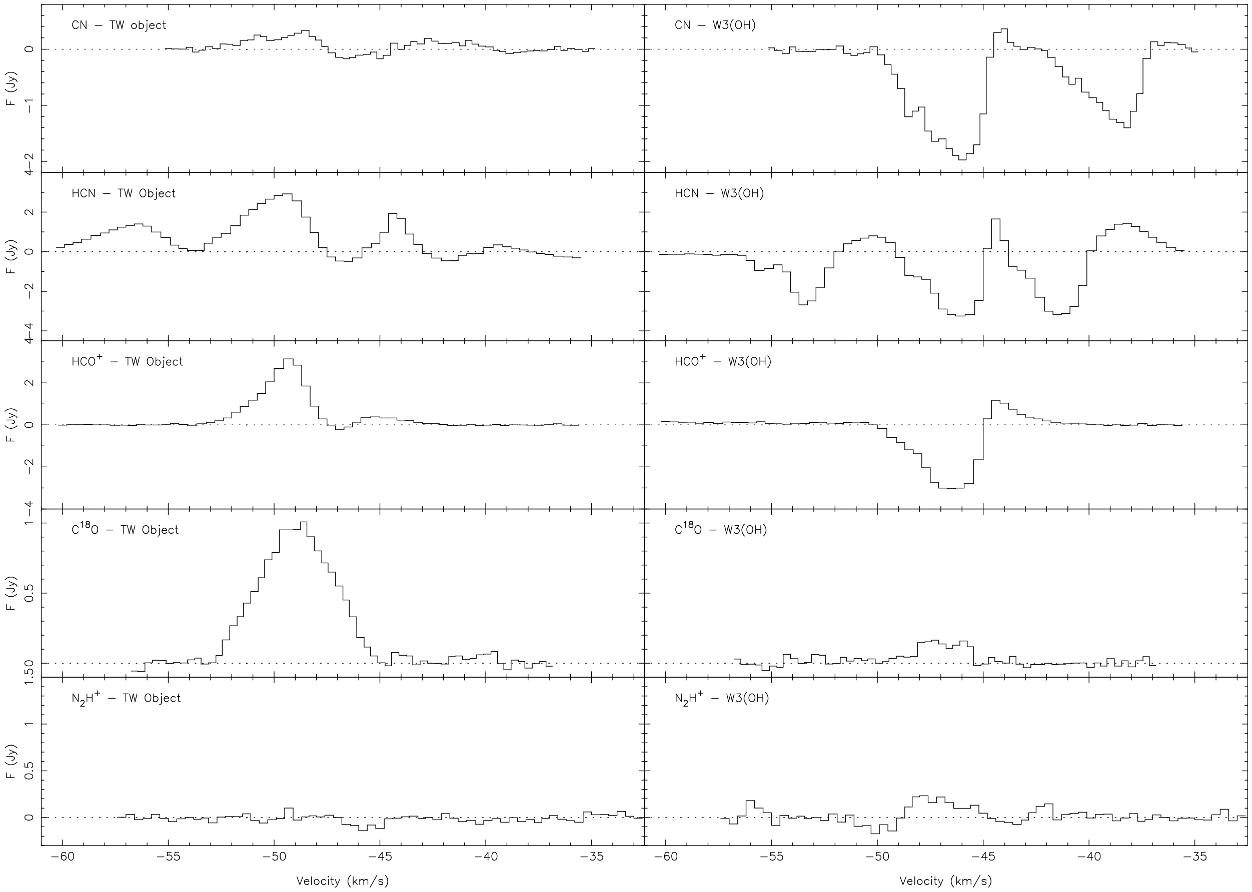

Figure 4.9 Sample spectra for each species, towards both the continuum source (W3OH) and the Turner-Welch object. For the CN, HCN, and N_2H^+ spectra, multiple hyperfine components are present. The velocity scale for all of these corresponds to that of the strongest hyperfine component. Three of the sources can be seen in absorption towards the continuum source, while the other two have little to no emission.

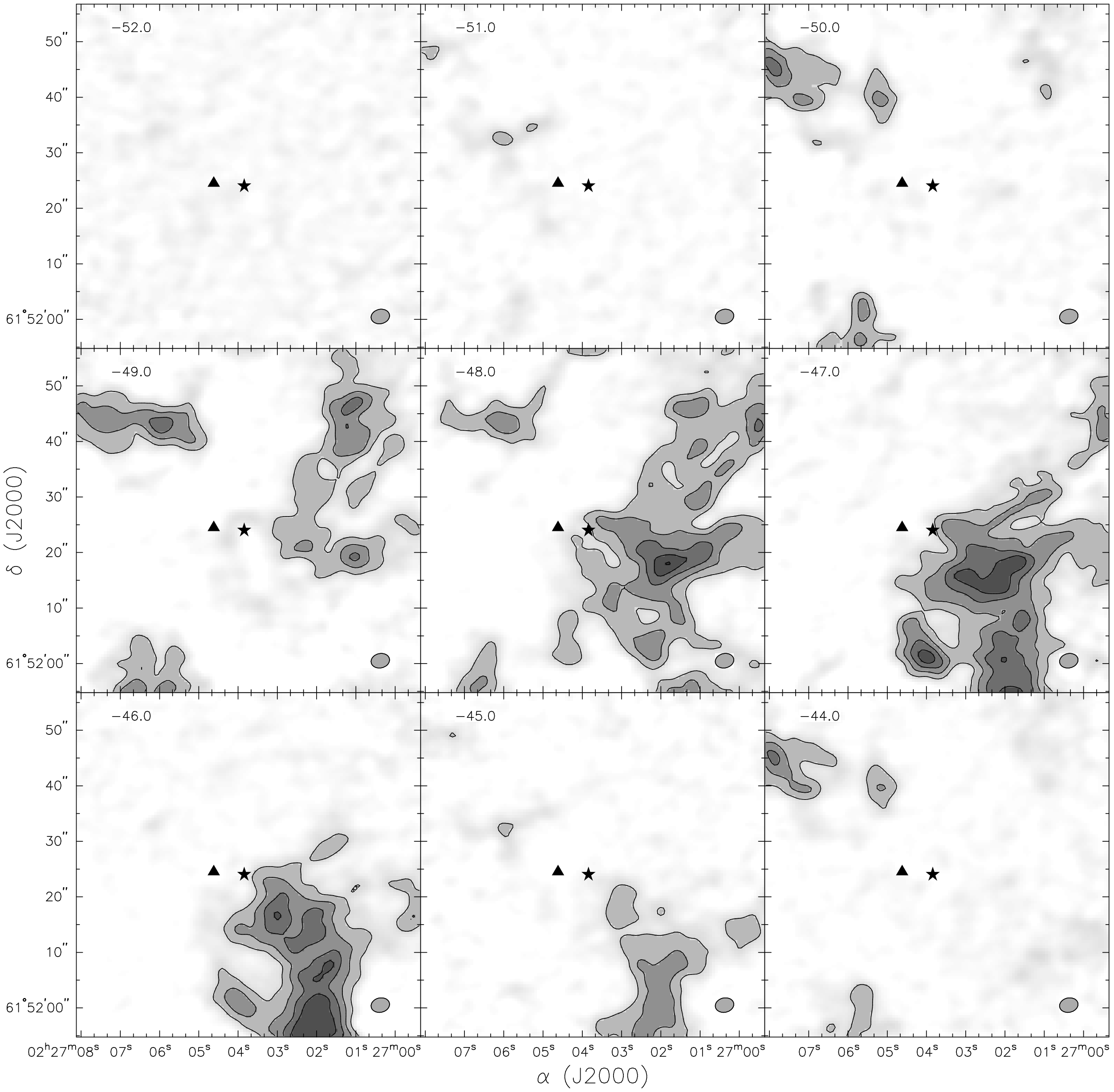

Figure 4.10 W3(OH) – N_2H^+ Channel maps, rebinned to 1 km s^{-1} velocity increments. The velocity scale is centered on the strongest CN hyperfine component at 93.17348 GHz. The spacial resolution of this map is 3.4 x 2.6 arcsec. The contour levels are 20, 40, 60, 80, 100 times 0.0129 Jy beam^{-1}. The ★ and ▲ represent the peak continuum positions of W3(OH) and the Turner-Welch object, respectively.

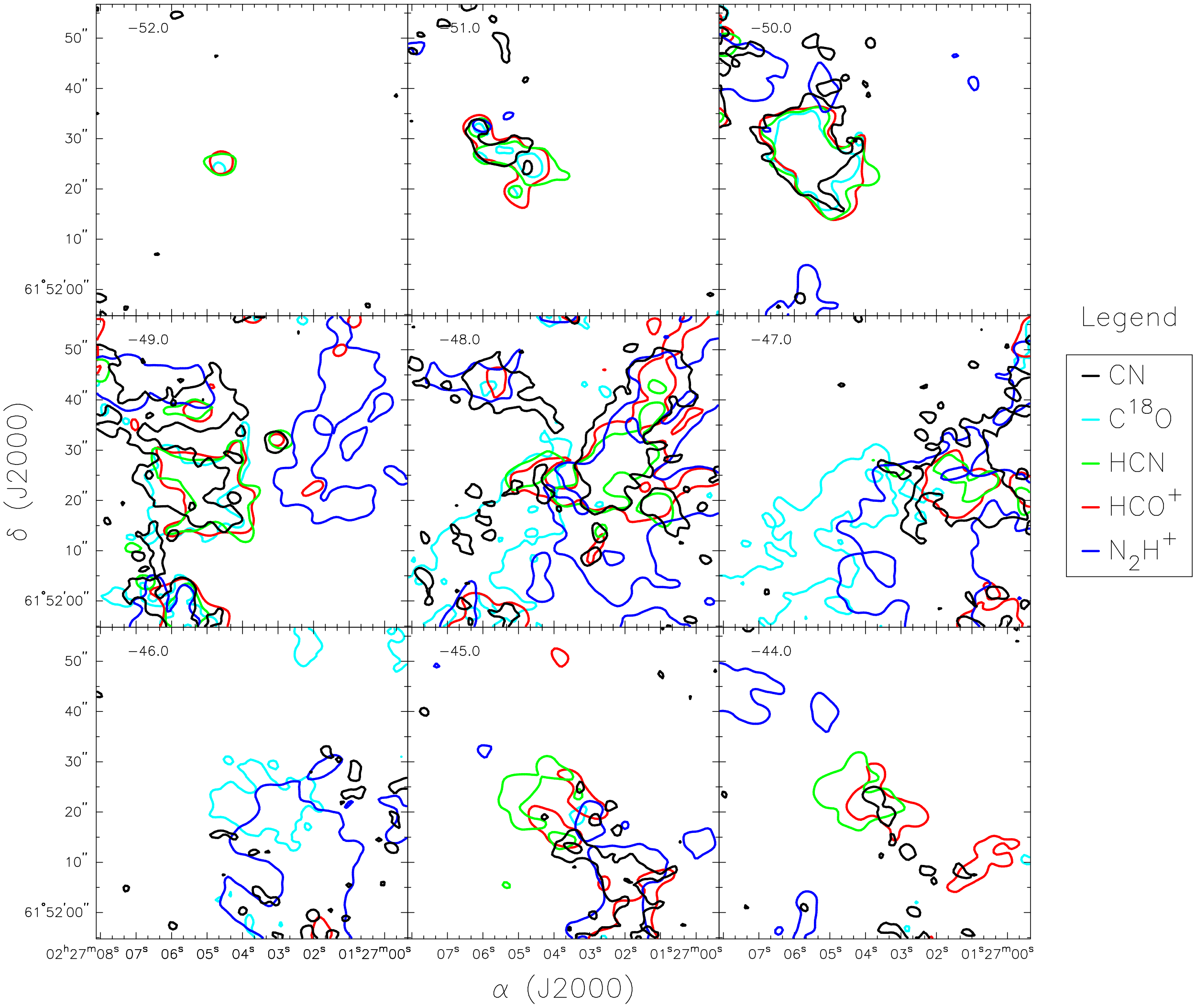

Figure 4.11 Channel map showing the 20% contour level of all the mapped species.

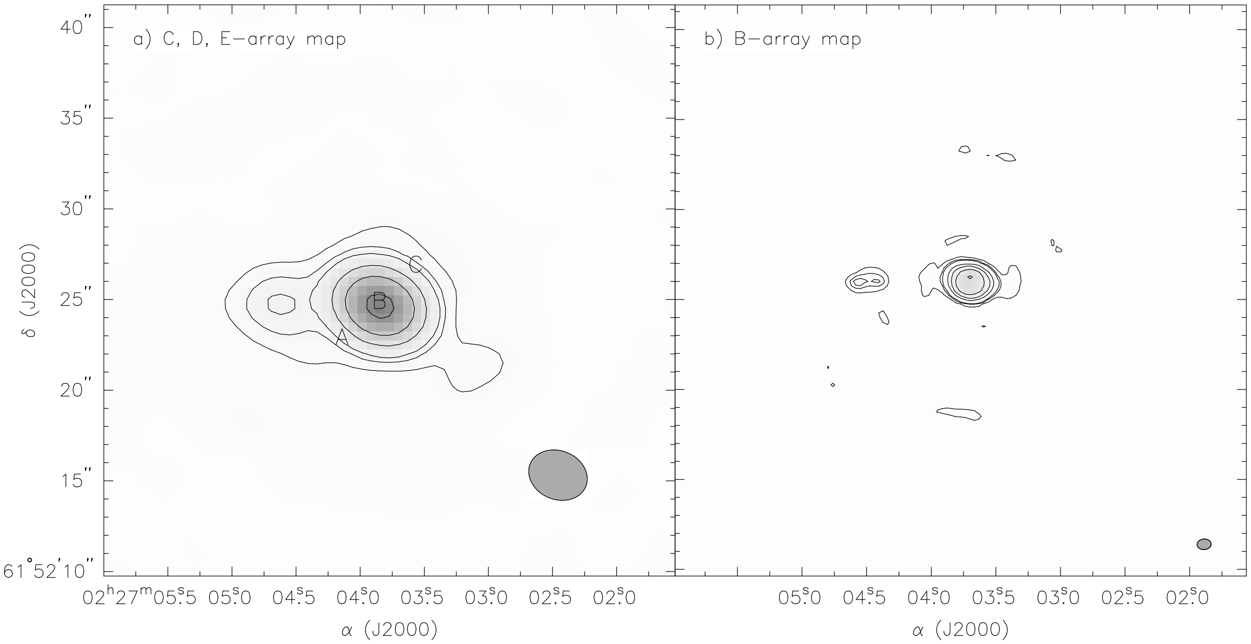

Figure 4.12 Continuum maps centered at 112 GHz. Panel a) has contour levels of 8, 16, 25, 64, 128, and 256 times 0.009 Jy beam^{-1}. Panel b) has contour levels of 3, 7, 10, 32, 64, 128, and 256 times 0.003 Jy beam^{-1}. The range in contour levels are to show the dynamic range of features visible in these maps. a) has a beam size of 3.3″x 2.7″, b) has a beam size of 0.77″x 0.59″. Positions A-C marked in the first panel represent the positions of spectra in Figure 5.1.

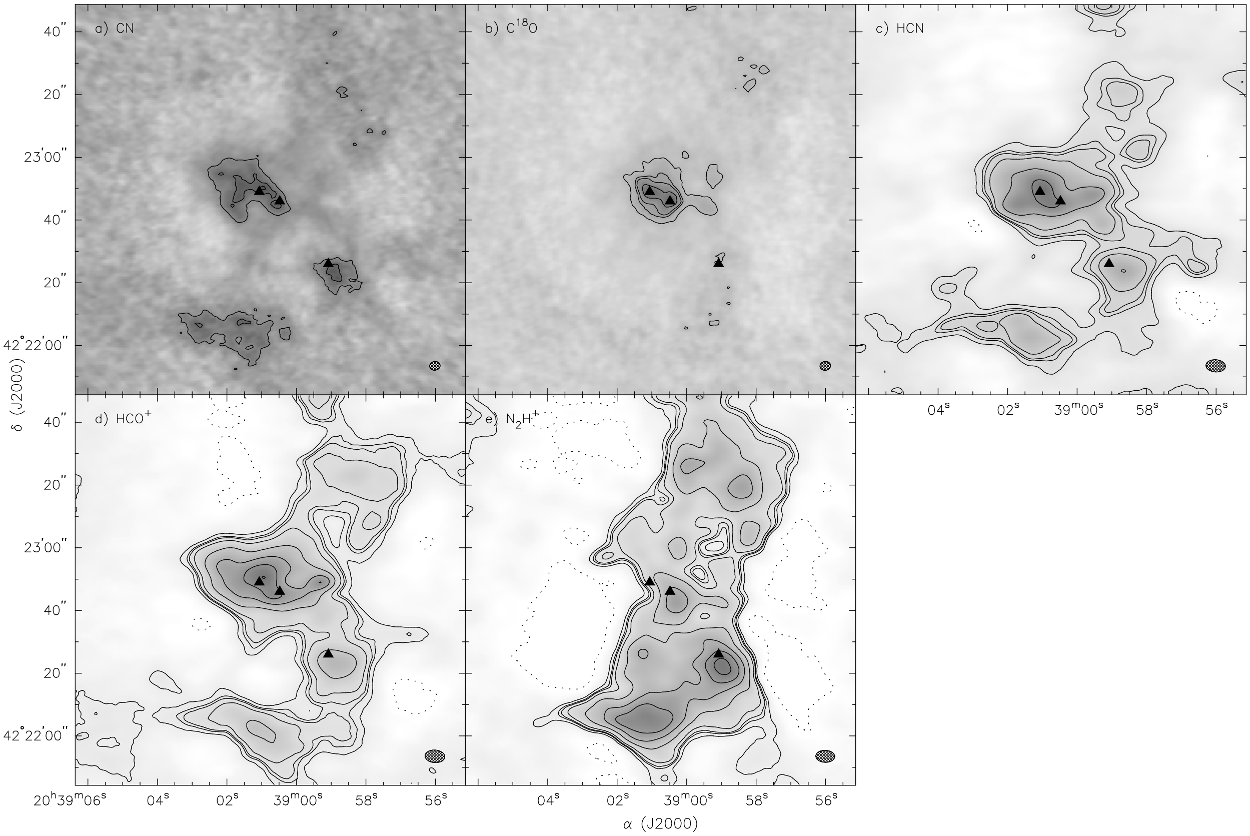

Figure 4.13 CARMA integrated line maps of DR21(OH). The contour levels are: 2, 4, 5, 7.5, 15, 25, 35, 45 × 0.04 Jy beam^{-1}. The beam sizes are: a) CN, 3.3″ × 2.8″; b) C^{18}O, 3.4″ × 2.8″; c) HCN, 6.3″ × 3.9″; d) HCO$^+$, 6.3″ × 4.0″; e) N$_2$H$^+$, 6.1″ × 3.9″. The ▲s represent the positions of the peak positions of the three brightest continuum sources.

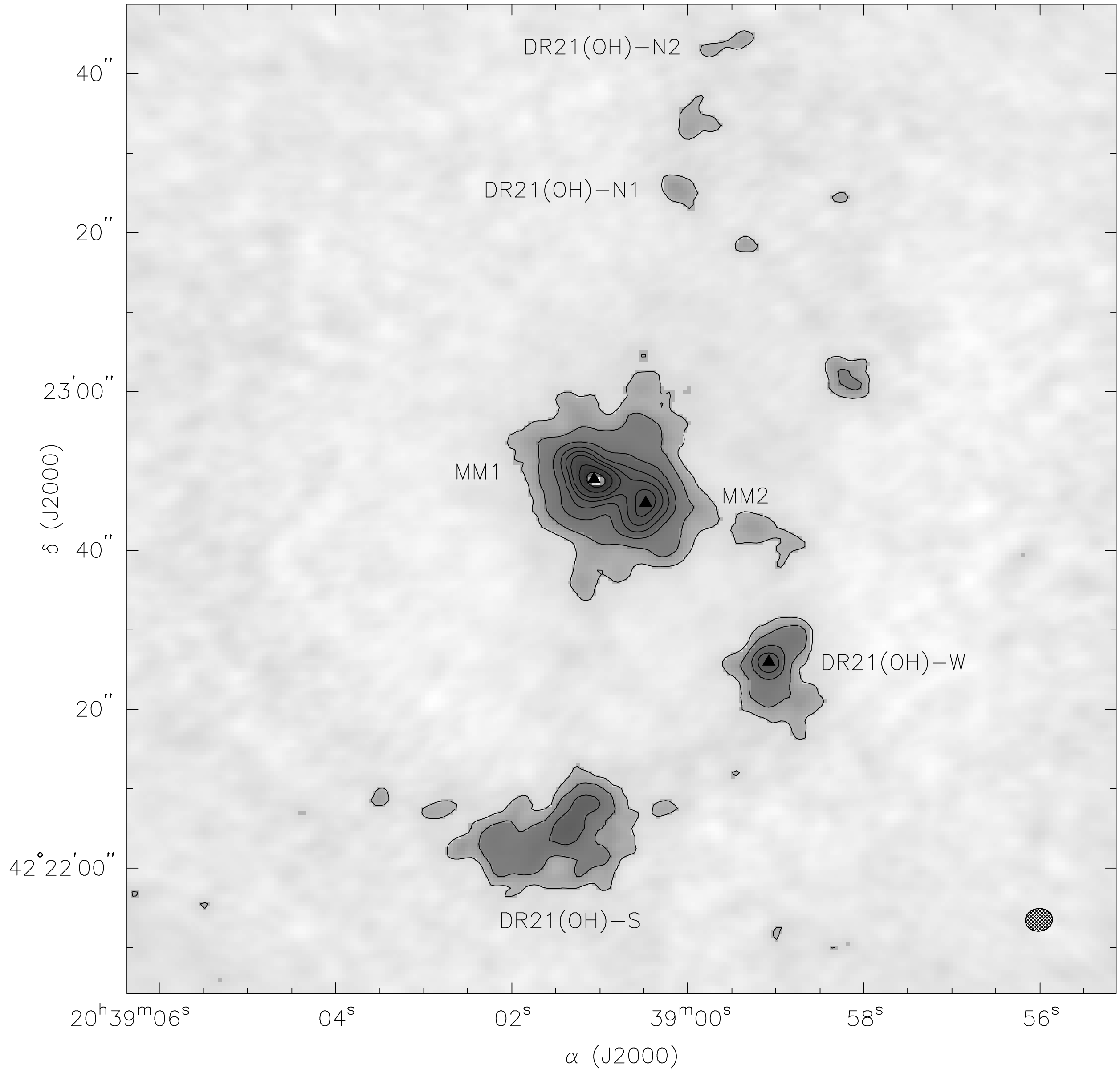

Figure 4.14 DR21(OH) continuum at 112 GHz. The contour levels are: 2, 4, 8, 12, 16, 20, 28, 36 times the noise level of 0.0025 Jy beam^{-1}. The beam size is 3.4″ × 2.8″. The source names are from Motte et al. (2007) with the exception of MM1 and MM2 which is referenced in Padin et al. (1989). The ▲s mark the positions of the three strongest continuum peaks which are 0.103 Jy beam^{-1}, 0.056 Jy beam^{-1}, and 0.041 Jy beam^{-1} for MM1, MM2, and DR21(OH)-W, respectively.

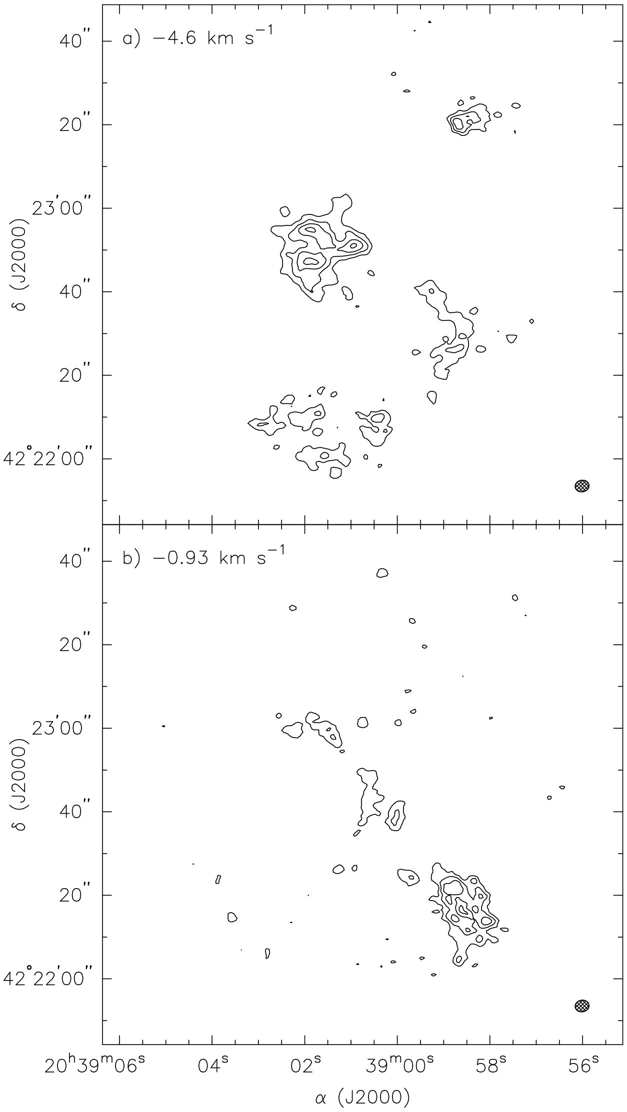

Figure 4.15 Maps of the two CN velocity components toward DR21(OH). The top panel is an integrated line map centered at -4.6 km s^{-1} with a line width of 2.3 km s^{-1}. The bottom panel is centered at -0.93 km s^{-1} and has the same linewidth. The velocities and the linewidths are from fits done by Crutcher et al. (1999b).

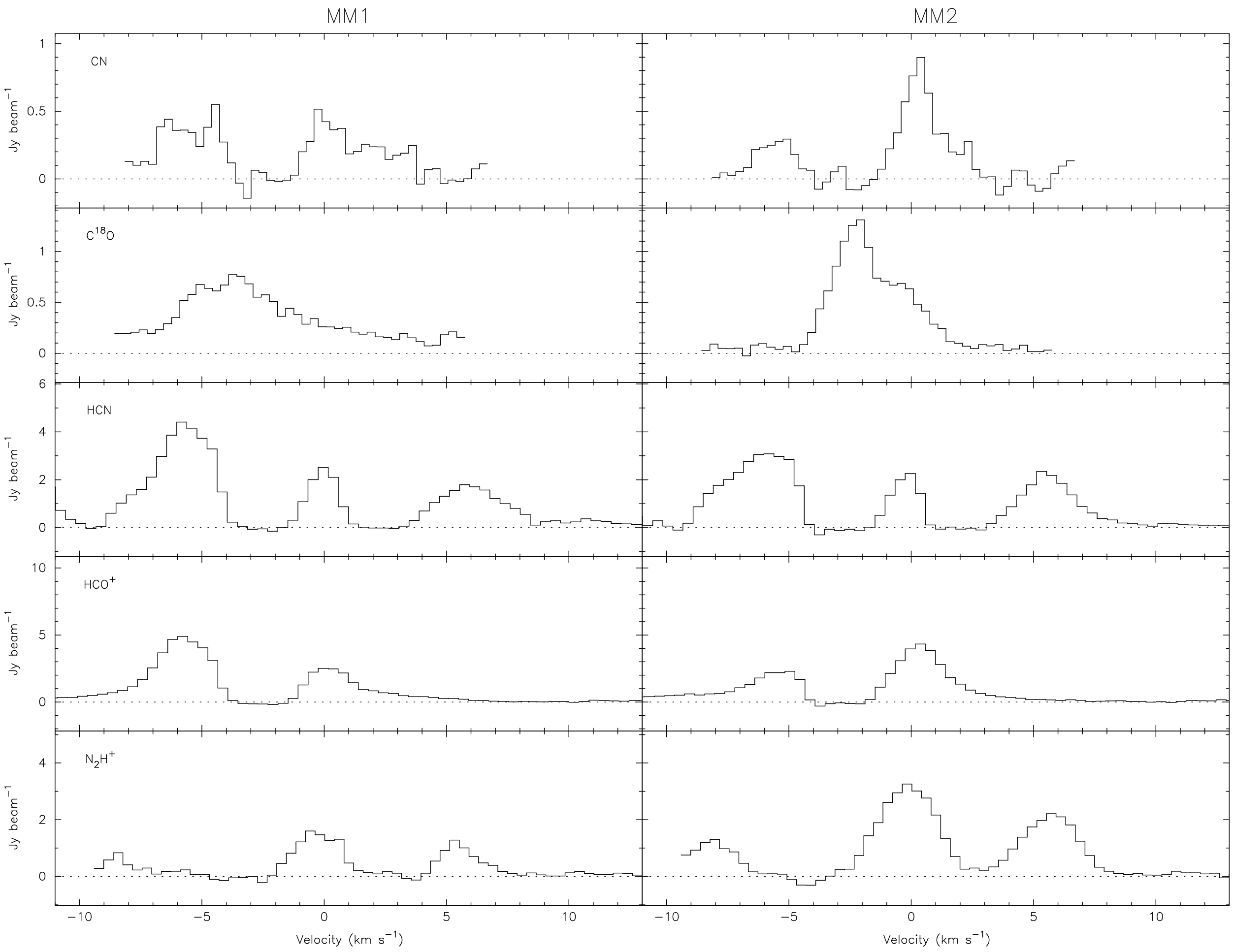

Figure 4.16 Molecular spectra of DR21(OH) continuum objects MM1 and MM2. The relative strengths of the velocity components suggest that the two continuum objects are associated with the two different velocity components (see CN and HCO$^+$ emission in particular). For HCN and N$_2$H$^+$ which have several hyperfine components, there is significant line confusion due to the multiple velocity components having almost the same velocity separation as the hyperfine components.

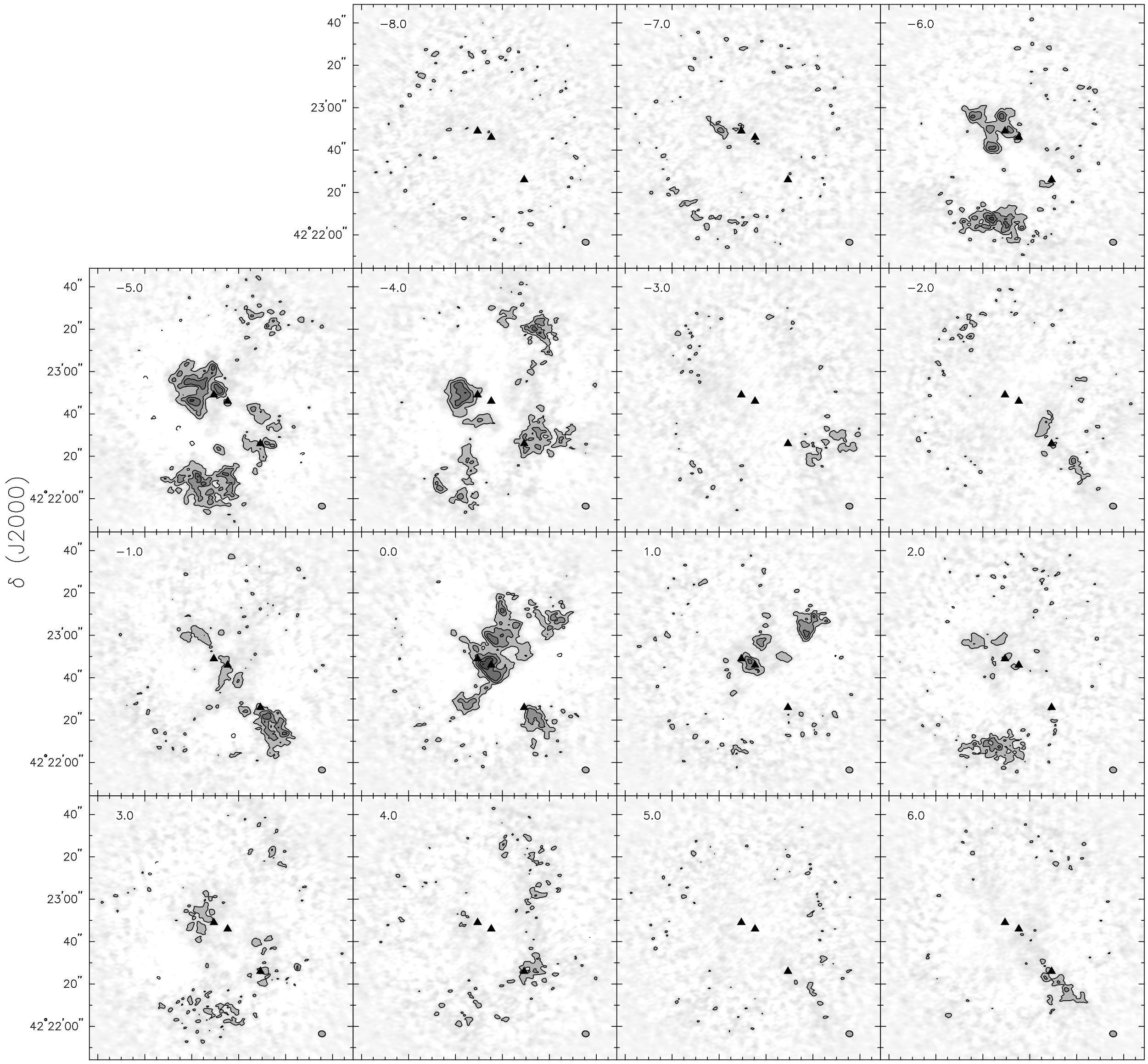

Figure 4.17 DR21(OH) – CN Channel Maps. The contour levels are -40, -80, 20, 40, 60, 80, 100 × 1.03 Jy beam^{-1}. The beam size is $3.33'' \times 2.77''$. The ▲ represent the peaks of the continuum sources.

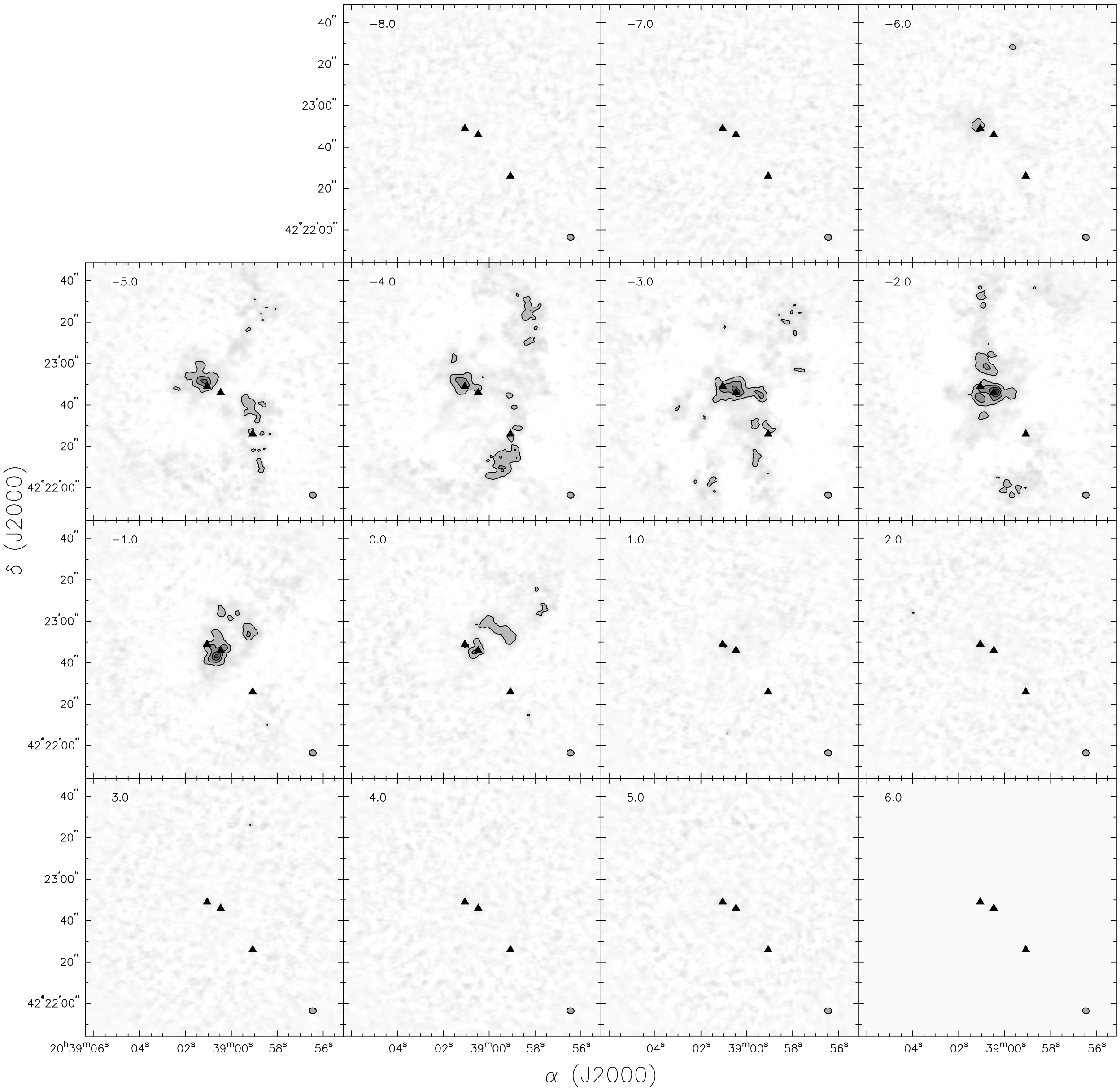

Figure 4.18 DR21(OH) – C^{18}O Channel Maps. The contour levels are -40, -80, 20, 40, 60, 80, 100 × 1.39 Jy beam^{-1}. The beam size is 3.41″ × 2.84″. The ▲ represent the peaks of the continuum sources.

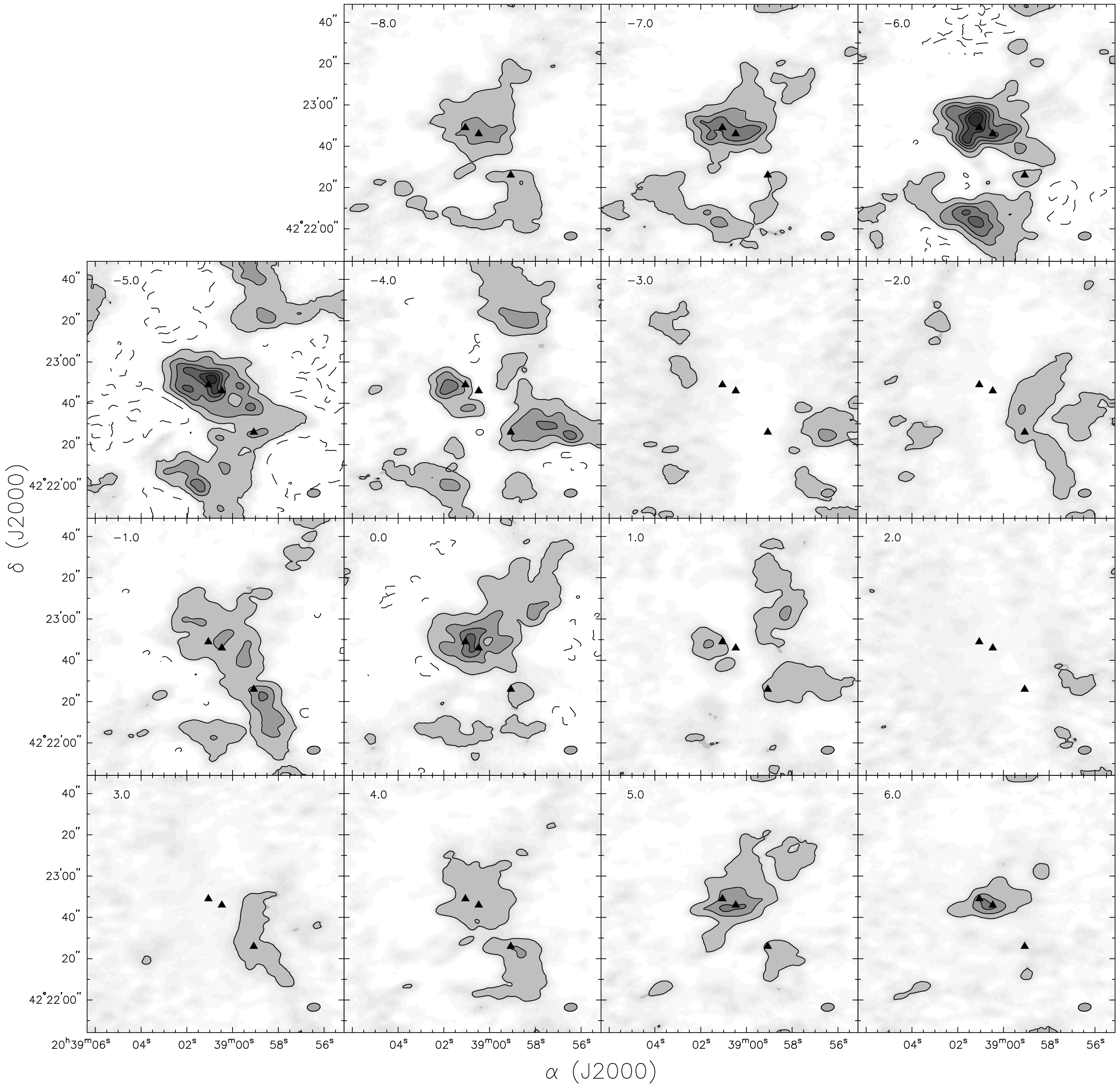

Figure 4.19 DR21(OH) – HCN Channel Maps. The contour levels are -10, 5, 20, 35, 50, 65, 80 × 5.57 Jy beam^{-1}. The beam size is $6.26'' \times 3.92''$. The ▲ represent the peaks of the continuum sources.

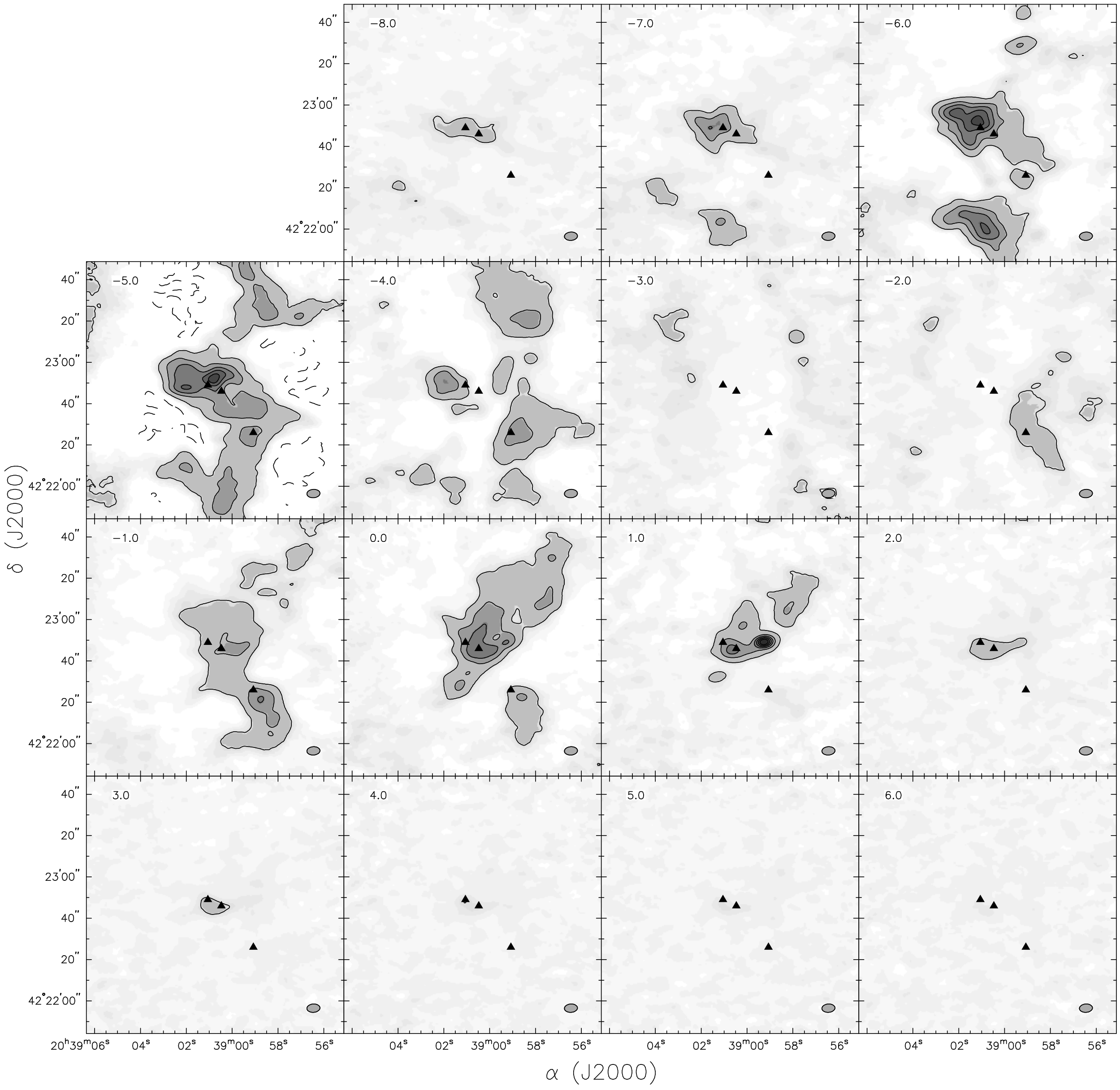

Figure 4.20 DR21(OH) – HCO$^+$ Channel Maps. The contour levels are -10, 5, 20, 35, 50, 65, 80 × 8.63 Jy beam^{-1}. The beam size is $6.33'' \times 4.03''$. The ▲ represent the peaks of the continuum sources.

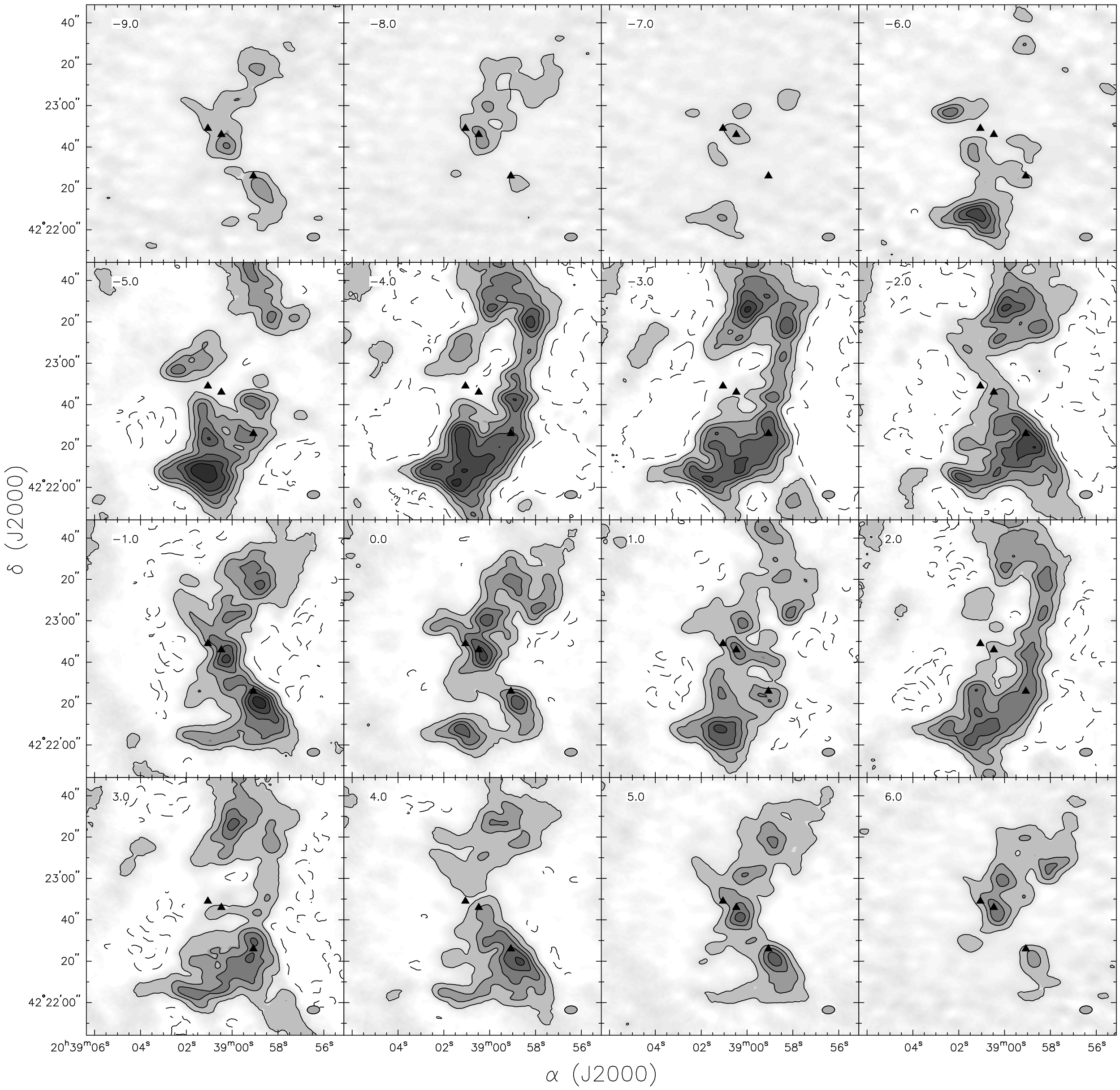

Figure 4.21 DR21(OH) – N_2H^+ Channel Maps. The contour levels are -10, 5, 20, 35, 50, 65, 80 × 4.84 Jy beam^{-1}. The beam size is $6.07'' \times 3.86''$. The ▲ represent the peaks of the continuum sources.

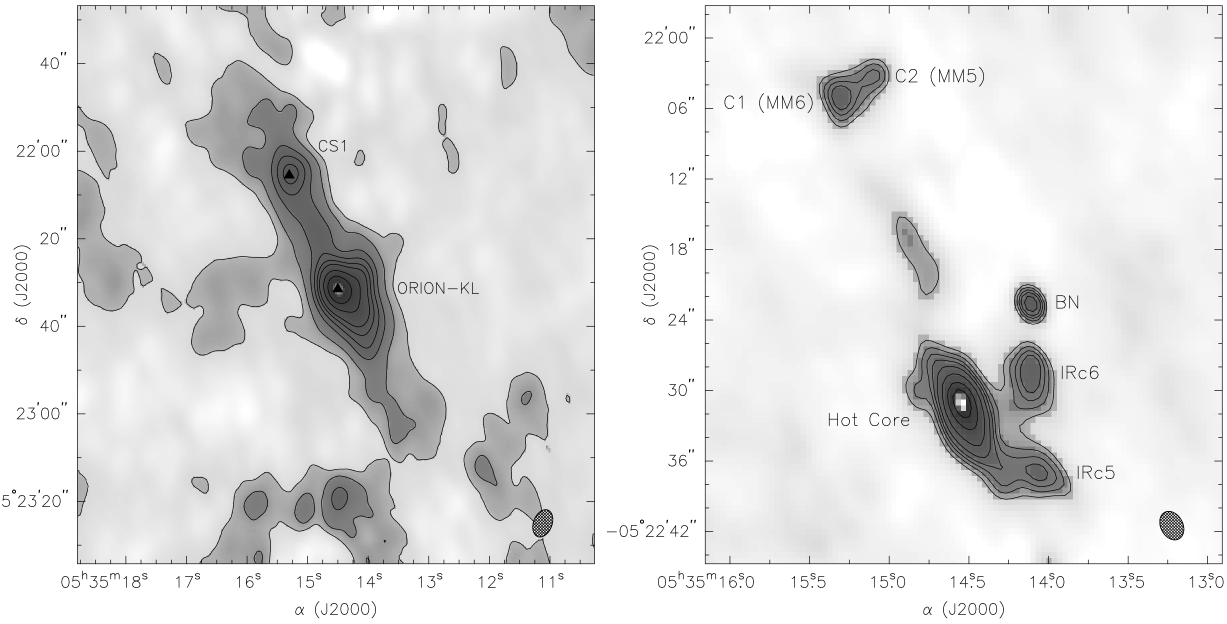

Figure 4.22 The left panel is the composite 112 GHz continuum map of OMC1. Two significant continuum peaks, Orion-KL (Kleinmann & Low, 1967), and CS1 (Friedel & Widicus Weaver, 2011), are observable at a resolution of 6.6″ × 4.5″. The contour levels are 2, 8, 20, 30, 40, 50, 70, 90 × 10 mJy beam^{-1}. The right panel is a CARMA C-array continuum map of the inner quarter region which resolves several additional objects not observable in the left panel: MM5 and MM6 (Eisner & Carpenter, 2006) which comprises CS1 in the large scale map, BN (Becklin & Neugebauer, 1967), a star also observable in the infrared, and two IR sources, IRc5 and IRc6, thought to be reflection nebulae (Rieke et al., 1973). The resolution of this map is 2.6″ × 2.0″ and the contour levels are 10, 14, 18, 22, 28, 40, 60, 80 × 2 mJy beam^{-1}.

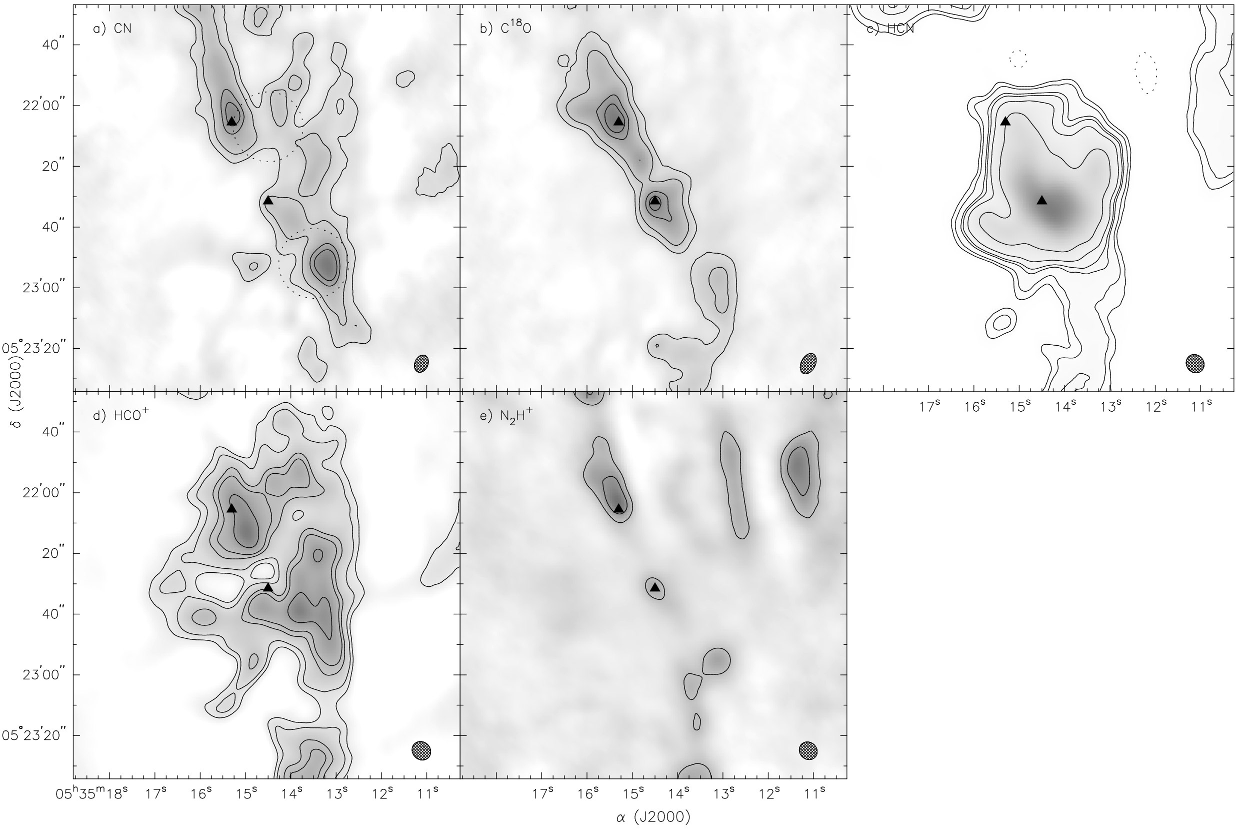

Figure 4.23 CARMA integrated line maps of OMC1. The contour levels are: 1, 2, 4, 5, 7.5, 15 × 0.3 Jy beam^{-1}. The beam sizes are: a) CN, 5.9″ × 4.3″; b) C^{18}O, 7.2″ × 4.6″; c) HCN, 6.3″ × 5.7″; d) HCO$^+$, 6.4″ × 5.8″; e) N$_2$H$^+$, 6.1″ × 5.6″.

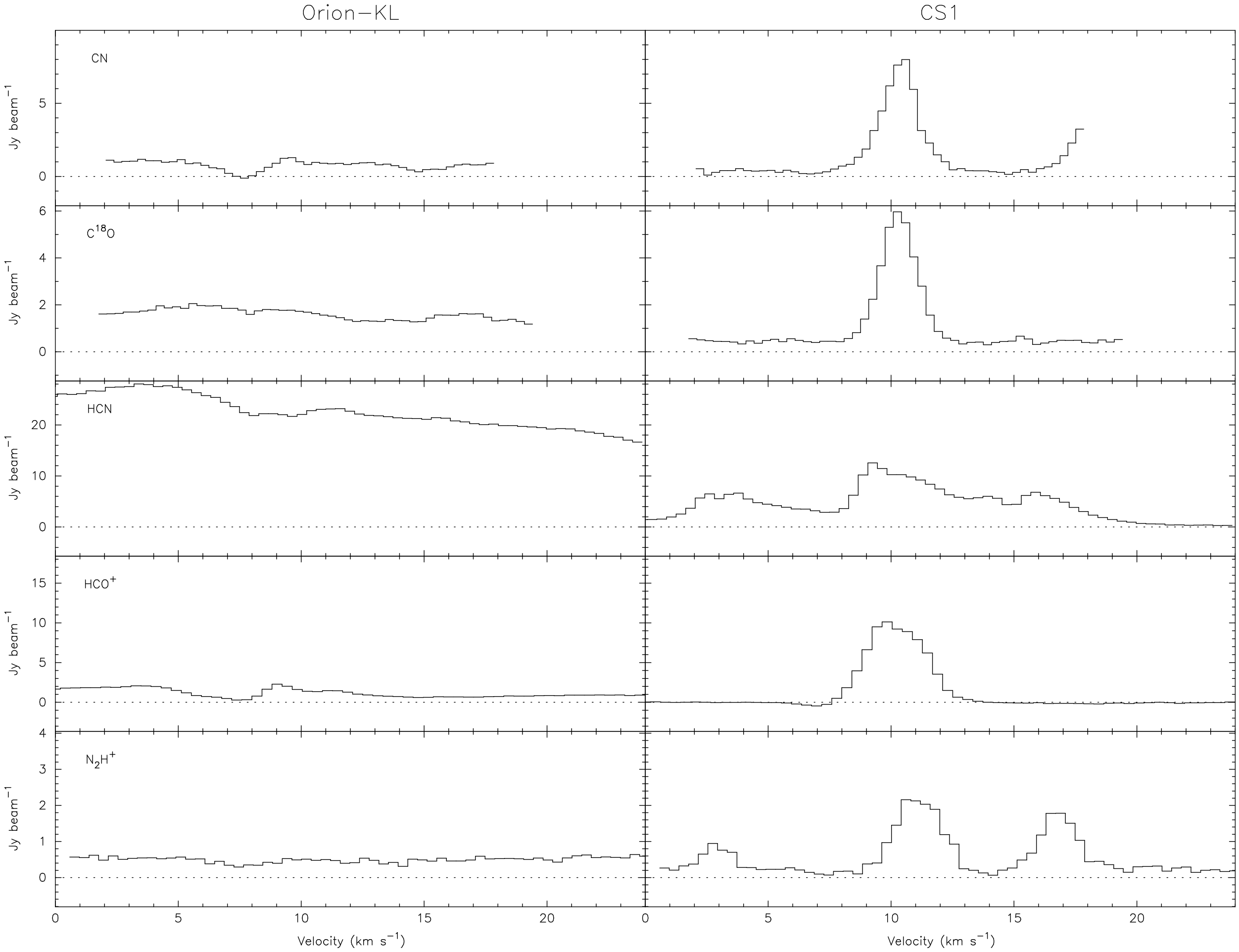

Figure 4.24 Molecular spectra of OMC1 continuum objects Orion-KL and CS1. With the exception of HCN, the molecular emission is significantly stronger towards CS1 than Orion-KL (and the hot core). The HCN emission towards Orion-KL is due to a known HCN envelope around the hot core (Schilke et al., 1992). The three hyperfine components are blended together due to the high linewidth (~ 20 km s^{-1}) of the HCN emission.

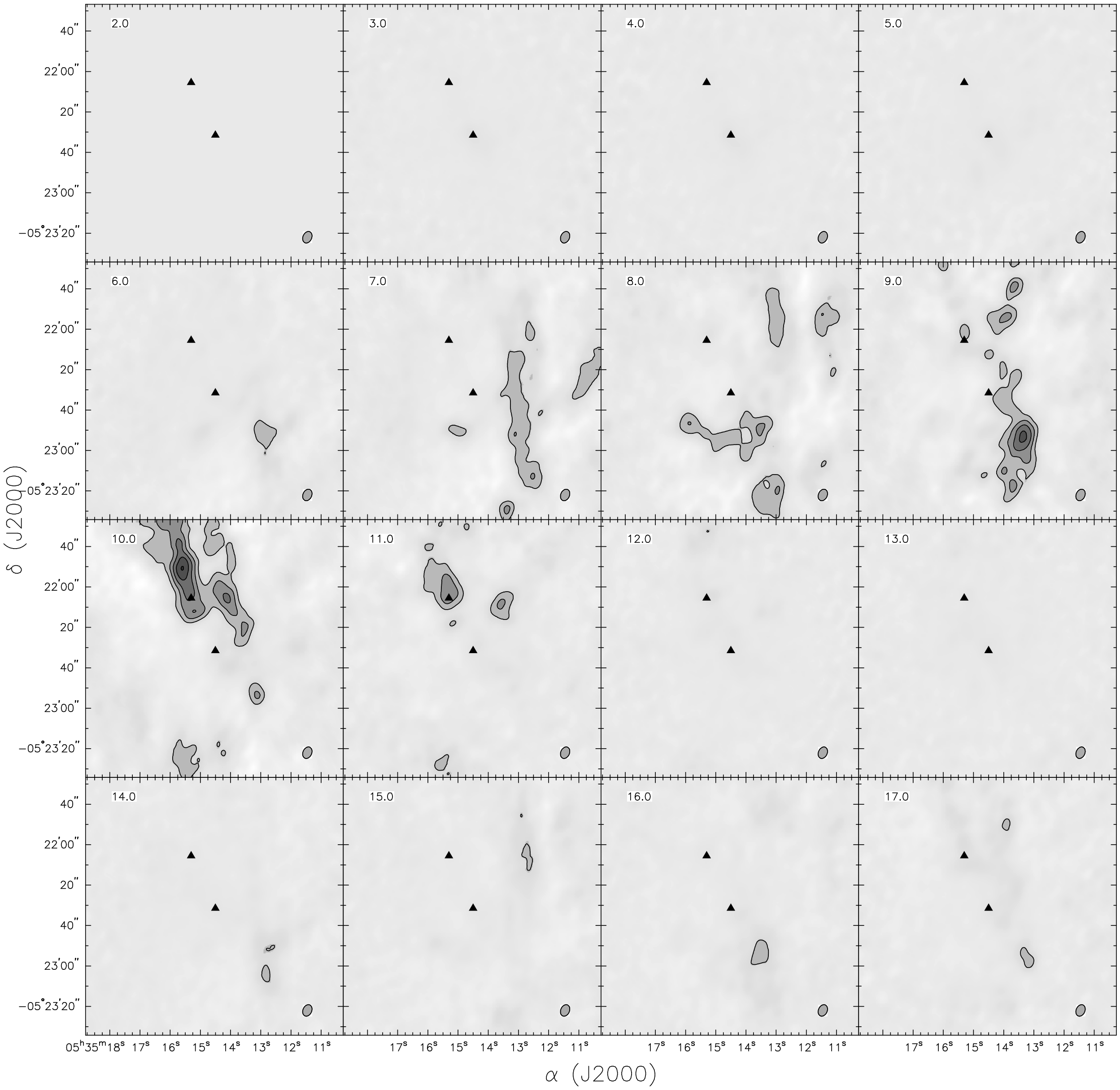

Figure 4.25 OMC1 – CN Channel Maps. The contour levels are -40, -80, 20, 40, 60, 80, 100 × 10.1 Jy beam^{-1}. The beam size is $5.94'' \times 4.32''$. The ▲ represent the peaks of the continuum sources.

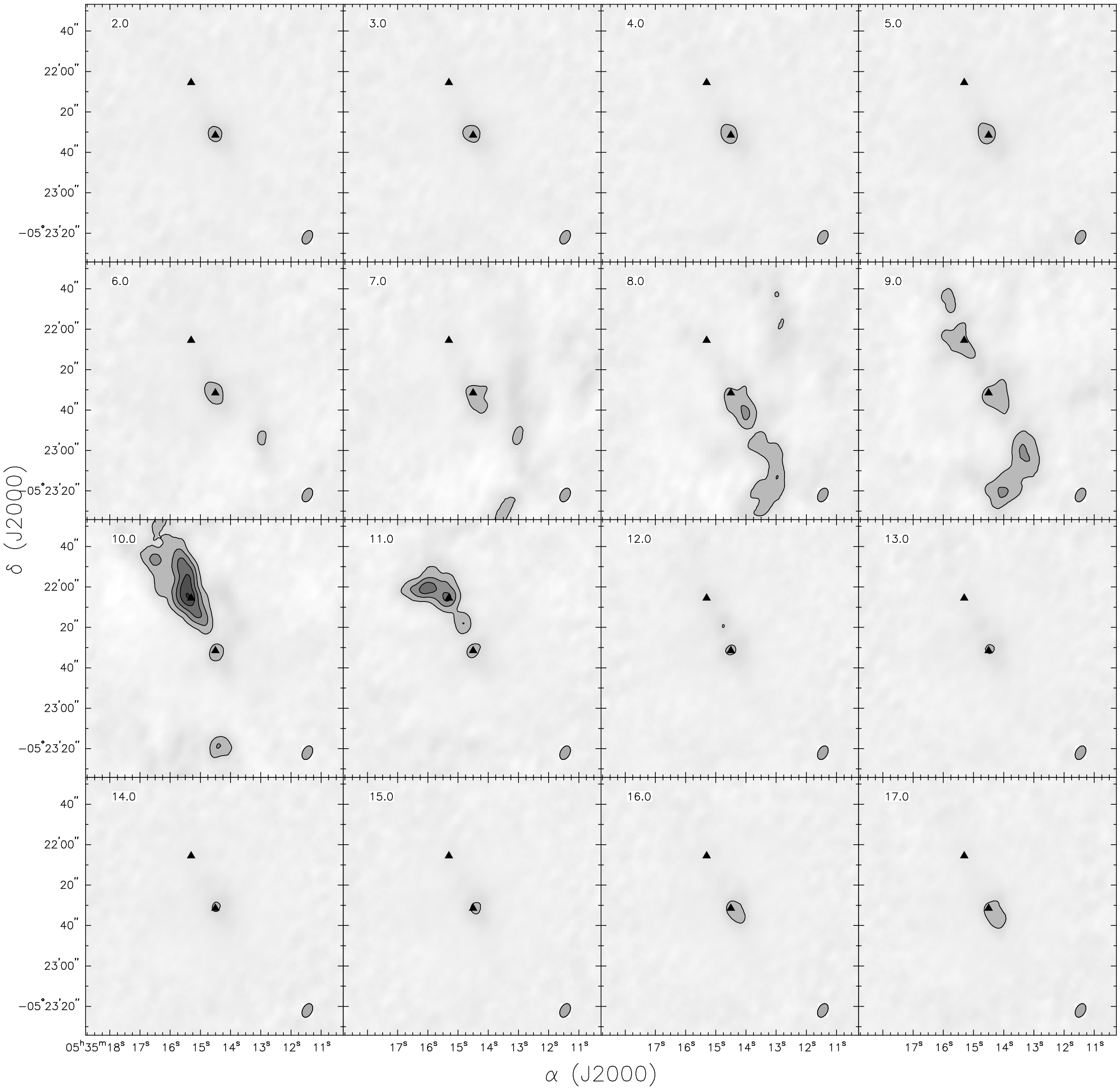

Figure 4.26 OMC1 – C^{18}O Channel Maps. The contour levels are -40, -80, 20, 40, 60, 80, 100 × 5.89 Jy beam^{-1}. The beam size is 7.21″ × 4.65″. The ▲ represent the peaks of the continuum sources.

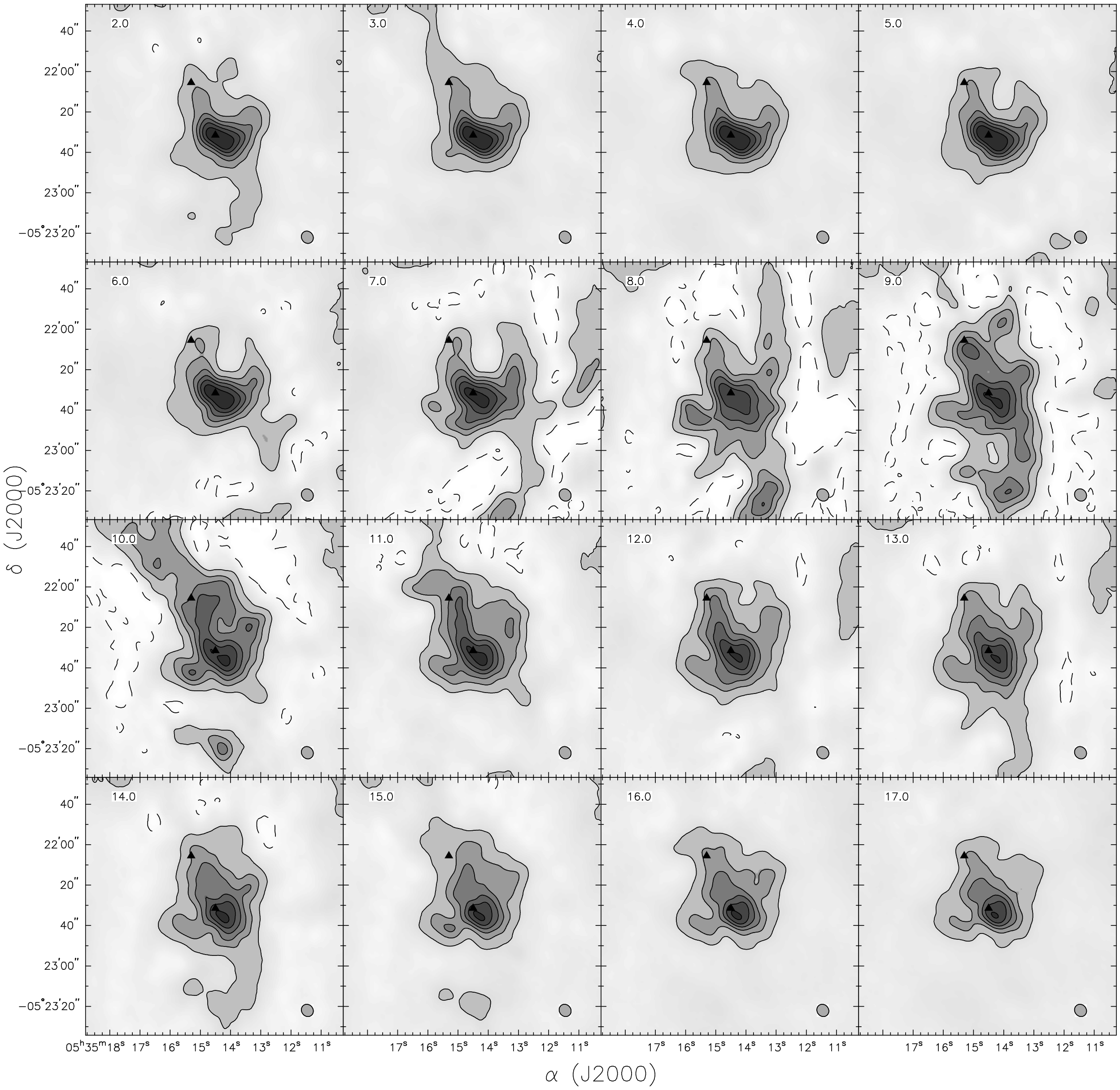

Figure 4.27 OMC1 – HCN Channel Maps. The contour levels are -10, 5, 20, 35, 50, 65, 80 × 28.4 Jy beam^{-1}. The beam size is $6.30'' \times 5.67''$. The ▲ represent the peaks of the continuum sources.

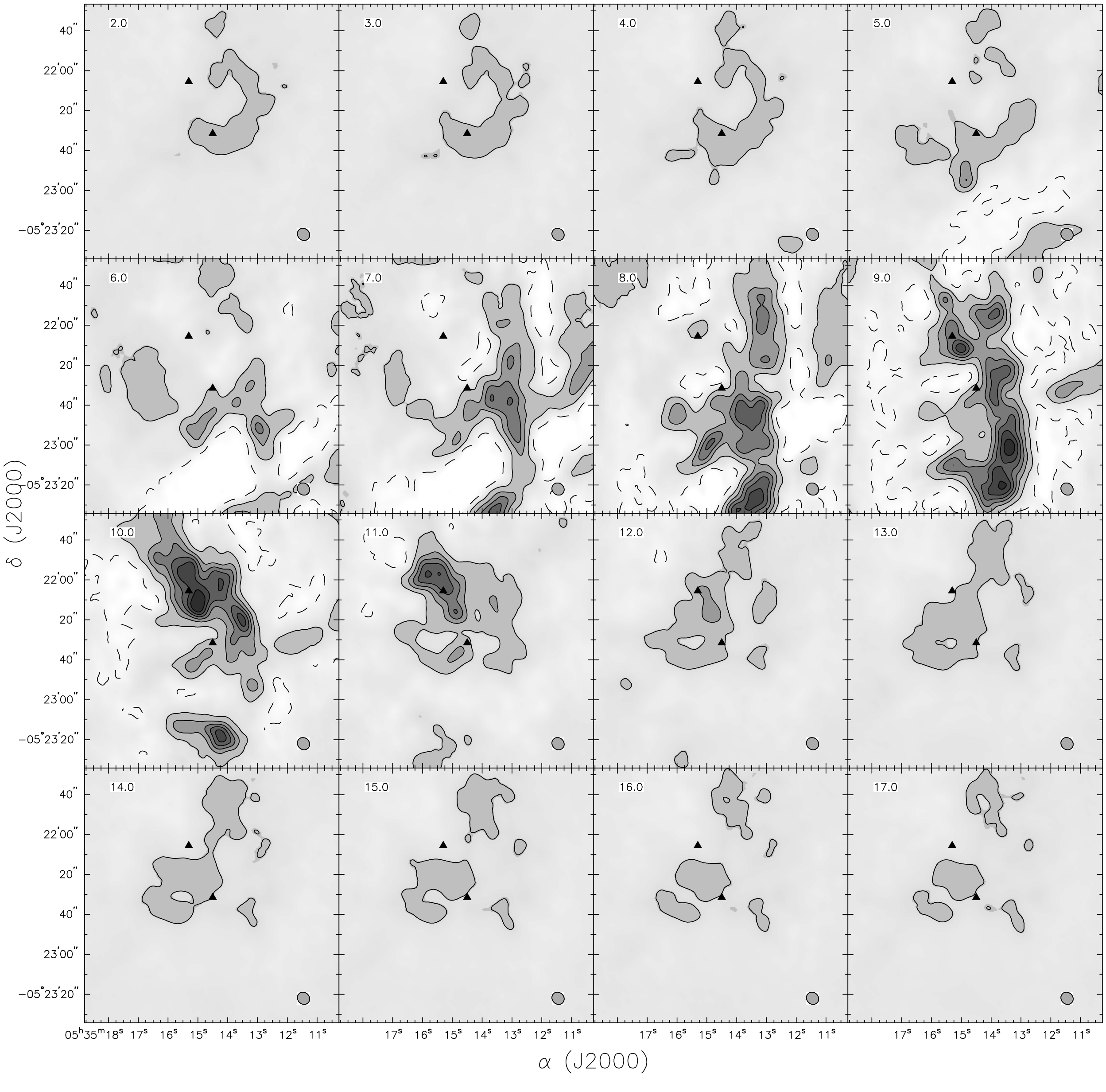

Figure 4.28 OMC1 – HCO$^+$ Channel Maps. The contour levels are -10, 5, 20, 35, 50, 65, 80 × 15.4 Jy beam^{-1}. The beam size is $6.45'' \times 5.80''$. The ▲ represent the peaks of the continuum sources.

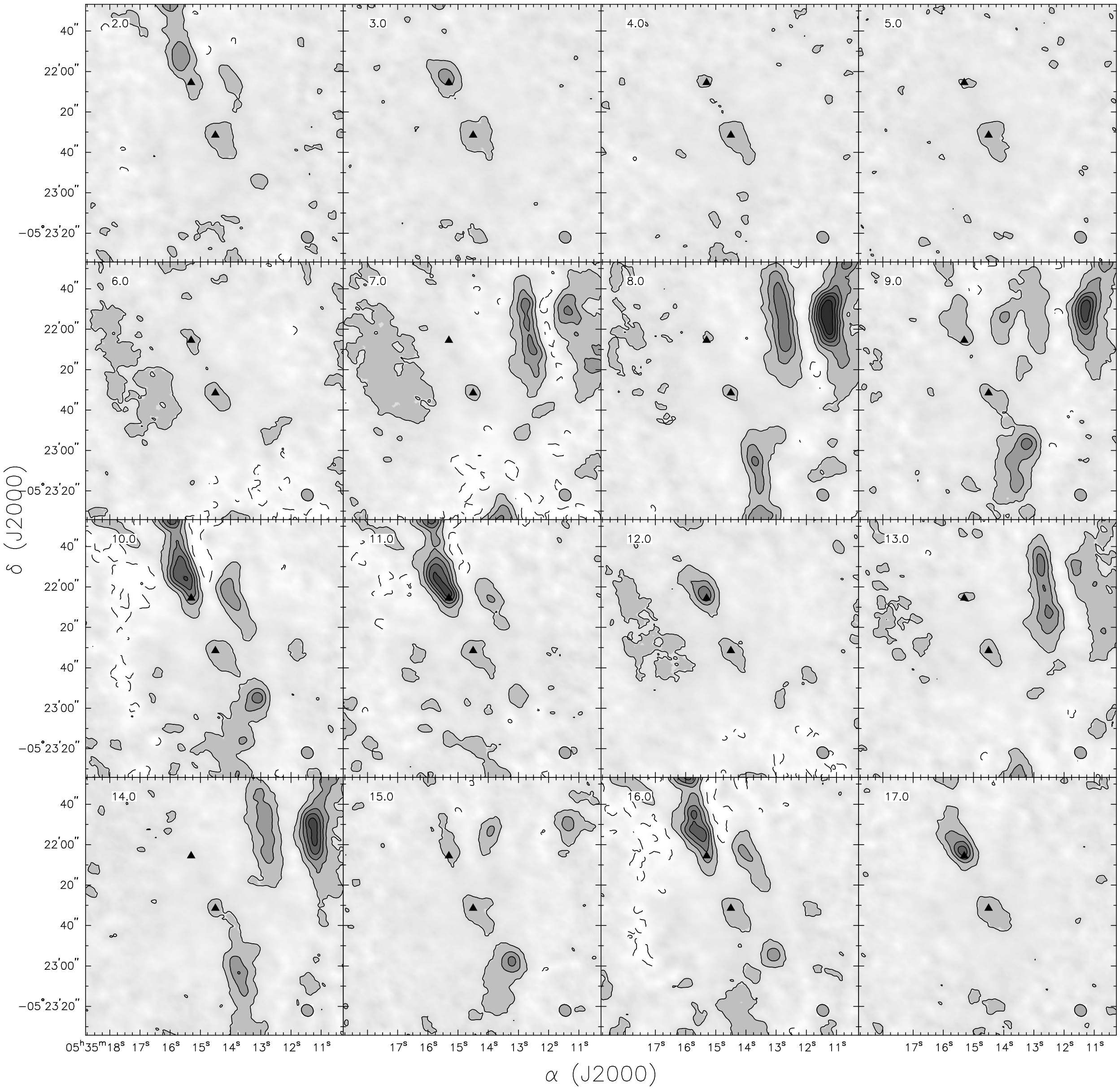

Figure 4.29 OMC1 – N_2H^+ Channel Maps. The contour levels are -10, 5, 20, 35, 50, 65, 80 × 3.45 Jy beam^{-1}. The beam size is $6.19'' \times 5.57''$. The ▲ represent the peaks of the continuum sources.

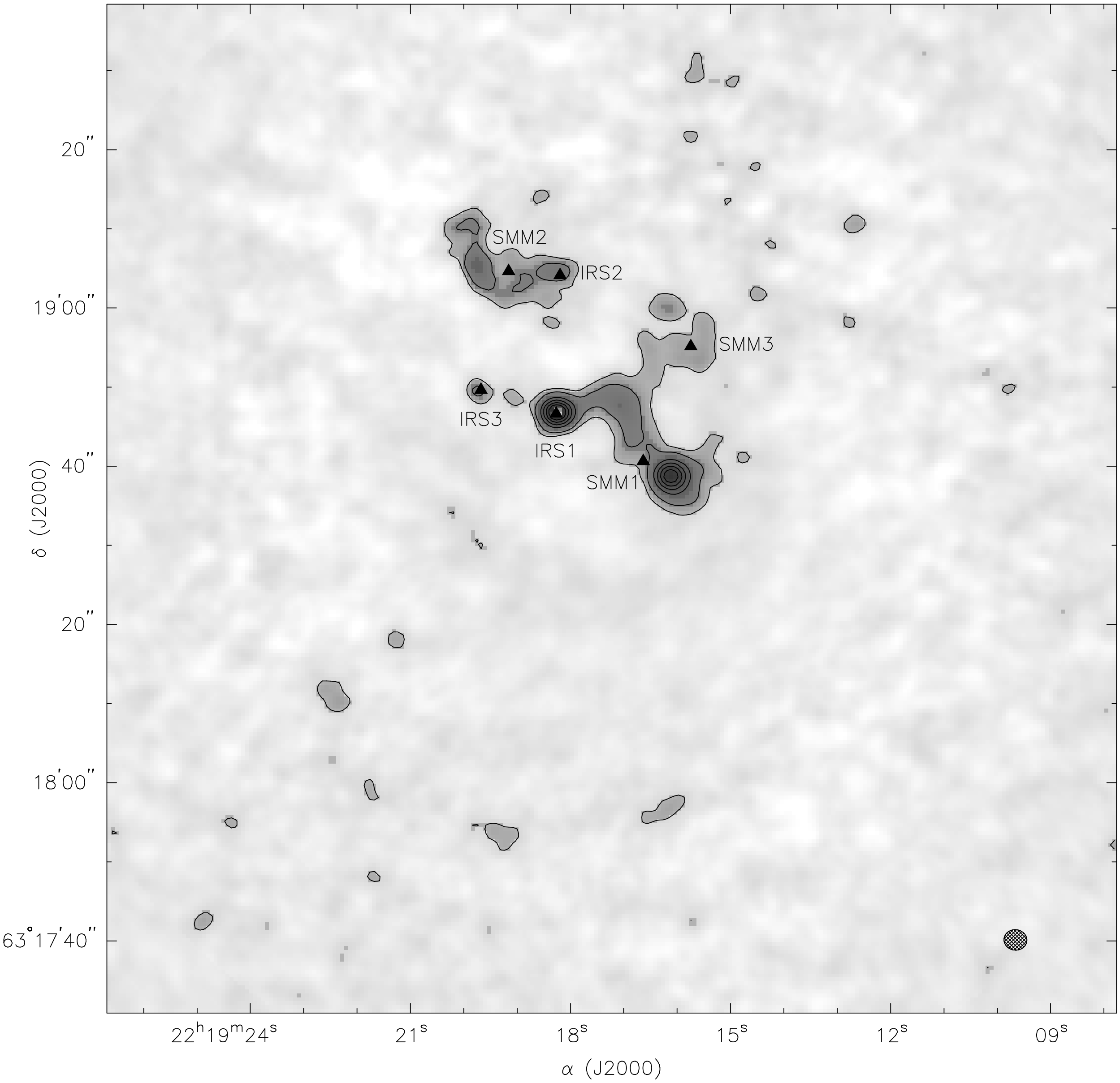

Figure 4.30 112 GHz continuum map of S140. Six continuum objects are observable at a resolution of 2.9″ × 2.6″. The contour levels are 4, 8, 20, 30, 40, 50, 70 × 1 mJy beam^{-1}. IRS1–3 source names from Beichman et al. (1979), SMM1–3 from Minchin et al. (1995).

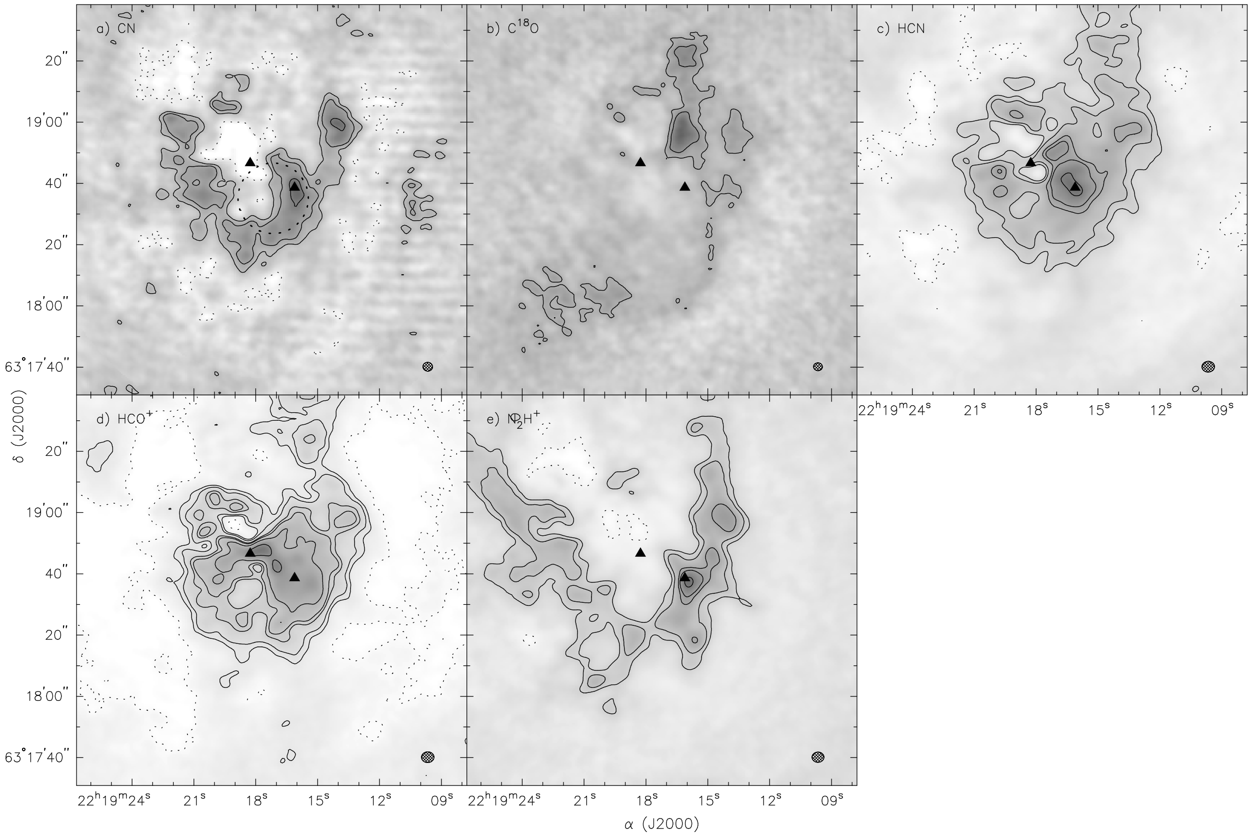

Figure 4.31 CARMA integrated line maps of S140. The contour levels are: 1, 2, 4, 5, 7.5, 13 × 0.09 Jy beam^{-1}. The beam sizes are: a) CN, $3.2'' \times 2.9''$; b) C^{18}O, $2.9'' \times 2.6''$; c) HCN, $4.1'' \times 3.5''$; d) HCO$^+$, $4.1'' \times 3.5''$; e) N$_2$H$^+$, $3.9'' \times 3.4''$.

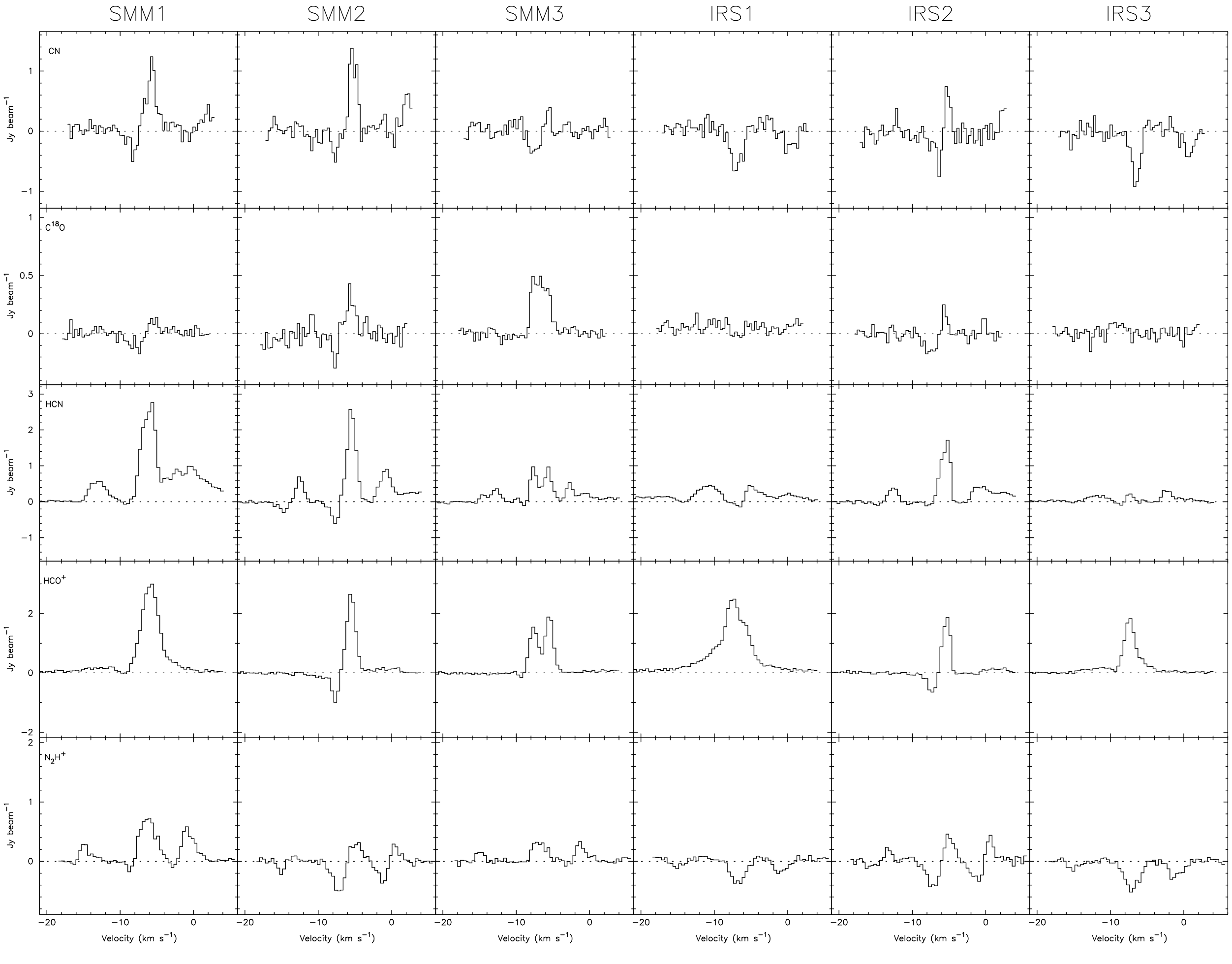

Figure 4.32 Spectra towards the six continuum sources in S140.

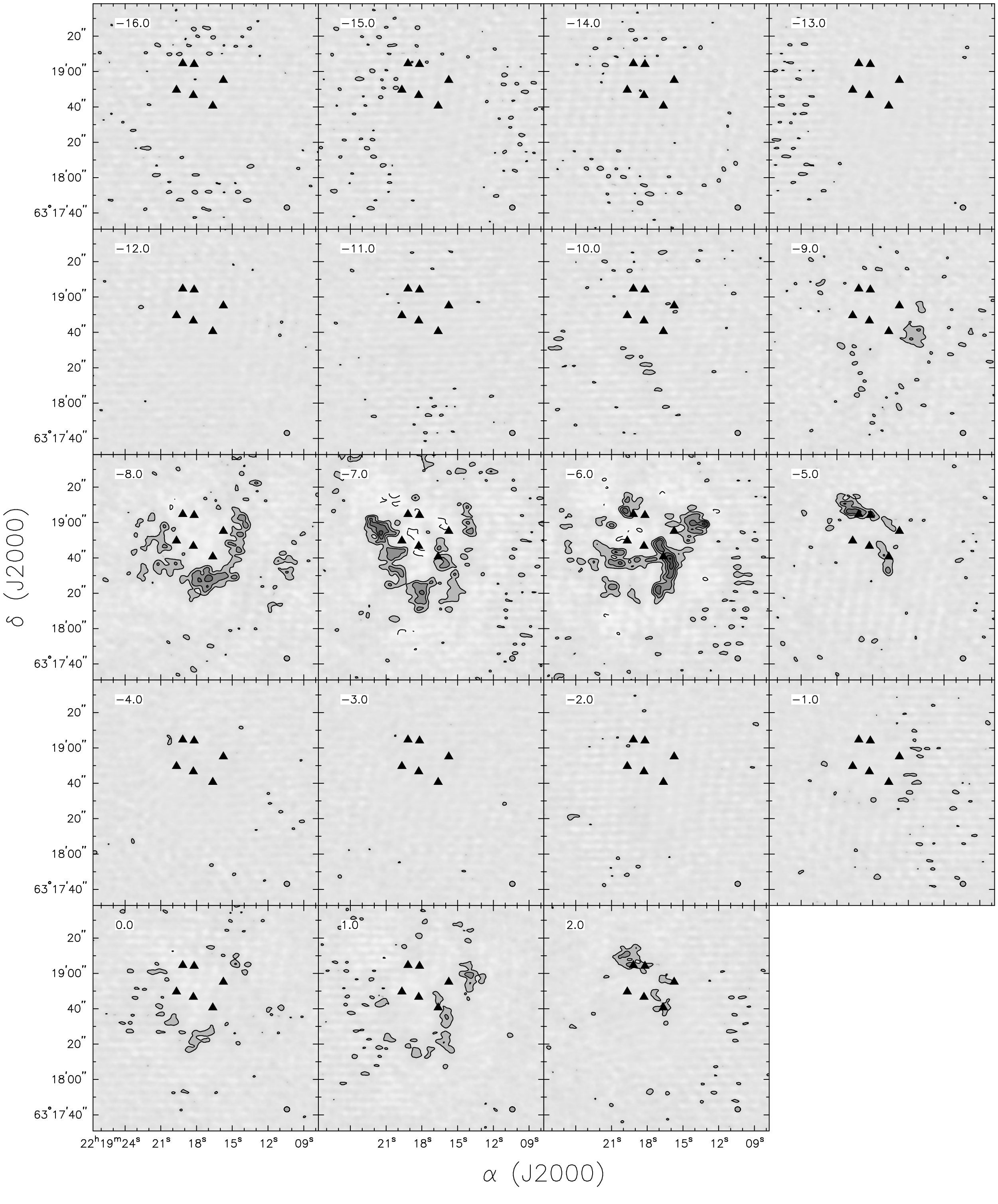

Figure 4.33 S140 – CN Channel Maps. The contour levels are -40, -80, 20, 40, 60, 80, 100 × 1.67 Jy beam^{-1}. The beam size is 3.15″ × 2.89″. The ▲ represent the peaks of the continuum sources.

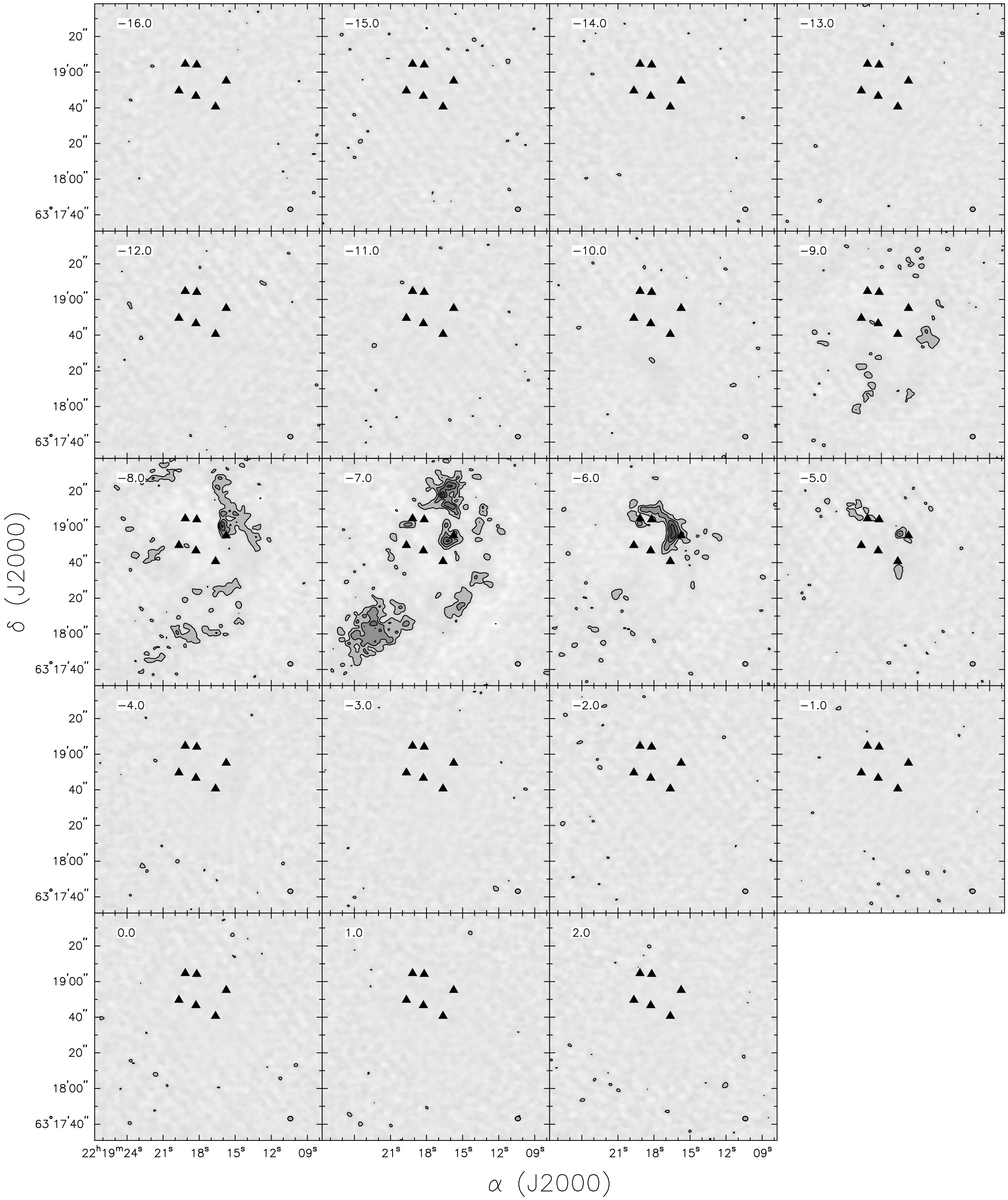

Figure 4.34 S140 – C^{18}O Channel Maps. The contour levels are -40, -80, 20, 40, 60, 80, 100 × 0.985 Jy beam^{-1}. The beam size is 2.90″ × 2.56″. The ▲ represent the peaks of the continuum sources.

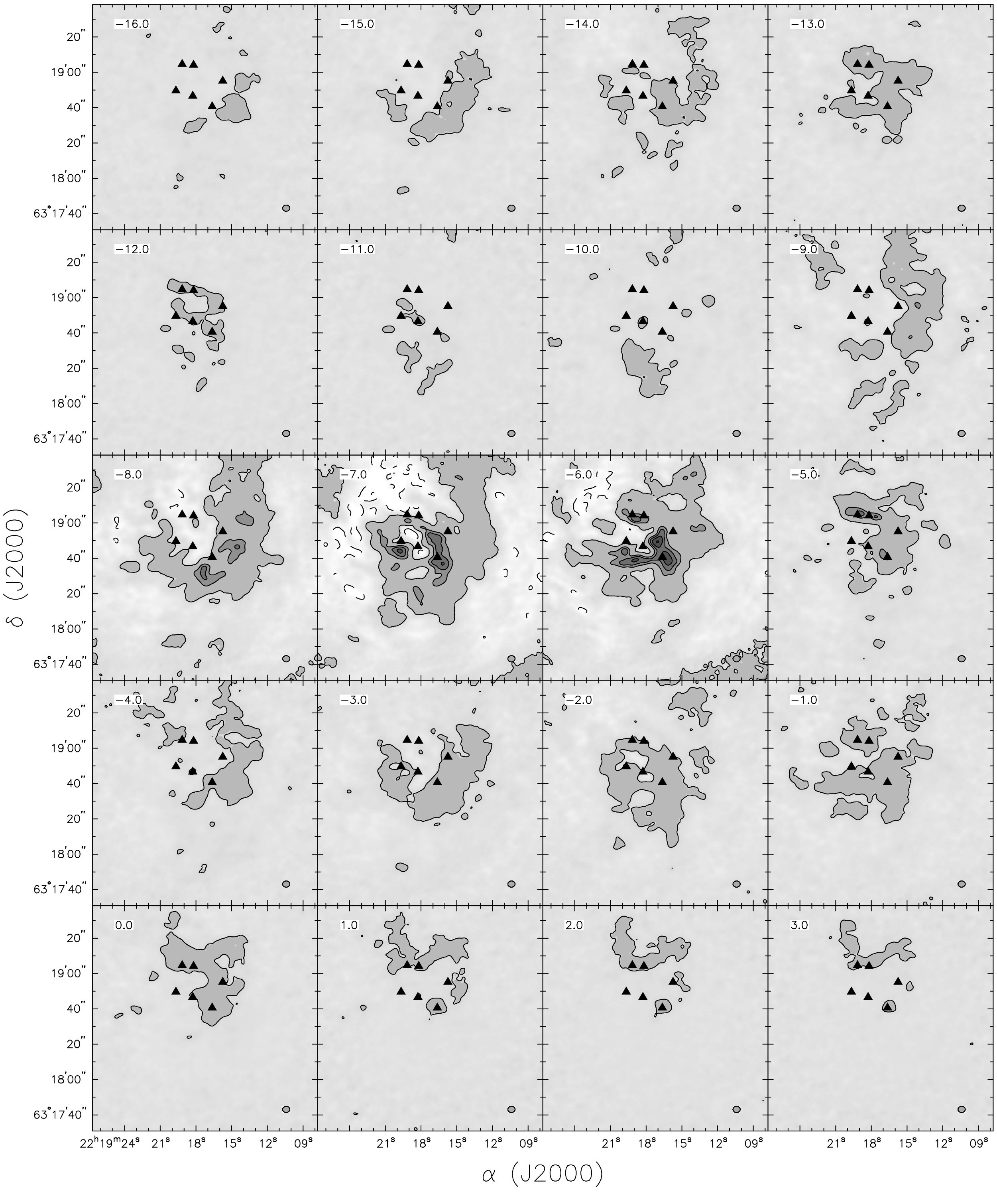

Figure 4.35 S140 – HCN Channel Maps. The contour levels are -20, 5, 40, 60, 80, 100 × 3.24 Jy beam^{-1}. The beam size is 4.10″ × 3.52″. The ▲ represent the peaks of the continuum sources.

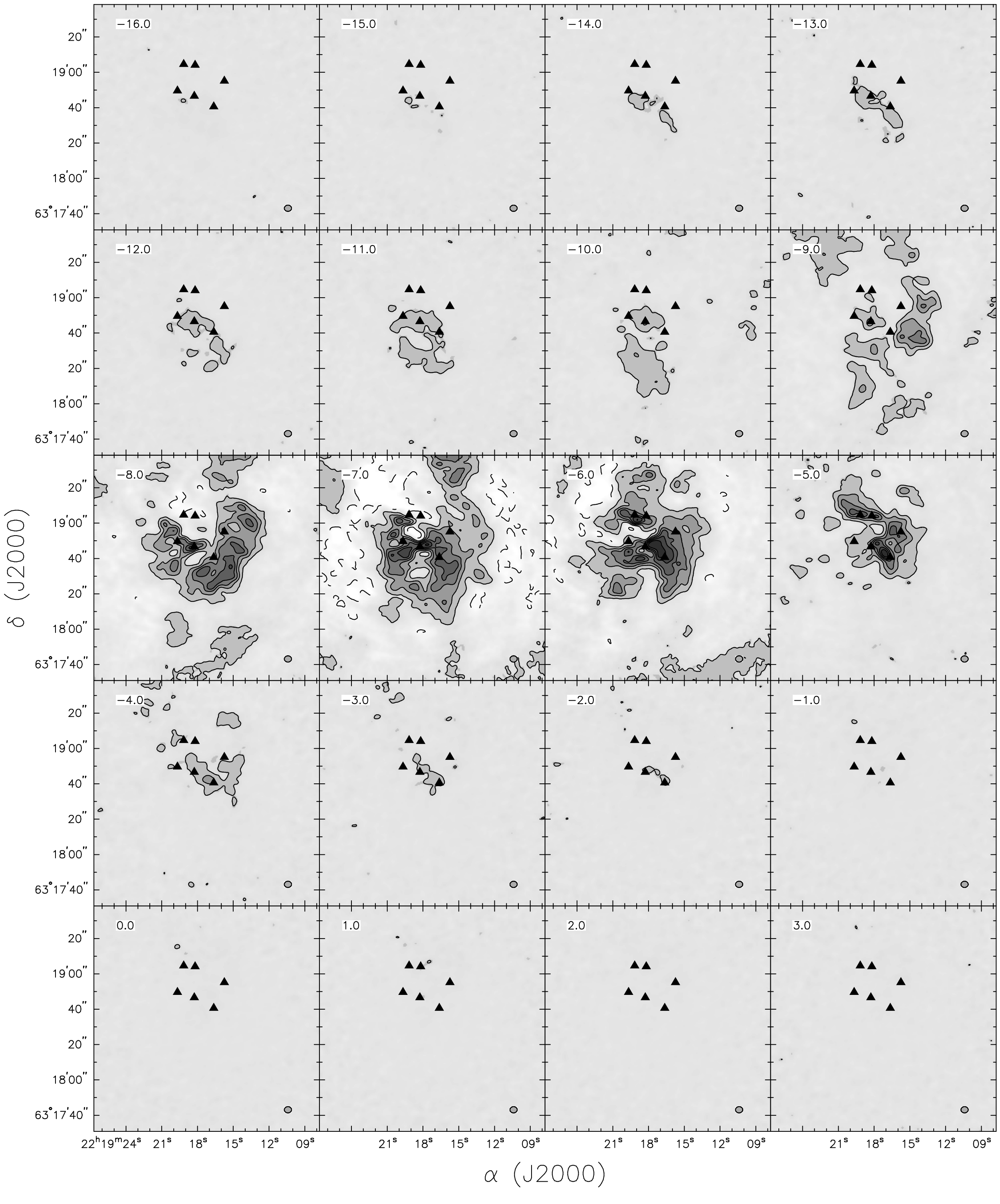

Figure 4.36 S140 – HCO$^+$ Channel Maps. The contour levels are -20, 5, 20, 35, 50, 65, 80 × 3.71 Jy beam^{-1}. The beam size is $4.09'' \times 3.52''$. The ▲ represent the peaks of the continuum sources.

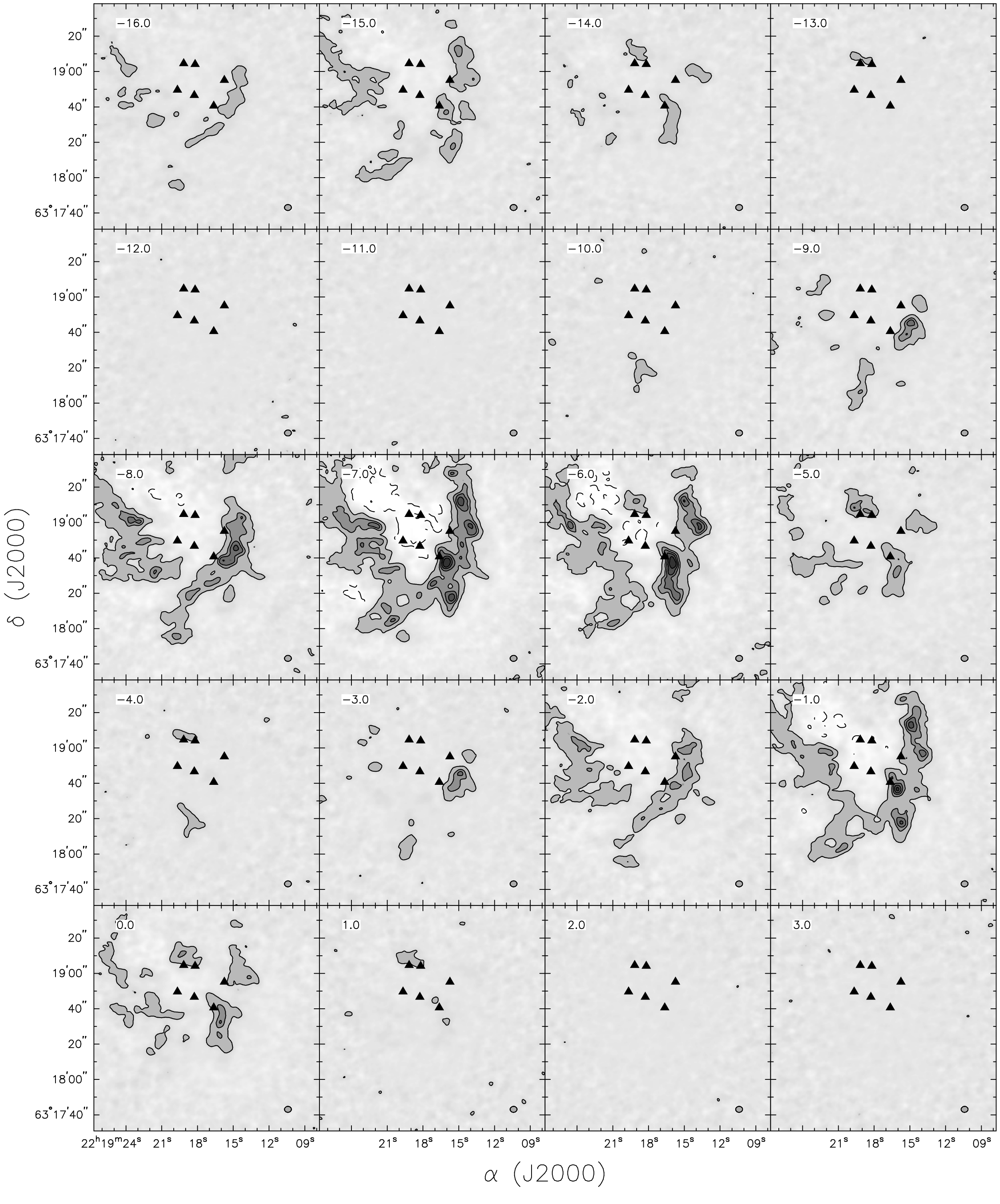

Figure 4.37 S140 – N_2H^+ Channel Maps. The contour levels are -20, 10, 35, 50, 65, 80 × 1.95 Jy beam^{-1}. The beam size is $3.90'' \times 3.36''$. The ▲ represent the peaks of the continuum sources.

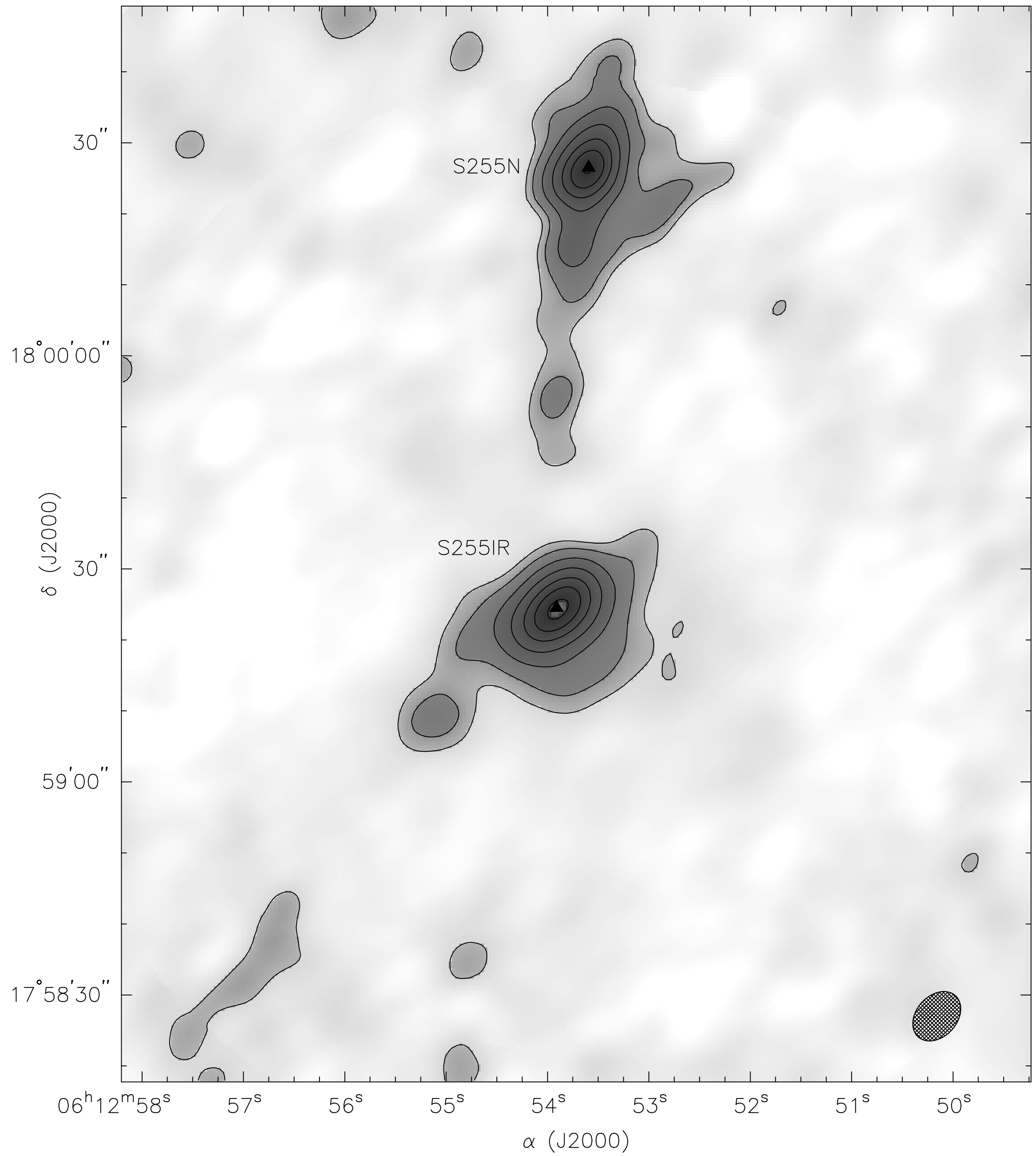

Figure 4.38 112 GHz continuum map of S255. Two continuum objects are observable at a resolution of 7.8″ × 5.7″. The contour levels are 4, 6.5, 12, 20, 30, 40, 50 × 1.5 mJy beam^{-1}.

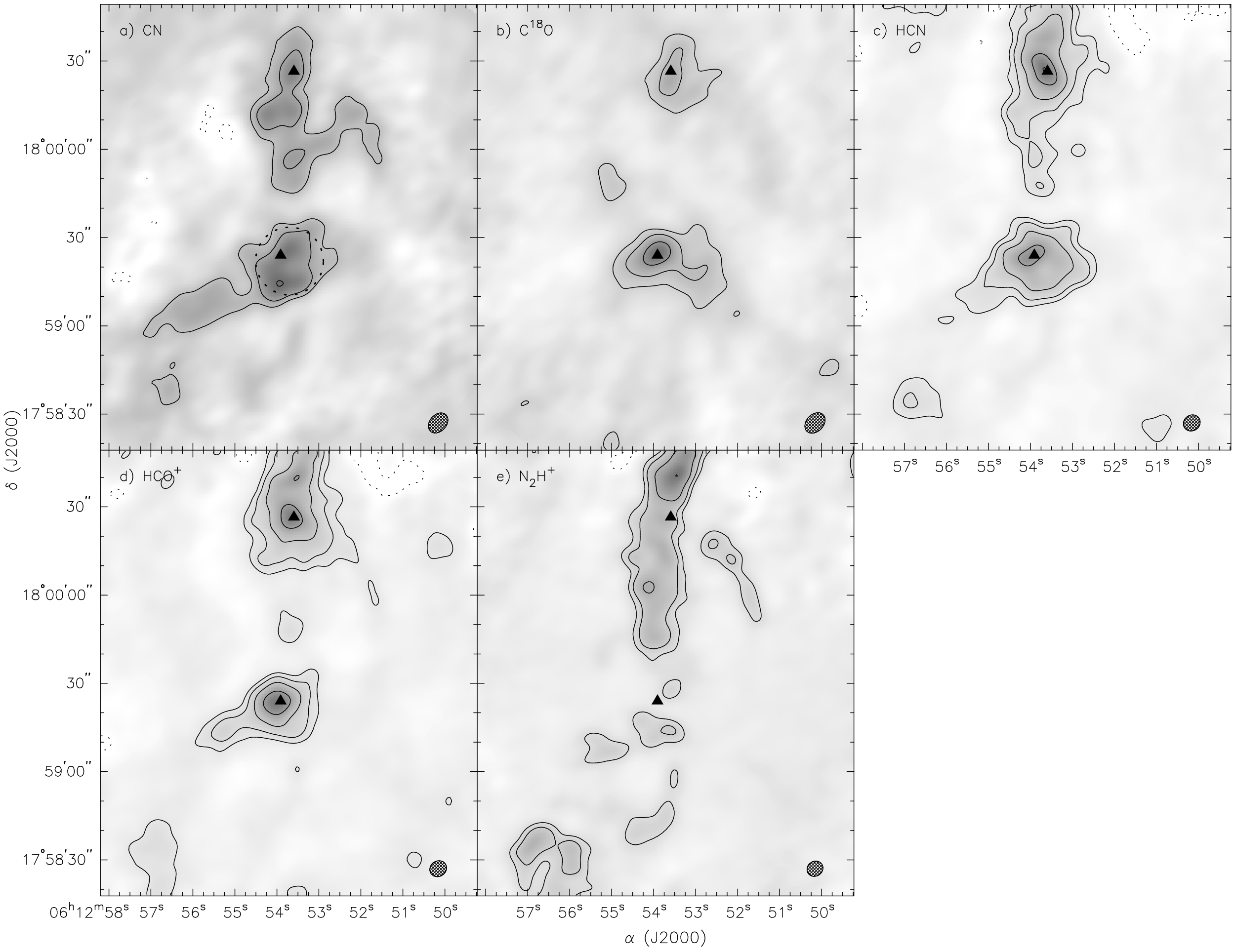

Figure 4.39 CARMA integrated line maps of S255. The contour levels are: 1, 2, 4, 8, 12 × 0.15 Jy beam^{-1}. The beam sizes are: a) CN, 7.7″ × 5.6″; b) C^{18}O, 7.9″ × 5.8″; c) HCN, 5.9″ × 5.3″; d) HCO$^+$, 5.9″ × 5.2″; e) N$_2$H$^+$, 5.6″ × 5.0″.

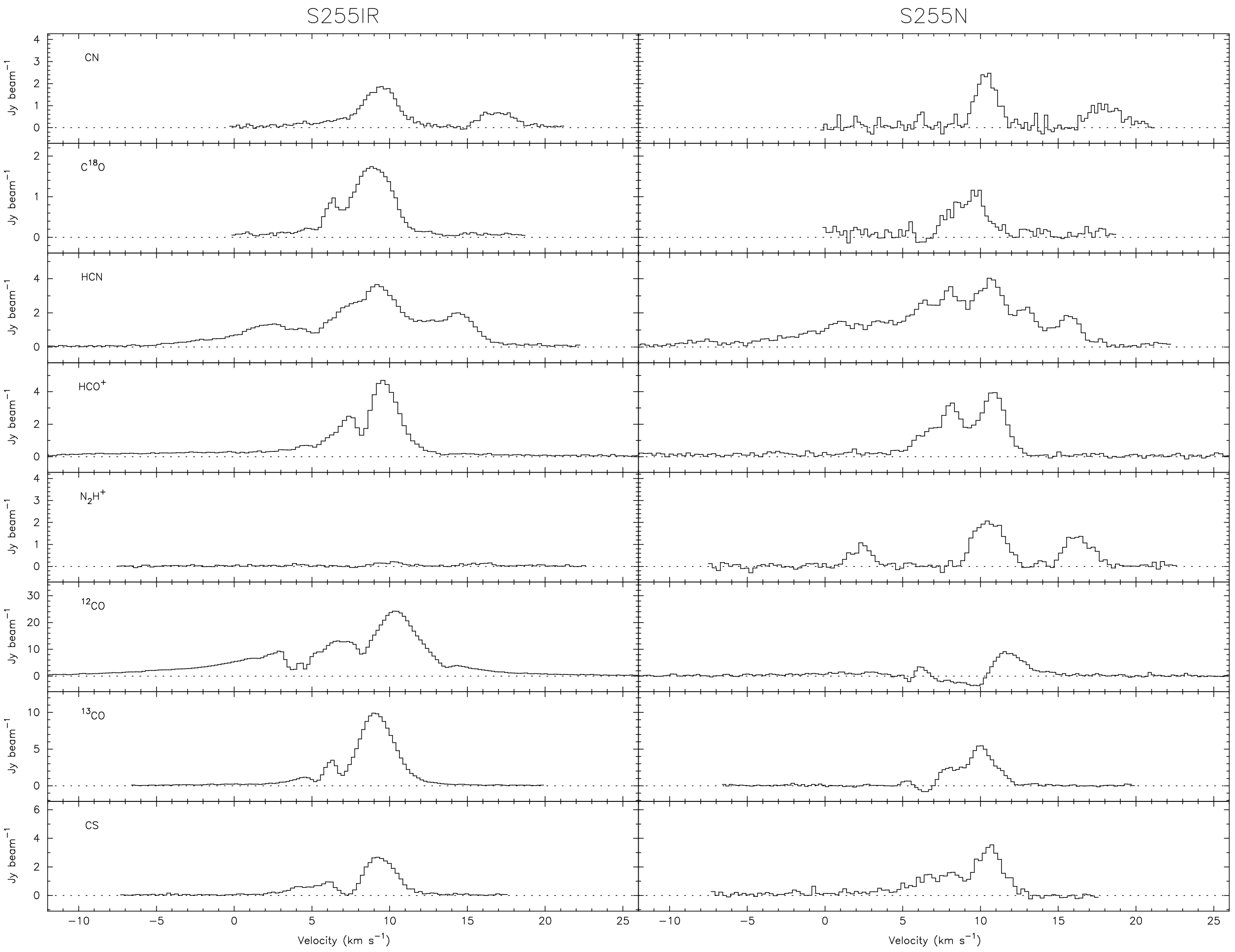

Figure 4.40 Spectra towards the two continuum sources in S255. This source is the only source in the CARMA dataset that has ^{12}CO, ^{13}CO, and CS observations in addition to the five other species. The signal-to-noise ratio of the spectra towards S255N is much smaller than that towards S255IR since the source lies near the edge of the primary beam of CARMA's 10-m dishes. The noise level is about 4.5 times greater at this edge position than the map center.

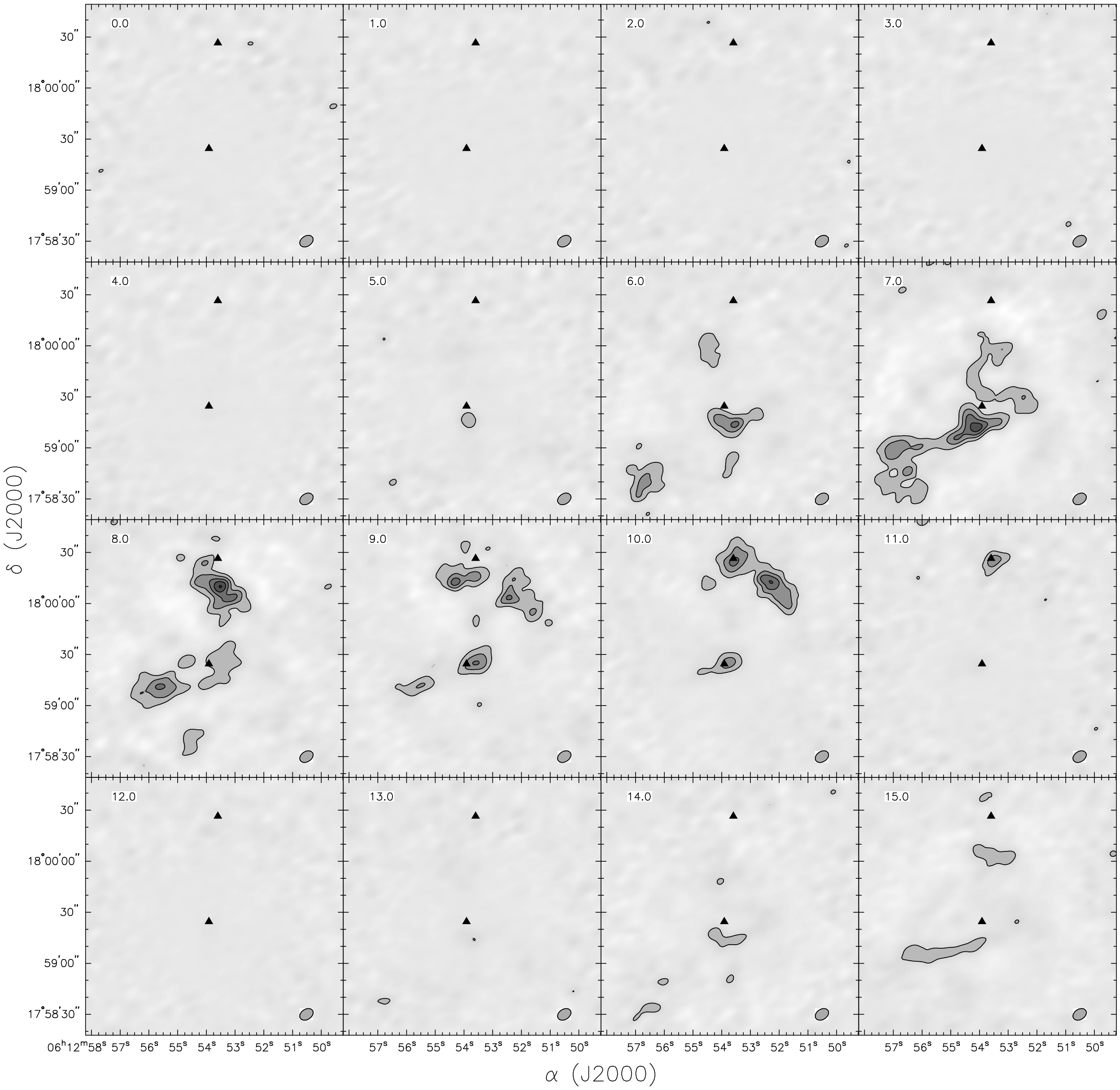

Figure 4.41 S255 – CN Channel Maps. The contour levels are -80, -40, 20, 40, 60, 80, 100 × 3.57 Jy beam^{-1}. The beam size is 7.66″ × 5.63″. The ▲ represent the peaks of the continuum sources.

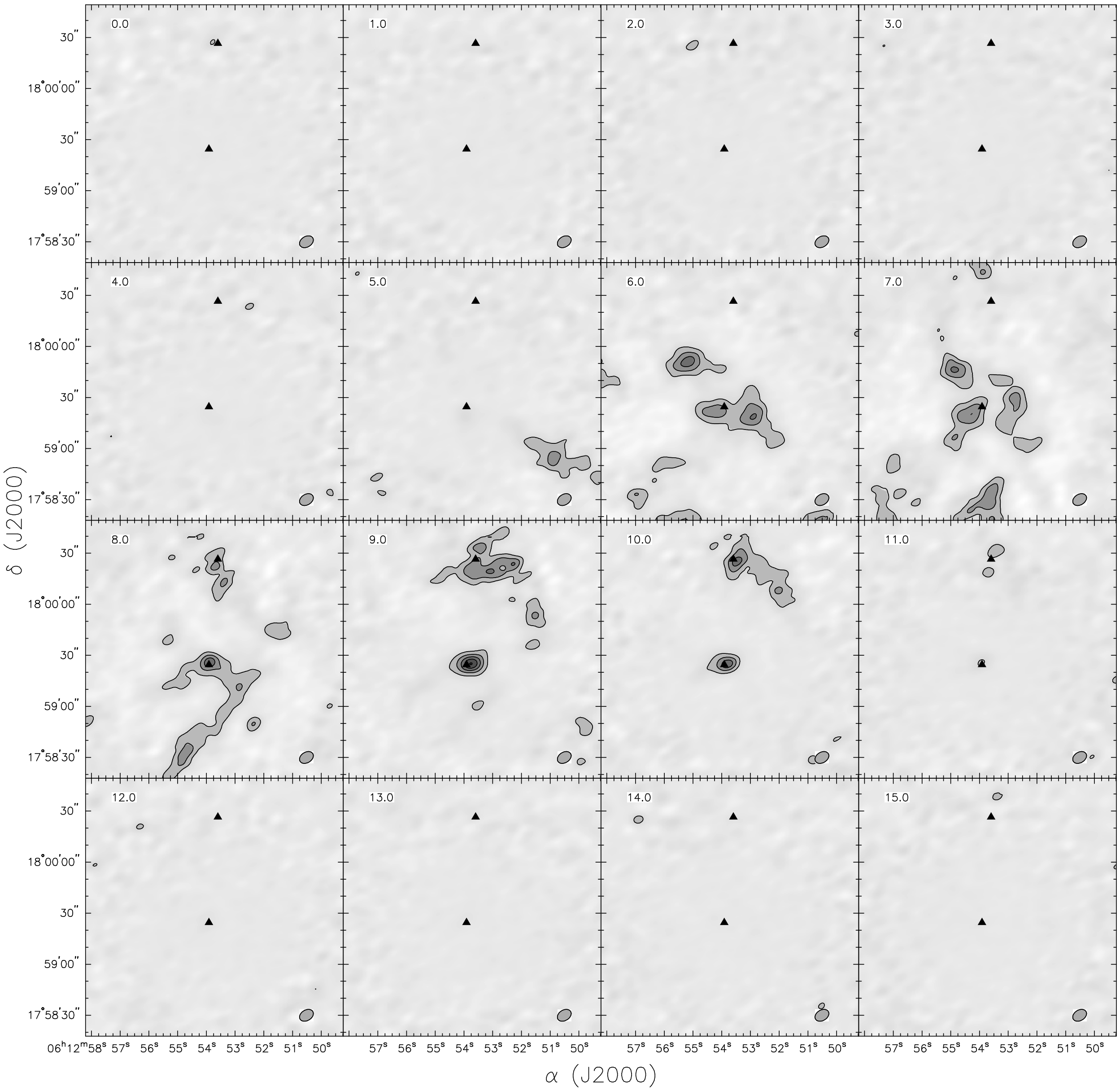

Figure 4.42 S255 – $C^{18}O$ Channel Maps. The contour levels are -80, -40, 20, 40, 60, 80, 100 × 1.92 Jy beam^{-1}. The beam size is $7.87'' \times 5.79''$. The ▲ represent the peaks of the continuum sources.

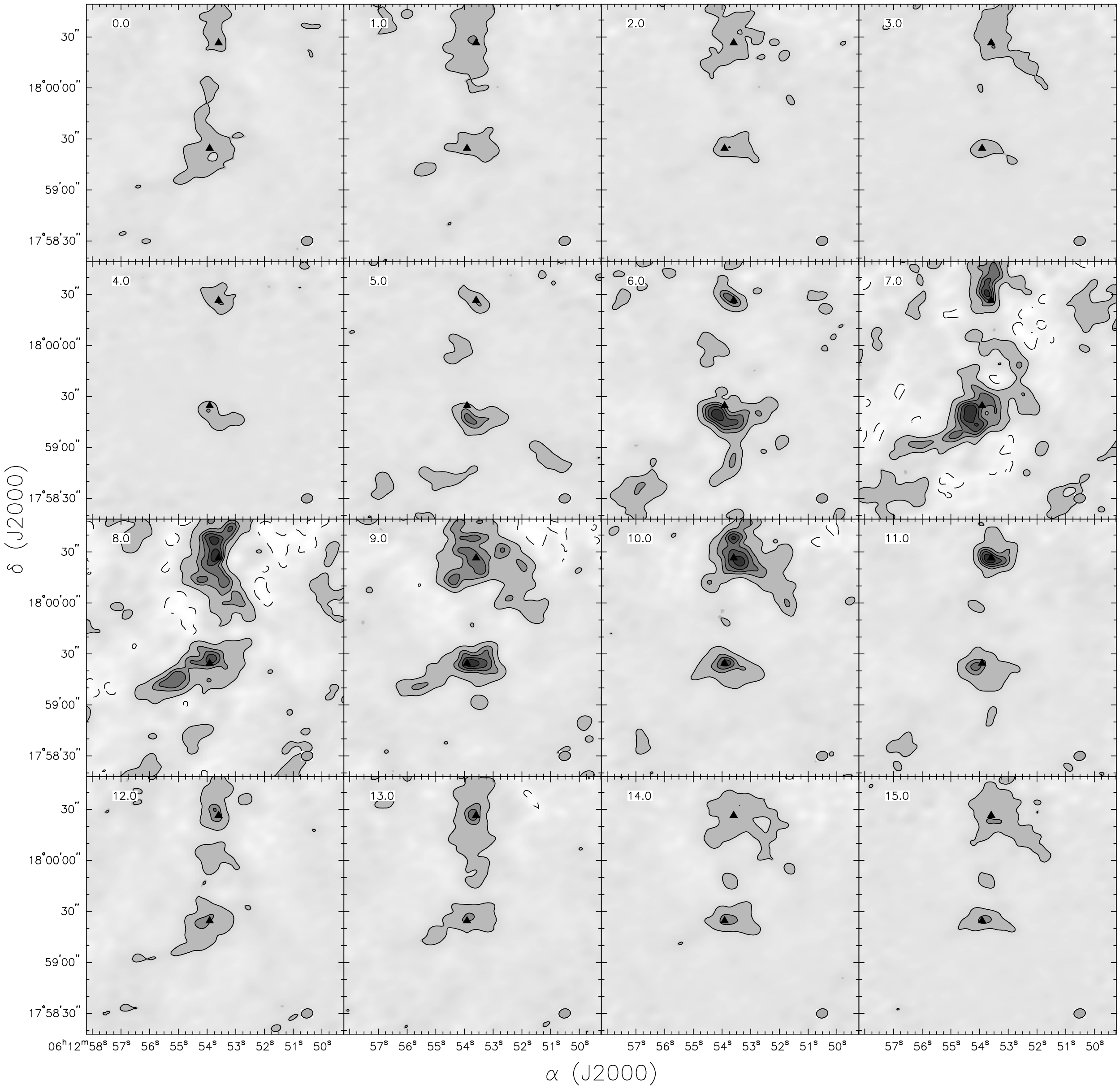

Figure 4.43 S255 – HCN Channel Maps. The contour levels are -20, 10, 35, 50, 65, 80 × 4.16 Jy beam^{-1}. The beam size is 5.88″ × 5.29″. The ▲ represent the peaks of the continuum sources.

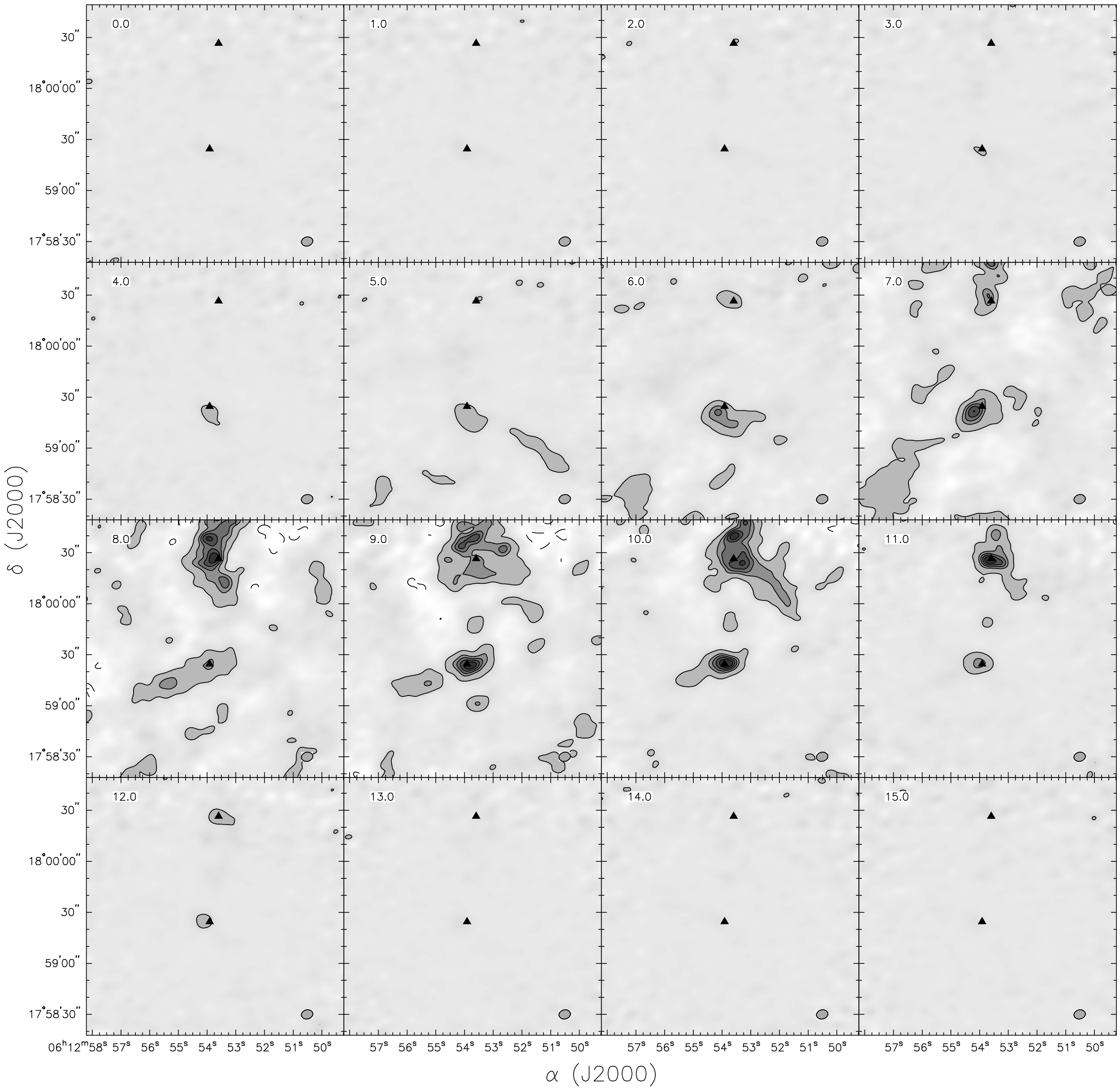

Figure 4.44 S255 – HCO^+ Channel Maps. The contour levels are -20, 10, 35, 50, 65, 80 × 4.29 Jy $beam^{-1}$. The beam size is $5.86'' \times 5.23''$. The ▲ represent the peaks of the continuum sources.

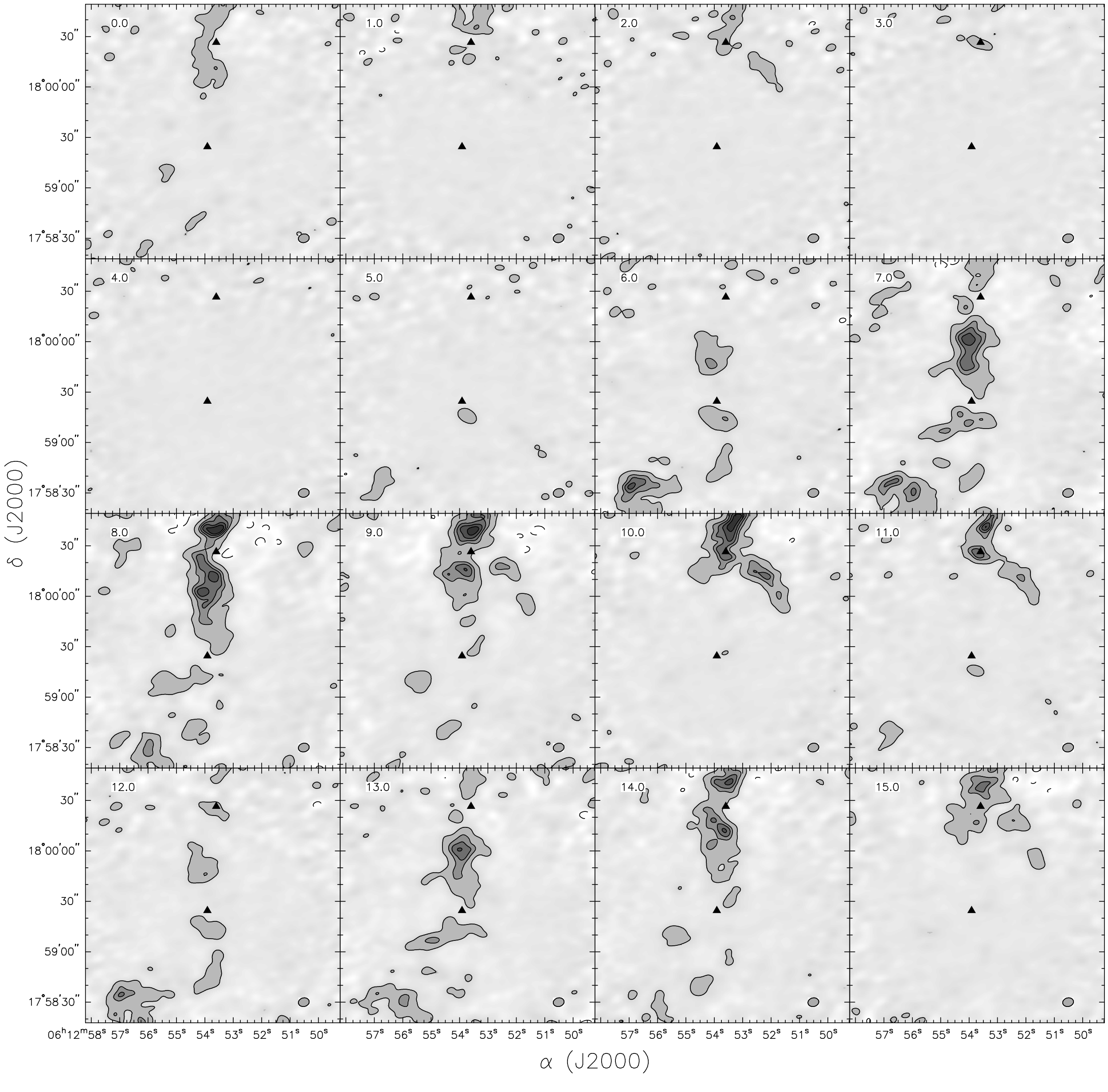

Figure 4.45 S255 – N_2H^+ Channel Maps. The contour levels are -20, 10, 35, 50, 65, 80 × 3.28 Jy beam^{-1}. The beam size is $5.60'' \times 5.00''$. The ▲ represent the peaks of the continuum sources.

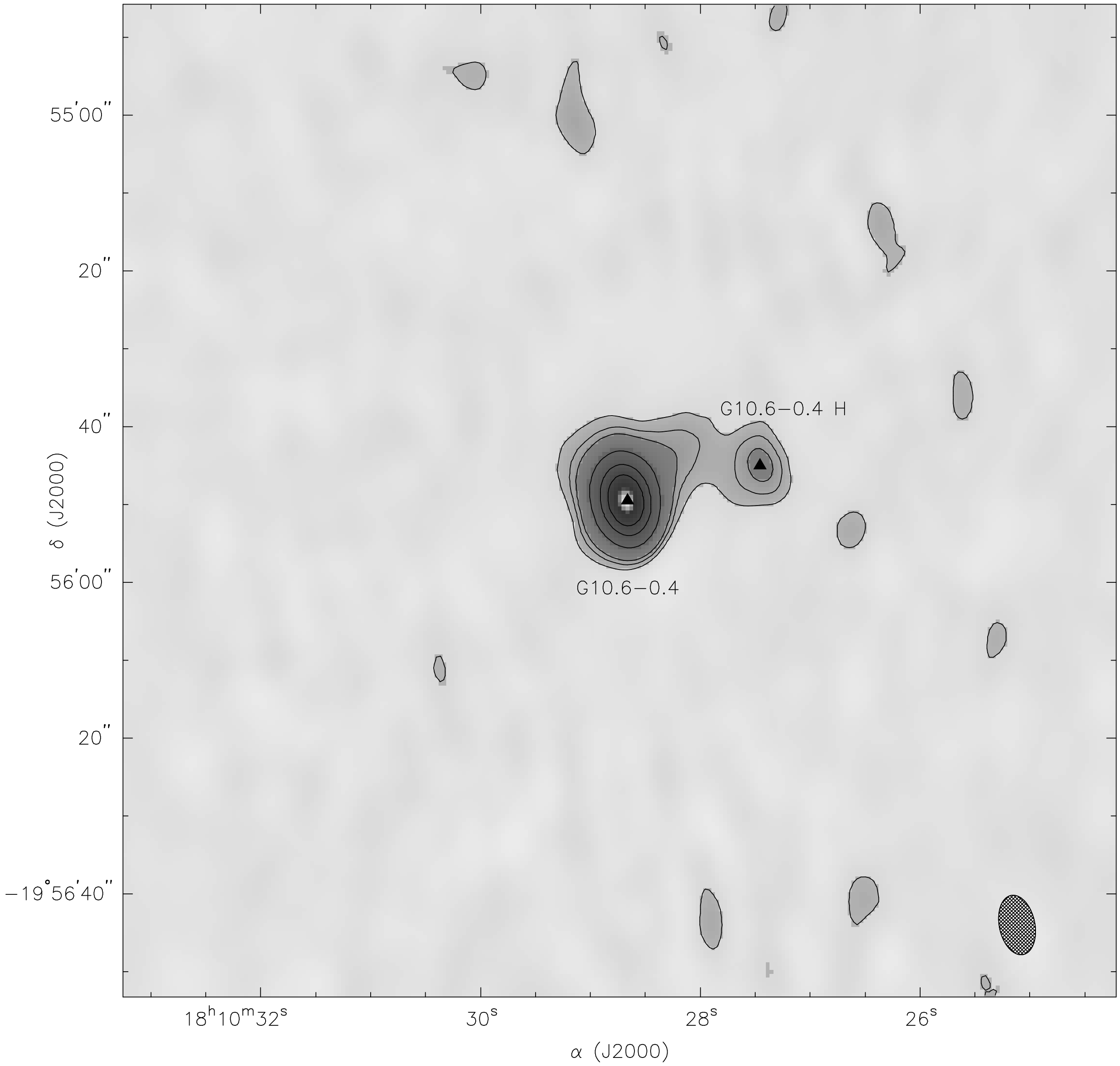

Figure 4.46 112 GHz continuum map of G10.6. Two continuum objects are observable at a resolution of 7.7″ × 4.6″. The contour levels are 6.6, 12, 18, 50, 100, 150 × 15 mJy beam^{-1}.

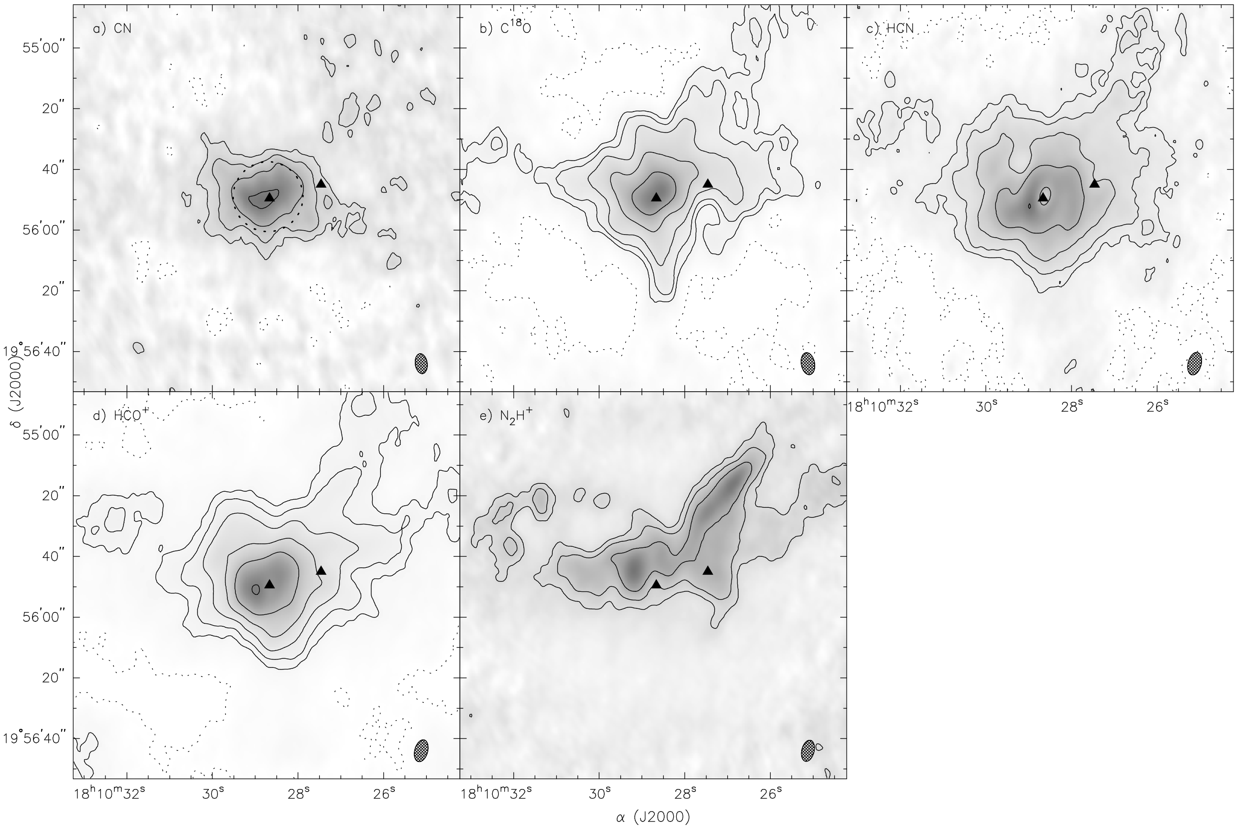

Figure 4.47 CARMA integrated and continuum subtracted line maps of G10.6. The contour levels are: 1, 2, 4, 8, 16, 32 × 0.15 Jy beam^{-1}. The beam sizes are: a) CN, 6.6″ × 3.9″; b) C^{18}O, 7.3″ × 4.4″; c) HCN, 7.6″ × 4.3″; d) HCO$^+$, 7.4″ × 4.3″; e) N$_2$H$^+$, 7.1″ × 4.1″.

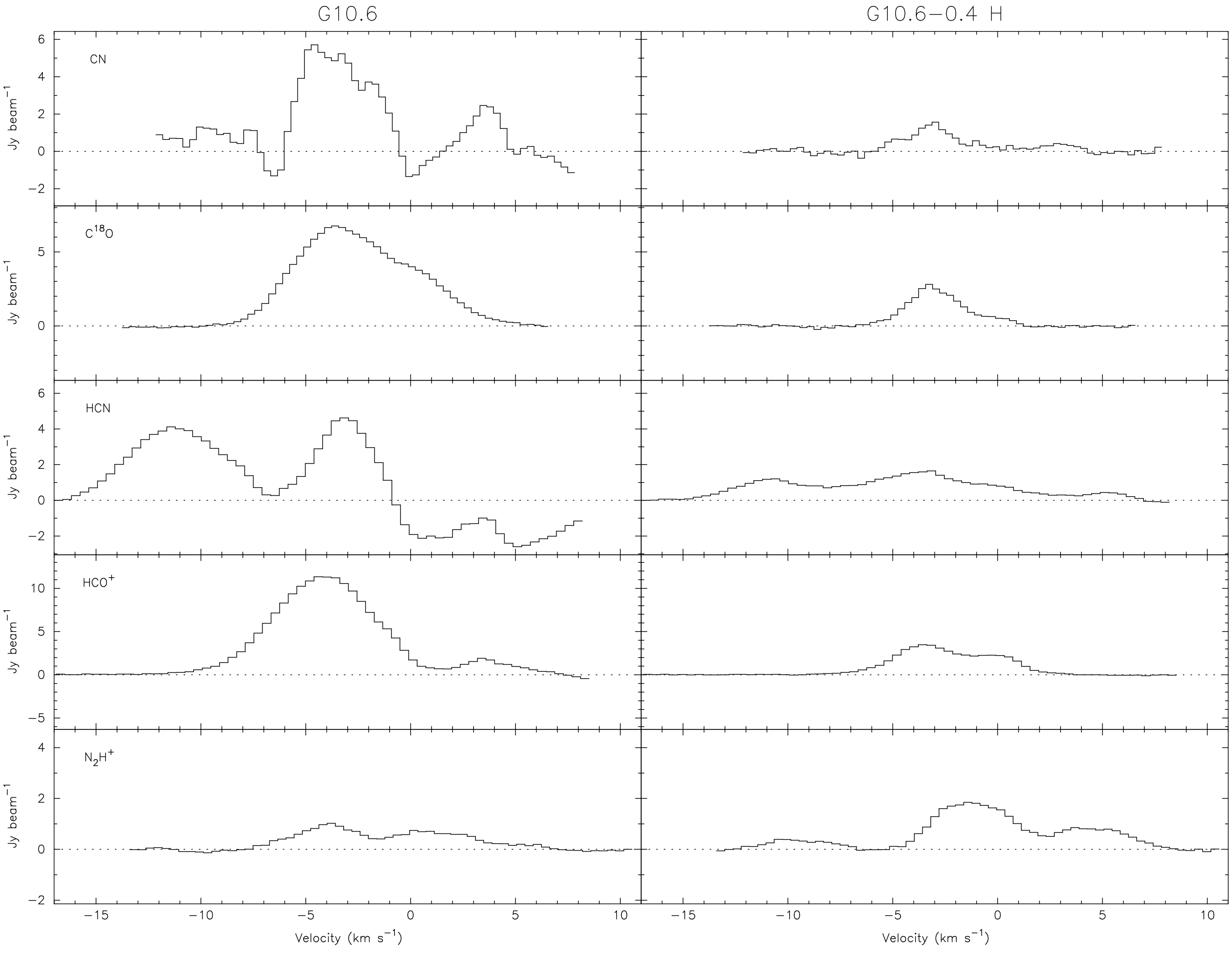

Figure 4.48 Continuum subtracted spectra towards the two continuum sources in G10.6.

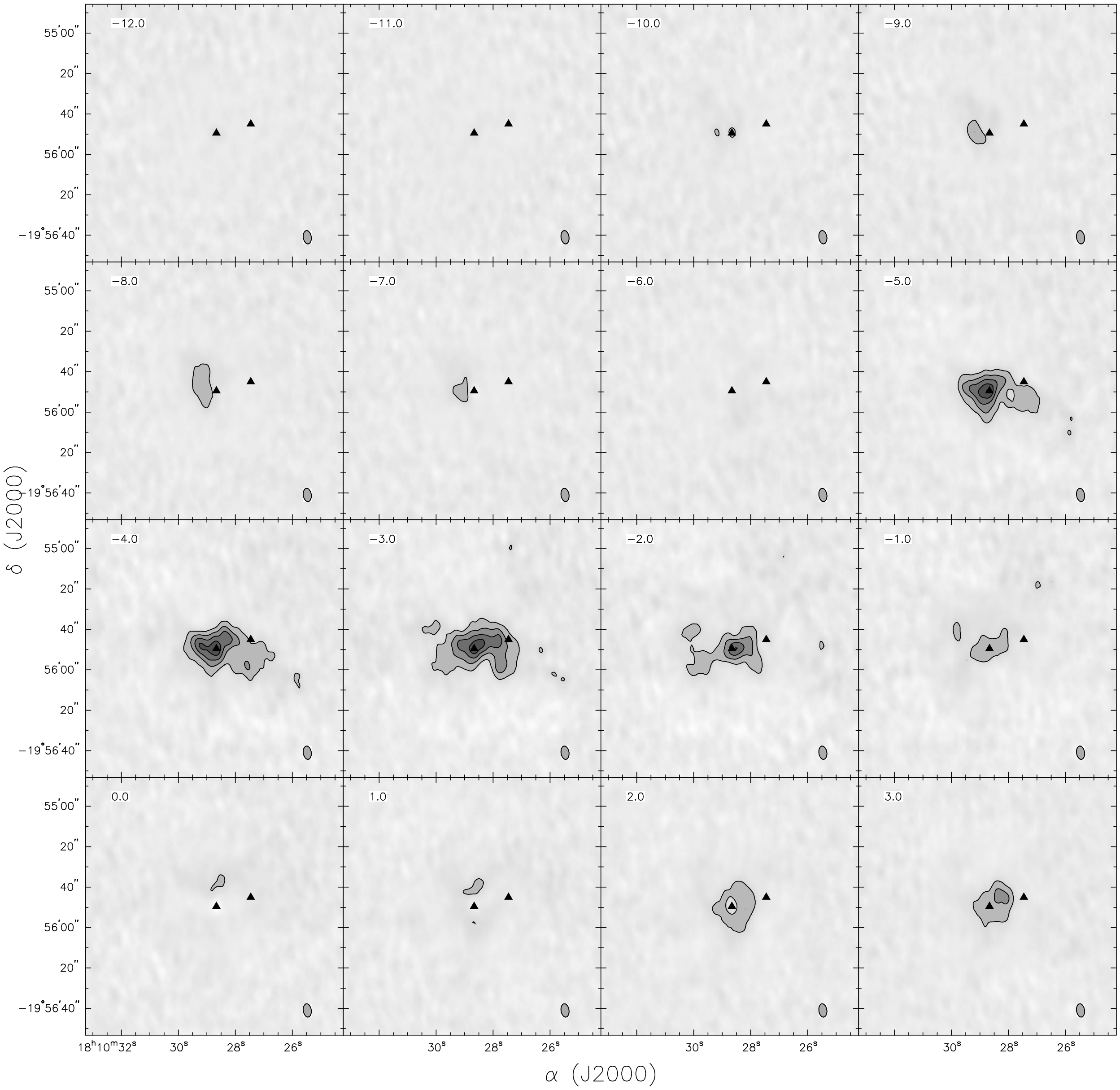

Figure 4.49 G10.6 – CN Channel Maps. The contour levels are -80, -40, 20, 40, 60, 80, 100 × 5.16 Jy beam^{-1}. The beam size is $6.61'' \times 3.95''$. The ▲ represent the peaks of the continuum sources.

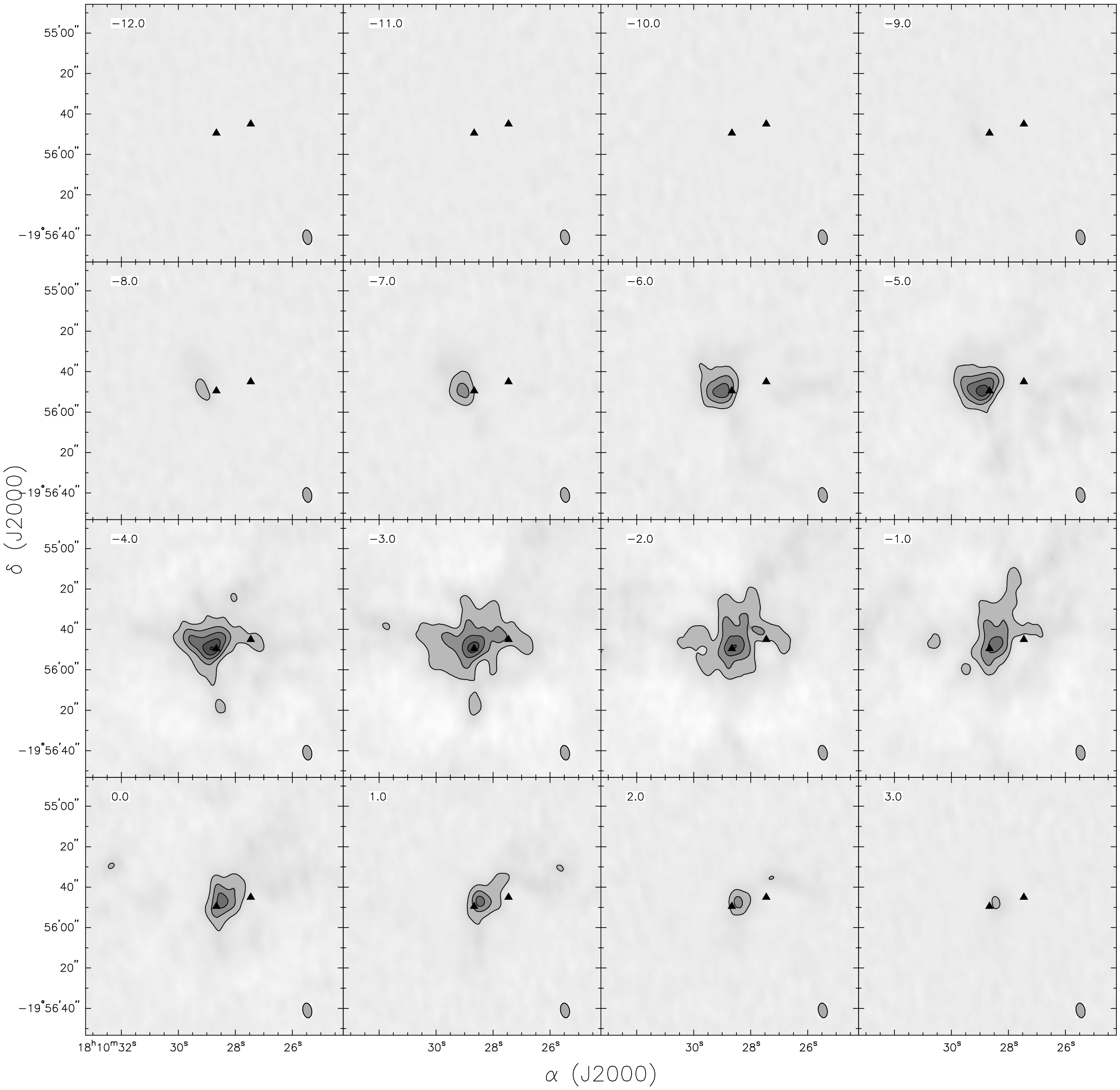

Figure 4.50 G10.6 – C^{18}O Channel Maps. The contour levels are -80, -40 20, 40, 60, 80, 100 × 7.26 Jy beam^{-1}. The beam size is $7.32'' \times 4.41''$. The ▲ represent the peaks of the continuum sources.

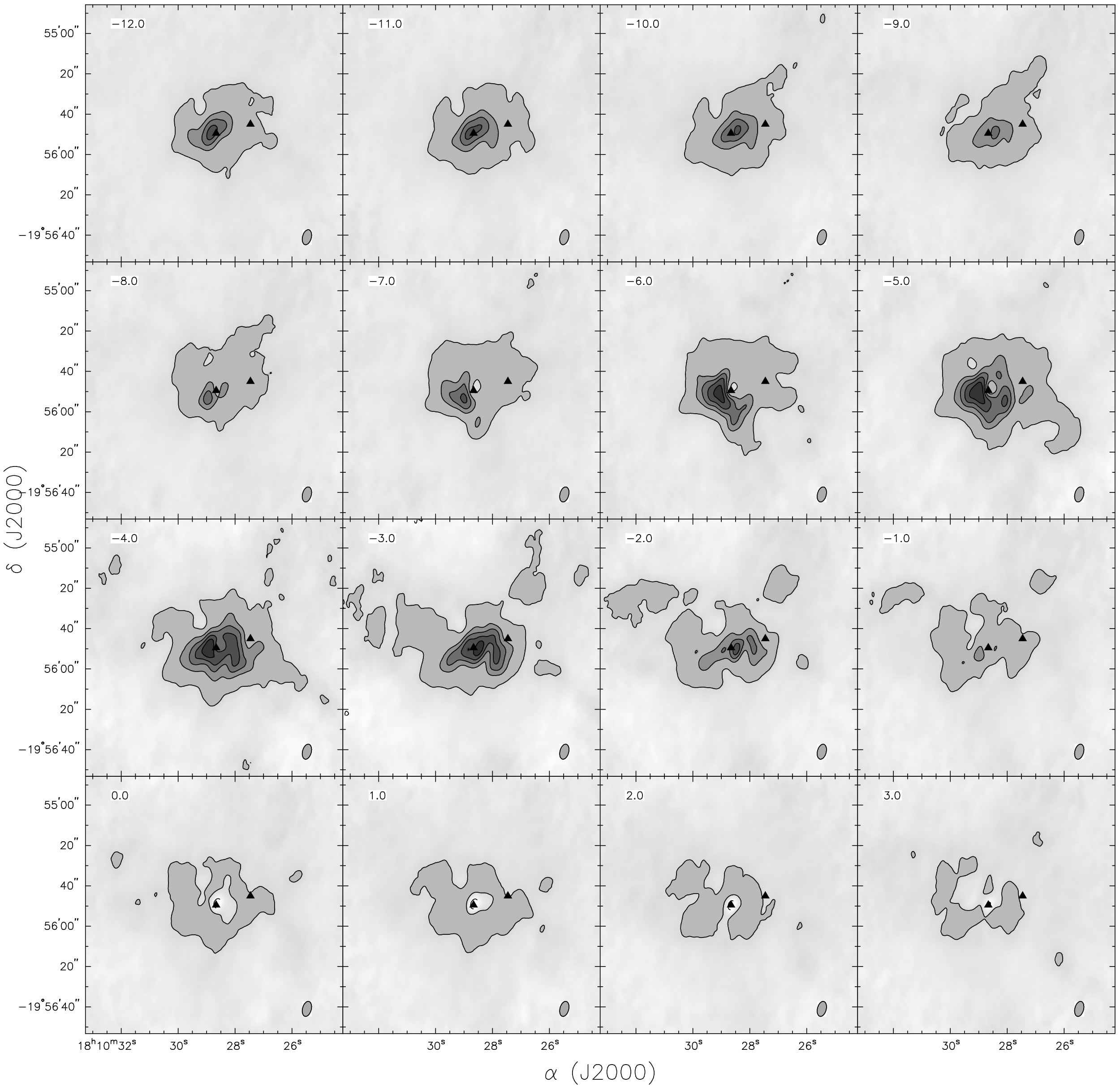

Figure 4.51 G10.6 – HCN Channel Maps. The contour levels are -20, 10, 35, 50, 65, 80 × 5.95 Jy beam^{-1}. The beam size is 7.60″ × 4.33″. The ▲ represent the peaks of the continuum sources.

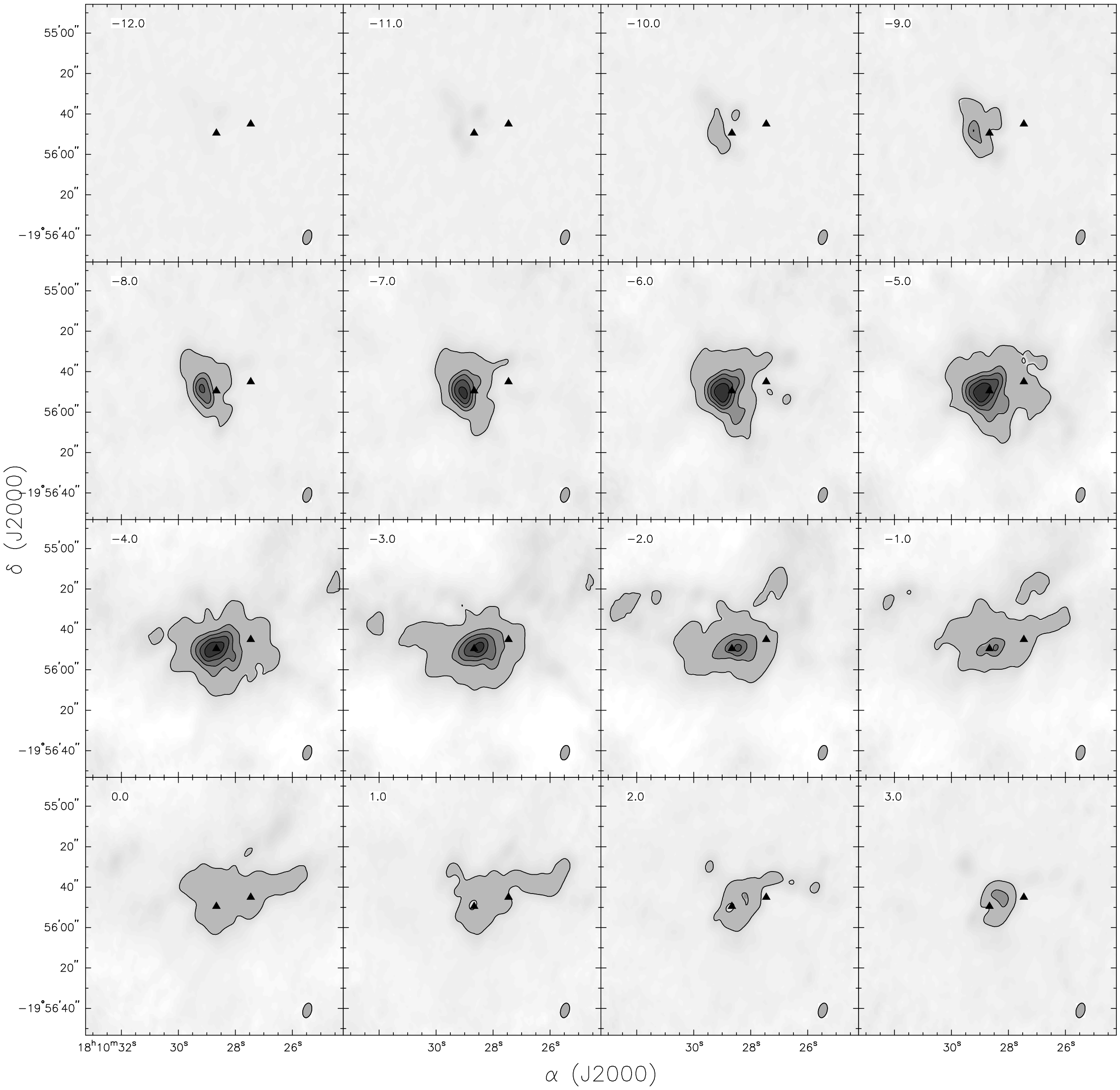

Figure 4.52 G10.6 – HCO$^+$ Channel Maps. The contour levels are -20, 10, 35, 50, 65, 80 × 12.6 Jy beam^{-1}. The beam size is $7.40'' \times 4.27''$. The ▲ represent the peaks of the continuum sources.

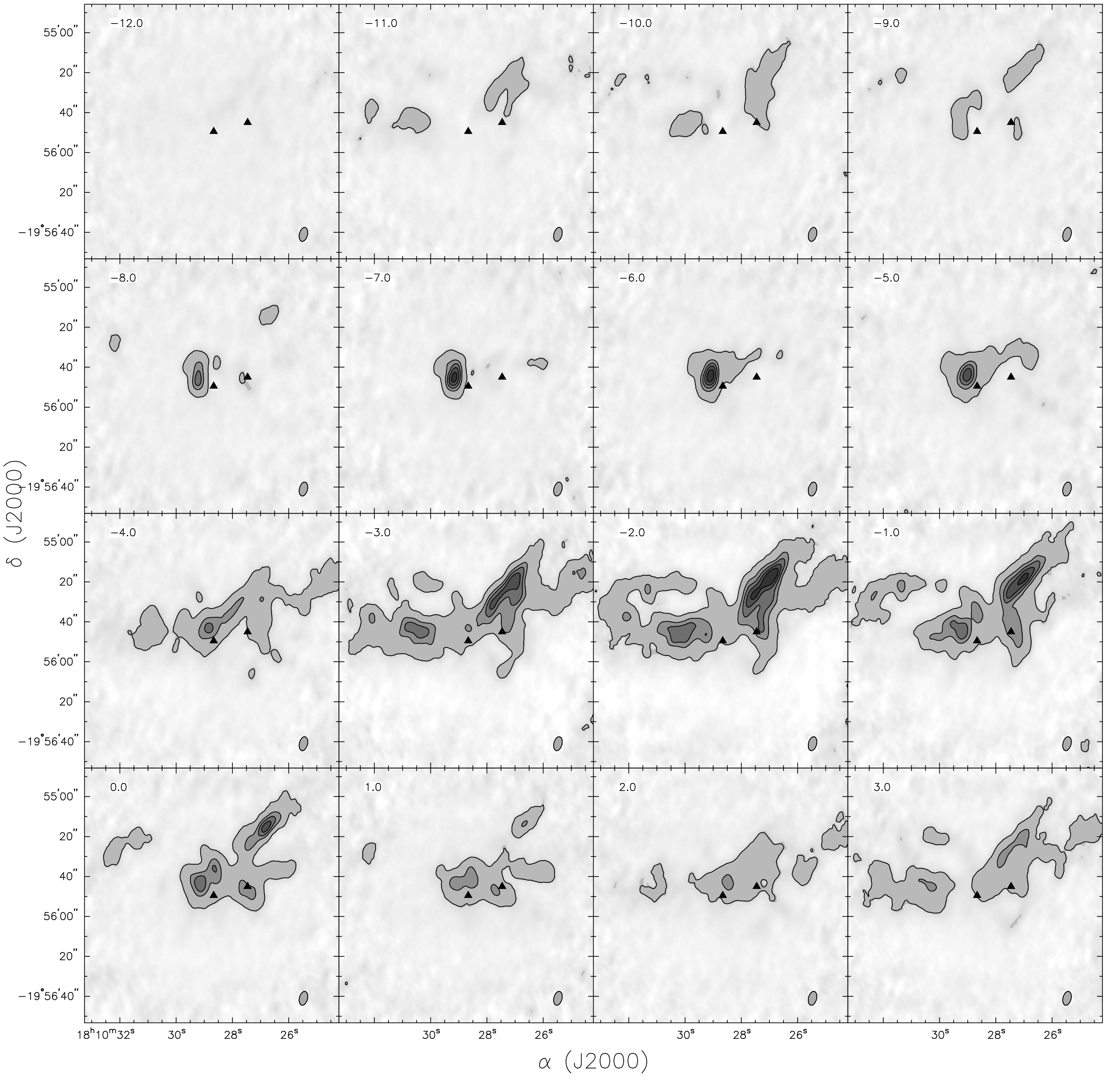

Figure 4.53 G10.6 – N_2H^+ Channel Maps. The contour levels are -20, 10, 35, 50, 65, 80 × 4.19 Jy beam^{-1}. The beam size is $7.11'' \times 4.06''$. The ▲ represent the peaks of the continuum sources.

Chapter 5

Structure and Composition of Molecular Clouds with CN Zeeman Detections II: Discussion*

For the purposes of comparison, a discussion of W3(OH) will be presented followed by a discussion comparing and contrasting the W3(OH) observations with those of DR21(OH), OMC1, S140, S255, and G10.6.

5.1 W3(OH) Discussion

5.1.1 W3(OH) Absorption Feature

As stated above, W3(OH) itself is a UCHII region with an embedded O7 star. Our data show that several of the molecular tracers we have observed can be seen in absorption towards this source. The nature and structure of this colder absorbing gas may be able to give us some insight into the properties of W3(OH). Figure 5.1 shows three spectra sampled across the continuum source in HCO^+. HCO^+ was chosen for this since it does not have any hyperfine components that could cause line profile confusion. $C^{18}O$, while also not having any hyperfine components, was not chosen to trace this feature as it is not seen in emission or absorption towards W3(OH). The composite emission and absorption spectra are consistent with a dense, hot region (containing HCO^+) surrounded by one or more cold, less-dense layers which also contain HCO^+. The absorption feature is evidence of cold, optically thick gas which is at a velocity of -46 km s^{-1} and has a FWHM of 4 km s^{-1}. In looking at non-continuum subtracted spectra (Figure 5.1b), this absorption line is saturated and extends completely down to zero flux. This implies that this cold region is in front of the emission region and the continuum source. The absorption feature is also seen in CN and HCN, however, it is seen slightly in emission in $C^{18}O$. The $C^{18}O$ emission feature is also centered at -46 km s^{-1} and has a FWHM of 4 km s^{-1}, the same as the HCO^+ absorption. It is very likely that it is from the same region, implying that the gas density is sufficient to raise the excitation temperature of the $C^{18}O$ line above that of the brightness temperature of the continuum source so the line appears in emission, while the higher critical densities of the HCO^+, HCN, and CN transitions lead their excitation temperatures to be less than that

---

*This chapter contains portions of the previously published papers, **"Structure and Composition of Molecular Clouds with CN Zeeman Detections I: W3OH"**, in The Astrophysical Journal (Hakobian & Crutcher, 2011), **"First Interstellar HCO^+ Maser"**, in The Astrophysical Journal Letters (Hakobian & Crutcher, 2012), as well as portions from a paper that is currently in preparation for publication.

brightness temperature, so they are seen in absorption. To note: Figure 5.1 is resolution limited since it is formed with C, D, and E array data and its three positions only cover an area of 1.5-2 beamwidths. This was part of the motivation to acquire B-array data as the same region would cover 5-8 beamwidths in a B-array map.

From the B-array spectra (Figure 5.2c), we only see HCO^+ in absorption against the continuum emission. The lack of emission either means that it is being resolved out at this high spatial resolution, or that the beam is completely filled by continuum emission, so we see no emission from the sides of the beam. In either case, this means that the emission does not come from the same gas that produces the absorption. To support this, we produced spectra that only includes E-array (largest beam size, shortest baselines) in order to inspect large scale emission. The E-array data (Figure 5.2a) shows emission towards the continuum between -43 km s^{-1} and -50 km s^{-1} with a self absorption feature at -46 km s^{-1}. This high velocity gas is not seen in $C^{18}O$ and therefore seems to be hot, optically thin gas that is behind the continuum source.

Therefore, we propose a multi-layered model of the region around W3(OH). Behind the UCHII region is a high velocity, hot, large spatial scale, optically thin region which appears to peak in intensity towards the Turner-Welch object (and may very well be associated with it). The UCHII region is optically thin, and has a small spatial scale of about $0.7''$in diameter which is extremely bright in the continuum, enough such that the narrow band 2 MHz windows are contaminated by continuum emission. In front of the continuum is a very cold, optically thick region at a velocity of -46 km s^{-1} which we primarily see in absorption, but we see slightly in emission in $C^{18}O$.

5.1.2 W3(OH) Flux Comparison

Our maps are comprised of C, D, and E array data and do not cover the entire UV space. We do not have zero-spacing data which would be required in order to reconstruct the most accurate map of the region. The IRAM data consists of only a single pointing and its beam does not cover the full area of the CARMA maps. In order to quantify the amount of flux that could be resolved out by using CARMA, we examined the single dish data taken by Falgarone et al. (2008). Since the IRAM-30 meter telescope has a resolution of $23''$, we smoothed our CARMA maps to match by convolving the data with a $23''$ Gaussian beam (Figure 5.3). Spectra, (5.4) were then extracted from the position corresponding to the IRAM-30 meter pointing center, as well as two other positions centered on the north-eastern and north-western components. According to the IRAM technical documentation (IRAM, 2009), the main beam efficiency is 78% for the band that includes CN. To compare the flux values, an estimate of CARMA's main beam efficiency is needed (White & Zauderer, 2008). CARMA does not have published main beam efficiency measurements, however, it can be estimated from single-dish aperture efficiency measurements which vary from 55% to 70% depending on the individual dish. From this, we estimate that the main beam efficiency (per dish) would be ~70-80%. By adopting a value of 75%, approximately the same as IRAM's, we can directly compare the IRAM and CARMA spectra. The IRAM peak was 2.2 K, while CARMA's was 1.4 K. This means that the peak of the CARMA spectra was at 64% of IRAM's (the area of the CARMA spectra is 48% of the IRAM spectra). CN is also seen in strong absorption towards the central source (W3OH), however, this absorption feature is not present in any of the IRAM data. This is possible for several reasons. First, the relatively small spatial size of the absorption feature covers a small fraction of the total IRAM beam. Any measured absorption would be diluted across the entire beam and masked by the significantly greater emission. In addition, the IRAM data baseline fitting procedure could contribute to hiding the presence of a weak absorption feature.

5.1.3 N_2H^+ Chemical Reaction

In regions with standard CO abundances (i.e. regions that are not depleted in CO), one of the formation mechanisms of HCO^+ is the destruction of N_2H^+ by CO (Bergin et al., 2002; Jørgensen et al., 2004). Since there is significant support that CN remains in the gas phase at densities greater than 10^5 cm^{-3} (same as N_2H^+) we would expect CN and N_2H^+ to have a very similar spatial distribution, however, there are some regions and velocities where we would expect to see more N_2H^+ emission than we do. The particular reaction that is thought to occur is:

$$N_2H^+ + CO \rightarrow HCO^+ + N_2 \tag{5.1}$$

If we compare the regions of strong N_2H^+ and HCO^+ emission, we would expect them not to be coincident. In addition, we expect CO to be depleted in regions of strong N_2H^+ emission, as the presence of CO would cause the formation of HCO^+, while regions with significant CO emission must be weak in N_2H^+, or the reaction between these two molecules would occur.

In the region surrounding the Turner-Welch object we can see considerable emission from both CO and HCO^+, however, there is no N_2H^+ within our detection limit. This depletion of N_2H^+ could be caused by the amount of $C^{18}O$ present along this sightline. Since there is significant CN emission from this region, we would also expect to see N_2H^+. The presence of CN and the relative strengths of HCO^+ and $C^{18}O$ is significant evidence of this reaction occurring and that N_2H^+ is being consumed by this reaction.

Above, we showed that there was a cold, dark region of gas towards the continuum source where HCO^+ is seen in strong absorption along with CN and HCN. Discounting the contribution from the continuum source, $C^{18}O$ is seen slightly in emission and N_2H^+ is seen slightly in emission and absorption. The presence of CN absorption implies conditions where N_2H^+ should also be strongly detectable. If we assume that the primary formation mechanism of HCO^+ in this region is by the CO and N_2H^+ chemical reaction, the relative depletion of these two chemical species in this cold dark cloud can be understood.

In regions with conditions similar to that of W3(OH), CN may be a more reliable tracer than N_2H^+ to directly sample regions at high densities. However, since the strongest CN hyperfine transition has significantly weaker line emission than the strongest hyperfine transitions of N_2H^+, it would require significantly greater telescope time to achieve a comparable signal-to-noise ratio. In our case, these sets of maps show not only that this chemical reaction is occurring, but is happening most strongly both along the sightlines associated with an active star forming clump, and in a cold cloud in front of an extremely bright UCHII region.

5.1.4 Structure of the Region Surrounding W3(OH)

Wilson et al. (1991) developed a model of the region surrounding W3(OH) based on $C^{18}O$, $C^{34}S$, and methanol (among others). They proposed a multi-layer model of low density molecular gas surrounding a high density molecular core. This low density cooler region extends in from of W3(OH) as well. Self-absorption in their CS data supports this model. In addition, the v_{LSR} of the self-absorption was up to 2 km s^{-1} more positive than the v_{LSR} of the hotter emitting region. This implies that the cloud envelope is contracting relative to the cloud core. We see similar offsets in the E-array spectrum of HCO^+ seen in Fig. 5.2a, however the offset appears to decrease at higher angular resolutions (Fig. 5.1).

We can compare the range of radial velocities at which we see molecular material. Wilson et al. (1991) data showed that $C^{18}O$ peaks towards W3(OH) at a radial velocity of -46.6 km s^{-1}, and peaks towards the Turner-Welch object at -48 km s^{-1}. We see the same radial velocities in our $C^{18}O$ data (even though our dataset was at 3mm, and theirs was at 1mm). For other species that trace related density regimes (HCN and HCO^+), we see them peak at a velocity of -47 km s^{-1} towards the Turner-Welch object. These species are seen strongly in absorption towards W3(OH), which makes it difficult to determine its radial velocity. These data show that the region around W3(OH) is extremely complex.

5.2 Discussion of Additional CARMA Sources

5.2.1 Comparison of CARMA and IRAM 30m Fluxes

Crutcher et al. (1996, 1999b) and Falgarone et al. (2008) established that magnetic field strengths can be

Table 5.1. CARMA / IRAM 30-m Line Comparison

Source	CARMA Line Area (K km s^{-1})	IRAM Line Area (K km s^{-1})	CARMA Peak Intensity (K)	IRAM Peak Intensity (K)	Percentage
W3(OH)	6.94	14.40	1.4	2.2	48%
DR21(OH)	10.7	25.1	2.4	4.9	43%
OMC1-N1	24.4	43.3	10.5	13.0	56%
OMC1-S	31.6	55.4	11.3	14.7	57%
S140	15.6	21.0	3.7	5.2	75%
S255	8.6	24.8	1.9	5.6	35%
G10.6	41.1	55.7	6.6	6.6	74%

sampled by measuring the normal Zeeman effect in CN. These observers used the IRAM 30-m telescope to search for the strongest CN peak in a number of molecular clouds, then performed a long integration measurement for the Zeeman effect detection. As a precursor to interferometric CN Zeeman mapping, it is useful to understand the distribution of CN molecular gas. If the CN spatial distribution does not vary at small scales, the CN emission may be completely resolved out. If small scale structure is visible, it is useful to quantify the amount of flux that is resolved out by an interferometer. In the extreme case that the CN emission is completely resolved out, CN Zeeman mapping would not be useful to measure the line-of-sight magnetic field strength. In order to directly compare the CARMA and IRAM 30-m line strengths, the CARMA data were smoothed to the beamsize of the 30 meter beam. The CARMA data also had data channels masked if the intensity was negative; this negative emission is an artifact caused by emission being resolved out. If this emission is left unmasked, it would artificially lower the flux contained in the smoothed beam. In this analysis, any values below the 1σ noise level are masked out. This prevents an artificial increase in the flux of the non-signal channels in the smoothed maps caused if only negative noise values are masked. Depending on the source and how much large scale structure is resolved out, masking the data in this manner can recover up to 30% additional flux in comparison to the non-masked smoothing. In addition, the main beam efficiency of both telescopes had to be estimated in order to directly compare flux values; in Hakobian & Crutcher (2011), the efficiencies of both antennas were estimated to be approximately equal and no additional correction factors are necessary.

Table 5.1 shows the relative line strengths and line areas between the CARMA and IRAM spectra. All of the sources appear to resolve out a significant fraction of large scale structure. Two values are reported for OMC1 since the Crutcher et al. (1999b) study measured the LOS magnetic field strength towards two positions in the cloud: one in the north, and one in the south. S255 appears to have the greatest amount of structure contained in large scale structure. Masking affected the flux of S140 the greatest; while the other sources averaged a $\sim 4\%$ increase in flux from masking, 29% additional flux was recovered for S140. Upon inspecting the data closely, S140 has significant negative peaks which are approximately 1/3 the magnitude of the positive peaks, consistent with this numerical calculation. These results favor the usefulness of performing interferometric Zeeman mapping in the future, when facilities capable of performing these measurements are available.

Ideally, the single dish data could be combined with the interferometric data in order to provide a map with greater UV coverage; however this is not possible with the single dish data from the IRAM 30-m antenna. The single dish dataset did not include any mapping of the region except for very short integrations on a coarse spatial scale to determine the strongest line position; long integrations were only carried out towards is peak. In addition, combining single dish with interferometric data generally requires some overlap of coverage in UV space, while the CARMA data does not include short enough UV spacings in order to provide the necessary overlap. In the CARMA E-array, which produces the shortest spacings in this dataset, the minimum baseline is approximately 6 meters. At this minimum distance it is possible for to antennas to physically collide; therefore it is not possible to achieve a compact enough configuration to achieve the needed baseline distance. While the projected baseline difference between two antennas could yield a shorter baseline, even this length does not meet the requirement. This could be achieved with CARMA's recently introduced 23 element mode with additional 3.5 meter antennas, these cannot tune reliably above 100 GHz and to the frequency of CN.

5.2.2 Absorption Features

The continuum subtracted spectra of G10.6 (Fig. 4.48) show an unusual feature in HCN: only one of three hyperfine lines is seen in absorption. This is most likely due to a varying optical depth between the three transitions. The small emission peak visible overlaid on the absorption could be due to an unresolved subregion within the $7.6'' \times 4.3''$ beam with an optical depth less than its surrounding material. This is supported by the spectra of the nearby region G10.6-0.4 H which is at a lower gas density where HCN is only seen in emission.

Absorption in OMC1 towards the hot core is visible to a lesser degree (Fig. 4.24), against the slight continuum contamination of the spectral line maps. This absorption occurs at $\sim 7 - 8$ km s^{-1} in CN, HCO$^+$, and to a very slight degree, in N$_2$H$^+$. This may also be slightly visible in the HCN spectra, but this spectral feature could also be due to two blended hyperfine lines with large linewidths. This signifies that N$_2$H$^+$ may not be completely frozen out or it could indicate the presence of a cold cloud in front of the hot core region. Due to the complexity of the source

5.2.3 CN as a High Density Tracer

To use CN as a tracer of magnetic fields, it is necessary to understand what gas CN traces. This is particularly important at high resolution, such as with an interferometer, since any measured magnetic field morphology will be that of the magnetic field coupled with the underlying gas. It has been hypothesized that CN is coupled with high density gas and samples densities on the order of 10^6 cm^{-3} (Hily-Blant et al., 2008). In particular, they showed that it does not freeze out at high densities, similar to other Nitrogen bearing species such as N_2H^+.

However, towards many of the sources in this CARMA dataset, many of the high-density hot cores have significant N_2H^+ depletion, and in some cases, are completely depleted. Of particular interest is S255IR, the Orion hot core, and W3(OH) (Hakobian & Crutcher, 2011). In these cases, N_2H^+ is severely depleted, however CN is not. The depletion has been seen in other sources in the past, however, the lack of CN depletion suggests that it may freeze out at a higher density than that of N_2H^+. This increases the usefulness of CN in objects such as those in the CARMA study. In these situations CN is a more useful tracer molecule, with the only drawback being its relative low line intensity. As a result, it requires a significantly greater observation time in order to achieve the same detection level.

5.2.4 Comparison with W3(OH)

In Hakobian & Crutcher (2011), similar types of source features were discussed in reference to W3(OH). Many of these same features are also seen in the latest dataset, however there are some notable differences. CN emission in the region surrounding W3(OH) was not constrained to the regions surrounding continuum sources as is generally seen in the five additional sources presented here. While the CN emission does cover the star forming region containing the Turner-Welch object $\sim 8''$ west of W3(OH), it peaks in a region $\sim 15''$ north. However there is low level CN emission with complex velocity structure that encompasses the entire region, another feature that remains unseen the the current study. W3(OH) contained complex absorption features seen towards the UCHII region in all molecular species; this was interpreted as being due to a cold, dark cloud in front of the hot emitting region. HCO^+ contained a saturated self-absorption line; none of the other sources in the CARMA dataset contained such absorption.

Even with the complex differences between sources, the conclusion remains the same as in Hakobian & Crutcher (2011). These sources are good candidates for interferometric Zeeman mapping. While every source has a significant fraction of large scale structure resolved out, on average $\sim 50\%$ of the CN flux remains with small scale structure such as would be detected with an interferometer at a resolution of $3'' - 5''$. Self-absorption is observed in some high density spectral lines; however, this does not appear to affect the regions surrounding the single dish CN Zeeman pointings, but rather hot, high density, compact cores. Additionally, more evidence is available that supports using CN as a tracer of high density gas, which provides insight into what underlying material any detected magnetic fields may be associated with. Currently, there is not a radio interferometer that has the capability to perform the full polarizations observations required in the CN 1–0 line; however, it is expected that this will be available with ALMA. A pilot project is currently scheduled to be observed this summer to study the use of the CN 2–1 transition using CARMA's 1mm full polarization receivers. This project will observe the prominent CN peak in W3(OH) and DR21(OH), weather permitting.

5.3 First Interstellar HCO^+ Maser

A previously unseen maser in the J = 1 - 0 transition of HCO^+ has been detected by CARMA. A sub-arcsecond map was produced of the 2 arcmin^2 region around DR21(OH), which has had previous detections of OH and methanol masers. This new object has remained undetected until now due to its extremely compact size. The object has a brightness temperature of > 2500 K and a FWHM linewidth of 0.497 km s^{-1}, both of which suggest non-thermal line emission consistent with an unsaturated maser. This object coincides in position and velocity with the methanol maser named DR21(OH)-1 by Plambeck & Menten (1990). No compact HCO^+ emission was present in the CARMA data towards the other methanol masers described in that paper. These new results support the theory introduced in Plambeck & Menten (1990) that these masers likely arise from strong outflows interacting with low mass, high density pockets of molecular gas. This is further supported by recent observations of a CO outflow by Zapata et al. (2012) that traces the outflow edges and confirms that the maser position lies along the edge of the outflow where interaction with molecular tracers can occur.

DR21(OH) contains numerous sites of strong maser emission in many species. Named for its particularly strong OH-masers, it was determined that the OH and H_2O masers were strongly coincident with millimeter continuum sources (Padin et al., 1989). Furthermore, a large number of methanol masers have been detected over a wide range of frequencies. Batrla & Menten (1988) detected methanol masers in the 81.6 GHz and 84 GHz methanol transitions. Plambeck & Menten (1990) conducted a study of 95 GHz methanol emission and found four strong methanol masers across a region associated with the MM2 millimeter source. Slysh et al. (1997) presented detections of a previously unseen 133 GHz methanol maser. More recently, Araya et al. (2009) present an extensive survey of over 30 44 GHz methanol masers, which appear to trace the shock fronts of two bow shocks along the red and blue shifted lobes of an outflow generated by MM2. Fish et al. (2011) present an analysis of all methanol maser detections and determine that all of the known masers appear to come from the interface region along the shock fronts of the outflow. The brightest of these masers appear along the western tip of the outflow and occur in a narrow velocity range of approximately 0.3-0.5 km s^{-1}. Additionally, they determine that all the methanol maser transitions are Class I masers, which arise from collisional excitations and are considered to be caused by shocks, especially those that arise from outflows, as opposed to Class II masers, in which the pumping mechanism is primarily derived from external radiation. Recent submillimeter continuum and 1mm CO detections of the outflow morphology (Zapata et al., 2012) give further support to the above model.

A bright, unresolved, and unusually narrow line feature was detected in the DR21(OH) map of HCO^+ (Fig. 5.5), at $20^h38^m59.3^s$ $+42^\circ22'49.0''$ (J2000) with a peak at V_{LSR} = 0.78 km s^{-1}. Each track was inspected to rule out the possibility of a transient instrumental issue; however, the compact source was visible in each track. The spatial and spectral location of the source additionally does not change between each of the tracks, indicating that an instrumental issue is unlikely. Follow-up observations in CARMA B-array configuration (Fig. 5.6) were performed in December 2011 in order to further constrain the physical size and brightness of the source. The B-array track has an improved spectral resolution of 0.14 km s^{-1} over the other tracks, due to being observed with the expanded CARMA 8-band correlator in the 8 MHz bandwidth mode with 384 Hanning smoothed spectral channels (Figure 5.6 shows the 192 spectrally independent channels).

Using the high resolution B-array data, we find that the angular size of this object is less than ~ 0.8 arcseconds and that it has a brightness temperature > 1900 K. Since the source remained unresolved in B-array, the parameters of this object can be further constrained by using only long baseline components of the data set. This effectively "resolves out" larger scale structure, leaving a constrained map behind. To achieve this, we limited the map to use baselines larger than 140 kλ ($\sim$ 470 meters). This procedure resulted in a map with an effective beam size of ~0.54" x 0.52" and a brightness temperature of > 2500 K. The source appears to be unresolved even at this resolution (Fig 5.6, top panel).

If the source were dominated by thermal emission, a lower bound on its linewidth can be estimated by calculating the degree by which the emission would be thermally broadened. The calculated full-width at half maximum (FWHM) linewidth would then be purely a function of the effective brightness temperature:

$$\begin{aligned}\Delta f &= \sqrt{\frac{8kT\ln 2}{mc^2}}f_0, \quad \frac{\Delta f}{f_0} = \frac{\Delta v}{c}, \quad m = Nm_p \\ \Delta v &= \sqrt{\frac{8\ln 2k}{m_p}}\sqrt{\frac{T}{N}} \\ &= 0.2139\sqrt{\frac{T}{N}}\ \text{km s}^{-1}\end{aligned} \tag{5.2}$$

where T is the brightness temperature of the source and N is the atomic weight of the molecule. The factor of $2\sqrt{2\ln 2}$ comes from the conversion of a Gaussian standard deviation to FWHM. For a source with a brightness temperature of 2546 K and RMS noise of 8.6 K (0.015 Jy beam^{-1}), the thermal linewidth would be 2.077 ± 0.004 km s^{-1}, which is significantly greater than the observed linewidth of 0.497 ± 0.002 km s^{-1} (obtained by least-squares Gaussian fitting to the line profile). The maser linewidth corrected for the instrumental smoothing is 0.477 ± 0.002 km s^{-1}. The observed high brightness temperature and linewidth narrowing are good indicators that this object is dominated by non-thermal emission. An assumption as to the type of maser emission can be made from this linewidth analysis. Saturated masers can have linewidths up to the thermal linewidth, while unsaturated masers will have a linewidth narrower than the thermal linewidth by a factor of 4 to 5 (Reid & Moran, 1988). Since our object has a linewidth that is 4.2 times narrower than the thermal linewidth, it is consistent with an unsaturated maser.

Plambeck & Menten (1990) observed this region with BIMA at the 95 GHz methanol line and discovered four methanol masers connected by large scale methanol emission. The brightest of these four sources, DR21(OH)-1, is centered at $20^{\rm h}38^{\rm m}59.24^{\rm s}$ $+42°22'49.04''$ (J2000) with a peak at $V_{\rm LSR}$= 0.32 km s^{-1}, which is approximately 0.1" from the center of our measured HCO$^+$ peak. The HCO$^+$ position has an approximate positional error of 0.2", and the methanol positions have an error of 0.3". From these data they estimated their methanol maser had an angular diameter <4.4" and a brightness temperature > 760 K. Three other methanol masers were also observed; however, there is no evidence of companion HCO$^+$ masers (Fig. 5.7). This could possibly be due to their relatively weaker strength or due to the fact that the conditions necessary to produce an HCO$^+$ maser do not exist at these other positions. The co-location of the HCO$^+$ object and the methanol maser suggest that both arise from similar conditions. Plambeck & Menten (1990) hypothesized that such regions could be created from the interaction of an outflow and small clumps of dense molecular gas.

In comparing the B-array maps (Figure 5.6), it appears as if the maser could be partially resolved since its intensity drops from 7.4 Jy beam^{-1} to 4.7 Jy beam^{-1} between them, with slight N-S structure. Araya et al. (2009) reports that there are three methanol masers within 2" of the HCO^+ emission; one strong and two weaker masers, slightly north and south of the strongest maser. If the HCO^+ maser is also a complex of three individual sources oriented in a N-S direction, the highest resolution B-array map may be beginning to distinguish them, giving an appearance of being resolved. In the D and E arrays, the sharp maser "peak" extends $\sim$ 7.5 Jy beam^{-1} above the extended emission, in agreement with the flux density in the B-array spectrum.

A small amount of HCO^+ absorption is visible in the E-array map; however, it is not apparent that the maser linewidth is affected by self-absorption. In this map, the shortest baselines will sample large enough size scales to include the western extension of the continuum that peaks with DR21(OH)-MM2. Furthermore, the HCO^+ emission includes two velocity components associated with extended gas, one at -4.7 km s^{-1}, and another peaking at $\sim$ 0 km s^{-1}. The peak positions of these two velocity components correspond to the continuum peaks of MM1 and MM2 respectively. The high velocity wing of the -4.7 km s^{-1} component is affected by absorption by the continuum in the E-array map, however, the 0 km s^{-1} component is not. The D and C array maps with smaller beam sizes (longer baselines) are not affected by this continuum contamination or the extended HCO^+ emission which is resolved out.

Zapata et al. (2012) performed 1mm observations of several spectral lines around DR21(OH). Included with these observations are CO(2-1) observations which trace an outflow from DR21(OH)-MM2. This outflow appears to be in the plane of the sky (Fig. 5.7). From this figure, we can see that both the methanol maser and our HCO^+ object appear along the edge of the outflow. This region would be highly shocked, and the energy released from this interaction has the potential to power the maser.

Goldsmith (1972) analyzed the J = 1 - 0 transition of CO and determined that a large range of rotational excitation temperatures, including population inversion, can be produced through collisional excitation in the range of kinetic temperatures and densities found in molecular clouds. It was also concluded that other linear molecules with simple rotational structure, such as HCO^+, would have the same result. Using the RADEX radiative transfer package (van der Tak et al., 2007), we performed a test calculation that showed that for collisional interaction such as is suggested here in DR21(OH), it is possible to achieve population inversion in the HCO^+ J = 1 - 0 transition with gas densities of $\sim 5 \times 10^5$ cm^{-3} and kinetic temperatures $\sim$50 K (consistent with kinetic temperatures in outflow shocked regions). This result further supports the conclusion that this HCO^+ is a maser.

5.4 Conclusions

We mapped the 2 arcmin^2 region around six molecular clouds with CARMA, in which previous single-dish CN Zeeman observations detected a strong magnetic field. In determining which gas was producing the magnetic field, we were able to see the following features and make the following conclusions from their presence:

- Comparison between CARMA spectra and spectra obtained with the IRAM-30 meter telescope (Falgarone et al., 2008) yields that CARMA detects approximately 50% of the material in this region.
- CN is an ideal high density tracer that in some situations maybe more useful than N_2H^+ (such as conditions where N_2H^+ is frozen out). However, its low line intensity requires a significantly greater amount of observing time in order to achieve an equivalent sensitivity.
- A strong absorption feature in HCO^+, HCN, and CN was detected towards the continuum source in W3(OH) whose strength and line saturation implies the existence of a cold, optically thick region in front of the continuum source.
- Selective depletion of N_2H^+ in comparison with the CN and HCO^+ distribution indicates that N_2H^+ is reacting with CO to form HCO^+. This reduces the effectiveness of N_2H^+ as a high-density tracer, and favors the use of species, such as CN, in objects with similar chemical composition to W3(OH). These measurements additionally support the usefulness of CN as a high density tracer and confirms the hypothesis that CN Zeeman mapping will probe the magnetic field strength in the high density regions of molecular cloud clumps.

These conclusions lead to the result that future CN Zeeman mapping at high resolution with an interferometer is feasible and that these targets are ideal to perform such mapping.

Observations of DR21(OH) have revealed the presence of a compact object which is dominated by non-thermal emission. The extremely compact size of this object coupled with its large brightness leads to the following conclusions:

- The source is co-located with a known strong methanol maser.
- It lies along the edge of an outflow which gives support to previous theories that masers can arise due to the interactions of high velocity outflows with cold, dense clumps of molecular gas.
- Its small spatial size most likely prevented its detection before now; emission from this source would be beam diluted to levels indistinguishable from thermal emission.
- This object is very likely an unsaturated maser, the first observed in HCO^+.

In order to further confirm that this source is indeed a maser, future observations to look for anomalous level populations in higher order HCO^+ transitions should be performed.

Support for CARMA construction was derived from the states of California, Illinois, and Maryland, the James S. McDonnell Foundation, the Gordon and Betty Moore Foundation, the Kenneth T. and Eileen L. Norris Foundation, the University of Chicago, the Associates of the California Institute of Technology, and the National Science Foundation. Ongoing CARMA development and operations are supported by the National Science Foundation under a cooperative agreement (NSF AST 08-38226), and by the CARMA partner universities.

5.5 Figures

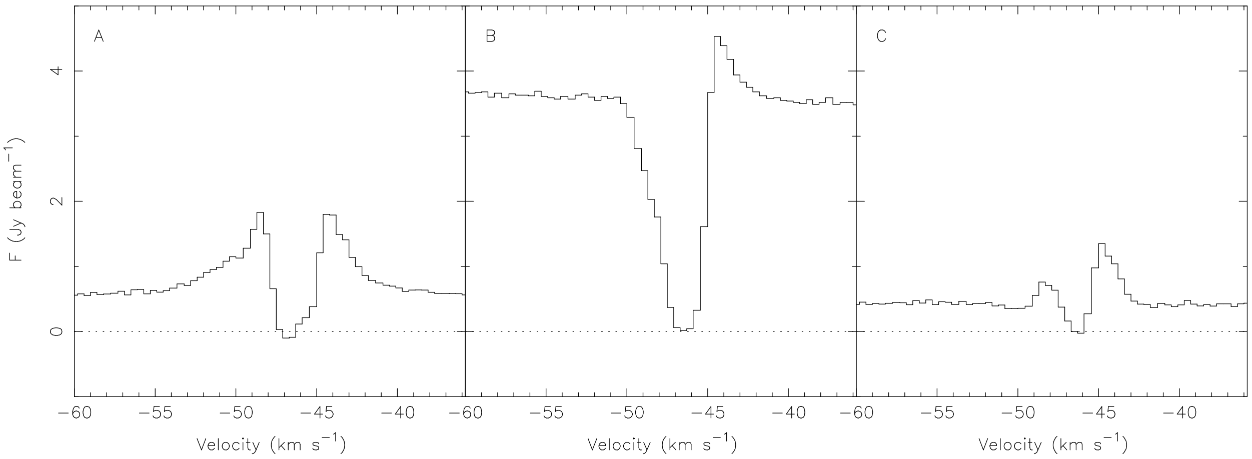

Figure 5.1 Panels A-C are HCO$^+$ spectra of W3(OH) at three positions with no continuum subtraction. This shows the change in emission and absorption spectra in HCO$^+$ across the W3(OH) Ultra-Compact HII region. Panel A is 2″ SE of the W3(OH) center position, and Panel C is 2″ NW of the W3(OH) center position. The positions of spectra A-C are marked on Figure 4.12a for reference.

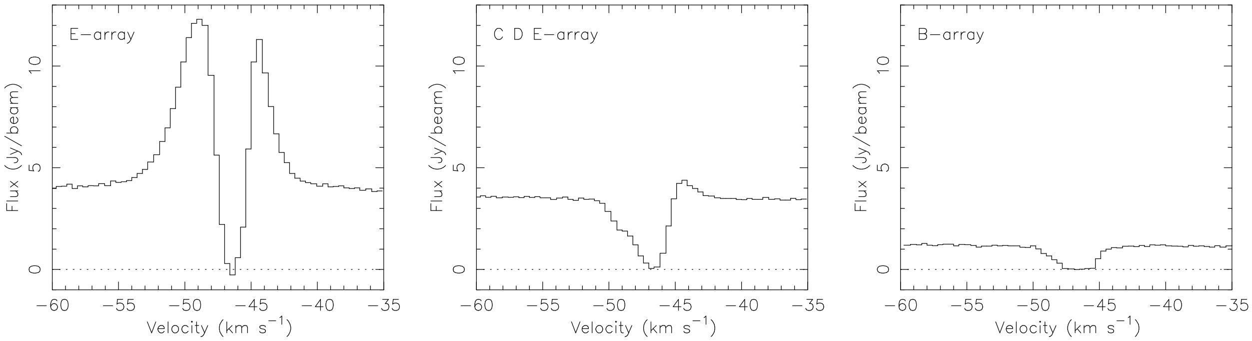

Figure 5.2 Comparison between spectra towards the center of the continuum source in a) E-array only, b) combined C, D, E array maps, and c) B-array only. In all three instances, the spectra are seen in absorption at the same velocities and with roughly the same linewidth which supports a model of a cold dark, optically thick cloud in front of the continuum source and emission regions in our map.

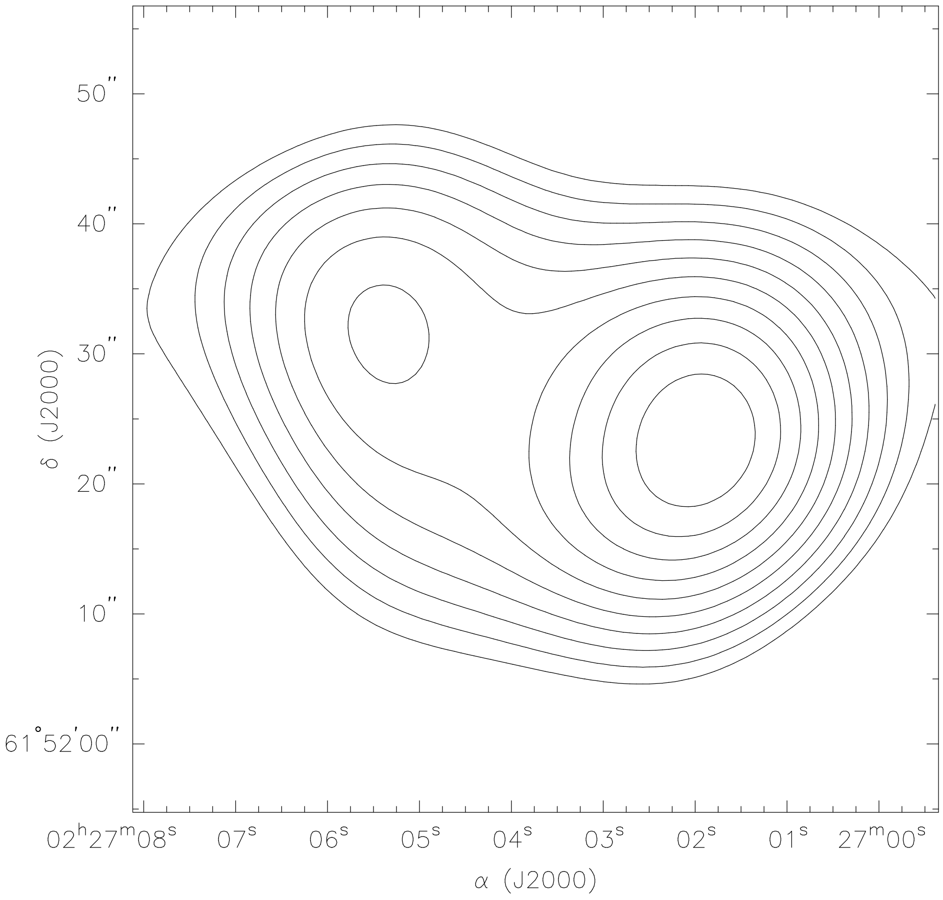

Figure 5.3 Smoothed CARMA CN map to the same resolution as the IRAM measurements (23″). This was produced by convolving a 23″ Gaussian beam with the integrated line map seen in Fig. 4.1. The contour levels are in increments of 0.158 Jy beam^{-1} from 1.89 Jy beam^{-1} to 3.47 Jy beam^{-1}.

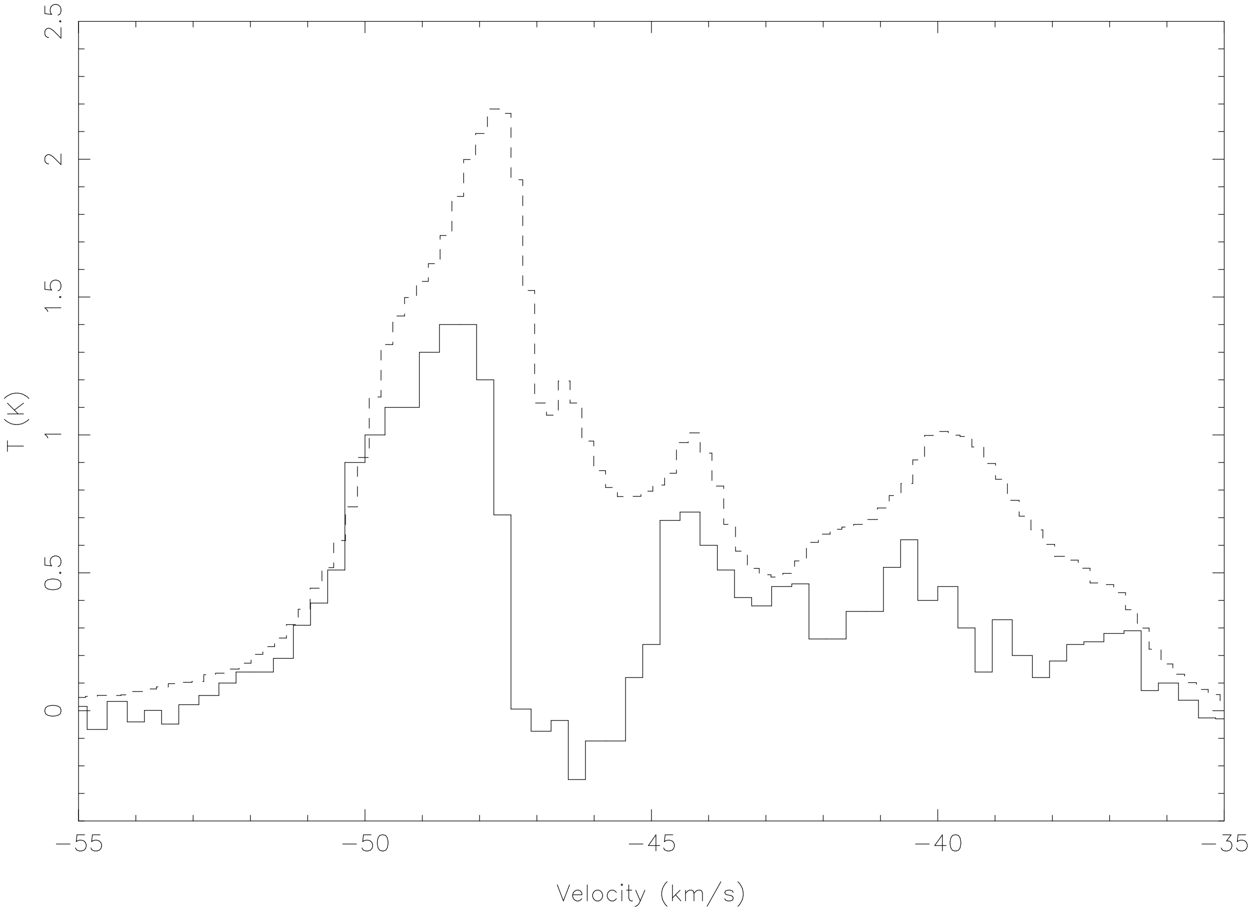

Figure 5.4 CARMA spectrum overlaid with the IRAM spectrum at a point near the IRAM pointing center. Note that there are two CN hyperfine lines in these spectra, separated by about 8 km s^{-1}. The velocity scale is for the stronger hyperfine line (at ∼48 km s^{-1}). The intensity scale is estimated by comparing the main beam efficiencies of IRAM and CARMA, however, there is an inherent 20% error in the CARMA flux measurements. From this, we estimated that CARMA resolves ∼65% of the CN emission within the IRAM beam.

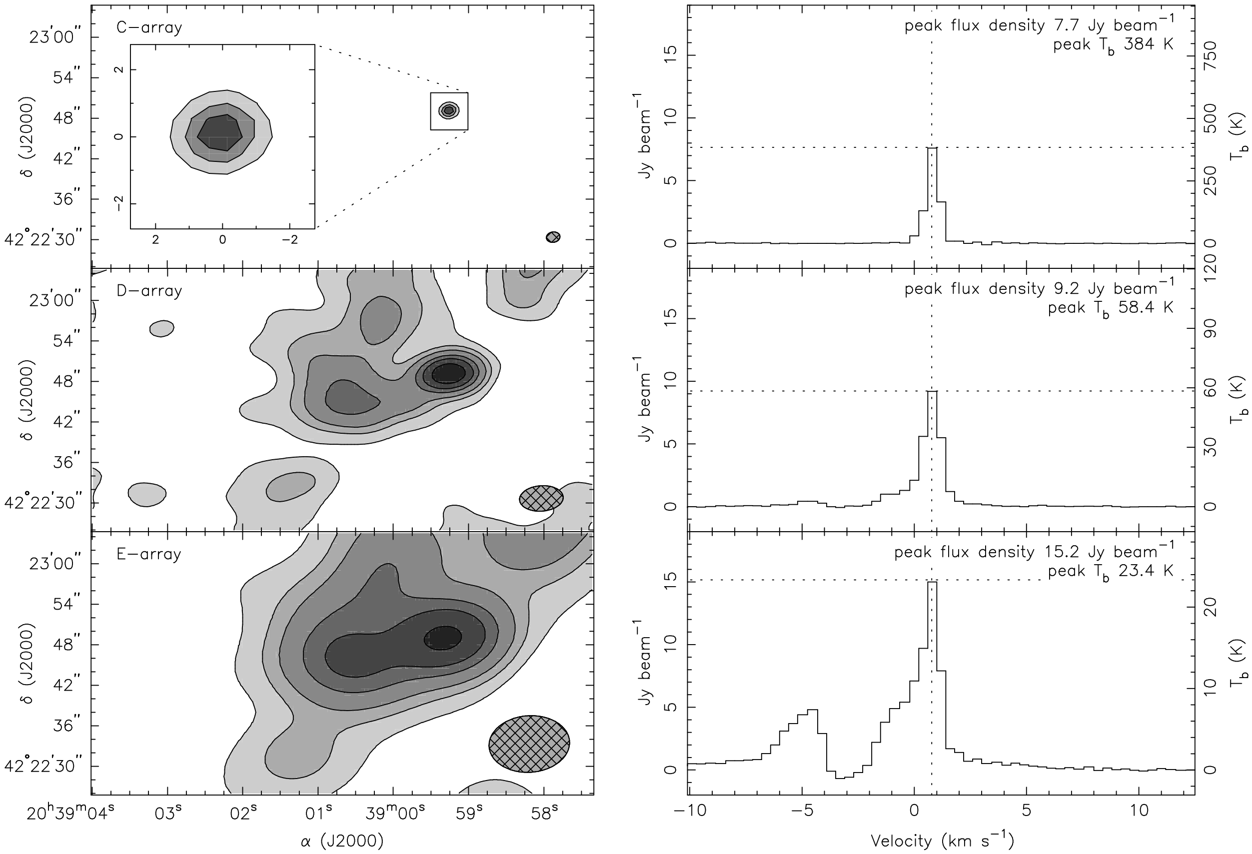

Figure 5.5 Comparison of maser emission in CARMA C, D, and E-arrays. Spectra (right) are of the peak positions in each map (left) of the 0.78 km s^{-1} channel, visible in shaded contours. The y-axis of the spectra are shown in both units of Flux density (Jy beam^{-1}) and Brightness Temperature (K) to emphasize the effect of the decreasing source/beam size. The beam sizes are 2.0” x 1.5”, 6.4” x 3.7”, and 11.9” x 8.4” for the C, D, and E-array maps, respectively. The contour levels for the C-array map are 0.25, 0.50, and 0.75 times the peak flux density. The contour levels for the D and E-array maps are 0.01, 0.075, 0.15, 0.30, 0.45, and 0.7 times the peak flux density. The RMS noise of the spectra are 0.042, 0.028, and 0.056 Jy beam^{-1} for the C, D, and E array maps, respectively.

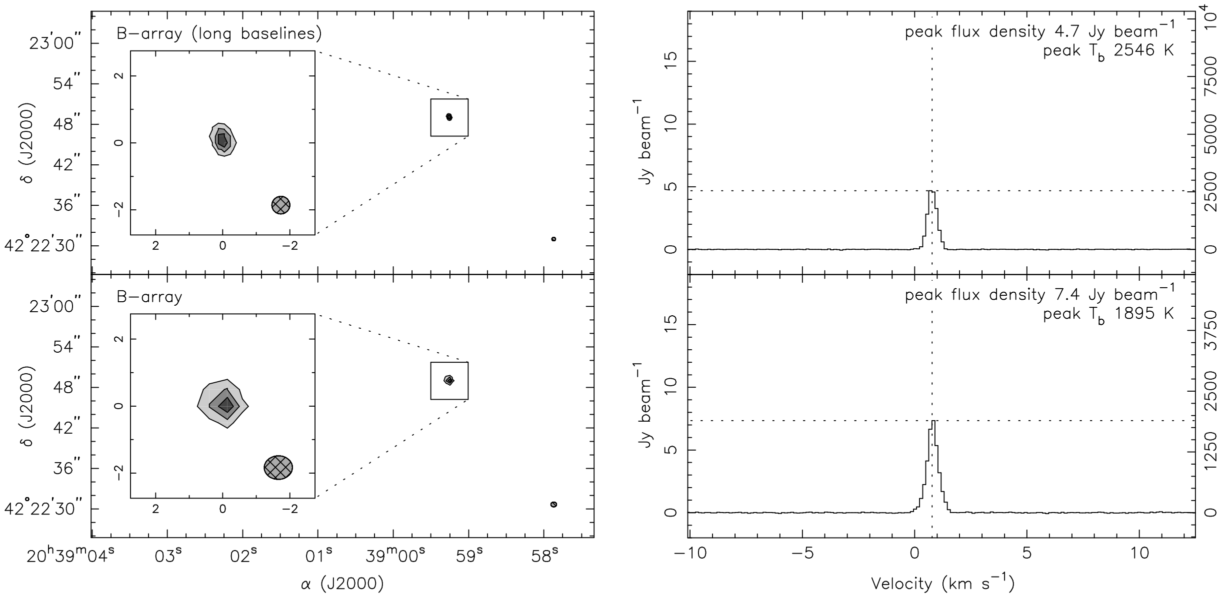

Figure 5.6 Comparison of maser emission in CARMA B-array. Spectra (right) are of the peak positions in each map (left) of the 0.78 km s^{-1} channel, visible in shaded contours. The y-axis of the spectra are shown in both units of Flux density (Jy beam^{-1}) and Brightness Temperature (K) to emphasize the effect of the decreasing source/beam size. The maps feature an inlay showing the 4 arcsecond^2 region around the maser due to its compact size. The top panel is of B-array data with baselines $> 140\text{k}\lambda$. The beam sizes are 0.54" x 0.52" for the top panel, and 0.85" x 0.70" for the bottom panel. The contour levels are 0.25, 0.50, and 0.75 times the peak flux density. The RMS noise of the spectra are 0.015 and 0.026 Jy beam^{-1}, for the top and bottom map, respectively.

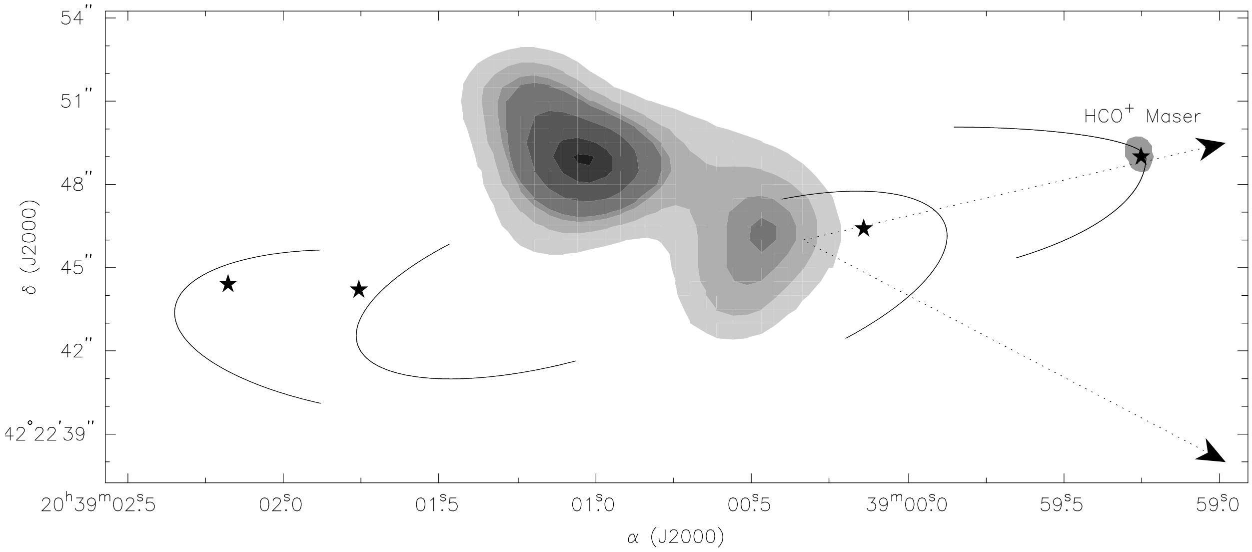

Figure 5.7 Diagram of the position of the HCO^+ maser with respect to other features of DR21(OH). The shaded contours are of the 112 GHz continuum of DR21(OH). The dotted arrows represent the CO outflow as observed by Zapata et al. (2012). The shaded oval represents the extent of the HCO^+ object as reported in this paper. The stars represent the positions of methanol masers from Plambeck & Menten (1990). The black curves represent the two sets of bow shocks determined by the loci of 44 GHz methanol masers from Araya et al. (2009). The positions of the masers along the edge of the outflow give strong support to the theory that shocked interactions between outflows and small, high density clumps of molecular gas give rise to these objects. The contour levels of the continuum emission are 0.3, 0.4, 0.49, 0.54, 0.7, 0.9, and 0.99 times the peak flux density of 0.103 Jy beam^{-1} in order to show the peaks of both continuum sources.

Chapter 6

Ion-Neutral Linewidth Analysis of Objects Observed with CARMA[*]

6.1 Introduction

Houde et al. (2000a) and Houde et al. (2000b) presented a technique for estimating the strength of the plane of sky magnetic field component based on the coupling between the magnetic field and ion and neutral molecular species. They theorized that magnetic fields will differentially interact with ion and neutral species and this difference will be expressed through the observed linewidths of the two molecular species. For this test, they suggested using HCN and HCO^+ as the neutral and ion species, respectively. Houde et al. (2002) presented an analysis of how these measurements can be used to reconstruct the total magnetic field vector when coupled with Zeeman measurements (for line-of-sight magnetic field component) and continuum dust polarization measurements (to assist in calibrating the relationship between ion-neutral linewidth and plane of sky magnetic field intensity). However, this technique has several issues that remained unsolved. Variations in optical depth between the two molecular tracers bring into question whether the technique consistently samples the same gas regions. Additionally, its unclear whether the ion-neutral analysis samples the same regions of a molecular cloud that Zeeman measurements do. These techniques are further summarized in Houde (2011).

In order to overcome some of these issues, a technique to derive the plane-of-sky magnetic field intensity was created that is independent of the dust polarization (Li & Houde, 2008). This technique operates on the assumption that the large linewidth observed in molecular clouds originates from localized supersonic turbulence. While the assumed turbulent cell size is smaller than the beam size of observations, they theorized that it can be calculated by fitting a Kolmogorov-like power spectrum to observed line width minima at several scale sizes. From the parameters defining the scale size, such as the decoupling length scale of the turbulence and the velocity dispersion at this length scale, Li & Houde (2008) derived a technique in which to estimate the magnetic field strength. However, before this technique can be applied to data, such as the CARMA dataset, the colocation of the spectral lines used in this analysis must be verified in order to ensure

---

[*] This chapter contains portions of a paper that is currently in preparation for publication.

that the comparison of measured linewidths are actually tracing the same gas.

6.2 Similarity Study of Molecular Tracers

The ion-neutral line width study requires that both the ion and neutral species used (in this case, HCO^+ and HCN, respectively) are spatially colocated. Instead of relying on a purely subjective visual estimate of whether two maps are similar, it was determined that a statistical study of similarity would be performed. To perform this calculation, we utilized the Pearson product-moment correlation coefficient (Rodgers & Nicewander, 1988). This function allows for comparison of two varying datasets and produces values between -1 and +1. A value of -1 signifies anti-correlation, 0 signifies no correlation, and +1 signifies correlation (Fig. 6.1). Since this correlation method uses the variance of data values about the mean, the computed correlation coefficients are independent of maximum intensity values in the dataset, but instead are dependent on the linear spread of pairs of data points. This correlation technique is very resilient to large changes in sensitivity or line strength as a result. For comparison of two datasets, x and y, the Pearson's correlation coefficient is defined as:

$$\begin{aligned} r &= \frac{\mathrm{cov}(x,y)}{\sigma_x \sigma_y} \\ &= \frac{\sum_{i=1}^{n}(x_i-\bar{x})(y_i-\bar{y})}{\sqrt{\sum_{i=1}^{n}(x_i-\bar{x})^2}\sqrt{\sum_{i=1}^{n}(y_i-\bar{y})^2}} \end{aligned} \tag{6.1}$$

The CARMA integrated line maps are used to calculate correlation values in order to compare the physical emission without a variance influenced by velocity offsets or hyperfine blending of individual components. For example, comparing three hyperfine components of HCN with the single line of HCO^+ would produce a correlation coefficient heavily weighted by the non-correlation of the two HCN components without respective HCO^+ components. In addition, a cutoff value is applied to each image in order to mask out noise. Systematic noise is, by definition, uncorrelated, and when comparing sources with low signal-to-noise, a large number of uncorrelated noise datapoints can significantly influence the calculated correlation coefficient. A pixel in an image is only masked when both species compared have values below their respective thresholds. If not performed in this manner, the correlation procedure would not be sensitive to signal anti-correlation in the case that a specific map position had no signal (below threshold) in one species, and strong signal in the other species. This procedure therefore produces correlation values that are independent of source size, complexity, and map sensitivity. Figures 6.2-6.7 show the correlation results over all six CARMA objects.

Table 6.1. Line Correlations

Line	W3(OH)	DR21(OH)	OMC1	G10.6	S140	S255
CN—$C^{18}O$	0.059	0.227	0.466	0.900	-0.369	0.505
CN—HCN	0.211	0.665	0.202	0.850	0.436	0.586
CN—HCO^+	0.225	0.629	0.480	0.947	0.400	0.418
CN—N_2H^+	-0.281	0.407	0.166	0.190	0.420	0.047
CN—Cont.	-0.036	0.429	0.222	0.659	0.346	0.562
$C^{18}O$—HCN	0.744	0.672	0.452	0.813	-0.025	0.732
$C^{18}O$—HCO^+	0.714	0.696	0.335	0.935	-0.018	0.664
$C^{18}O$—N_2H^+	-0.298	0.076	0.280	0.367	-0.230	-0.116
$C^{18}O$—Cont.	0.110	0.779	0.696	0.716	-0.270	0.805
HCN—HCO^+	0.788	0.918	0.399	0.897	0.746	0.905
HCN—N_2H^+	-0.201	0.225	-0.123	0.238	0.402	0.326
HCN—Cont.	0.446	0.701	0.801	0.453	0.259	0.833
HCO^+—N_2H^+	0.065	0.217	-0.059	0.351	0.364	0.367
HCO^+—Cont.	0.330	0.647	0.253	0.606	0.393	0.796
N_2H^+—Cont.	-0.134	0.248	-0.132	0.014	0.283	0.012

Table 6.1 shows the results of the correlation study on CARMA data. The W3(OH) values were calculated from integrated line maps presented in Hakobian & Crutcher (2011). Of all the calculated correlations, HCN and HCO^+ are most frequently found in high correlation ($\gtrsim 0.75\%$), with the exception of OMC1. OMC1 contains abnormally wide and strong HCN lines (see § 4.3.3 for more information) which breaks this trend and prevents an ion-neutral line width analysis from being carried out on this source. The remaining five sources are extremely good candidates for performing the ion-neutral linewidth analysis using these two species due to their high correlation. N_2H^+ has the least correlation with any of the other species and the continuum. This is not unexpected, as N_2H^+ is depleted towards bright compact continuum sources in our fields, which was not seen in other lines. CN correlates unusually well in G10.6 with every map (except N_2H^+). This gives support to the supposition that due to the extreme distance of G10.6, the CARMA maps do not trace the interior structures of G10.6 as they do towards other objects (§ 4.3.6). The correlation between CN—HCN and CN—HCO^+ may be lower than that of HCN—HCO^+ due to the low line strength of CN. With greater sensitivity, larger regions of CN may be detected which would increase the correlation between these three high density tracers.

6.3 Line Fitting Technique

In order to calculate the linewidths of various spectral lines, a standardized method of fitting spectral data needs to be created. This issue is further complicated by the presence of multiple velocity components in sources such as DR21(OH). In these cases, it is important to account for all significant velocity components since each component may be associated with different material, each with unique properties. In the case of ion-neutral linewidth comparisons, the analysis uses HCO^+ and HCN as the two tracer molecules. The HCN 1–0 transition has three hyperfine components which makes fitting somewhat more complex since multiple velocity components will cause significant line blending. The three HCN hyperfine lines will be fit simultaneously as their frequency separation remains constant and the linewidths do not vary from component to component.

The custom fitting routine was built in the Python programming language with the assistance of routines from the SciPy (Jones et al., 2001) analysis package. SciPy provides several convenience functions to call low level non-linear least squares fitting routines in the library MINPACK (Moré et al., 1980; Cowell, 1984). These fitting routines are an application of the Levenberg-Marquardt algorithm (Levenberg, 1944; Marquardt, 1963) which essentially is a combination of the Gauss-Newton Method of performing least squares and the method of gradient descent, that determines localized parameter minima by varying parameters in the direction of steepest descent in parameter space. It strength lies in its fast computation speed at the expense of only determining a localized minimum between compared datasets near an initial estimate. In the case for this fitting routine, we are estimating the line profile shape to be Gaussian. Spectral lines are not guaranteed to be Gaussian; however, for the purposes of this analysis, it is an adequate estimate. This estimate is limited, especially in the case of HCO^+ that is frequently seen with a high optical depth in molecular clouds. In essence, this fitting procedure iteratively fits Gaussian components to a spectrum from the CARMA data cube, chooses components with a high statistical significance, and calculates the full-width at half maximum (FWHM) linewidth from these values.

Even with a fast converging least squares fitting routine such as the one in the MINPACK package, there are some constraints that have to be considered. The MINPACK package was written in Fortran which has severe multi-threading limitations on more recent computer architectures. While there are methods to overcome this limitation, adding such a feature would have greatly increased the development time; instead it was decided to use other techniques in order to reduce the number of fits necessary to perform this analysis. Radio interferometer data are very frequently spatially oversampled during the image creation process in order to account for varying sizes and non ideal shapes, such as elongated ellipses, of the convolved beam. For the reduction of the CARMA dataset, all maps (with the exception of sub-arcsecond B-array data) were oversampled onto a pixel grid of $0.5''$ while the smallest beamsize was $\sim 2.0''$. For an image with dimensions of 256 px on a side, this would amount to 65536 individual fits necessary. Since each pixel carries redundant data due to this oversampling, the number of necessary fits can be greatly reduced if the dataset is resampled to one pixel per beam. For example, in DR21(OH) where the beamsize is $\sim 5''$, we can pick one pixel out of every 10 which regrids the dataset onto a 26×26 pixel grid (676 fits) reducing the number of calculations performed by a factor of ~ 2500. Since the intensity values are already in the units of Jy beam^{-1}, these values do not require any scaling to remain in the correct units.

The fitting procedure is performed over several stages. Due to the complex nature of the HCN hyperfine structure and the high occurrence of blending due to multiple velocity components, the initial fits are performed on HCO$^+$. Since it was already determined that the two species are spatially colocated, we can use the results of the HCO$^+$ fits to bootstrap the HCN fitting procedure that takes into account its complex structure. This procedure assumes that both input datasets have the same pixel and map size. Otherwise a technique to interpolate or extrapolate specific spectra at a specific map position would be necessary.

For HCO$^+$, several values must be determined from the dataset such as initial values for line intensity, linewidth, and center velocity. The initial line intensity is determined by finding the peak value in the spectra, the center velocity from the velocity at the peak intensity value, and assuming the linewidth to be 1.0 km s^{-1}. An initial estimate of 1.0 km s^{-1} is not unreasonable for thermal emission at the expected gas temperatures; however, during the development process several initial linewidth values were tested in order to determine how the initial linewidth value influenced the quality of the results. As long as the initial estimate was not unphysical, the fit converged. Extremely small values of linewidth frequently caused the fit to converge on noise fluctuations if the signal-to-noise of the data was low. It is not necessary to provide an exact number for the initial values; an estimate is adequate as long as the fitting routine can minimize the difference between the model dataset and measured data.

In the case that there is no signal or very low signal-to-noise present at a map position, it is likely that the least-squares fitting will converge on noise. The least-squares fitting routine returns, in addition to the fitted coefficients, a covariance matrix representing the likelihood that the fitted parameters represent the source data. The standard deviation between the model and the data for a specific fitted parameter is the square root of the diagonal components of this matrix (the diagonals are the variance of a parameter with itself). A fit is considered not significant and is rejected if the fitted value for intensity or linewidth is less that 5 times its corresponding standard deviation, essentially setting a 5σ confidence in fitted parameters. In practice, a 3σ cutoff would probably be sufficient, however, the process of calculating the minimum turbulence scalesize is sensitive to a single fitted linewidth minima. A 3σ cutoff would be insufficient since there would be a significant chance that a noise fluctuation would be mistaken as real signal. In a Gaussian distribution, a 3σ variation will include 99.7% of all possible values in the distribution, however, 0.3% of values are unrepresented. If the fitting routine attempts to fit a Gaussian distribution to spectra only containing noise, using a 3σ cutoff would mean that 99.7% of such fits would be rejected for not satisfying the cutoff condition; however, 0.3% of fits would still pass (1 out of 370). Fitting a Gaussian to a noise peak additionally has a high likelihood of fitting an unphysically narrow linewidth that would negatively influence the turbulence scalesize analysis. For a large sample set such as the CARMA dataset with 676 individual fits per source, it would be highly likely that several fits representing noise would pass the rejection phase. Increasing the cutoff to 4σ would mean that there would be a 1 in 15,787 chance that a noise value would be accepted; with 6 sources, over 2 spectral lines, and 676 fits each, that would represent 8112 individual fits. There would still be a significant chance that a noise value would be fit. Increasing this value to 5σ decreases this chance to 1 in 1,744,277 which significantly reduces the likelihood of including a Gaussian fit to noise. In addition to the statistical rejection method described above, any intensity value with a negative intensity is rejected. Negative intensity values can represent resolved out emission (from incomplete UV sampling). Since these values do not represent real emission, their linewidths are not representative of any real structure. Rejection of Gaussian profiles with negative intensity is further supported since line absorption can be represented in this manner. Saturated absorption lines are not necessarily Gaussian shaped and cannot be accurately fit since their true intensity is not known.

The iterative process used for fitting is designed in order to fit to an undefined number of components; however, in the current datasets there are a maximum of 2 (in DR21(OH)). The fitting process occurs in several stages: determination of initial conditions, least squares fitting using those initial conditions, rejection of poor fits, and the calculation of the residual for determination of initial values for the next iteration. The residual is only used for calculation of these values; the fitting is performed as a simultaneous fit over all sets of parameters. Overall, this increases the quality of the fits, especially in the case that the two components are partially or completely blended. Initially, the rejected components are kept for the purpose of residual calculation; this prevents identical components from being fit on consecutive iterations. This procedure is repeated until one of two conditions is met; either a maximum number of statistically significant (5σ) components have been reached, or two statistically insignificant components (noise) have been fit in a row. Negative intensity rejected components do not trigger this limit in the case that there is an additional weak, but still statistically significant, component present in the spectra. After this is complete, any components marked as rejected or as noise are removed, and the spectrum is re-fit with only the significant components. If any of the components in this new fit are below the statistically significant threshold, they are removed and it is refit without this new component (and is retested for significance). This second set of fitting tests is required in the case that a component converges on a rejected component. Due to the least squares procedure fitting to local minima, a component rejected in this second round of fitting usually means that the component was an artifact caused by fitting a Gaussian to a non-Gaussian spectral shape. This conservative fitting procedure, while complex, leads to a significant improvement in the quality of the linewidths produced.

This fitting procedure is used to produce Gaussian components from HCO^+ spectra; due to the significant line blending from multiple hyperfine components and multiple velocity components in HCN, it is impractical to attempt the identical procedure with it. Instead, the initial conditions for fitting are the calculated components from HCO^+. To account for the hyperfine components, the fitting function was expanded to simultaneously fit three Gaussians. Since the relative frequency offsets between the components are well known, the linewidths remain constant between the components, and the relative line intensities are known, the number of free parameters for the HCN fits remains the same as the HCO^+ fits. Leaving the relative intensities of each component as a free parameter was tested and proved to be troublesome; in many cases, the least squares routine favored fits where one component had zero intensity, an unphysical result. This often was caused by the presence of multiple velocity components or the intensities differing from the expected line ratios. The line ratios commonly differ from their expected values as each component may have a different optical depth. More reliable results were obtained from the fitting routine by fixing the intensity components to their expected values. The quality of fits technique described above was performed on the results as it is not guaranteed that components in HCO^+ correspond with HCN, nor is the noise level guaranteed to be identical in both spectra, leading to some HCN components being rejected due to their low statistical significance.

After fits have been performed on both species, the HCO^+ and HCN spectra have to be matched up. An arbitrary separation of 0.5 km s^{-1} was enforced between the center velocity of HCO^+ and HCN; if they differ by an amount greater than this, the chance that these two components are not associated with the same gas increases. The measurement of the smallest turbulent scale size requires that the two species are colocated; the similarity study only compared spatial correlation between two species, not velocity correlation. In the case that a component exists in one species but not the other, both components are removed from the final dataset as the two species are no longer guaranteed to be colocated.

As a final step, the Gaussian standard deviations produced by the least squares fitting routine need to be scaled to the full width at half max (FWHM) linewidth values. This scaling factor can be derived by calculating the positions where a Gaussian function is equal to half of its peak intensity (Eqn. 6.2), then by using these values to calculate the FWHM (Eqn. 6.3):

$$\begin{aligned} f(x_i) = Ae^{-\frac{(x_i-b)^2}{2\sigma^2}} &= \frac{A}{2} \\ -\frac{(x_i-b)^2}{2\sigma^2} &= \ln\left(\frac{1}{2}\right) \\ (x_i-b)^2 &= -2\sigma^2 \ln\left(\frac{1}{2}\right) \\ (x_{\pm i} \mp b) &= \pm\sqrt{2\ln 2}\ \sigma \end{aligned} \tag{6.2}$$

$$\begin{aligned} \mathrm{FWHM} &= \Delta x_i \\ &= +(x_i-b) - (x_{-i}+b) \\ &= \sqrt{2\ln 2}\ \sigma - \left(-\sqrt{2\ln 2}\ \sigma\right) \\ &= 2\sqrt{2\ln 2}\ \sigma \end{aligned} \tag{6.3}$$

6.4 Multi-scale Gridding

In order to calculate the minimum linewidth at multiple velocity scales, a procedure to grid the data must be developed. Li & Houde (2008) used a variant of the technique introduced by Ostriker et al. (2001) in which a dataset is broken down into beam sized cells and linewidths were extracted in each cell. To measure the linewidths at successively larger sizescales, neighboring cells were averaged together, producing a set of linewidths at sizescales at multiples of the smallest scale size. However, they modified this technique to additionally extract linewidths at half-bin averaged intervals. This is performed to account for cases where high intensity clumps of molecular gas are split between multiple grid elements where otherwise each piece would be down weighted in intensity. In this analysis, we further modified the procedure to account for the large field-of-view in the CARMA data by adding two additional gridding types at large size scales.

The first gridding type is equivalent to that used in Li & Houde (2008). The smallest grid size is constructed by extracting approximately beam-sized pixels from the oversampled image dataset (described above). Since there is no sub-pixel information at this smallest grid size, no half-grid interval grids are produced. Each successive grid size, d, with an effective beamsize of $d\times$ beamsize, spatially averages groups of $d \times d$ spectra. The half grid size offset averages are then produced by offsetting the first grid by $\frac{1}{2}d$ and repeating the averaging procedure. This effectively grids the dataset as if a $\frac{1}{2}d$ region is removed from every edge. Finally, these averaged spectra are fit by the fitting routine described above using all the conditions of low-signal rejection and the linewidths are recorded.

When the grid size becomes large enough such that two cells no longer fit across the region, it is more effective to replace the previous cell layout with a group of four, each aligned with one of the four corners of the region. The cells will then overlap in the center of the map. As the cell size keeps increasing, the four-box model again becomes redundant since all the cells tend to cover the same material. We then switch to a single box model centered on the map, until a single cell will no longer fit across the map. Figure 6.8 visually shows the relationship between the three gridding methods. Unfortunately, the large cell sizes covered by these two additional techniques frequently did not yield any useful spectral line fits; the line shapes frequently differed significantly from being Gaussian such that they no longer met the 5σ criteria, and the fits that did meet the criteria frequently had center velocities that differed significantly between HCO^+ and HCN. Data points at such large scales are most likely not of much significance due to the source sizes being significantly smaller.

Using these scale dependent linewidths, the goal is to determine if the minimum linewidth values for HCO^+ and HCN follow a Kolmogorov-type spectral law (Larson, 1981) of $\sigma \propto L^{0.38}$. To perform this calculation, Li & Houde (2008) fit linewidth minima to the function,

$$\sigma_l^2 = a + bL^n \tag{6.4}$$

where σ_l are the linewidth minima, a is the linewidth difference between the two species, L is the scalesize (in arcseconds), and b and n are the power law parameters for the fit. In order to simultaneously fit the two datasets to the same power law, we can make the following relationships (Hezareh et al., 2010):

$$\sigma^2_{\mathrm{HCO^+}} = a + bL^n$$

$$\sigma^2_{\mathrm{HCN}} = bL^n$$

$$\sigma^2_{\mathrm{HCO^+}} - \sigma^2_{\mathrm{HCN}} = a \tag{6.5}$$

$$\sigma^2_{\mathrm{HCO^+}} + \sigma^2_{\mathrm{HCN}} = a + 2bL^n \tag{6.6}$$

Performing a least squares fit on the dataset using Equation 6.5 effectively constrains the value of a, so it can be used as a fixed parameter for a least squares fit using Equation 6.6 that then constrains the parameters of the power law (b, n).

Table 6.2. Parameter Fits

Source	a	σ_a	b	σ_b	n	σ_n
DR21(OH) – -5 km s^{-1}	0.348	0.164	0.087	0.091	0.888	0.271
DR21(OH) – -1 km s^{-1}	0.326	0.148	0.265	0.244	0.565	0.243
W3(OH) – -47 km s^{-1}	-0.047	0.101	0.279	0.107	0.626	0.127
W3(OH) – -44 km s^{-1}	-0.778	0.312	1.598	0.842	0.275	0.196
S140	-0.184	0.851	0.004	0.004	2.083	0.264
S255	-0.253	0.145	0.024	0.041	1.221	0.435
G10.6	1.421	1.535	0.001	0.004	2.645	0.976

6.5 Gridding Results

The gridding and fitting technique was applied to all of the sources in the CARMA dataset, with the exception of OMC1. The ion-neutral analysis could not be performed on OMC1 due to HCN and HCO$^+$ not being co-located. Both DR21(OH) and W3(OH) have two significant velocity components. Each velocity component was fit separately since each represents an individual element of the molecular cloud. In every plot with the exception of W3(OH), the scale size is calculated up to a size of about 60$''$. For W3(OH), this is calculated to only 30$''$ since the image size was 1 arcmin^2. As discussed above, the overlapping grid technique only works until two grids fit across the map; since the W3(OH) map is smaller, there are fewer data points.

Table 6.2 shows the parameter fits and their associated error values for fitting the function $\sigma_i^2 = a + bL^n$. The error values represent the confidence that a parameter fits the data. Only one out of the 7 fits (S255) has an offset (a) between HCN and HCO$^+$ indicative of linewidth narrowing. However, the power law exponent for S255 is 1.2 ± 0.4, which is not a Kolmogorov-like power law. None of the other fits have a power law exponent which is consistent; the smallest is the -1 km s^{-1} component of DR21(OH) with $n = 0.565$, which is significantly greater than the expected value of 0.38.

Figure 6.9 shows plots of the scalesize (L, in arcseconds) versus linewidth squared for the 7 regions over 5 objects. Of note is a “bump” in the linewidth in several of the plots (both DR21(OH) plots, S255) at around 40$''$. This is most likely due to both the low statistics at these large size scales and these objects having intrinsic sizes of about 40$''$. Therefore the averages will include all the emission from the object, and the linewidth will appear wider due to any velocity gradients across the source. In the case of DR21(OH), the cutoff for the separation of the two velocity components is somewhat arbitrary as the two are situated very close in velocity space; any fitted component near this cutoff value has a chance to be incorrectly sorted into the wrong velocity component bin. The cutoff for the two components was chosen for their physical separation in addition to their velocity separation, which minimizes the chance for incorrect sorting; however, positions where both components are present still can contribute.

S140 and G10.6 in particular deviate the greatest from the expected power law. The increasing linewidths with scalesize in S140 could be partially due to high velocity wings most likely belonging to a high velocity outflow. In addition the multiple sources spanning $\sim 1'$ could contribute to this. In G10.6, the low number of data points at the larger scale sizes could contribute to the poor fit to these data.

6.6 DR21(OH) Linewidth Comparison

The unexpected results from the fitting procedure led to comparing with additional results reported in Li et al. (2010). The authors performed a detailed spectral analysis to determine how the HCN and HCO^+ linewidths varied in different conditions within a specific source. For their test they used DR21(OH) and the $H^{13}CN$ and $H^{13}CO^+$ data observed by Lai et al. (2003), who observed a ridge between two regions, one which had high B-field line densities (B), and another with low B-field line densities (A). The B-field line densities are lines derived from B-field line segments that show plane-of-sky field directions and are used to visualize the number of B-field lines in an area. It is assumed that these are proportional to the length (strength) of the magnetic field in that region. Figure 6.10 is a CARMA map of the HCO^+ emission (grayscale and contours) with regions A and B as defined by Li et al. (2010). In both cases, the beam size is about the size of the two regions; therefore when a point is sampled near the northern edge of the region, it actually samples material significantly outside the boxed region. The points in the CARMA dataset do not sample the exact positions in the Lai et al. (2003) dataset due to pixel sizes differences in the two generated maps; however, the differences are significantly smaller than the beamsize ($\sim 0.3''$, 5% of the beamwidth) and would not significantly affect the results.

Figure 6.11 show the spectra of HCN and HCO^+ 1–0 at the four positions in the map. It was not necessary to scale the intensities for visual alignment purposes since the intensities between the two species are comparable in these data. Additionally, while HCO^+ was visibly narrower in the equivalent figure presented in Li et al. (2010), there is no noticeable difference in linewidth between the two, which is supported by the linewidth fitting results presented above. An interesting differing spectral feature is in region A(a). In Li et al. (2010), there is no visible second velocity component in HCO^+, however one is visible in HCN. In these data, both components are visible. In region B(b), the opposite is visible: there is no noticeable second velocity component in the CARMA dataset, but one exists in the Li et al. (2010) spectra. These differences paint a picture of a region that differs significantly between the two isotopologues of HCN – $H^{13}CN$ and

HCO^+ – $H^{13}CO^+$.

This linewidth narrowing was also found to be dependent on whether the region was that of high B-line density or low. Region A, with the lowest B-field line density, was the region with the most significant $H^{13}CO^+$ linewidth narrowing. Figure 6.12 shows the fitted linewidth plots between HCN and HCO^+. Region A (triangles) and Region B (squares) appear much different from the Li et al. (2010) result. In general, the data lies along a line with 1 to 1 correspondence between the two species, which signifies that the linewidths of the two species are approximately equal. If linewidth narrowing of HCO^+ was occurring, it would be expected to see the datapoints fitting to a line below the 1 to 1 correspondence. Region B, the high B-field line density position, has significantly larger linewidths than region A by about 1-1.5 km s^{-1}. To determine how well these data fit the 1 to 1 line (dotted), two least squares fits were performed. The Region A (triangles) has an offset of 0.086 ± 0.001, while Region B (squares) has an offset of -0.112 ± 0.003. In addition, the 1σ confidence (error) values from the fits are plotted for comparison. The large number of datapoints (significantly greater than the 9 defined in Li et al. (2010)) were calculated using the gridding procedure described above, for a single grid size corresponding to the beamsize.

6.7 Serpens Main Results

The ion-neutral linewidth analysis was repeated using a $3.7' \times 4.0'$ region in the Serpens Main molecular cloud, observed as part of the CLASSy project. This particular region was chosen as it is one of the brightest objects in the region. The effective beamsize of this region is approximately $8''$. These data are unique as it is one of the first projects to use the 3.5m antennas of CARMA to form a complete 23 element array, in addition to using autocorrelation data from the 10m antennas to form single dish maps. The combination of all these techniques produces a map that is free from artifacts produced by material resolved out by an interferometer.

Figure 6.13 shows the results of the ion-neutral linewidth analysis on this small section of the CLASSy dataset. The linewidth separation (a) was calculated as -0.156 ± 0.074 km^2 s^{-2}, the slope $b = 0.018 \pm 0.012$, and the power law exponent $n = 0.974 \pm 0.166$. There is a very small amount of HCO^+ linewidth narrowing visible; however, the power law exponent of the fitted function is very close to 1. This is not consistent with the expected result of Kolomogorov-like turbulence. While there are some differences between the HCN and HCO^+ emission, they are not significant enough to affect to results of the analysis, and the two datasets are highly correlated. These results appear to mirror that of the other CARMA objects observed. This suggests that the spatial filtering of an interferometer without including single-dish data is not the reason for not seeing the linewidth difference in the other sources.

6.8 $H^{13}CO^+$ and $H^{13}CN$ Results

We applied the ion-neutral technique to DR21(OH) $H^{13}CO^+$ 4–3 and $H^{13}CN$ 4–3 data observed with the SMA by Shih-Ping Lai (private communication). This provides an additional look at high-density regions within the molecular core. These data have the benefit of being at a much greater resolution than any of the other observations analyzed thus far, with a beamsize of $\sim 1''$. In the gridding process, no data were produced at gridsizes greater than $23''$ due to the compact nature of the emission measured. Figure 6.14 shows integrated spectral line maps of both the ion and neutral species in addition to the plot of gridsize versus linewidth squared. The $H^{13}CO^+$ data had a significantly lower signal-to-noise than the $H^{13}CN$ data. Since $H^{13}CN$ is only fit at positions with statistically significant $H^{13}CO+$ fits (due to the colocation requirement), it is highly likely that much of the actual source emission is not included in the gridding results. The apparent difference is size of the source in both maps is most likely an effect of this signal-to-noise difference. The four regions away from the map center (only three visible in Figure 6.14) are most likely reflections of the primary source near the map center that was not completely removed during the image cleaning process. This is most likely due to the low SNR of the source emission. The results of these fits do not show anything conclusive due to large error values on the fitting parameters. However, the power law exponent appears to be near one, which is consistent with the observations of the other sources.

6.9 Gridding Discussion

From analyzing these data, one result remains constant: there is no statistically significant evidence of line width narrowing. The various observation types compare multiple types of objects, both single dish and interferometers, and span a wide range of effective resolutions. One significant difference between these current data and that of Li & Houde (2008) is the use of an interferometer (CARMA) with these current data. Using the Serpens Main dataset from the CLASSy project as an example, it shows that interferometric mapping is not responsible for the effects seen in this study. The Serpens Main data combines interferometric data and single dish data to produce a map that is free from artifacts caused by the absence of low spatial frequency sampling that interferometers typically produce (when not complimented with single dish mosaics). If interferometer sampling were responsible for the lack of line width narrowing, we would expect the results from the Serpens Main region to be significantly different from the other sources.

Another possibility is that there are actual source differences between the Li & Houde (2008), Li et al.

(2010), Hezareh et al. (2010), and the CARMA dataset. However, due to the large number of sources sampled in the CARMA dataset, it is unlikely that all of them share the same non-detection of linewidth narrowing, especially since DR21(OH) has been previously observed by Li et al. (2010) and Hezareh et al. (2010) where linewidth narrowing was seen. From this, it is more likely that a systemic effect between the current (CARMA) observations and the previous observations is the cause for the observed differences.

The primary difference between the CARMA dataset and the previous observations is the effective resolution of the observations. Li & Houde (2008) mentioned that the ambipolar diffusion scale and the characteristic velocity of a turbulent eddy at that scale could possibly be directly observed through higher resolution observations with an interferometer such as CARMA or the SMA. Such a signature would be observed as a significant drop in velocity or as a divergence in the spectra of the ion and neutral species. None of the observed datasets appear to have such a signature; however, the finest spatial resolution of the CARMA datasets is $2.5''$ (in W3(OH)). Hezareh et al. (2010) calculated the effective ambipolar diffusion scale (L') to be $1.2''$ and its associated characteristic velocity $V_n{}' = 0.26$ km s^{-1} using H^{13}CN and H^{13}CO$^+$ 4–3 in DR21(OH). This size scale is significantly smaller that what is observable with the CARMA dataset; however, this is approximately the size scale observable in the data provided by Lai (described above). Unfortunately, to measure a drop in linewidth at the characteristic scale would require even higher resolution observations than what is available. Both the Hezareh et al. (2010) and the Lai data are of the same source and transition; however, the Hezareh et al. (2010) data have an exceedingly large beamsize. The authors note that there are only a few beamwidths across the map; as a result, the statistical significance of the result is low. Therefore the significance of the parameters may also be low.

The only other difference between the observations are the differing optical depths between the HCN and HCO$^+$ 1–0 lines. If HCO$^+$ is highly optically thick and HCN is only moderately optically thick, the deviation of the HCO$^+$ line shape from being Gaussian will effectively broaden the line. If this broadening is approximately the same magnitude as the line width narrowing due to coupling with a magnetic field, it could prevent the line width narrowing from being detected. However, it seems unlikely that this is occurring as such non-Gaussian fits to data would be discarded by the fitting procedure, which only accepts fits which are statistically similar to the source data.

6.10 Modified Technique

Under suggestion from Martin Houde (private communication), several modifications were performed to the fitting technique in order to better reproduce the analysis in Li & Houde (2008). The basic fitting routine was altered to independently fit HCO^+ and HCN (without bootstrapping the HCN fits from the HCO^+ results) and to remove the limitation on the number of Gaussians that the procedure fits. The first and second moments of all the fits are then calculated (for Gaussian lines, the first moment corresponds to the center velocity, while the second component corresponds to the standard deviation). If a profile was fit by several Gaussians, the first and second moments are averaged together to calculate a modified line width. If there are several significant velocity components in the spectra (as is with DR21(OH)), the fits have to be grouped by central velocity in order to ensure that the correct linewidths are associated with the correct velocity components.

The reason behind these modifications is to account for the possibility that the HCO^++ line may be fit by a single Gaussian component, while HCN may be fit with multiple Gaussians. This modified technique would be able to detect if one of the HCN fits has a mean velocity and line width equal to the HCO^+ line and a second, broader fit that corresponds to the ion-neutral line width broadening effect. The original technique, in which only the individual Gaussians are compared, would find that that one Gaussian component has the same line width in the two species, while the extra HCN broad component does not have a corresponding HCO^+ component and would be discarded. If the second moments are computed from the purely Gaussian description of the observed line profiles, a broader linewidth would be measured for the HCN line due to the broader second Gaussian component that does not exist for the HCO^+ line. The gridding technique remains unchanged from that described above.

This modified technique was applied to the CARMA observations of DR21(OH) (Fig. 6.15). From this analysis there was no change to the results. Visual inspection of the fits resulted in no additional Gaussian components being fit; in fact, this modified procedure resulted in fewer overall matches between HCO^+ and HCN. From previous measurements of the ion-neutral line width effect (Li & Houde, 2008), the magnitude of the effect was measured as several tenths of a km s $^{-1}$. Since the velocity resolution of the CARMA data is ~ 0.4 km s^{-1}, it is possible that the CARMA data cannot measure the line width widening effect. Additionally, if the intensity of the wide HCN component is low enough, the CARMA dataset may not have a high enough signal-to-noise in order to detect it.

6.11 Conclusions

The aims of this project was to reproduce the technique of Li & Houde (2008) and apply it to the CARMA datasets. From these analyses we have been able to conclude the following:

- Based on our analysis technique, there is no evidence of line width narrowing (or broadening) using the CARMA datasets.

- In attempting to recreate the linewidth comparison in two different regions of DR21(OH) originally presented by Li et al. (2010), we did not observe the line width variations presented in that analysis.
- The linewidth analysis technique was applied to the Serpens Main dataset presented in the CLASSy project without any detection of linewidth narrowing.
- The linewidth analysis technique was applied to $H^{13}CO^+$ and $H^{13}CN$ data of DR21(OH) provided by Shih-Ping Lai with no observable linewidth narrowing.
- A modified technique suggested by Martin Houde (private communication) was applied to the CARMA DR21(OH) dataset, with no noticeable linewidth narrowing.
- Through analysis of the modified technique, we determined that the limited velocity resolution and limited signal-to-noise ratio of the CARMA data may be preventing the detection of the larger linewidth associated with the HCN component.
- The 1–0 transitions do not show the linewidth narrowing effect, however higher order transitions (such as the 4–3 line) do. There may be a yet undiscovered effect which is causing this disparity.

From these results, it has become apparent that this technique may be significantly dependent on the velocity resolution and sensitivity of the source dataset. A further analysis to test this hypothesis is necessary to determine if there is an effect caused by the HCN and HCO^+ 1–0 lines, or if the lack of detection in this study is purely dependent on spectral resolution and sensitivity.

Support for CARMA construction was derived from the states of California, Illinois, and Maryland, the James S. McDonnell Foundation, the Gordon and Betty Moore Foundation, the Kenneth T. and Eileen L. Norris Foundation, the University of Chicago, the Associates of the California Institute of Technology, and the National Science Foundation. Ongoing CARMA development and operations are supported by the National Science Foundation under a cooperative agreement (NSF AST 08-38226), and by the CARMA partner universities.

6.12 Figures

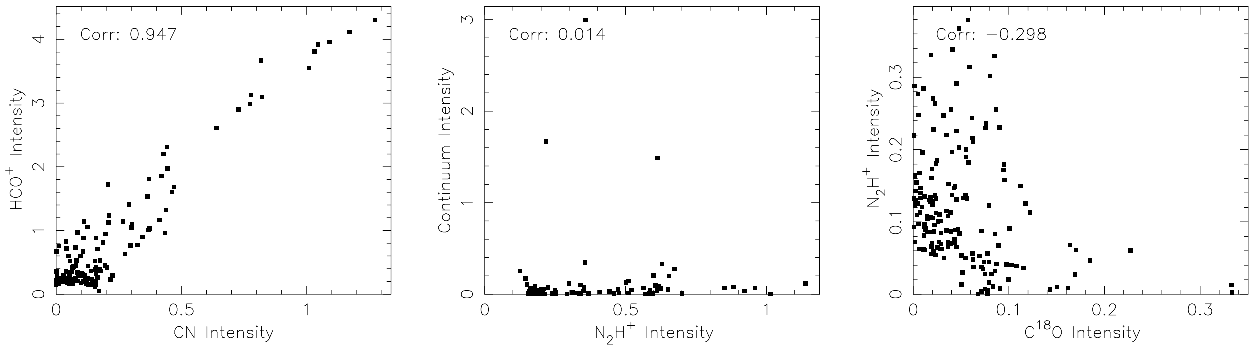

Figure 6.1 Examples of correlation value extrema in the CARMA dataset with respect to intensity comparison plots. The figure on the left (G10.6, CN-HCO$^+$ correlation) represents the largest correlation (0.947) calculated. The figure from the center (G10.6, N$_2$H$^+$-Continuum correlation) represents a value close to no correlation (0.014). The figure on the right (W3(OH), (C^{18}O-N$_2$H+ correlation) represents the largest anti-correlation (-0.298) seen in the CARMA data.

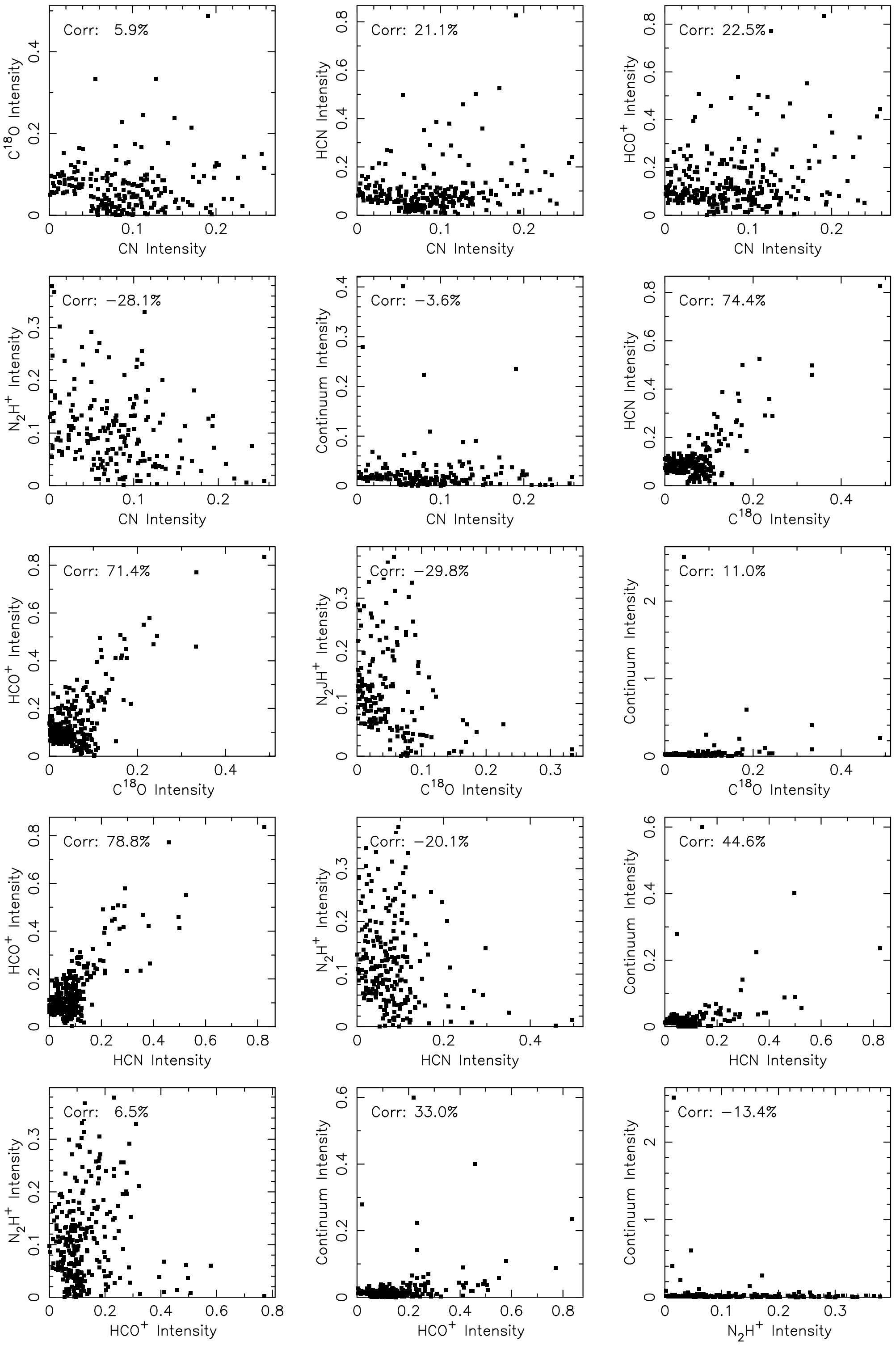

Figure 6.2 W3(OH) Correlation Map. Each potential pair of species to compare are represented. Each point represents a pair of intensity values. Since interferometer data is generally spatially oversampled, a data value is only sampled once per beam area.

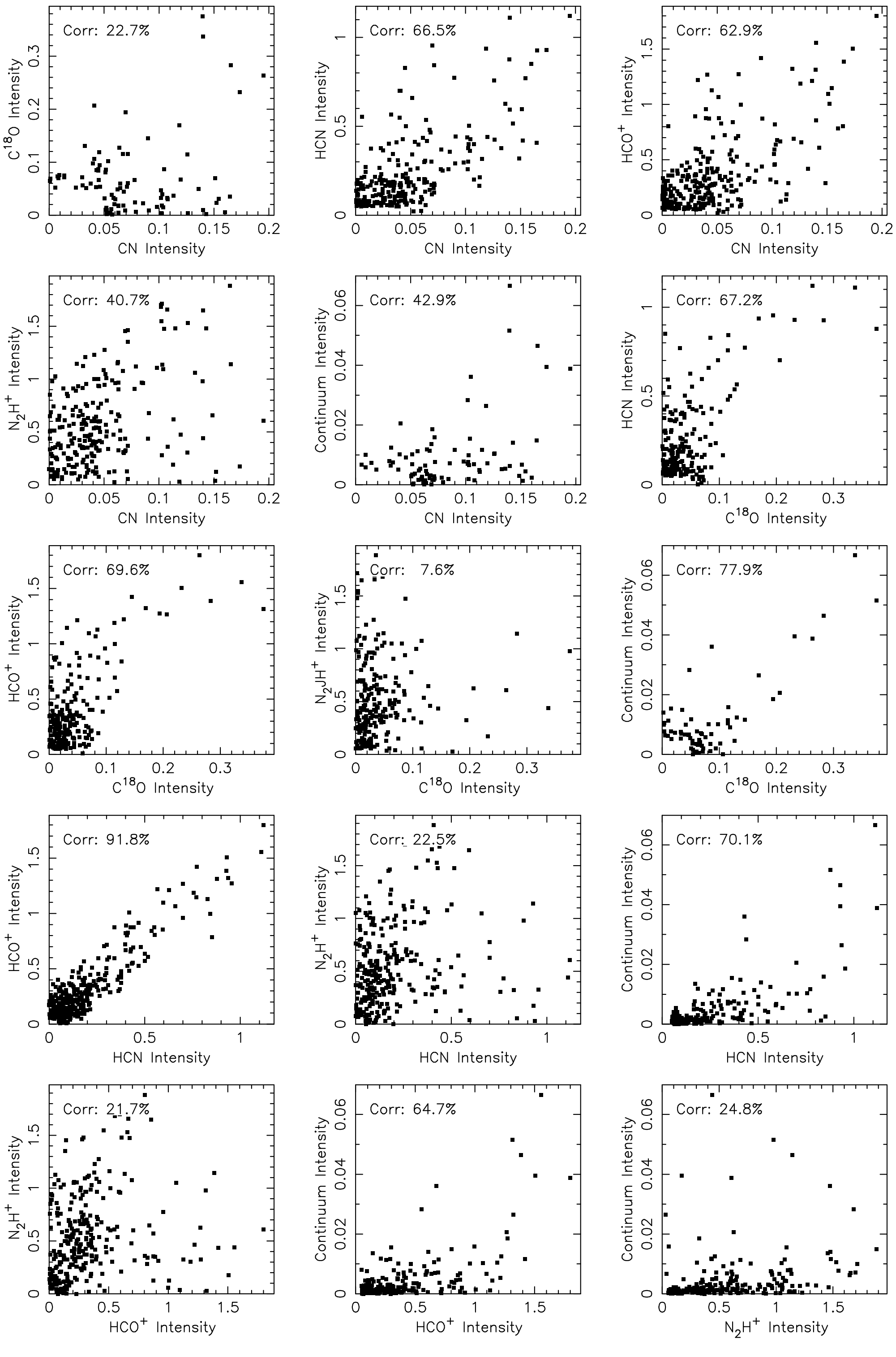

Figure 6.3 Same as Figure 6.2 but for DR21(OH).

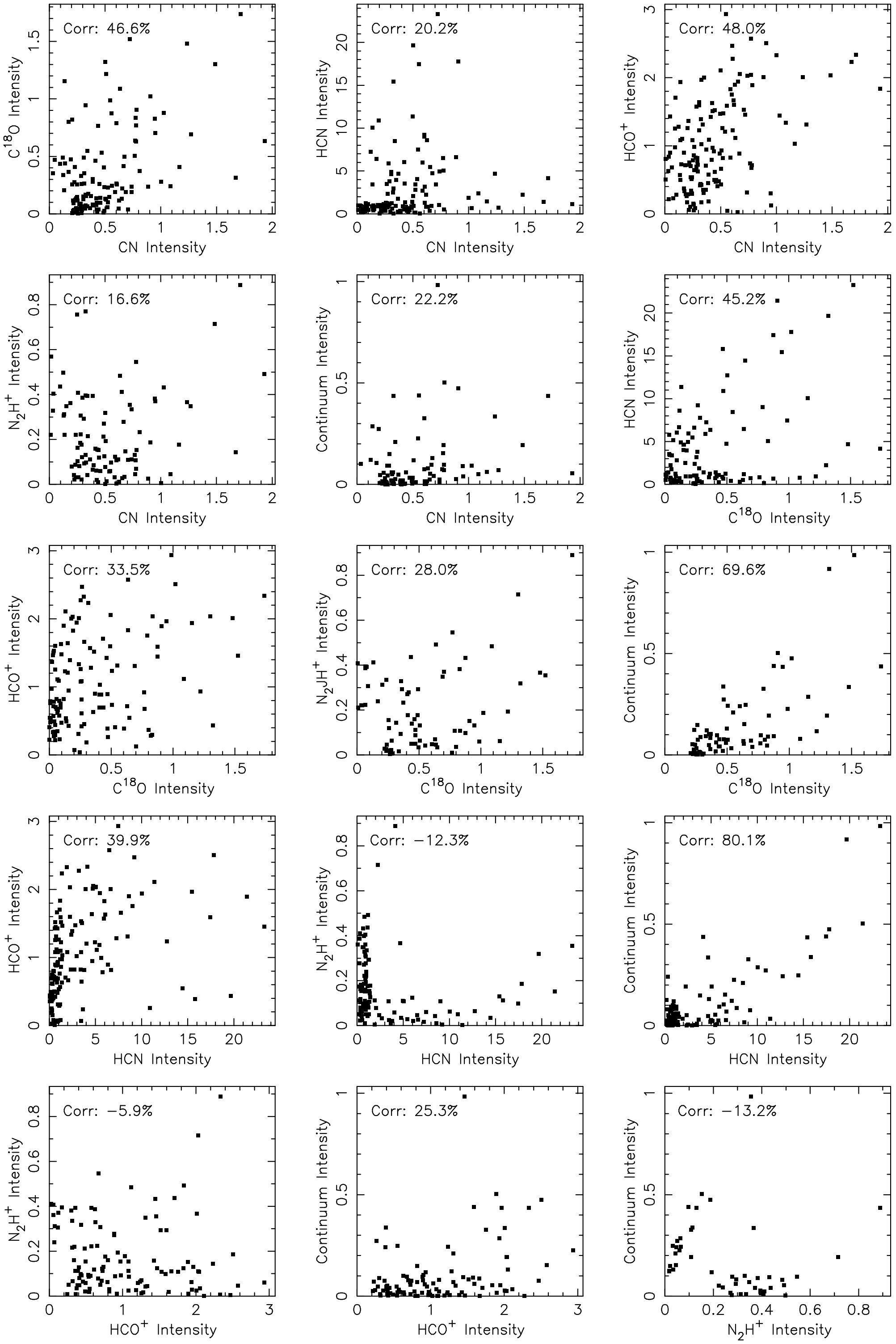

Figure 6.4 Same as Figure 6.2 but for OMC1.

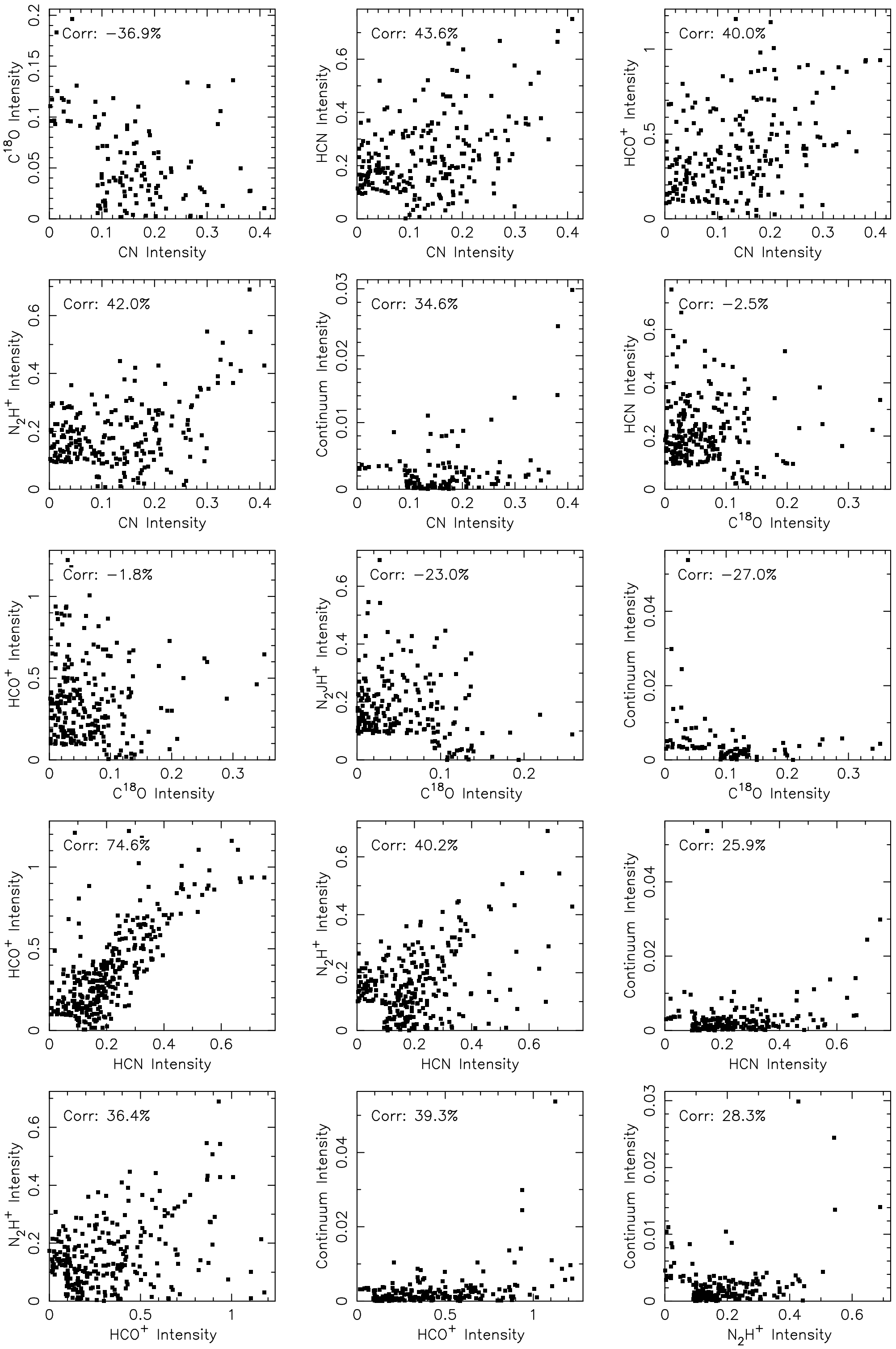

Figure 6.5 Same as Figure 6.2 but for S140.

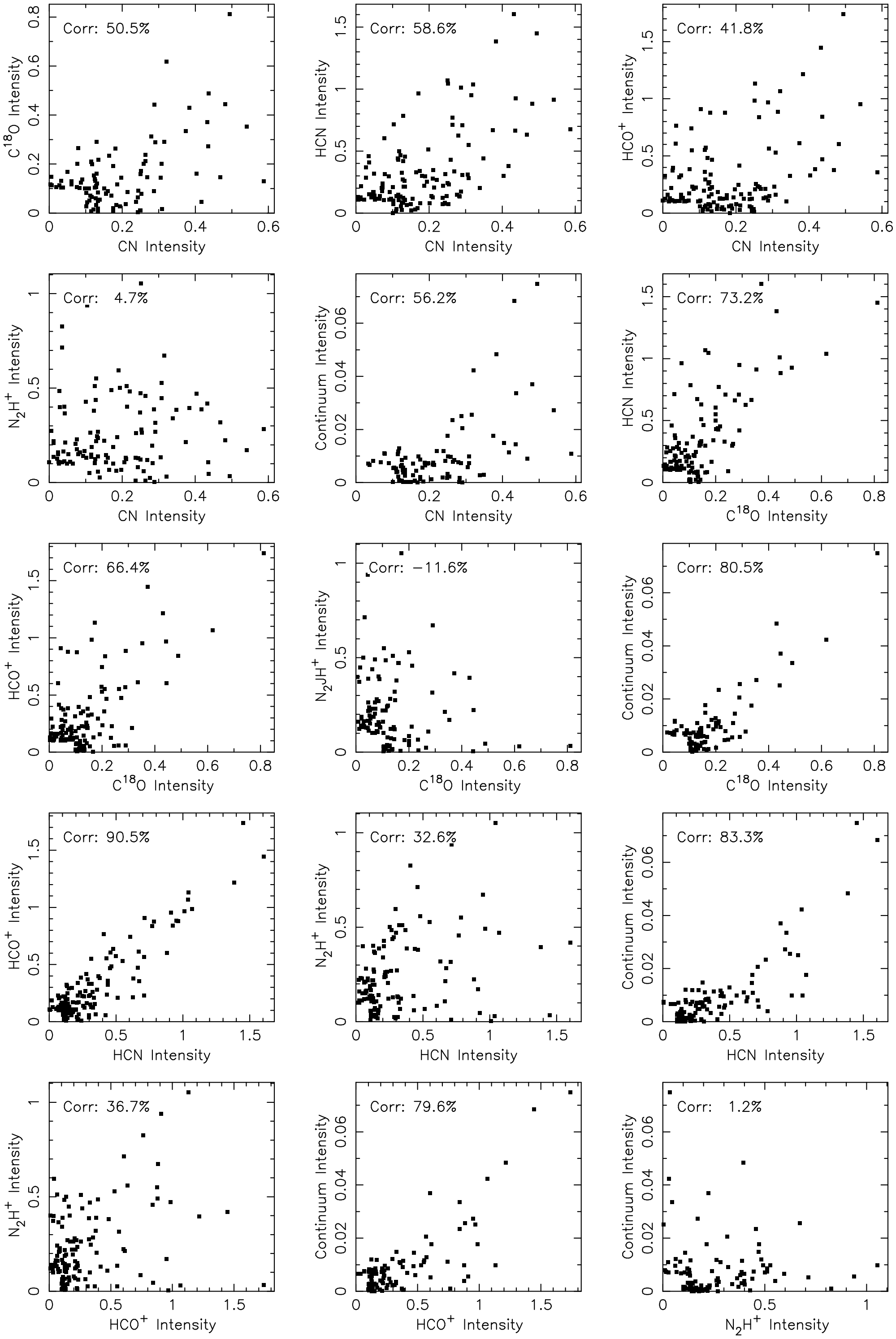

Figure 6.6 Same as Figure 6.2 but for S255.

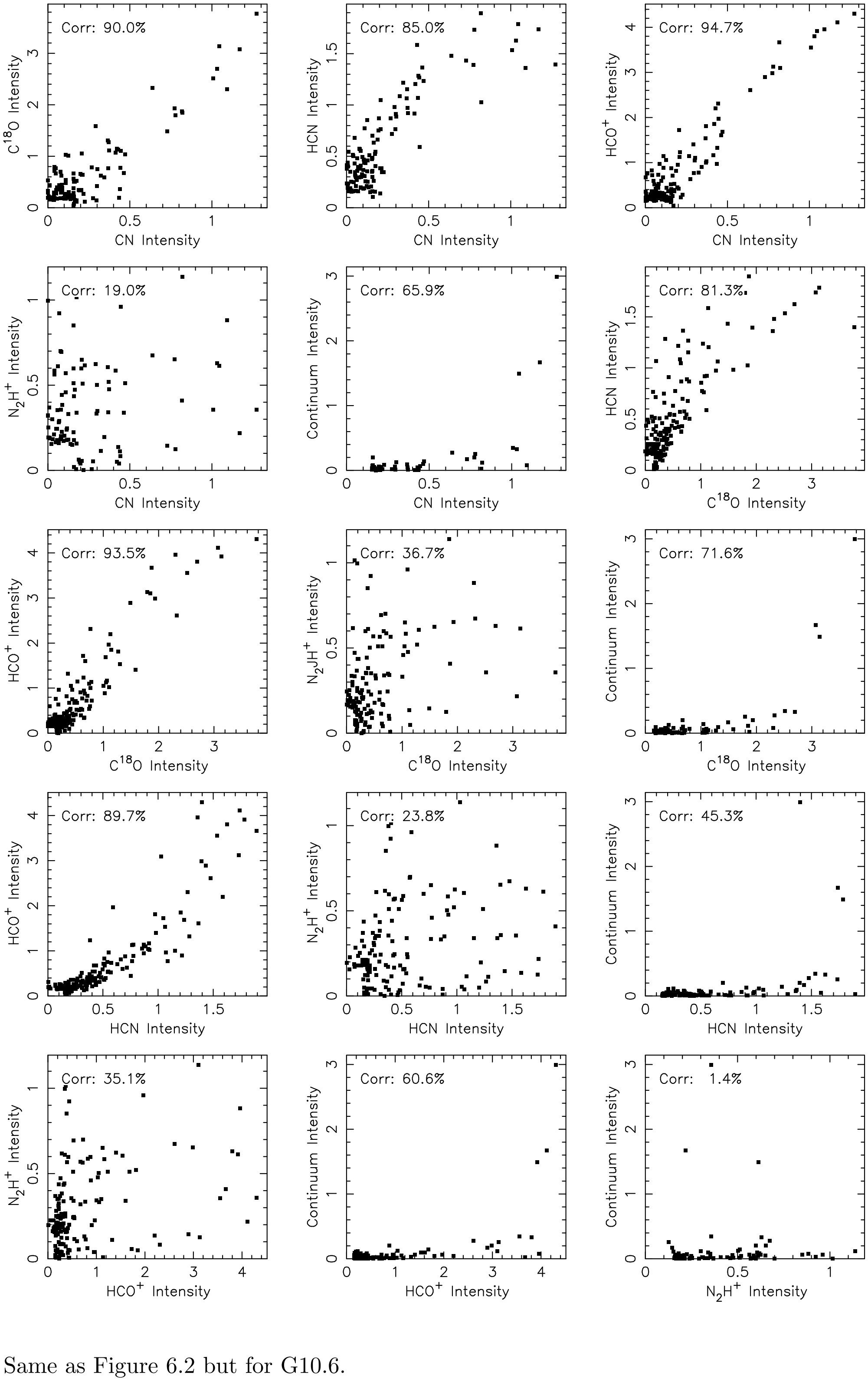

Figure 6.7 Same as Figure 6.2 but for G10.6.

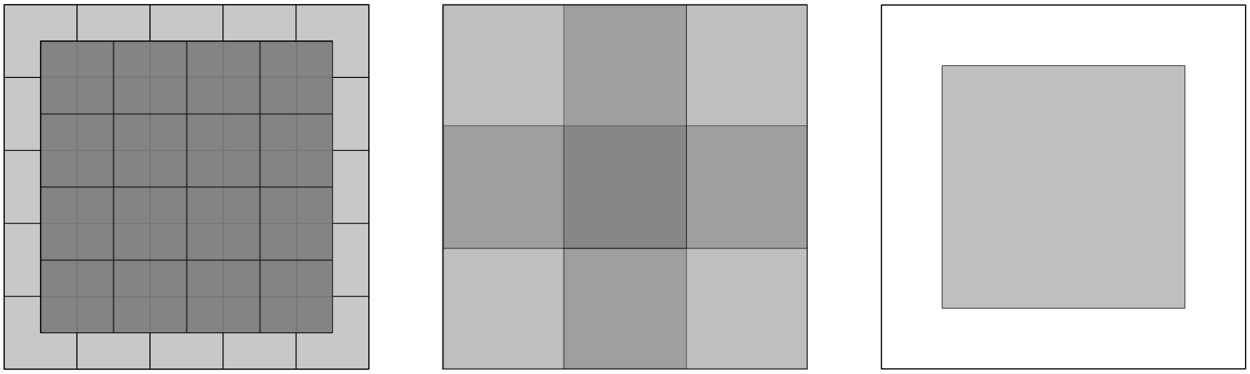

Figure 6.8 Examples of the three gridding techniques. The primary gridding technique (left), shows how the additional grids at half-gridsize spacings are oriented with respect to the rest of the grids. The corner box grid type (middle), and the center box grid type (right), usually did not yield any useful results since the line shapes greatly differed from being Gaussian, and large frequency differences between the two species were observed. In the CARMA datasets, these two grid types would be used to attempt to calculate linewidths at size scales above $64''$.

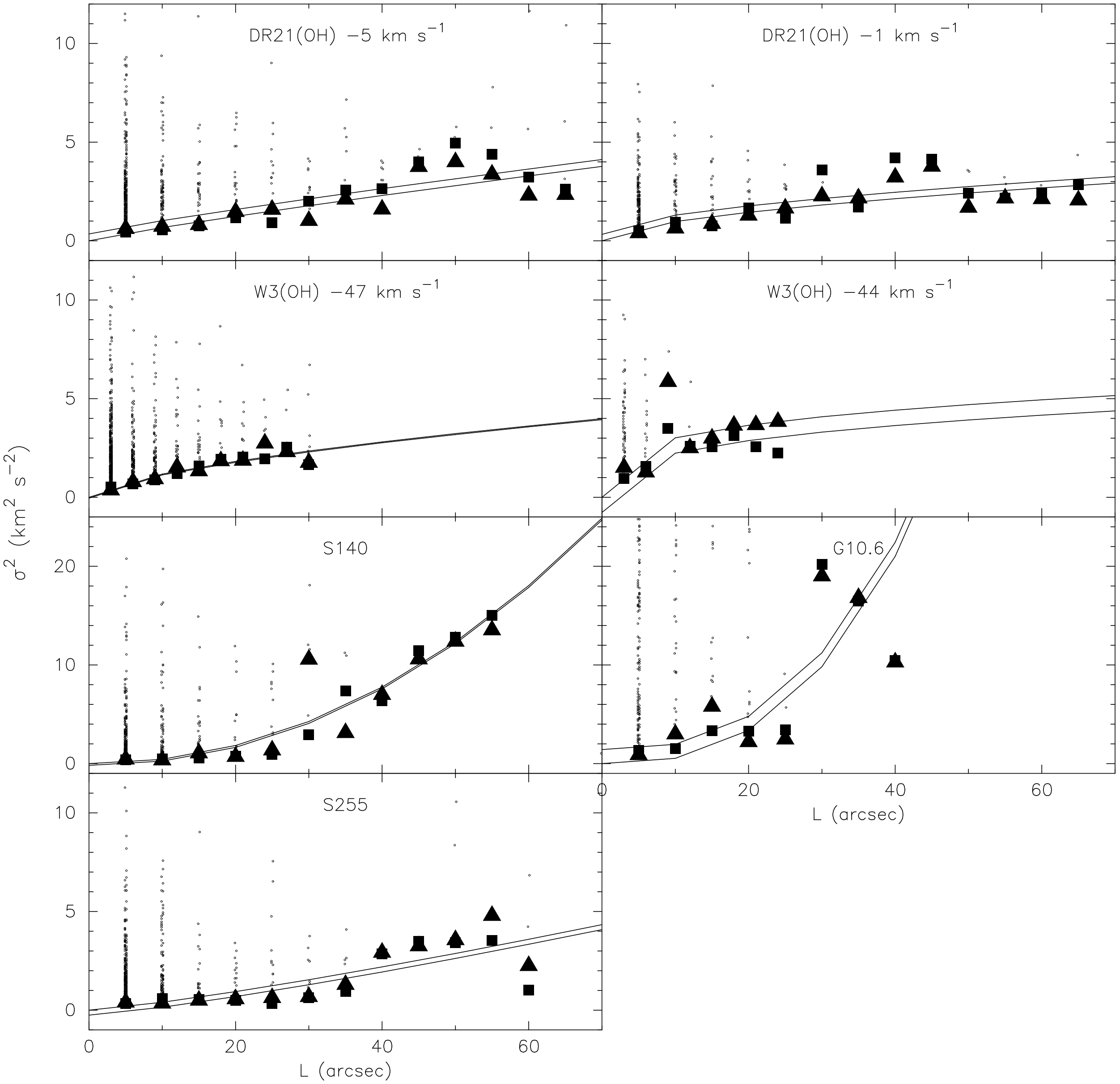

Figure 6.9 Scalesize (L) versus minimum linewidth squared fits for each object in the CARMA dataset. None of the objects show ion species linewidth narrowing to a statistically significant amount; the uncertainties in the parameter fits show that the data does not support the model of linewidth minima following a Kolmogorov-like power law.

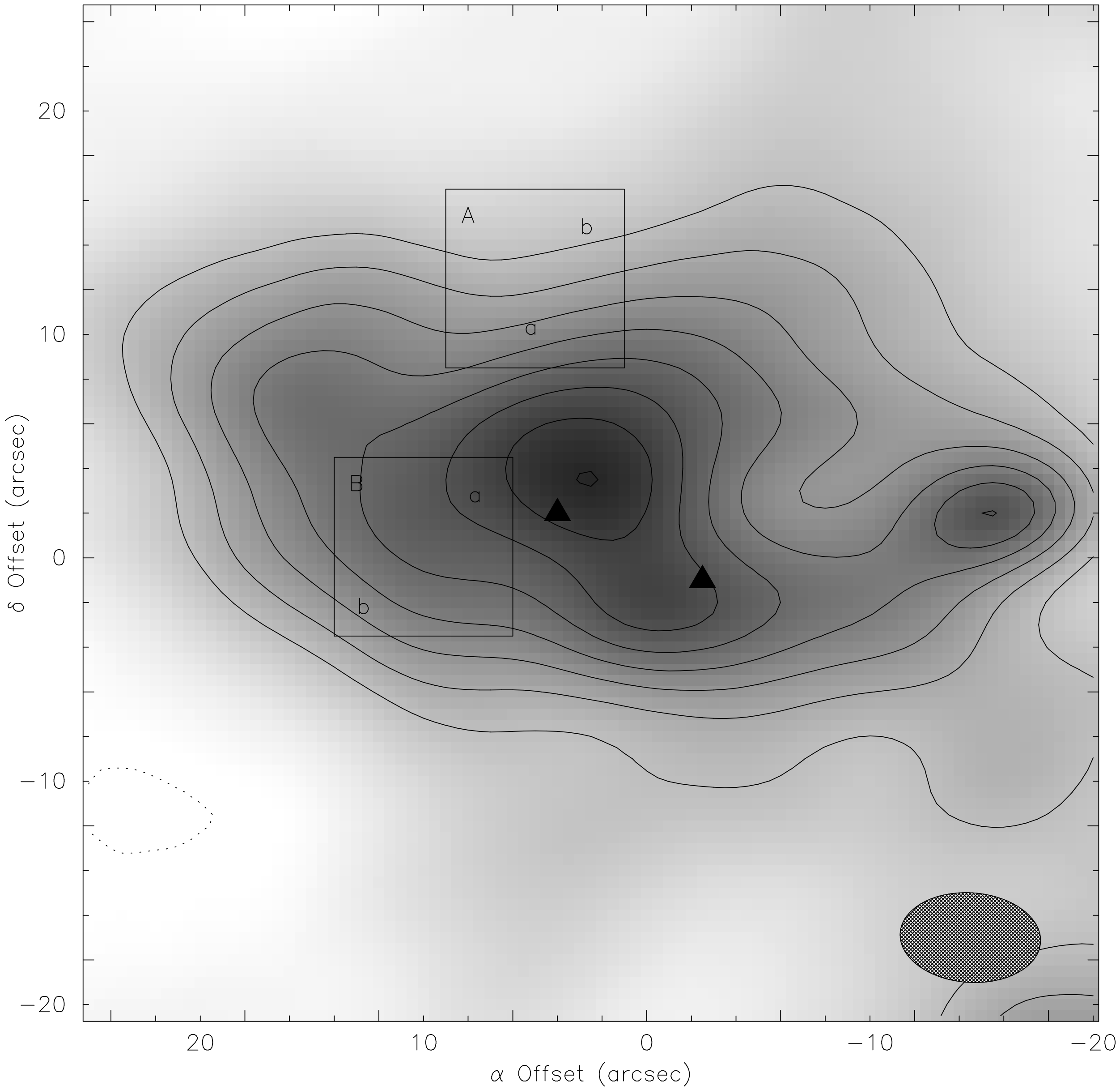

Figure 6.10 Grayscale image and contours of HCO$^+$ 1–0 emission of DR21(OH). The square boxes are two regions, one weak field (A) and one strong field (B), as determined by Li et al. (2010). Each box has two subregions that are additionally plotted. The triangles represent the peak positions of the two continuum sources.

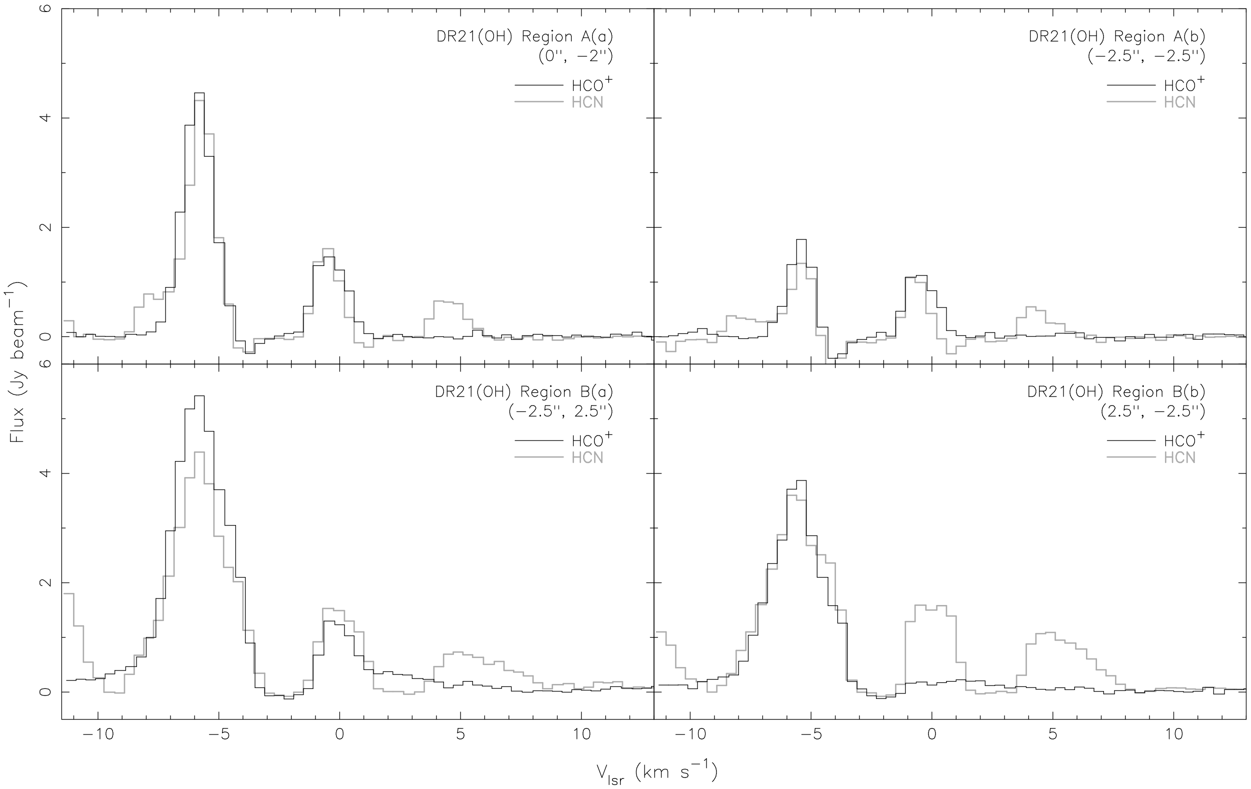

Figure 6.11 Equivalent positions in the CARMA dataset to those found in Li et al. (2010) representing the strongest and weakest line strengths in the regions A and B of DR21(OH).

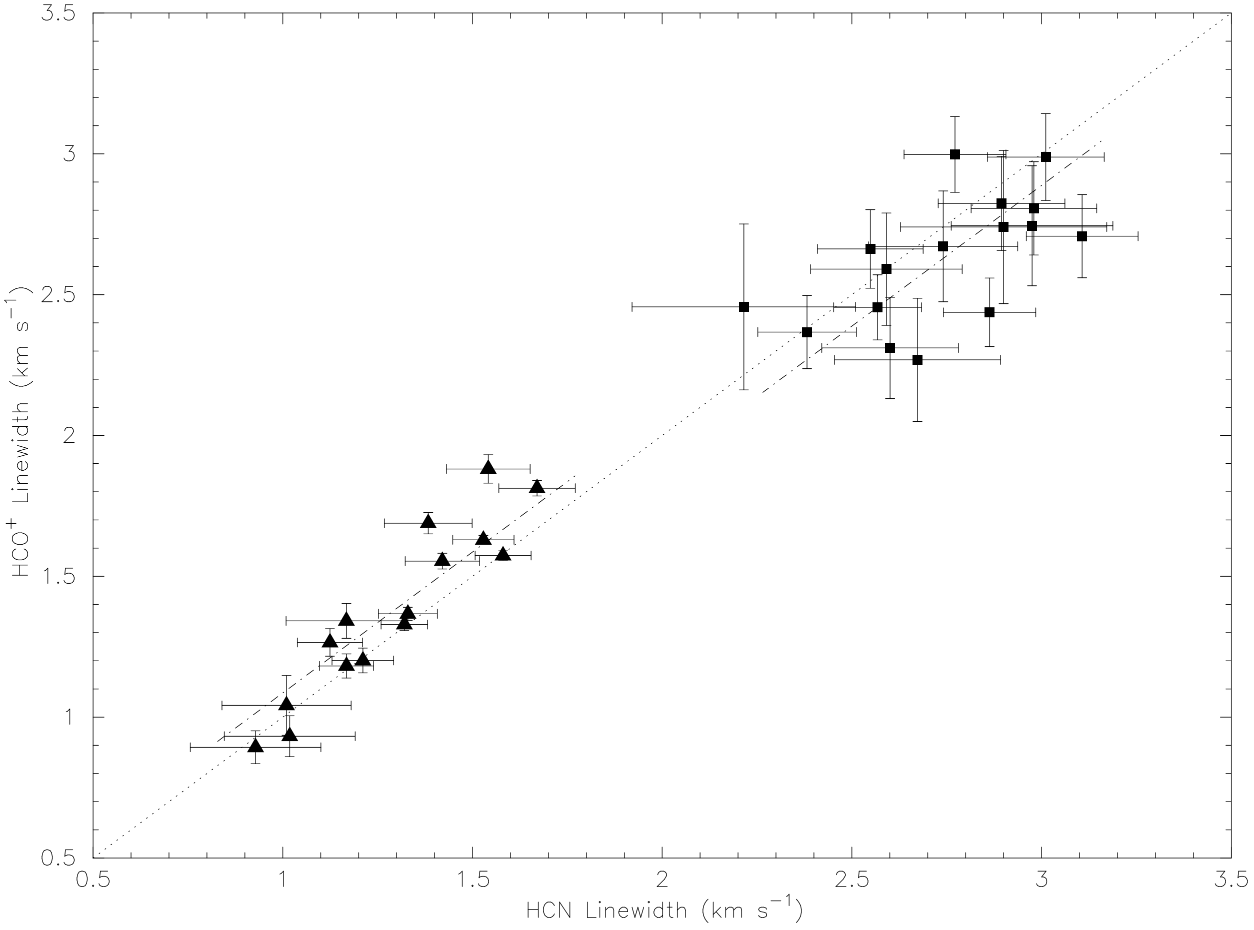

Figure 6.12 HCN linewidth versus HCO$^+$ linewidth in the two regions A (triangles) and B (squares). The dotted line represents a 1 to 1 relationship in linewidth, while the dashed lines are a least squares fit of the datapoints in A and B to a straight line. Not only do the points in A tend to be about 1 km s^{-1} larger in both HCN and HCO$^+$, but both regions fall almost exactly on the 1 to 1 line, significantly different to what Li et al. (2010) observed in the H^{13}CO$^+$ and H^{13}CN lines. The errorbars show the 1σ (68%) confidence values for each linewidth fit.

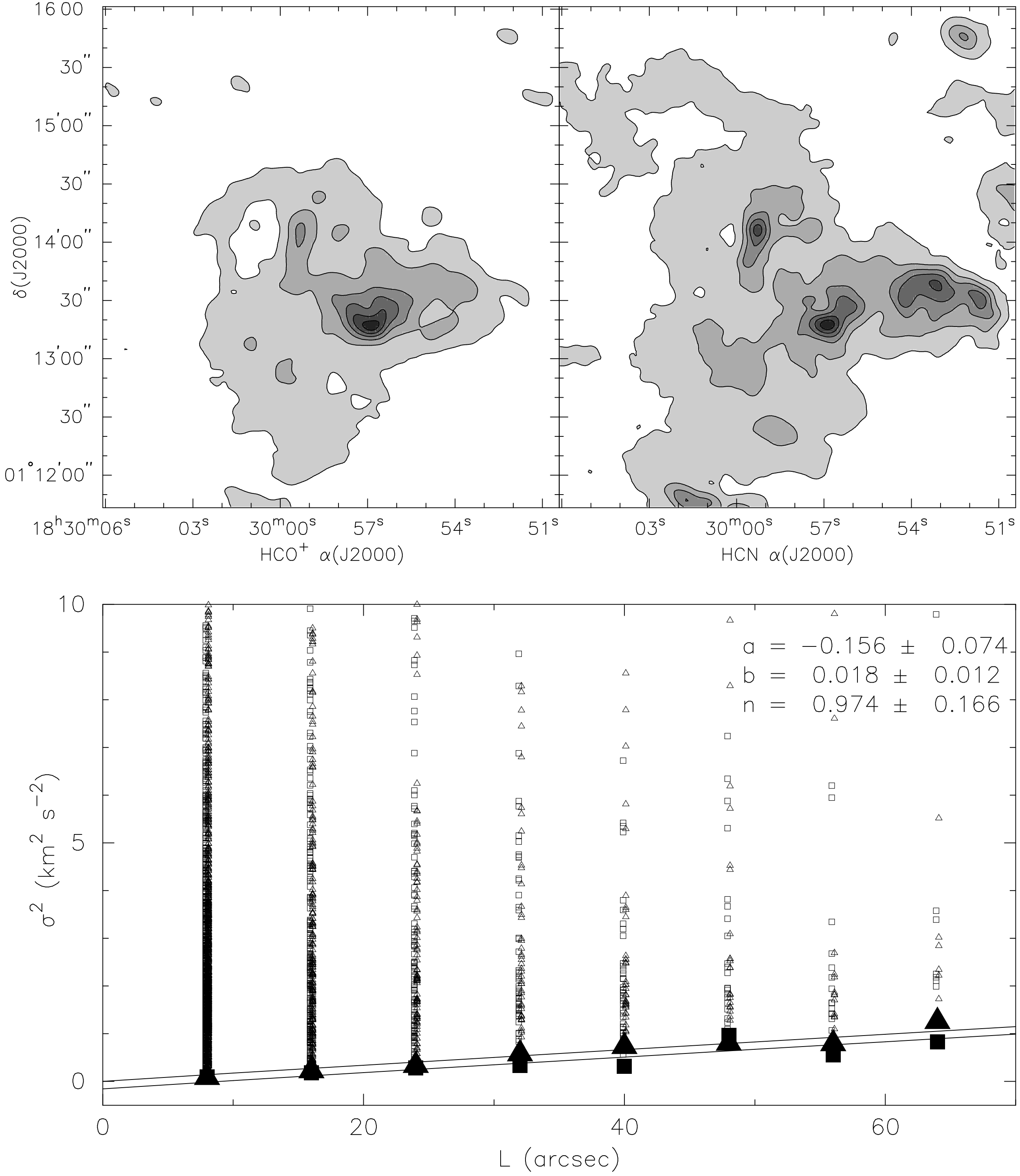

Figure 6.13 The top panels show integrated HCO$^+$ and HCN emission from a $3.7' \times 4.0'$ region of the Serpens Main molecular cloud as part of the CLASSy survey. The bottom panel is a plot of the results from the ion-neutral linewidth fitting technique described in the previous sections. While there is a slight signature of HCO$^+$ linewidth narrowing, the power law exponent is near 1, unlike that of Kolmorgorov-like turbulence.

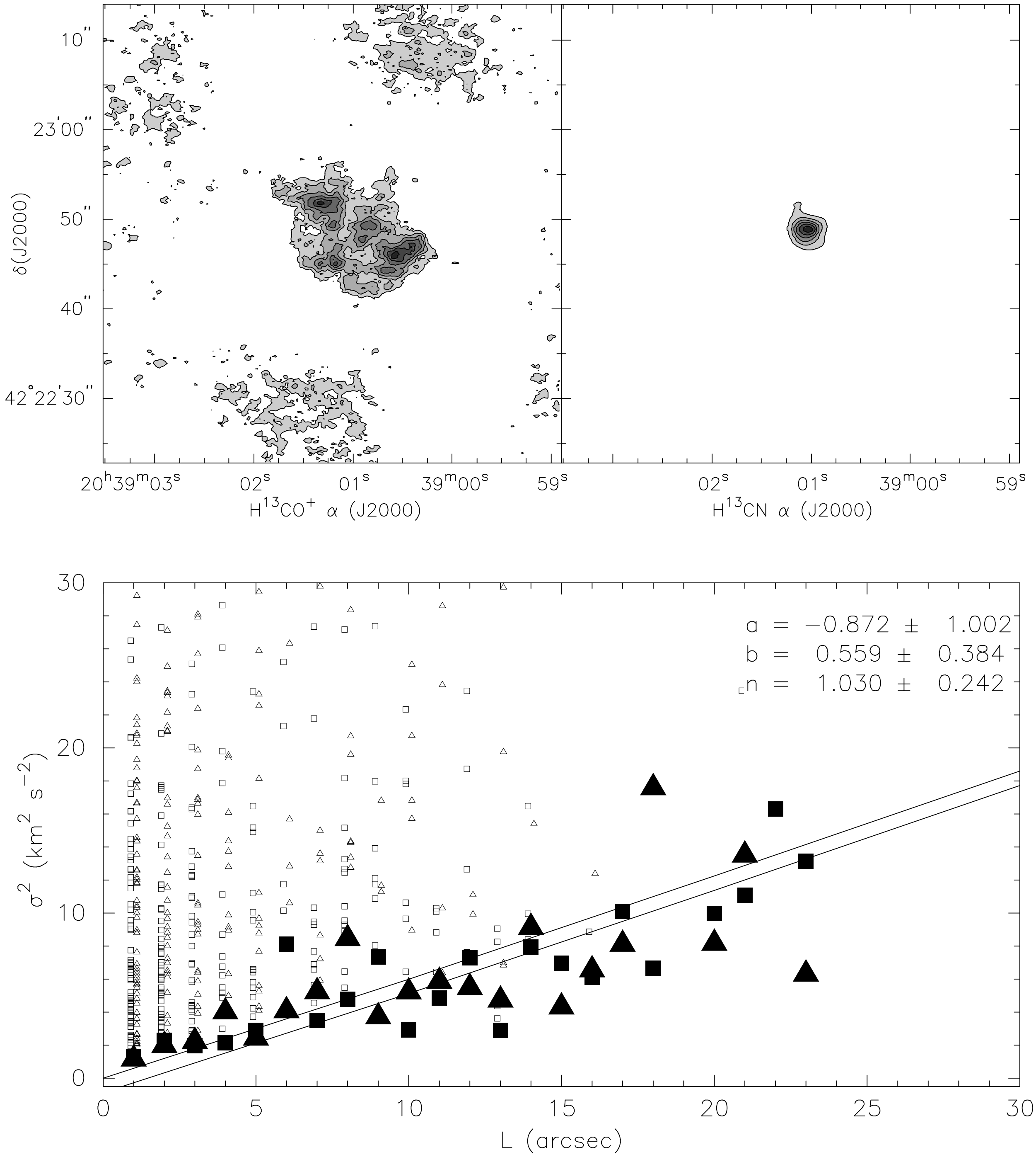

Figure 6.14 Results from the ion-neutral linewidth analysis using $H^{13}CO^+$ and $H^{13}CN$ 4–3 emission from DR21(OH) using the SMA provided by Shih-Ping Lai. The results from this analysis are similar to the rest of the objects sampled; no clear signature of linewidth narrowing was observed. However, the $H^{13}CO^+$ data had a very low signal-to-noise ratio resulting in large sections of the region not containing many matching fits.

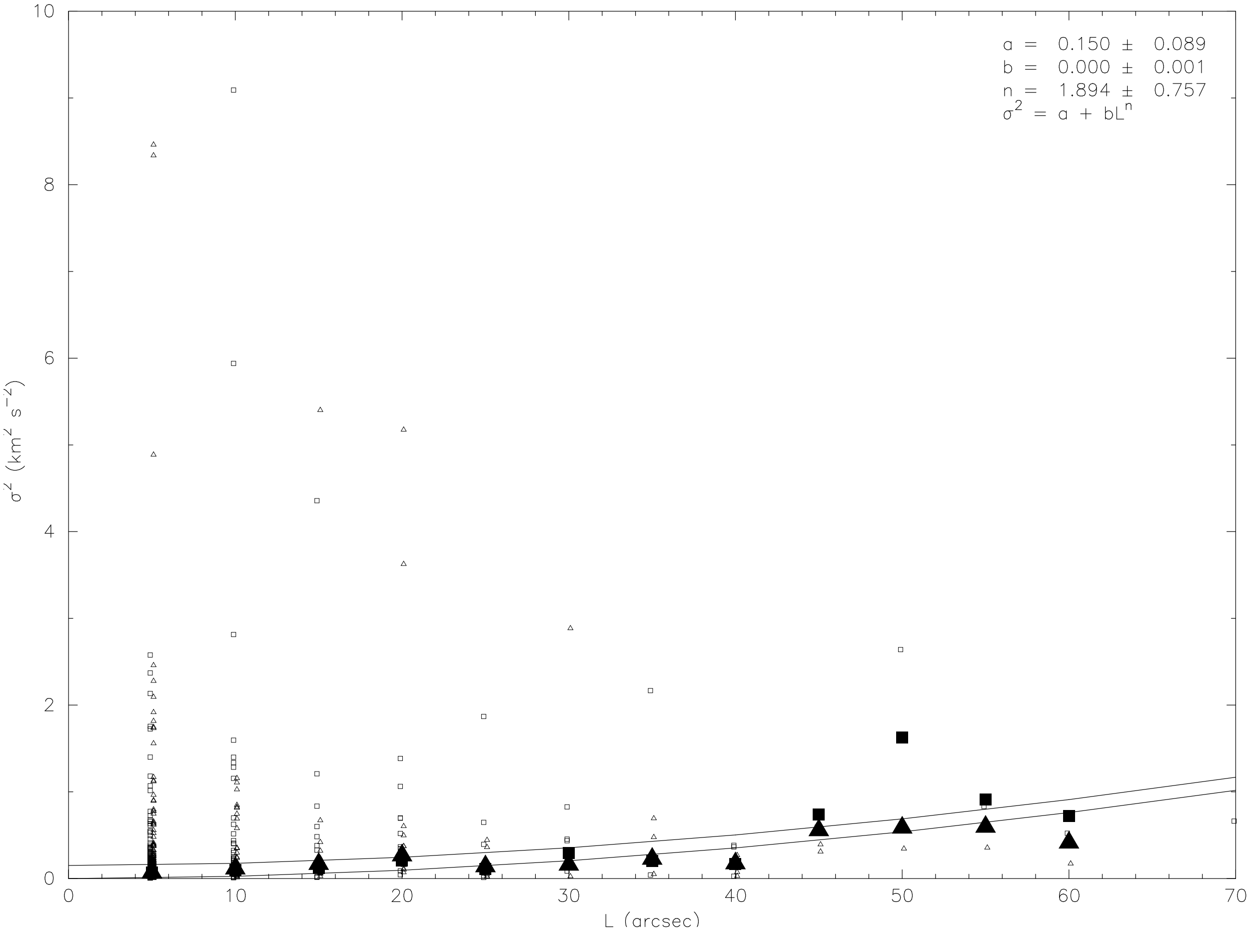

Figure 6.15 Results from the modified ion-neutral linewidth analysis on DR21(OH).

Chapter 7

Conclusions

The various topics covered in this project resulted in several conclusions. To summarize, they are repeated here:

Testing Magnetic Star Formation Theory

Previous Zeeman studies of magnetic fields in molecular clouds have not been definitive in testing the two extreme-case models of star formation. The mean mass-to-flux ratios M/Φ found from these statistical studies were slightly supercritical – consistent with either theory. Detailed ambipolar diffusion models for two clouds found excellent agreement with the observations, although both required the field to be nearly in the plane of the sky in order not to produce line-of-sight fields much stronger than observed. Uncertainties in the angle between $\mathbf{B}$ and the line of sight and in the total hydrogen column density are inherent in measuring with Zeeman observations. In order to mitigate these uncertainties, we have measured the ratio of M/Φ between the envelopes and cores of four molecular clouds in order to test ambipolar diffusion (strong magnetic fields) versus turbulence (weak magnetic fields) driven star formation theory. The theory of star formation that hypothesizes clouds initially supported by strong magnetic fields, with evolution and core formation being driven by ambipolar diffusion, predicts that the central M/Φ must increase as ambipolar diffusion acts. Idealized models predict that the increase in M/Φ up to the point when the core becomes supercritical and gravitational collapse proceeds is approximately equal to the inverse of the amount by which the original cloud was subcritical; that is, $\mathcal{R}' > 1$. The probability that all four of our clouds have $\mathcal{R}' > 1$ is 3×10^{-7}, a highly significant result. On the other hand, simulations which form clouds and cores by turbulence acting in a weak magnetic field environment preferentially yield a M/Φ ratio between core and envelope $\mathcal{R} < 1$, in agreement with our results.

Telescope availability limitations allowed only four clouds to be observed; unfortunately the extremely large amount of telescope time required precludes expanding this experiment beyond four clouds for the foreseeable future. The theoretical predictions of $\mathcal{R}$ and $\mathcal{R}'$ are based on idealized ambipolar diffusion models and idealized turbulence simulations. Nonetheless, the clear conclusion from our experiment is that at least for these four clouds, the prediction of the idealized ambipolar diffusion models does not agree with our observational results, while the prediction of initially supercritical turbulence-driven simulations does. Still untested is whether simulations that include both significant magnetic fields and turbulence better match the data than either of the extreme cases. We suggest that all theorists who simulate the formation and evolution of molecular clouds and cores test their simulations against the results of this experiment in the manner of Lunttila et al. (2008); that is, by calculating Stokes I and V spectra of OH from the simulations and "observing" B_{LOS} with our beam patterns (Figure 2.1).

Self-Consistent Analysis of OH Zeeman Observations

CHT concluded that their measurements of the ratios of M/Φ between envelopes and cores did not agree with the prediction of the ambipolar diffusion model. Here we have shown that the CHT analysis is internally self consistent; their conclusions are valid within the framework of the assumptions they made. The validity of the MT paper rests on two pillars: (1) that the CHT data analysis procedure is unambiguously inconsistent with the data itself, and (2) that MT have a superior analysis technique. We have demonstrated that neither of these pillars of their paper is correct. The conclusions of Crutcher et al. (2009) therefore stand – the observed variations of M/Φ from envelope to core are not consistent with the prediction of the ambipolar diffusion driven theory of star formation. This conclusion does not, of course, rule out the possibility that there are structures in magnetic field morphology near dark cloud cores; higher resolution and higher sensitivity observations would be necessary to investigate this possibility.

The approach of CHT to test the ambipolar diffusion driven model of star formation by measuring the change in M/Φ between envelope and core is a powerful one that should be further exploited, since it reduces uncertainties in actual values of magnetic field direction and mass estimates by taking ratios. Unfortunately, such experiments will require very large amounts of telescope time. However, use of the eVLA for OH Zeeman mapping and ALMA for CN Zeeman mapping may make it possible to extend this technique to smaller scales without requiring such large assignments of telescope time.

Although the apparent field reversals are supported by the data, the presence of field reversals is contrary to ambipolar diffusion theory.

Structure and Composition of Molecular Clouds with CN Zeeman Observations

We mapped the 2 arcmin^2 region around six molecular clouds with CARMA, in which previous single-dish CN Zeeman observations detected a strong magnetic field. In determining which gas was producing the magnetic field, we were able to see the following features and make the following conclusions from their presence:

- Comparison between CARMA spectra and spectra obtained with the IRAM-30 meter telescope (Falgarone et al., 2008) yields that CARMA detects approximately 50% of the material in this region.
- CN is an ideal high density tracer that in some situations may be more useful than N_2H^+ (such as conditions where N_2H^+ is frozen out). However, its low line intensity requires a significantly greater amount of observing time in order to achieve an equivalent sensitivity.
- A strong absorption feature in HCO^+, HCN, and CN was detected towards the continuum source in W3(OH) whose strength and line saturation implies the existence of a cold, optically thick region in front of the continuum source.
- Selective depletion of N_2H^+ in comparison with the CN and HCO^+ distribution indicates that N_2H^+ is reacting with CO to form HCO^+. This reduces the effectiveness of N_2H^+ as a high-density tracer, and favors the use of species, such as CN, in objects with similar chemical composition to W3(OH). These measurements additionally support the usefulness of CN as a high density tracer and confirms the hypothesis that CN Zeeman mapping will probe the magnetic field strength in the high density regions of molecular cloud clumps.

These conclusions lead to the result that future CN Zeeman mapping at high resolution with an interferometer is feasible and that these targets are ideal to perform such mapping.

First Interstellar HCO^+ Maser

Observations of DR21(OH) have revealed the presence of a compact object which is dominated by non-thermal emission. The extremely compact size of this object coupled with its large brightness leads to the following conclusions:

- The source is co-located with a known strong methanol maser.
- It lies along the edge of an outflow which gives support to previous theories that masers can arise due to the interactions of high velocity outflows with cold, dense clumps of molecular gas.
- Its small spatial size most likely prevented its detection before now; emission from this source would be beam diluted to levels indistinguishable from thermal emission.
- This object is very likely an unsaturated maser, the first observed in HCO^+.

In order to further confirm that this source is indeed a maser, future observations to look for anomalous level populations in higher order HCO^+ transitions should be performed.

Ion-Neutral Linewidth Analysis

The aims of this project was to reproduce the technique of Li & Houde (2008) and apply it to the CARMA datasets. From these analyses we have been able to conclude the following:

- Based on our analysis technique, there is no evidence of line width narrowing (or broadening) using the CARMA datasets.
- In attempting to recreate the linewidth comparison in two different regions of DR21(OH) originally presented by Li et al. (2010), we did not observe the line width variations presented in that analysis.
- The linewidth analysis technique was applied to the Serpens Main dataset presented in the CLASSy project without any detection of linewidth narrowing.
- The linewidth analysis technique was applied to $H^{13}CO^+$ and $H^{13}CN$ data of DR21(OH) provided by Shih-Ping Lai with no observable linewidth narrowing.
- A modified technique suggested by Martin Houde (private communication) was applied to the CARMA DR21(OH) dataset, with no noticeable linewidth narrowing.
- Through analysis of the modified technique, we determined that the limited velocity resolution and limited signal-to-noise ratio of the CARMA data may be preventing the detection of the larger linewidth associated with the HCN component.
- The 1–0 transitions do not show the linewidth narrowing effect, however higher order transitions (such as the 4–3 line) do. There may be a yet undiscovered effect which is causing this disparity.

From these results, it has become apparent that this technique may be significantly dependent on the velocity resolution and sensitivity of the source dataset. A further analysis to test this hypothesis is necessary to determine if there is an effect caused by the HCN and HCO^+ 1–0 lines, or if the lack of detection in this study is purely dependent on spectral resolution and sensitivity.

7.1 Future Work

From the mapping performed in this project, it has been determined that long integration interferometric Zeeman mapping on these objects is feasible. From this, detailed mapping can be performed on these objects and core to envelope magnetic field intensities can be measured.

A project is currently scheduled to be observed with CARMA this summer to study the Zeeman effect in the CN 2–1 transition. This will focus on two regions in the DR21(OH) and W3(OH) molecular cloud regions, as determined by the mapping results presented in this thesis. It is currently unknown if the Zeeman effect can be measured in this transition; this project should be able to determine its feasibility. Being able to use the 2–1 transition of CN would allow Zeeman measurements to be performed with CARMA's 1mm dual polarization receivers. Although ALMA will have greater sensitivity than other observatories, having an instrument in the northern hemisphere that can perform this type of analysis will allow analysis of many sources (such as W3(OH)) that could not be observed otherwise.

References

Araya, E. D., Kurtz, S., Hofner, P., & Linz, H. 2009, ApJ, 698, 1321

Bally, J., & Lada, C. J. 1983, ApJ, 265, 824

Batrla, W., & Menten, K. M. 1988, ApJ, 329, L117

Becklin, E. E., & Neugebauer, G. 1967, ApJ, 147, 799

Beichman, C. A., Becklin, E. E., & Wynn-Williams, C. G. 1979, ApJ, 232, L47

Bergin, E. A., Alves, J., Huard, T., & Lada, C. J. 2002, ApJ, 570, L101

Bock, D. C.-J., Bolatto, A. D., Hawkins, D. W., et al. 2006, in Society of Photo-Optical Instrumentation Engineers (SPIE) Conference Series, Vol. 6267, Society of Photo-Optical Instrumentation Engineers (SPIE) Conference Series

Bourke, T. L., Myers, P. C., Robinson, G., & Hyland, A. R. 2001, ApJ, 554, 916

Briggs, D. S., Schwab, F. R., & Sramek, R. A. 1999, in Astronomical Society of the Pacific Conference Series, Vol. 180, Synthesis Imaging in Radio Astronomy II, ed. G. B. Taylor, C. L. Carilli, & R. A. Perley, 127

Caswell, J. L., Murray, J. D., Roger, R. S., Cole, D. J., & Cooke, D. J. 1975, A&A, 45, 239

Chen, H.-R., Welch, W. J., Wilner, D. J., & Sutton, E. C. 2006, in Astronomical Society of the Pacific Conference Series, Vol. 356, Revealing the Molecular Universe: One Antenna is Never Enough, ed. D. C. Backer, J. M. Moran, & J. L. Turner, 270

Ciolek, G. E., & Basu, S. 2000, ApJ, 529, 925

Ciolek, G. E., & Mouschovias, T. C. 1994, ApJ, 425, 142

Cowell, W. R., ed. 1984, Sources and Development of Mathematical Software, Prentice-Hall Series in Computational Mathematics, Cleve Moler, Advisor (Upper Saddle River, NJ 07458, USA: Prentice-Hall), xii + 404

Crampton, D., & Fisher, W. A. 1974, Publications of the Dominion Astrophysical Observatory Victoria, 14, 283

Crutcher, R. M. 1979, ApJ, 234, 881

Crutcher, R. M. 1999, ApJ, 520, 706

Crutcher, R. M., Hakobian, N., & Troland, T. H. 2009, ApJ, 692, 844

Crutcher, R. M., Hakobian, N., & Troland, T. H. 2010, MNRAS, 402, L64

Crutcher, R. M., & Kazes, I. 1983, A&A, 125, L23

Crutcher, R. M., Mouschovias, T. C., Troland, T. H., & Ciolek, G. E. 1994, ApJ, 427, 839

Crutcher, R. M., Roberts, D. A., Troland, T. H., & Goss, W. M. 1999a, ApJ, 515, 275

Crutcher, R. M., & Troland, T. H. 2000, ApJ, 537, L139

Crutcher, R. M., Troland, T. H., Goodman, A. A., et al. 1993, ApJ, 407, 175

Crutcher, R. M., Troland, T. H., Lazareff, B., & Kazes, I. 1996, ApJ, 456, 217

Crutcher, R. M., Troland, T. H., Lazareff, B., Paubert, G., & Kazès, I. 1999b, ApJ, 514, L121

Daniel, F., Cernicharo, J., & Dubernet, M.-L. 2006, ApJ, 648, 461

Dickel, J. R., Dickel, H. R., & Wilson, W. J. 1978, ApJ, 223, 840

Downes, D., & Rinehart, R. 1966, ApJ, 144, 937

Eisner, J. A., & Carpenter, J. M. 2006, ApJ, 641, 1162

Elmegreen, B. G. 2000, ApJ, 530, 277

Elmegreen, B. G., & Scalo, J. 2004, ARA&A, 42, 211

Evans, II, N. J., Mundy, L. G., Kutner, M. L., & Depoy, D. L. 1989, ApJ, 346, 212

Falgarone, E., & Gilmore, W. 1981, A&A, 95, 32

Falgarone, E., Troland, T. H., Crutcher, R. M., & Paubert, G. 2008, A&A, 487, 247

Fish, V. L., Muehlbrad, T. C., Pratap, P., et al. 2011, ApJ, 729, 14

Friedel, D. N., & Widicus Weaver, S. L. 2011, ApJ, 742, 64

Galli, D., & Shu, F. H. 1993, ApJ, 417, 220

Garay, G., Reid, M. J., & Moran, J. M. 1985, ApJ, 289, 681

Genzel, R., & Downes, D. 1977, A&AS, 30, 145

Goldsmith, P. F. 1972, ApJ, 176, 597

Goodman, A. A., Crutcher, R. M., Heiles, C., Myers, P. C., & Troland, T. H. 1989, ApJ, 338, L61

Hachisuka, K., Brunthaler, A., Menten, K. M., et al. 2006, ApJ, 645, 337

Hackwell, J. A., Grasdalen, G. L., & Gehrz, R. D. 1982, ApJ, 252, 250

Hakobian, N. S., & Crutcher, R. M. 2011, ApJ, 733, 6

Hakobian, N. S., & Crutcher, R. M. 2012, ApJ, 758, L18

Heiles, C., & Crutcher, R. 2005, in Lecture Notes in Physics, Berlin Springer Verlag, Vol. 664, Cosmic Magnetic Fields, ed. R. Wielebinski & R. Beck, 137

Heiles, C., & Stevens, M. 1986, ApJ, 301, 331

Heiles, C., Perillat, P., Nolan, M., et al. 2001a, PASP, 113, 1247

Heiles, C., Perillat, P., Nolan, M., et al. 2001b, PASP, 113, 1274

Heyer, M. H., Snell, R. L., Morgan, J., & Schloerb, F. P. 1989, ApJ, 346, 220

Hezareh, T., Houde, M., McCoey, C., & Li, H.-b. 2010, ApJ, 720, 603

Hily-Blant, P., Walmsley, M., Pineau Des Forêts, G., & Flower, D. 2008, A&A, 480, L5

Ho, P. T. P., & Haschick, A. D. 1981, ApJ, 248, 622

Ho, P. T. P., & Haschick, A. D. 1986, ApJ, 304, 501

Ho, P. T. P., Terebey, S., & Turner, J. L. 1994, ApJ, 423, 320

Ho, P. T. P., Vogel, S. N., Wright, M. C. H., & Haschick, A. D. 1983, ApJ, 265, 295

Hoare, M. G. 2005, Ap&SS, 295, 203

Houde, M. 2011, in Astronomical Society of the Pacific Conference Series, Vol. 449, Astronomical Society of the Pacific Conference Series, ed. P. Bastien, N. Manset, D. P. Clemens, & N. St-Louis, 213

Houde, M., Bastien, P., Peng, R., Phillips, T. G., & Yoshida, H. 2000a, ApJ, 536, 857

Houde, M., Peng, R., Phillips, T. G., Bastien, P., & Yoshida, H. 2000b, ApJ, 537, 245

Houde, M., Bastien, P., Dotson, J. L., et al. 2002, ApJ, 569, 803

IRAM. 2009, IRAM 30m Efficiencies

Jones, E., Oliphant, T., Peterson, P., et al. 2001, SciPy: Open source scientific tools for Python

Jørgensen, J. K., Schöier, F. L., & van Dishoeck, E. F. 2004, A&A, 416, 603

Kawamura, J. H., & Masson, C. R. 1998, ApJ, 509, 270

Kleinmann, D. E., & Low, F. J. 1967, ApJ, 149, L1

Kudoh, T., & Basu, S. 2008, ApJ, 679, L97

Lai, S.-P., Velusamy, T., & Langer, W. D. 2003, ApJ, 596, L239

Larson, R. B. 1981, MNRAS, 194, 809

Levenberg, K. 1944, Quarterly of Applied Mathematics, 2, 164

Li, H.-b., & Houde, M. 2008, ApJ, 677, 1151

Li, H.-b., Houde, M., Lai, S.-p., & Sridharan, T. K. 2010, ApJ, 718, 905

Lunttila, T., Padoan, P., Juvela, M., & Nordlund, Å. 2008, ApJ, 686, L91

Mac Low, M.-M., & Klessen, R. S. 2004, Reviews of Modern Physics, 76, 125

Marquardt, D. W. 1963, Journal of the Society for Industrial and Applied Mathematics, 11, 431

McKee, C. F., & Ostriker, E. C. 2007, ARA&A, 45, 565

Menten, K. M., Reid, M. J., Forbrich, J., & Brunthaler, A. 2007, A&A, 474, 515

Minchin, N. R., Ward-Thompson, D., & White, G. J. 1995, A&A, 298, 894

Moré, J. J., Garbow, B. S., & Hillstrom, K. E. 1980, User Guide for MINPACK-1, Tech. Rep. ANL-80-74, Argonne National Laboratory, Argonne, IL, USA

Morgan, J. A., Snell, R. L., & Schloerb, F. P. 1985, in Bulletin of the American Astronomical Society, Vol. 17, Bulletin of the American Astronomical Society, 563

Motte, F., Bontemps, S., Schilke, P., et al. 2007, A&A, 476, 1243

Mouschovias, T. C. 1991, in NATO ASIC Proc. 342: The Physics of Star Formation and Early Stellar Evolution, ed. C. J. Lada & N. D. Kylafis, 61

Mouschovias, T. C., & Ciolek, G. E. 1999, in NATO ASIC Proc. 540: The Origin of Stars and Planetary Systems, ed. C. J. Lada & N. D. Kylafis, 305

Mouschovias, T. C., & Spitzer, Jr., L. 1976, ApJ, 210, 326

Mouschovias, T. C., & Tassis, K. 2009, MNRAS, 400, L15

Nakamura, F., & Li, Z.-Y. 2005, ApJ, 631, 411

Nakamura, F., & Li, Z.-Y. 2008, ApJ, 687, 354

Nakano, T. 1978, PASJ, 30, 681

Norris, R. P., Booth, R. S., Diamond, P. J., & Porter, N. D. 1982, MNRAS, 201, 191

Ostriker, E. C., Stone, J. M., & Gammie, C. F. 2001, ApJ, 546, 980

Padin, S., Sargent, A. I., Mundy, L. G., et al. 1989, ApJ, 337, L45

Padoan, P., Jimenez, R., Juvela, M., & Nordlund, Å. 2004, ApJ, 604, L49

Padoan, P., & Nordlund, Å. 1999, ApJ, 526, 279

Plambeck, R. L., & Menten, K. M. 1990, ApJ, 364, 555

Raimond, E., & Eliasson, B. 1969, ApJ, 155, 817

Reid, M. J., & Moran, J. M. 1988, Astronomical masers, ed. K. I. Kellermann & G. L. Verschuur, 255

Rieke, G. H., Low, F. J., & Kleinmann, D. E. 1973, ApJ, 186, L7

Rodgers, J. L., & Nicewander, W. A. 1988, The American Statistician, 42, 59

Ruiz, A., Rodriguez, L. F., Canto, J., & Mirabel, I. F. 1992, ApJ, 398, 139

Rygl, K. L. J., Brunthaler, A., Reid, M. J., et al. 2010, A&A, 511, A2

Sault, R. J., Teuben, P. J., & Wright, M. C. H. 1995, in Astronomical Society of the Pacific Conference Series, Vol. 77, Astronomical Data Analysis Software and Systems IV, ed. R. A. Shaw, H. E. Payne, & J. J. E. Hayes, 433

Schilke, P., Walmsley, C. M., Pineau Des Forets, G., et al. 1992, A&A, 256, 595

Schneider, N., Csengeri, T., Bontemps, S., et al. 2010, A&A, 520, A49

Shepherd, D. S., Kurtz, S. E., & Testi, L. 2004, ApJ, 601, 952

Shu, F. H., Allen, A., Shang, H., Ostriker, E. C., & Li, Z.-Y. 1999, in NATO ASIC Proc. 540: The Origin of Stars and Planetary Systems, ed. C. J. Lada & N. D. Kylafis, 193

Simpson, J. P., Burton, M. G., Colgan, S. W. J., et al. 2009, ApJ, 700, 1488

Slysh, V. I., Kalenskii, S. V., Val'tts, I. E., & Golubev, V. V. 1997, ApJ, 478, L37

Snell, R. L., & Bally, J. 1986, ApJ, 303, 683

Tieftrunk, A. R., Megeath, S. T., Wilson, T. L., & Rayner, J. T. 1998, A&A, 336, 991

Troland, T. H., & Crutcher, R. M. 2008, ApJ, 680, 457

Turner, J. L., & Welch, W. J. 1984, ApJ, 287, L81

van der Tak, F. F. S., Black, J. H., Schöier, F. L., Jansen, D. J., & van Dishoeck, E. F. 2007, A&A, 468, 627

Vázquez-Semadeni, E., Kim, J., Shadmehri, M., & Ballesteros-Paredes, J. 2005, ApJ, 618, 344

Vogel, S. N., Bieging, J. H., Plambeck, R. L., Welch, W. J., & Wright, M. C. H. 1985, ApJ, 296, 600

Wang, Y., Beuther, H., Bik, A., et al. 2011, A&A, 527, A32

White, S. M., & Zauderer, B. A. 2008, CARMA Memorandum Series #49, Single-Dish Aperture Efficiency Measurments at CARMA

Wilner, D. J., Welch, W. J., & Forster, J. R. 1995, ApJ, 449, L73

Wilson, T. L. 1974, A&A, 31, 83

Wilson, T. L., Gaume, R. A., & Johnston, K. J. 1993, ApJ, 402, 230

Wilson, T. L., Johnston, K. J., & Mauersberger, R. 1991, A&A, 251, 220

Wink, J. E., Duvert, G., Guilloteau, S., et al. 1994, A&A, 281, 505

Wright, M. C. H., Plambeck, R. L., & Wilner, D. J. 1996, ApJ, 469, 216

Wynn-Williams, C. G., Becklin, E. E., & Neugebauer, G. 1972, MNRAS, 160, 1

Wyrowski, F., Hofner, P., Schilke, P., et al. 1997, A&A, 320, L17

Zapata, L. A., Loinard, L., Su, Y.-N., et al. 2012, ApJ, 744, 86

Zuckerman, B., Ball, J. A., Dickinson, D. F., & Penfield, H. 1969, Astrophys. Lett., 3, 97